Global modeling of pollutant transport and deposition from anthropogenic emission hot spots on global scale

DISSERTATION
zur Erlangung des Grades
"Doktor der Naturwissenschaften"
(Dr. rer. nat.)

am Fachbereich 08 für Physik, Mathematik und Informatik
der Johannes Gutenberg-Universität
in Mainz

Daniel Kunkel
geboren in Lohr am Main

Mainz, November 2012

Tag der mündlichen Prüfung: 18.01.2013

D77 - Mainzer Dissertationen

Abstract

Urban centers significantly contribute to anthropogenic air pollution, although they cover only a minor fraction of the Earth's land surface. Since the worldwide degree of urbanization is steadily increasing, the anthropogenic contribution to air pollution from urban centers is expected to become more substantial in future air quality assessments. The main objective of this thesis was to obtain a more profound insight in the dispersion and the deposition of aerosol particles from 46 individual major population centers (MPCs) as well as the regional and global influence on the atmospheric distribution of several aerosol types. For the first time, this was assessed in one model framework, for which the global model EMAC was applied with different representations of aerosol particles. First, in an approach with passive tracers and a setup in which the results depend only on the source location and the size and the solubility of the tracers, several metrics and a regional climate classification were used to quantify the major outflow pathways, both vertically and horizontally, and to compare the balance between pollution export away from and pollution build-up around the source points. Then in a more comprehensive approach, the anthropogenic emissions of key trace species were changed at the MPC locations to determine the cumulative impact of the MPC emissions on the atmospheric aerosol burdens of black carbon (BC), particulate organic matter (POM), sulfate (SO_4^{2-}), and nitrate (NO_3^-).

Ten different mono-modal passive aerosol tracers were continuously released at the same constant rate at each emission point. The results clearly showed that on average about five times more mass is advected quasi-horizontally at low levels than exported into the upper troposphere. The strength of the low-level export is mainly determined by the location of the source, while the vertical transport is mainly governed by the lifting potential and the solubility of the tracers. Similar to insoluble gas phase tracers, the low-level export of aerosol tracers is strongest at middle and high latitudes, while the regions of strongest vertical export differ between aerosol (temperate winter dry) and gas phase (tropics) tracers. The emitted mass fraction that is kept around MPCs is largest in regions where aerosol tracers have short lifetimes; this mass is also critical for assessing the impact on humans. However, the number of people who live in a strongly polluted region around urban centers depends more on the population density than on the size of the area which is affected by strong air pollution. Another major result was that fine aerosol particles (diameters smaller than 2.5 micrometer) from MPCs undergo substantial long-range transport, with about half of the emitted mass being deposited beyond 1000 km away from the source. In contrast to this diluted remote deposition, there are areas around the MPCs which experience high deposition rates, especially in regions which are frequently affected by heavy precipitation or are situated in poorly ventilated locations. Moreover, most MPC aerosol emissions are removed over land surfaces. In particular, forests experience more deposition from MPC pollutants than other land ecosystems. In addition, it was found that the generic treatment of aerosols has no substantial influence on the major conclusions drawn in this thesis. Moreover, in the more comprehensive approach, it was found that emissions of BC, POM, sulfur dioxide (SO_2), and nitrogen oxides (NO_x) from MPCs influence the atmospheric burden of various aerosol types very differently, with impacts generally being larger for secondary species, SO_4^{2-} and NO_3^-, than for primary species, BC and POM. While the changes in the burdens of SO_4^{2-}, BC, and POM show an almost linear response for changes in the emission strength, the formation of NO_3^- was found to be contingent upon many more factors, e.g., the abundance of sulfuric acid, than only upon the strength of the NO_x emissions.

The generic tracer experiments were further extended to conduct the first risk assessment to obtain the cumulative risk of contamination from multiple nuclear reactor accidents on the global scale. For this, many factors had to be taken into account: the probability of major accidents, the cumulative deposition field of the radionuclide cesium-137, and a threshold value that defines contamination. By collecting the necessary data and after accounting for uncertainties, it was found that the risk is highest in western Europe, the eastern US, and in Japan, where on average contamination by major accidents is expected about every 50 years

Zusammenfassung

Urbane Ballungsräume tragen in großem Maße zur heutigen Luftverschmutzung bei, obwohl sie nur einen kleinen Teil der Landoberfläche einnehmen. Da die Urbanisierung weltweit zunimmt, wird erwartet, dass der Eintrag anthropogener Schadstoffe aus urbanen Zentren in zukünftigen Luftreinhaltungsstudien eine große Rolle spielen wird. Um den Beitrag der Ballungszentren besser einordnen und quantifiziern zu können, wurden in dieser Arbeit zum ersten Mal in einem Modellsystem mit dem globalem Model EMAC die Ausbreitung und Deposition von Aerosolpartikeln aus 46 einzelnen Ballungszentren sowie der regionale und globale Einfluss von Emissionen aus diesen Zentren auf die Konzentrationen verschiedener Aerosoltypen berechnet. Zum einen wurde ein Ansatz mit passiven Tracern gewählt, bei dem mit Hilfe von Metriken und einer Klimaklassifikation der Ferntransport sowie die lokale Luftverschmutzung quantifiziert worden sind, wobei die Resultate nur vom Ort der Emissionen sowie der Größe und der Löslichkeit der Aerosole abhängen. Zum anderen wurden in Sensitivitätsstudien die anthropogenen Emissionen wichtiger Schadstoffe in den Ballungszentren geändert, um den Einfluss auf elementaren Kohlenstoff (englisch: black carbon, BC), organischen Feinstaub (englisch: particulate organic matter, POM), Sulfat (SO_4^{2-}) und Nitrat (NO_3^-) zu bestimmen.

Im Modell wurden am Ort jedes Ballungszentrums mono-modale, passive Aerosoltracer kontinuierlich und mit konstanter Rate emittiert. Dabei zeigte sich, dass im Mittel der bodennahe Ferntransport von Aerosolen um das fünffache größer ist als der Export in die obere Troposphäre, wobei der bodennahe Ferntransport hauptsächlich vom Emissionsort abhängt, der vertikale Transport hingegen mehr vom Hebungspotential der Luftmassen in einer Region und der Löslichkeit der Tracer. Der stärkste Ferntransport von Aerosolen ist wie für nicht lösliche Gase in mittleren und hohen Breiten am stärksten, wohingegen der stärkste vertikale Transport von Aerosolen nicht in den Regionen auftritt (winter-trockene, gemäßigte Zonen), in denen er am stärksten ist für nicht lösliche Gase (Tropen). Starke Verschmutzungen um die Emissionspunkte treten dagegen generell in den Regionen auf, in denen die Lebenszeit der Aerosole kurz ist. Darüber hinaus sind um die Emissionsgebiete herum die meisten Menschen von starker Luftverschmutzung betroffen, wobei die Zahl der Betroffenen mehr von der Bevölkerungsdichte als von der Größe der stark belasteten Region abhängt. Eines der Hauptergebnisse dieser Studie war, dass in etwa die Hälfte der Feinstaubemissionen (Partikeldurchmesser kleiner als 2.5 Mikrometer) aus den Ballungszentren mehr als 1000 km weit transportiert wird, bevor es zur Deposition kommt. Hingegen wird im Umland der Emissionspunkte Aerosolmasse in hoher Konzentration deponiert, vor allem in Regionen, in denen es häufig zu Starkregen kommt oder dort wo die lokale Zirkulation keine günstige Ventilation erlaubt. Ferner wird ein Großteil der Emissionen über Land deponiert, wobei vor allem Wälder betroffen sind. Zusätzlich wurde der Einfluss der generischen Darstellung von Aerosolen untersucht, der, wie sich herausstellte, keinen großen Einfluss auf die Ergebnisse hat. Die Sensitivitätsstudien bezüglich des Einflusses von BC, POM sowie Schwefeldioxid und Stickoxiden aus den Ballungszentren schwankt stark nach Aerosoltyp: sekundäre Aerosole zeigen dabei größere Änderungen als primäre Aerosole. Die atmosphärischen Konzentrationen von SO_4^{2-}, BC und POM ändern sich annähernd linear mit Änderungen in den entsprechenden Emissionen. Dagegen spielen bei der Bildung von Nitrat neben der Emissionstärke weitere Faktoren eine wichtige Rolle, vor allem die Menge der verfügbaren Schwefelsäure und die Umgebungstemperatur.

Die generischen Tracer wurden ferner dafür benutzt die erste globale Risikoanalyse über die Kontamination nach nuklearen Reaktorunfällen anzufertigen. Dabei müssen viele Faktoren berücksichtigt werden, unter anderem die Wahrscheinlichkeit eines größtmöglichen Unfalls, das Depositionsfeld von Cäsium-137 und ein Grenzwert, über den die Kontamination definiert ist. Nachdem diese Faktoren sowie die Unsicherheiten berücksichtigt worden sind, wurde bestimmt, dass das Risiko in Westeuropa, im Osten der USA und in Japan am höchsten ist. In diesen Regionen tritt dabei Kontamination durch größtmögliche Unfälle im Schnitt alle 50 Jahre auf.

Contents

Part I Methodology

Part II Urban Emission Hot Spots

Part III Nuclear Power Plants

Part IV Conclusions

Part V Appendix

1

Introduction

Both natural and anthropogenic emissions have major implications on the Earth's atmosphere. While the natural emissions are considered to contribute to the background atmosphere, the emissions from human activities add additional amounts of trace species and even some purely anthropogenic gases and particles. Independent of their physical phase state, these species are often referred to as air pollutants (UNECE, 1979).

Humans recognized their contribution already in ancient Greece and Rome, where blackening of houses was reported and later in the Middle Ages when producing quicklime and burning limestone or sea coal. However, at these times anthropogenic pollution was a local problem which first increased substantially after the Industrial Revolution and the introduction of new means of locomotion, i.e., the railroad and the automobile. In the beginning of the twentieth century the term smog, i.e., a combination of smoke and fog, was introduced, which was typically present in cities in Great Britain in the nineteenth century. Next to this so-called London-type smog, another smog-type was observed, which originates from photochemical reactions, the so-called LA-type smog (Finlayson-Pitts and Pitts, 1997; Jacobson, 2002).

Air pollution from anthropogenic sources occurs on different spatial and temporal scales. Emissions can rapidly lead to a decrease in air quality near their source, in particular by degrading visibility (Watson, 2002) or affecting human health (Dockery et al., 1993; Pope et al., 2009). However, some anthropogenic emissions need first to be transformed to different pollutants, which are considered as harmful, e.g., nitrogen oxides as catalysts to form ozone. These pollutants often decrease the air quality several hundred to thousand kilometers downwind of their source. Moreover, chemically long-lived species can even have global impacts. Many of these agents such as carbon dioxide, methane or the chlorofluorocarbons (CFCs) are subjects in the climate warming debate since they have a large global warming potential (Solomon et al., 2007). The CFCs also play the most important role in reducing the stratospheric ozone (e.g., Jacobson, 2002).

Anthropogenic pollutants are released from agriculture, the energy sector, industry and manufacturing, housing, and mining. In many regions the emissions from one or several of these sectors dominate over natural emissions and can cause severe air quality problems under unfavorable meteorological conditions. Especially in urban environments, where many pollutants are released on a small scale, the effects are quite large. These strong localized emissions can either lead to strong localized pollution build-up or pollution export, affecting downwind regions. This depends to a large extent on the geographical location and the prevailing meteorological conditions. Since 2007 the urban population represents the majority of the human population, with an ongoing growth of urban agglomerations (UNFPA, 2007). The largest urban centers are so-called megacities or major population centers. In 1975, only three cities were categorized as megacities, but until today their number increased to over 20. Research was first focused on the air quality in the megacities, but has changed in the last years to focusing more on the regional and global impacts from megacities. For this, detailed knowledge is required about the megacity emissions and the mechanisms driving the pollutant dispersion in and away from the megacities. Especially the global impacts are not well quantified yet, and thus far only studies for gas phase species emissions and transport have been conducted (Lawrence et al., 2007; Butler and Lawrence, 2009; Butler et al., 2012). In contrast, aerosol species from major population centers have been neglected, although they affect both human health and climate.

To obtain an overview of many source points, a global model of the atmosphere is a valuable tool to study the pollutant dispersion. Observations are commonly limited to local or regional aspects, focusing on one to a few source points. Similarly, regional models cannot provide one consistent framework to investigate anthropogenic source points that are distributed over the entire globe.

Another anthropogenic emission source of global importance are major accidents of nuclear power plant reactors. These emission source points can be treated similarly to megacities in terms of emission and dispersion modeling. The interest in such accidents mainly relies on the fact that the pollutants are radioactive and thus emit radiation that can harm humans and the environment, both in the atmosphere and after deposition.

1.1 Anthropogenic emissions

While both aerosol particles and trace gases are released from anthropogenic sources, this thesis concentrates mainly on different types of aerosols, either being represented generically or within a modal aerosol scheme. When it is appropriate, the aerosols are compared to trace gases.

The distribution of trace gases in the atmosphere is mainly determined by their atmospheric lifetimes and their solubilities. The lifetime depends on how fast a species reacts kinetically or photochemically (Jacobson, 2002), and varies between several hours to days, for instance nitrogen oxides (NO_x), and weeks, for example ozone (O_3), or up to several months, for example carbon monoxide (CO) or some nonmethane hydrocarbons (NMHCs). The solubility of a trace species determines how well a species can dissolve in liquid water and is reflected in its Henry's law coefficient (Seinfeld and Pandis, 1998). However, the generic aerosol tracers are only compared to insoluble, inert trace gases, which decay exponentially. In contrast, for the majority of the tropospheric aerosol particles the lifetime is between a day and two weeks and is mainly determined by two key aerosol properties: size and solubility. This is discussed in detail in the following paragraph, after which an introduction will be given to two different anthropogenic emission source points: major population centers and nuclear power plants.

1.1.1 Atmospheric aerosols

Aerosols are characterized by their size distribution and composition. The size distribution is the variation of one of the descriptive properties, i.e., number, surface area, volume, or mass of particles per unit volume of air, with size (e.g., Jacobson, 2002). The size of aerosol particles ranges from nanometers up to several tenths of micrometers (Figure 1.1a). Aerosol particles are larger than gas molecules but usually smaller than atmospheric hydrometeors such as fog drops, cloud drops, drizzle or raindrops. Furthermore, aerosol particles can be divided in so-called modes which are regions of the size spectrum in which distinct peaks in concentration occur. The modes can be analytically described with a lognormal function (example given in Figure 1.1b, Seinfeld and Pandis, 1998).

The smallest mode is defined as the nucleation mode (also sometimes called the Aitken mode, with mean diameter less than 0.1 µm). It contains small emitted or newly formed particles which originate from the gas phase and it dominates the number size distribution (Figure 1.1b). Often only the smallest, newly formed aerosol particles (less than 10 nm) are defined as nucleation mode particles, while the particles between 10 and 100 nm are classified as Aitken mode particles. Both directly emitted particles and newly formed particles grow in size by coagulation, i.e., collision of particles, and/or condensation of gases like sulfuric acid, water, and various organic species onto particles. This growth moves the particles into the accumulation mode, where diameters are between 0.1 and 2.0 µm. The accumulation mode dominates the surface area size distribution (Figure 1.1b). The particles in this size range are commonly removed by rain, but they are still too light to gravitationally settle down to the Earth's surface within a relevant time frame. Aerosol particles in the nucleation and Aitken modes range, but also to an extent in the accumulation mode are likely to affect health since the particles can penetrate deep into the lungs (Pöschl, 2005). Moreover, their size is close to the peak wavelength of visible light and thus can efficiently degrade visibility (Jacobson, 2002). Particles with diameters less than 2.0 µm are commonly referred to as fine particles[1]. Larger particles are in the coarse mode. These particles originate from wind-blown dust, sea spray, volcanoes or plants. The particles are rapidly removed from the atmosphere by sedimentation. The coarse mode is most prominent in the volume size distribution (Figure 1.1b). Since fine particles grow only to a size of about one micrometer by condensation and coagulation, the large particles have to be either emitted directly or grow by cloud processing, that is by acting as a cloud condensation or ice nuclei, into the coarse mode (Jacobson, 2002).

Figure 1.2 summarizes the aerosol processes in the atmosphere. Aerosol particles originate from a wide variety of natural and anthropogenic sources, which have strong effects of the initial composition of the aerosols. Aerosol particles directly emitted as liquids or solids to the atmosphere are defined as primary particles. Secondary particles are formed in the atmosphere by gas-to-particle conversion and/or condensation of gaseous compounds on pre-existing aerosols (Monks et al., 2009). Emissions from sources such as biomass burning, incomplete combustion of fossil or bio-fuels, or wind-driven suspension of mineral dust introduce more insoluble particles into the atmosphere. These particles have a low wettability

---

[1] Especially in air quality assessments, a diameter of 2.5 µm is often applied to define the particulate mass of fine aerosols ($PM_{2.5}$).

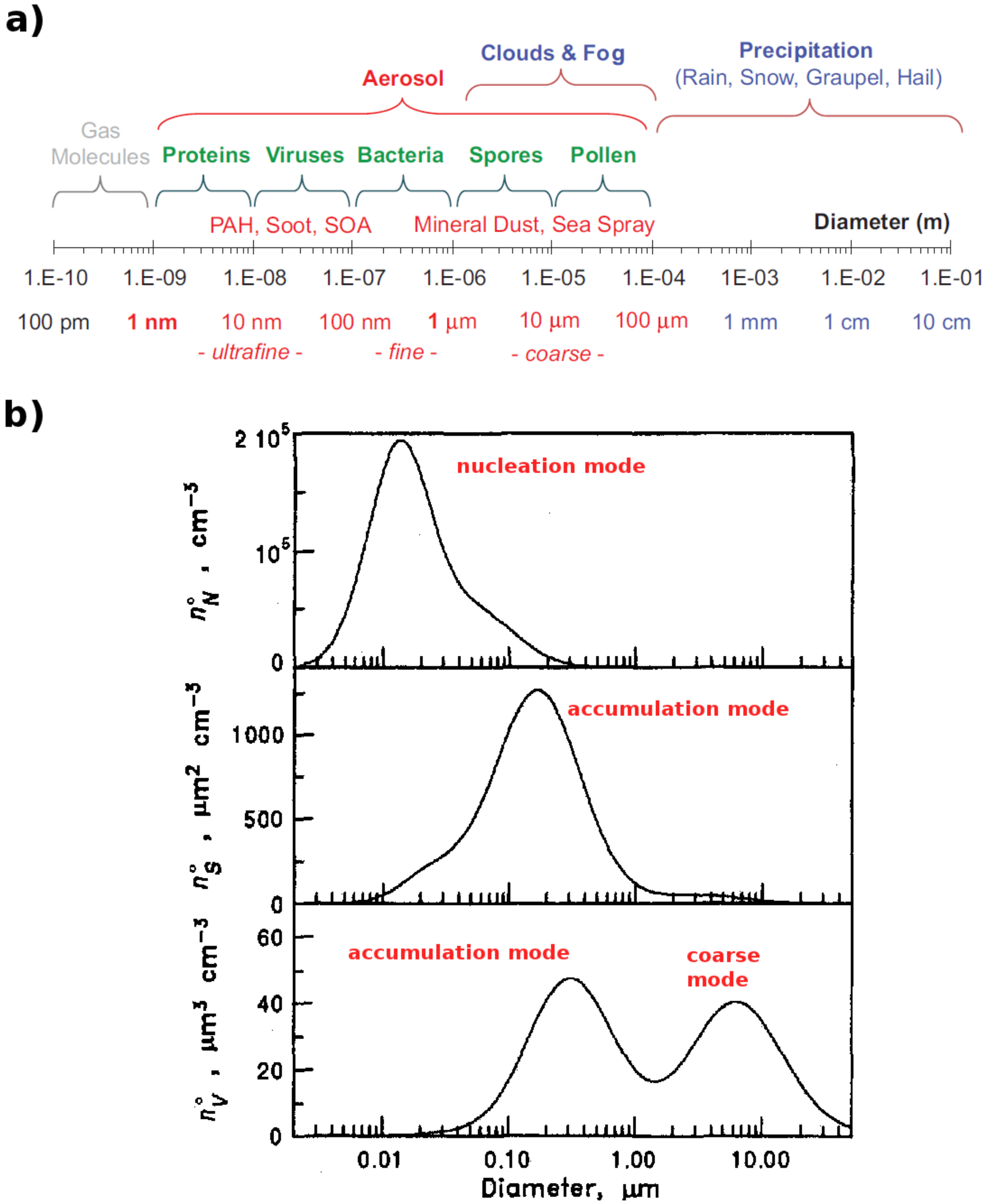

Figure 1.1: a) Aerosol particle size range with typical anthropogenic, natural and biogenic aerosol types (lecture notes, U. Pöschl, 2011). b) Example of an aerosol size distribution, shown for urban aerosol as number distribution (n°_N, in cm^{-3}) with a distinct nucleation mode (upper panel), surface area distribution (n°_S, in $\mu m^2\, cm^{-3}$) with a distinct accumulation mode (middle panel), and volume distribution (n°_V, in $\mu m^{-3}\, cm^{-3}$) with distinct accumulation and coarse mode (lower panel), from Seinfeld and Pandis (1998).

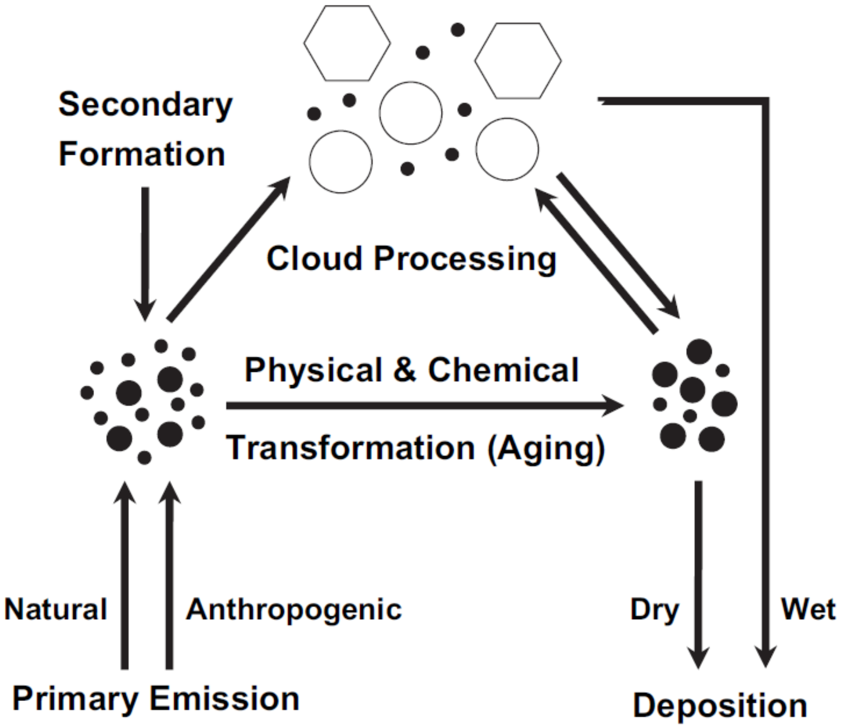

Figure 1.2: Schematic depiction of the atmospheric aerosol lifecycle: primary emissions, secondary formation, and atmospheric processing of natural and anthropogenic emissions, adopted from Pöschl (2005).

of the surface and hence a low efficiency to become a cloud condensation nuclei (Pöschl, 2005). In contrast, many secondary particles and some directly emitted particles such as sea spray are soluble and can act as cloud condensation nuclei. Insoluble particles can become coated by gaseous compounds or coagulate with soluble aerosol particles to also increase their solubility (sometimes referred to as aerosol aging).

The generally most abundant individual compounds in aerosols from anthropogenic activities are black carbon and organic matter, which are directly emitted from combustion, along with sulfate, nitrate, and ammonium, which are formed from precursor gases sulfuric acid, nitric acid, and ammonia. However, in most cases aerosol particles are mixtures of these compounds with other minor abundant species such as metals or fly ash. Most of the anthropogenic aerosols are emitted as fine aerosols. Aerosols from natural sources comprise additional sources, especially those of dessert dust, sea spray, and biogenic emissions. Moreover, the emissions from natural sources contribute to the concentration of both fine and coarse particles (e.g., Seinfeld and Pandis, 1998; Jacobson, 2002; Andreae and Rosenfeld, 2008; Monks et al., 2009).

1.1.2 Emissions from urban agglomerations

Since 2007, the majority of the human population now lives in urban regions, with the prospect that the trend of human inflow into urban areas will continue throughout this century (UNFPA, 2007). Projections show that in 2030 the urban population will increase to nearly five billion people, but little is known about exact future locations, magnitudes, and rates of urban expansion (Seto et al., 2012). The largest of these agglomerations are the so-called megacities or major population centers (MPCs), with populations of at least five or ten million people (depending on definition, e.g., UNFPA, 2007; Baklanov et al., 2010). These generally develop often much faster than the country in which they are located in and promote human development as well as generation of knowledge, technology, and wealth (Kraas, 2007; Gurjar and Lelieveld, 2005). Furthermore, they can offer a significant chance for climate mitigation strategies as the per capita emission of CO_2 is often smaller when many people live close together (Parrish and Zhu, 2009). However, these human agglomerations are very heterogeneous with respect to possible lifestyle of different groups, and consequently manifest different awareness in the handling of energy, water, and waste. Moreover, both increased residential housing as well as the clustering of industry in these metropolitan areas lead to the strong localized release of air pollutants, which generally decreases the air quality for local dwellers as well as in regions downwind (Molina and Molina, 2004). The urban growth occurs on less than 3 % of the global land surface, but with global consequences (Grimm et al., 2008), especially for land-cover and land-use (Kalnay and Cai, 2003).

This has led to considerable research efforts on megacities during the last decade. Large megacity projects have been conducted at several supersites, e.g., PRIDE-PRD-2004[2], PRIDE-PRD-2006[3], CAREBEIJING[4], MCMA-2003[5], MILAGRO[6], CityZEN[7], and MEGAPOLI[8]. In general, the focus of such large projects is on pollutant levels in the megacities and on the question, where the pollution originates from. Thus, the local and regional effects are generally investigated, sometimes only for a single supersite.

Satellites can be also used to examine megacities. One example is given by Cermak and Knutti (2009). They compared aerosol optical depths during the Beijing Olympic Games in 2008 to those from previous years and showed that emission reductions appeared to be less important than meteorological conditions and thus that transport of aerosols is important to determine the local aerosol burden. Another study by Beirle et al. (2011) used satellite data to simultaneously estimate the emission and lifetime of nitrogen oxides from several megacities. Satellite observations have a large potential but are still limited in data coverage, especially for surface pollution in cloudy regions.

---

[2] Program of Regional Integrated Experiments on Air Quality over Pearl River Delta of China 2004, Zhang et al. (2008)

[3] see special issue in Atmospheric Chemistry and Physics: http://www.atmos-chem-phys.net/special_issue164.html, as of 20.10.2012

[4] Regional formation processes and controlling effects of air pollution before and during the Beijing Olympics, see special issue in Atmospheric Chemistry and Physics: http://www.atmos-chem-phys.net/special_issue198.html, as of 20.10.2012

[5] Mexico City Metropolitan Area Field Campaign 2003, see special issue in Atmospheric Chemistry and Physics: http://www.atmos-chem-phys.net/special_issue21.html as of 20.10.2012 and Molina et al. (2007)

[6] Megacity Initiative: Local And Global Research Observations, see special issue in Atmospheric Chemistry and Physics: http://www.atmos-chem-phys.net/special_issue83.html as of 20.10.2012, the project web page: http://www.eol.ucar.edu/projects/milagro/ as of 20.10.2012, and Molina et al. (2010)

[7] see project web page: http://www.cityzen-project.eu/, as of 20.10.2012 and Gauss (2011)

[8] Megacities: Emissions, urban, regional and Global Atmospheric POLlution and climate effects, and Integrated tools for assessment and mitigation, see special issue in Atmospheric Chemistry and Physics: http://www.atmos-chem-phys.net/special_issue229.html, as of 20.10.2012, the project web page: http://www.megapolit.info as of 20.10.2012, and Baklanov et al. (2010)

In many of the megacity projects have not only measurements been conducted but also numerical model studies (e.g., Karydis et al., 2010; Emmons et al., 2010; Wang et al., 2010; Gao et al., 2011). Furthermore, observations and model results have been used to compare megacities in various regions and their cumulative impact on the atmospheric composition (e.g., Guttikunda et al., 2003; Molina and Molina, 2004; Guttikunda et al., 2005; Cuvelier et al., 2007; Chan and Yao, 2008; Parrish et al., 2009; Kanakidou et al., 2011; Parrish et al., 2011).

In contrast to the numerous assessments of the local to regional impacts, there is only a sparse number of global modeling studies of pollution from megacities. Butler et al. (2008) took a first step to assess the representation of megacities in global emission inventories and how they relate to regional inventories. They focused on gas phase species CO, NO_x, and NMHCs and found that there are large uncertainties between the emissions for individual cities, although the different inventories are in many cases based on the same data and construction methodology. In a next step, Butler and Lawrence (2009) examined the effects of megacity emissions on global atmospheric gas phase chemistry by using a global three-dimensional chemical transport model. For year 2000 conditions they found that the effects on air quality, radiative forcing, and atmospheric oxidation are smaller than expected. In contrast, the effects of megacities on reactive nitrogen are comparably large. Moreover, they showed that tropical and extra-tropical megacities respond differently with respect to the ozone formation. In extra-tropical megacities the emissions lead to local ozone reduction and downwind production, while ozone is generally produced in the tropics. In a follow-up study, Butler et al. (2012) focused on the impact of megacities on atmospheric chemistry under four different RCP (Representative Concentration Pathway) scenarios and on the impact of emissions from outside on the megacities. They expect that future air quality is less influenced by local emissions within the cities, but instead more influenced by emission sources outside of the cities.

Another possible approach to study megacities on the global scale was developed in Lawrence et al. (2007). They used artificial tracers in a chemical transport model, generally representing the complex effects of chemical reactions, to study the outflow of pollutants from megacity source points. They show that low-level export is strongest at middle and high latitudes. Vertical export is strongest in the tropics and is furthermore found to be the most efficient process for diluting the surface layer pollution build-up. However, they only used artificial insoluble gas phase tracers with fixed decay lifetimes and did not consider tracers with variable lifetimes or which have different solubilities, e.g., aerosols.

1.1.3 Emissions from nuclear power plant accidents

Power plants which generate electricity are also considered as anthropogenic emission source points. They are often the subject of regional air quality assessments, since they release pollutants from fossil or bio fuel burning which can degrade visibility and have impacts on human health. One type of power plant is typically not considered in pollution dispersion studies, but can have significant implications in the case of an accident: nuclear power plants (NPPs). For the Chernobyl accident in 1986, detailed observations are available on the spatial distribution of radioactive soil contamination (e.g., De Cort et al., 1998), which show that radionuclides released during major nuclear reactor accidents can contaminate large regions close to the source, and also farther away. Measurements even indicated that radionuclides from the Chernobyl accident have been deposited around the entire Northern Hemisphere (e.g., Dorrian, 1997).

Even before Chernobyl, nuclear power plants have been subject to risk assessment studies (e.g., NRC, 1975; GRS, 1980), which have been re-assessed afterwards (e.g., NRC, 1990; GRS, 1990). These reports concentrated on the possibilities of failures of the technical and safety facilities of the nuclear power plants. Moreover, various tools have been used to obtain probability maps of regions which are most vulnerable to nuclear accidents (e.g., http://flexrisk.boku.ac.at or Baklanov and Mahura, 2004, and references therein). However, all approaches concentrated on local to regional impacts, with a global assessment missing.

1.2 Transport of trace species

Once emitted from the source, trace species undergo transport and transformation processes before they are removed from the atmosphere. As described earlier, aerosol particles are physically and chemically transformed, while gas phase species either undergo kinetic reactions or become photolysed. Meanwhile, the trace species are transported in the atmosphere, before they are removed from the atmosphere by wet and dry deposition processes such as scavenging in and below clouds or turbulent mixing in the surface layer. The transport pathways depend on the large-scale circulation as well as on local and regional meteorological phenomena.

In the extra-tropics, the background flow is dominated by westerly winds. On the regional scale, frontal systems, especially in winter but also in summer (e.g., Li et al., 2005; Fang et al., 2009; Itahashi et al., 2010), and convective systems, especially in summer (e.g., Dickerson et al., 1995), can have major influence on the distribution of trace species. Thus, the transport can be either at low tropospheric levels, e.g., in the planetary boundary layer, or in the free troposphere, depending on whether lifting in warm conveyor belts or convective systems takes place (e.g., Liu et al., 2003; Mari et al., 2004; Cooper et al., 2004; Verma et al., 2011; Moteki et al., 2012). On some occasions the surface emissions can also be lifted into the upper troposphere or even directly into the lowermost stratosphere (e.g., Fischer et al., 2003). Zonal transport occurs more frequently and can be very rapid, for instance in fast moving cyclones (e.g., Wilkening et al., 2000; Stohl et al., 2002, 2003b). Nevertheless, pollutants can also be efficiently transported in the meridional direction, contributing for instance to Arctic haze formation (e.g., Stohl et al., 2002; Di Pierro et al., 2011).

In the tropics, the circulation is dominated by the mean meridional Hadley cells of the two hemispheres. Moreover, regional monsoon circulation systems in India, West Africa, South-East Asia, and South America, low-level convergence zones, and upper tropospheric jets have strong influence on the fate of trace species in the tropical atmosphere (see e.g., Hastenrath, 1985). Since the major wind direction of monsoon circulations changes by definition, the export pathways vary consequently by season. Moreover, during the rainy season large mesoscale convective systems often develop, which have diameters of several hundred kilometers. These thunderstorm systems can lift surface pollution into the upper troposphere (up to about 18 km) or efficiently remove soluble trace species by scavenging (e.g., Dickerson et al., 1987; Houze, 2004; Lawrence and Salzmann, 2008).

Trace species can undergo transport from local to intercontinental scales on timescales varying between several hours to weeks (e.g., Stohl et al., 2002; Holloway et al., 2003; Liu et al., 2005). In particular, the long transport distances and long timescales lead to pollution transport being considered in policy making because of transboundary pollution potentials (Bergin et al., 2005). For instances, it is well known that emissions of trace gases and aerosols from East Asia can travel over the northern Pacific and increase the concentrations of trace species at low levels as well as in the free troposphere in North America (e.g., Berntsen et al., 1999; Jaffe et al., 1999; Takemura et al., 2002; Heald et al., 2006; Hadley et al., 2007; Clarisse et al., 2011). In principle, the same occurs for emissions from North America, which can cross the North Atlantic and enhance the concentration in Europe (e.g., Huntrieser et al., 2005; Owen et al., 2006; Christoudias et al., 2012). In extreme occasions of long-range transport, emissions from Europe can mix with those from East Asia and travel to North America (e.g., Newell and Evans, 2000; Staudt et al., 2001; Price et al., 2004; Lin et al., 2008) and pollution from Asia can be seen over Europe after circling the globe (Lelieveld et al., 2002). Generally, pollutant concentrations are diluted during transport, but it is also possible that pollutants accumulate in particular regions. This can cause severe pollution events such as Arctic haze or ABCs (Atmospheric Brown Clouds, e.g., Ramanathan et al., 2007; Lawrence and Lelieveld, 2010).

The lifetime in the atmosphere strongly depends on properties of the species and on meteorological conditions. Aerosol particles which have lifetimes of days to weeks are generally thought to undergo less transport than long-lived gas phase species and contribute more to regional air pollution problems. However, observations and model simulations show that small and large aerosol particles can also travel long distances in the atmosphere, from continental (e.g., Park et al., 2003; Wagstrom and Pandis, 2010, 2011) to intercontinental scales (e.g., Prospero et al., 1970; Betzer et al., 1988; Chin et al., 2007; Liu et al., 2009). However, long-range transport of aerosols from small scale sources on the global scale is more associated with natural emissions from volcanic eruptions (e.g., Schmale et al., 2010) or pyrogenic convection (e.g., Andreae et al., 2001; Fromm and Servranckx, 2003), which can, however, be caused by anthropogenic activities, too. In both cases, aerosol particles are directly emitted in large quantities in the upper troposphere, sometimes even in the lower stratosphere. In general, anthropogenic surface emissions from small scale sources are often difficult to identify in observations since they mix with other emissions in the outflow plume and can only be traced back on some occasions (e.g., Stohl et al., 2003a).

Studies of the transport of anthropogenic emissions from specific sources have been focusing on emissions from larger source regions (e.g., Stohl et al., 2002), or on impacts on regional scales (e.g., Guttikunda et al., 2005; Wagstrom and Pandis, 2011). To my knowledge, the before mentioned study of Lawrence et al. (2007) is the only study which investigated the pollution outflow and build-up from major population centers worldwide in one model framework. However, their study was limited to insoluble gas phase tracers, which had various, but fixed lifetimes and were removed from the atmosphere only by an exponential decay.

1.3 Goals of this work and outline

This thesis starts where Lawrence et al. (2007) left off, still focusing on transport pathways, but also on deposition patterns of pollutants released from anthropogenic source points. The main focus is on aerosols which have varying atmospheric lifetimes, which depend on aerosol properties, especially size and solubility, and on prevailing meteorological conditions in different regions.

By applying a global, three dimensional, state-of-the-art atmospheric chemistry general circulation model, the trade-off between pollution build-up and export is studied as well as the deposition of aerosols from major population centers. It will further be shown that passive tracers can be used to efficiently represent atmospheric pollutants in transport studies. However, to quantify the impact of megacity emissions on the atmospheric burden of aerosols and trace gases, passive tracers are not sophisticated enough, since no chemistry and microphysical effects are considered. By using a comprehensive chemistry scheme and aerosol module, in which aerosol microphysics and thermodynamics are considered along with global emission inventories for various trace gases and aerosol types, the impact of megacity emissions on regional and global scales will be quantified.

Furthermore, since the passive tracers represent a useful tool in transport studies, they have been applied in a probabilistic risk assessment to study the risk of contamination from radioactive fallout after nuclear reactor accidents. This is the first such risk assessment which has been conducted on global scale.

The thesis is structured in five parts. In the first part, the tools are described, that are the numerical model (Chapter 2) and the analysis tools (Chapter 3). In the second part of the thesis, the work on urban emission sources is presented. The atmospheric dispersion of generic aerosol tracers from urban centers is discussed in Chapter 4, while the subsequent deposition is the topic of Chapter 5. The passive aerosol tracers, which are used in Chapters 4 and 5 are not explicitly treating for aerosol microphysics and aerosol thermodynamics. In Chapter 6, it is shown that these processes are less important in global aerosol transport studies. In contrast to the chapters before, where an arbitrary emission scenario is applied, the focus turns to real world emissions in Chapter 7, represented by global emission inventories, and how anthropogenic emissions from megacities affect regional and global budgets of aerosols and gas phase species.

In the third part, the results of the nuclear power plant accident risk assessment study are presented (Chapter 8). The overall conclusions and future prospects are given in Chapter 9 (fourth part). The last part of the thesis includes the appendix with additional information on several topics regarding the results which are presented in Chapters 4 - 8.

Part I

Methodology

2

Model description

To study the transport and deposition of pollutants from anthropogenic emission source points, the global three dimensional state-of-the-art atmospheric chemistry general circulation model (AC-GCM) system EMAC (ECHAM5/MESSy Atmospheric Chemistry) was applied. In this chapter a general overview of the model system is given along with a detailed description of the essential physical and chemical atmospheric processes which were essential for this work.

The chapter is divided into three parts: 1) the meteorological base model (ECHAM5), 2) the Modular Earth Submodel System (MESSy), and 3) the meteorological reanalysis data from the European Centre for Medium-Range Weather Forecasts (ECMWF), which has been used to nudge the model towards an observed atmospheric state.

2.1 The general circulation model ECHAM5

The meteorological core model of EMAC is the 5th generation European Centre Hamburg general circulation model (further denoted ECHAM5, Roeckner et al., 2006) which was developed at the Max-Planck Institute for Meteorology in Hamburg, Germany, based on the weather prediction model of the ECMWF. The version 5.3.01 of the climate model (Roeckner et al., 2003) has been combined with the Modular Earth Submodel System (further denoted MESSy, Jöckel et al., 2005) at the Max-Planck Institute for Chemistry, with contributions from the Deutsches Zentrum für Luft- und Raumfahrt (DLR) to study questions regarding the interactions between bio-physico-chemical processes[1].

The global three dimensional model can perform simulations in various horizontal and vertical resolutions. In the vertical, a depth of the atmosphere was chosen to cover the troposphere and lower stratosphere up to 10 hPa ($\sim$ 30 km)[2]. Thirty-one hybrid sigma-pressure levels are used in the vertical which are terrain following close to the surface and at constant pressure levels for the upper troposphere and stratosphere, with annual mean level midpoints (in hPa) for the year 2005: 981.7, 968.4, 945.1, 914.3, 878.0, 838.0, 795.0, 751.6, 662.3, 617.8, 574.0, 531.1, 489.2, 448.5, 409.1, 371.2, 334.8, 300.1, 267.2, 236.3, 207.3, 180.4, 155.4, 132.2, 110.6, 90.1, 70.0, 50.0, 30.0, and 10.0. Instead of 31 it is also possible to use 19 levels. Furthermore, the atmosphere can be represented up to 0.01 hPa ($\sim$ 80 km) (middle atmosphere version,

---

[1] more information: www.messy-interface.org, as of 13.09.2012

[2] more information: http://www.mpimet.mpg.de/en/wissenschaft/modelle/echam/echam5.html, as of 13.09.2012

Table 2.1: Horizontal resolutions and corresponding time step lengths in ECHAM5. The time step length also depends on the vertical resolution and is given for 31 layers in the vertical (L31) except for T21 with only 19 layers (L19). T stands for the triangular truncation. Bold marked resolutions have been used in this work.

Horizontal resolution	Number of grid boxes	Approximate box size (°)	Approximate box size (km)	Time step length (s)
T21	64 × 32	5.6 × 5.6	621 × 621	2400
T31	96 × 48	3.7 × 3.7	415 × 415	1800
T42	128 × 64	2.8 × 2.8	311 × 311	1200
T63	192 × 96	1.9 × 1.9	200 × 200	720
T85	256 × 128	1.4 × 1.4	156 × 156	480
T106	320 × 160	1.1 × 1.1	122 × 122	360
T159	480 × 240	0.7 × 0.7	81 × 81	180

often denoted as MAECHAM5, Giorgetta et al., 2006). Since the main focus of this work is the dispersion of anthropogenic surface emissions, the tropospheric version is satisfactory.

The horizontal resolution relies on the truncation of the spherical harmonics of the basic prognostic variables: vorticity, divergence, temperature, and the logarithm of the surface pressure (Roeckner et al., 2003). The standard truncation in ECHAM5 are at wave numbers 21, 31, 42, 63, 85, 106, or 159. Larger wave numbers are possible but rarely used in climate models. Table 2.1 summarizes the horizontal resolutions; the bold resolutions mark those which have been used to obtain the results presented in this work. The time step length for model simulations depends on the chosen horizontal and vertical resolution in order to fulfill the Courant-Friedrich-Levi criterion (Courant et al., 1928).

Time integration is centered in time (leapfrog scheme). A filter is applied to inhibit the growth of spurious computational modes (Asselin, 1972), and semi-implicit corrections are made to facilitate larger time steps. The set of the primitive equations for the moist atmosphere also requires, in addition to the four variables mentioned above, water vapor, cloud water, and cloud ice. Tracer transport is performed with a semi-Lagrangian flux-form scheme (Lin and Rood, 1996), which is mass conserving by definition. However, the different treatments of transport for surface pressure and temperature, as compared to other tracers, can lead to a lack of mass conservation (Jöckel et al., 2001). Other processes, such as condensation and convection of the ECHAM5 model are explained in the following section since they are all represented in MESSy submodels.

2.2 The Modular Earth Submodel System (MESSy)

The Modular Earth Submodel System (MESSy) is used to link multi-institutional computer codes. MESSy provides the interface to include emissions, transport, physical and chemical transformations, and removal processes of trace gases and aerosols. The individual processes are represented by submodels within the MESSy infrastructure (Jöckel et al., 2005). A complete overview of all submodels is given by Jöckel et al. (2006), with updates by Jöckel et al. (2010) and on the MESSy web page[3]. The submodels can use meteorological variables provided by ECHAM5 and also change these. Thus feedbacks from chemical and physical processes to meteorological variables are possible. Furthermore, the highly modularized and flexible structure of MESSy allows the inclusion of only the processes which are necessary to study a scientific question. For example, in this work two different model configurations have been applied, one with a generic, and one with a comprehensive representation of aerosols. Both model configurations are discussed in detail at the end of this section. The submodels which are used in the two model configurations are first described in the following paragraphs and summarized in Table 2.2:

Radiation (`RAD4ALL`)

The original ECHAM5 radiation routines have been slightly modified and re-implemented in the modularized submodel `RAD4ALL` (for further information see Jöckel et al., 2006, and www.messy-interface.org). The radiation scheme requires input parameters which can either come from prognostic variables, uniform volume mixing ratios, or from external climatologies. Here, cloud cover, water, and ice as well as specific humidity are used as prognostic variables whereas uniform mixing ratios are used for CO_2, CH_4, N_2O, and the CFCs trichlorofluoromethane ($\mathrm{CFC}-11$) and dichlorodifluoromethane ($\mathrm{CFC}-12$). For ozone and aerosols, climatological fields are used. More detailed information on the processes and parameterizations of the original code is provided in the ECHAM5 documentation (Roeckner et al., 2003).

Large-scale condensation (`CLOUD`)

The large scale condensation is calculated in the MESSy-submodel `CLOUD`, which is the original ECHAM5 implementation in a modularized MESSy conform structure. The scheme comprises prognostic equations for all water phases, bulk microphysics (Lohmann and Roeckner, 1996), and a statistical cloud cover scheme with prognostic equations for the distribution moments (Tompkins, 2002). The microphysics scheme consist of four parts: phase changes between the water components, the precipitation process (auto-conversion, accretion, aggregation), evaporation of rain and melting of snow as well as sedimentation of ice. The cloud cover scheme is based on a probability density function (based on the beta-distribution) of the total water content and the sub-grid cloud formation is only caused by fluctuations of the total water content. The original cloud scheme is described in Roeckner et al. (2003).

Convective cloud parameterization (`CONVECT`)

The process of convection needs to be parameterized since it cannot be resolved by the grid sizes applied in global models. The default scheme in MESSy is the mass-flux approach based parameterization from Tiedtke (1989) with modifications from Nordeng (1994) who used an adjustment closure by relating the cloud base mass-flux to the degree of convective available potential energy (CAPE) and using a relaxation time for which the convective scheme should remove the instability. Commonly convection is either described by an ensemble of

---

[3] www.messy-interface.org

sub-grid-scale clouds (e.g., Arakawa and Schubert, 1974) or, as done here, by a bulk formulation (e.g., Yanai et al., 1973; Tiedtke, 1989), with modifications in the large-scale budgets of the environmental dry static energy, the specific humidity, and the potential energy.
In total, six different parameterization are applicable in EMAC which have been compared by Tost et al. (2006b, 2010) regarding their closure assumptions, representation of entrainment, trigger conditions to initialize convection, precipitation formation, and their impact on atmospheric chemistry. In this work only the default parameterization is employed.

Convective tracer transport (`CVTRANS`)

As mentioned before, advection is calculated in the core model with the scheme of Lin and Rood (1996). However, this describes only transport of tracer mixing ratios in the large-scale circulation. Vertical transport also occurs in convective clouds which is explicitly treated in the submodel `CVTRANS`. Based on the bulk formulation of Lawrence and Rasch (2005) a monotonic, positive definite, and mass conserving algorithm is applied to calculate the tracer mixing ratios in the updrafts and downdrafts as well as the entrained and detrained tracer mass fluxes. Details on the MESSy implementation are provided by Tost (2006).

On-line, off-line emissions (`ONLEM`, `OFFLEM`) and tracer nudging (`TNUDGE`)

Natural and anthropogenic emissions are treated by four submodels `ONLEM`, `OFFLEM`, `TNUDGE`, and `LNOX`. Emissions either depend on environmental conditions such as surface winds or are independent of such conditions. In the latter case, emissions are commonly taken from pre-compiled emission inventories and are treated in the submodel `OFFLEM` (off-line emissions). In the other case, commonly applied for natural species, for example dessert dust or sea salt, the emissions are calculated on-line depending on meteorological model variables in the submodel `ONLEM`. Emissions of long-lived species like CFCs, CH_4, N_2O and H_2 are calculate from prescribed boundary condition with the submodel `TNUDGE` (tracer nudging) by relaxing the tracer values towards a prescribed value. Details on `ONLEM`, `OFFLEM`, and `TNUDGE` are given in Kerkweg et al. (2006b). Nitrogen oxides (NO_x) from lightning are calculated in a separate submodel (`LNOX`) described later.
Emissions for this study vary between the different model configurations and are thus given in detail at the beginning of each chapter.

Deposition processes

Removal from the atmosphere occurs by various deposition process which determine to a large part the lifetime of atmospheric pollutants, in particular, aerosols. Wet and dry deposition processes are simulated in three different submodels, `SCAV`, `DRYDEP`, and `SEDI`:

Dry deposition (`DRYDEP`) : Dry deposition represents the loss of gas molecules and aerosol particles from the atmosphere onto the earth's surface by turbulent transfer and uptake processes in absence of clouds or precipitation. The implementation in MESSy is described by Kerkweg et al. (2006a) following the prior work of Ganzeveld and Lelieveld (1995) for gas phase species and Stier et al. (2005) for aerosol tracers according to the 'Big-Leaf Approach'

(Hicks et al., 1987; Ganzeveld et al., 1998). The dry deposition flux F_{D} is calculated by multiplying the concentration c of species X with the dry deposition velocity V_{D}:

$$F_{\mathrm{D}} = c(X) \times V_{\mathrm{D}}(X) \qquad . \tag{2.1}$$

The dry deposition velocity depends on several parameters such as atmospheric conditions in the boundary layer, molecular diffusion or in the case of aerosols on the aerosol radius and density, and the surface type and is calculated by using a multi-resistance approach which links V_{D} to the inverse of the sum of three resistances which are used to represent these parameters: 1) the aerodynamic resistance R_{a}, 2) the quasi-laminar boundary layer resistance R_{qbr}, and 3) R_{s} the surface resistance. Furthermore, the surface type is relevant for the determination of the deposition velocity.

For aerosols there are three different land types: vegetation, bare soil and snow, and water. The overall deposition velocity is the sum of deposition velocities for these types, multiplied with surface fractions of snow, bare soil, water, vegetation, wet skin, and ice. The surface type dependent deposition velocities themselves depend on R_{a} and R_{s} which are calculated individually for each surface type and the latter also depending on aerosol properties such as aerosol radius, density, and in the case of modal aerosol size distributions the standard deviation of the mode. R_{qbr} is usually small compared to the other two resistance and therefore often negligible.

Generally, aerosol particles show a minimum dry deposition velocity at particle diameter between 0.1 and 1.0 µm and larger velocities for smaller and larger diameters (Ganzeveld et al., 1998). Smaller particles behave much like trace gases and cross the quasi-laminar layer by Brownian motion. Larger particles are efficiently transported across this layer by inertial impaction and gravitational settling. In between there are no efficient transport mechanisms (Seinfeld and Pandis, 1998).

In contrast to aerosols, four different surface types are applied for trace gases: snow/ice, bare soil, vegetation, and water in the wet skin reservoir (i.e., the fraction of the vegetation and bare soil wetted due to rain fall interception and dew fall). This leads to surface resistances which depend on the surface type and the properties of the respective trace gas. The calculation follows the scaling approach of Wesely (1989) and is also discussed in the appendix of Kerkweg et al. (2006a).

Sedimentation (`SEDI`) : Dry deposition changes tracer burdens only in the lowest layer. In contrast, sedimentation or gravitational settling occurs throughout the entire atmosphere and is an important process in changing the distribution of aerosols in the atmosphere, especially for aerosols with diameters larger than a micrometer. The terminal fall speed v_{t} of a particle is determined by equating the downward force of gravity with the opposing drag force that arises from air viscosity (Jacobson, 2002). Sedimentation is negligible for gas molecules as the gravity force is too small in this case. For aerosol particles, v_{t} can be assessed by multiplying the Stokes velocity v_{St} with the Slinn factor f_{Slinn} and the Cunningham-slip-flow correction f_{Csf}. The Slinn factor f_{Slinn} accounts for the fact that in the case of lognormal aerosol size distributions the mean sedimentation velocity of all particles of a lognormal mode is larger than the sedimentation velocity of a particle with mean radius. For aerosol bins and aerosol

numbers this factor is equal one, for lognormal modes it calculates to $\sigma(k)^{2\ln\sigma(k)}$ with $\sigma(k)$, being the standard deviation of the mode k. The Cunningham-slip-flow correction f_{Csf} is applied to account for non-spherical particles (Kerkweg et al., 2006a).
In MESSy the default sedimentation scheme is a simple upwind scheme which was used in all simulations. In this scheme the assumption is made that all particles are equally distributed in one grid box and that a certain fraction of these particles, which is determined by the geometric vertical extension of the grid box, is falling out per time step. Figuratively speaking, tracer mass located in the lowermost part of an upper grid box is transferred to the uppermost part of the grid box below. Further details are given in Kerkweg et al. (2006a).

Scavenging by nucleation and impaction (SCAV) : Scavenging and aqueous phase chemistry in clouds and falling precipitation can substantially alter the abundance of trace gases and aerosols. In fact, for small aerosols this represents the major sink in the atmosphere (Seinfeld and Pandis, 1998). In the submodel SCAV (Tost et al., 2006a, 2007a) both gas phase and aerosol scavenging can be simulated as well as cloud and rain droplet chemistry. For gases, two approaches can be chosen to simulate the scavenging, one with fixed, empirically derived scavenging coefficients and one with a system of coupled ordinary differential equations which resolve feedback mechanisms between the multi-phase chemistry and transport processes involved. For the second approach, the numerical equation solver KPP (Kinetic PreProcessor Damian et al., 2002; Sandu and Sander, 2006) is applied to account for the uptake and release processes of gases from cloud or rain droplets. This process is described following the Henry's law equilibrium and a correction for gas phase diffusion limitation and the accommodation coefficients (Tost et al., 2006a).
Aerosol particles are scavenged either by nucleation or by impaction. Nucleation scavenging takes into account Brownian motion for small aerosols (less than 10 nm and nucleation and growth into droplets. The scavenging efficiency of Brownian motion follows a semi-empirical formula (Pruppacher and Klett, 2000):

$$\Lambda_{\mathrm{B}} = \frac{1.35 \cdot LWC \cdot D_{\mathrm{p}}}{r_{\mathrm{rain}}^2} \tag{2.2}$$

with Λ_{B} the scavenging coefficient for Brownian motion in 1/s, the liquid water content (LWC) in g cm^{-3}, D_{p} the diffusivity of the particle in m^2/s, and the cloud droplet radius r_{rain} in m. The scavenging coefficient is then applied in an exponential approach for each aerosol species:

$$c\,(t_0 + \Delta t) = c\,(t_0) \cdot \exp\left(-\Lambda_{\mathrm{B}} \cdot \Delta t\right) \tag{2.3}$$

with c being the concentration of an aerosol species and Δt (for more details see also Seinfeld and Pandis, 1998). The nucleation and growth into droplets is assessed through the scavenging ratio (not the scavenging coefficient):

$$c = c_0 \cdot \left(1 - \arctan\left(\left(5.0 \cdot 10^6 \cdot r_{\mathrm{p}}\right)^6\right) \cdot 2/\pi\right) \tag{2.4}$$

where the aerosol radius r_{p} in m is used (Tost et al., 2006a, and references therein).
Impaction scavenging is based on Brownian motion, interception, and impaction and is

parameterized by an equation originally given in Slinn (1984). For this a dimensionless collection efficiency E is calculated which depends on the Reynolds number of the rain droplet, the Schmidt and Stokes numbers of the collected aerosol particle, the ratio of radii of particle and droplet, and the viscosity ratio of water and air. Together with the effective rain flux F_{rain} (in $\text{kg}/(\text{m}^2\text{s})$) and the droplet radius r_{rain} (in mm) the scavenging efficiency Λ is calculated:

$$\Lambda = E/r_{\text{rain}} \cdot 0.75 \cdot F_{\text{rain}} \tag{2.5}$$

where the rain flux pertains to the fractional part of the grid box which is covered by precipitating clouds. Thus, the scavenging efficiency depends on the rain intensity which, in particular, differs between large-scale and convective clouds. For the scavenging by frozen hydro-meteors the parameterization of Stier et al. (2005) is used in which a constant scavenging coefficient is applied for each mode of the modal aerosol distribution.
Nucleation scavenging is very efficient for particles larger than 0.2 µm but has a minimum efficiency at around 30 nm. At smaller sizes the Brownian motion is more efficient, at larger sizes the nucleation and growth of cloud droplets is dominant. Conversely, impaction scavenging becomes important for particles larger 2.5 µm with a minimum between 0.1 µm and 1.0 µm (the so-called Greenfield gap, Greenfield, 1957). Below this size range Brownian motion is responsible for the impaction while interception is dominant for particles slightly larger than 1.0 µm, and impaction for even larger particles. Furthermore, the coupling between aerosol scavenging and liquid phase chemistry can be simulated in such a way that scavenged aerosols can serve as initial concentrations for liquid phase species. As a result, species which have been in the aerosol phase can partly be transferred to the gas phase and gas phase species can affect the aerosol burden, e.g., the oxidation of SO_2 to SO_4^{2-}. Dissolved species can also be released when cloud or rain droplets evaporate. Neutral, volatile compounds are added to the corresponding gas phase concentration while aerosols are redistributed into the aerosol distribution.

Generic tracer initialization (`PTRAC`)

Tracers can generally be initialized in each submodel due to the flexible handling of tracers in the generic MESSy-submodel `TRACER` (Jöckel et al., 2008). The submodel `PTRAC` (passive tracers) is dedicated to defining and initializing any kind of tracers in EMAC which are neither part of the chemical mechanism nor of the aerosol microphysical scheme. In this study PTRAC is utilized to define properties of generic gas phase tracers and of generic aerosol tracers such as radius, standard deviation, and density.

Aerosol microphysics and gas-aerosol partitioning (`GMXe`)

Aerosol microphysics and gas-aerosol partitioning are treated in the Global Modal-aerosol eXtention (`GMXe`) submodel (Pringle et al., 2010b,a; Pozzer et al., 2012a; Tost and Pringle, 2012). GMXe is based on the microphysical core in M7 (Vignati et al., 2004) but extends in the representation of the emissions, the microphysics, the number of species, and the gas-aerosol partitioning (Pringle et al., 2010a). The following processes are included in the scheme: condensation, gas-aerosol partitioning, nucleation, coagulation, and transfer of coated hydrophobic particles to hydrophilic modes. Seven interactive lognormal modes are used to describe the aerosol size distribution which span over four size categories: nucleation (radii smaller 5 nm), Aitken (radii between $5 - 50$ nm), accumulation (radii between $50 - 500$ nm), and coarse (radii larger 500 nm). Four modes represent hydrophilic modes and three modes hydrophobic modes (no nucleation mode). The total aerosol size distribution follows the superposition of these seven lognormal modes:

$$n(\ln(r)) = \sum_{k=1}^{7} \frac{N_\mathrm{k}}{\sqrt{2\pi}\ln\sigma_\mathrm{k}} \exp\left(-\frac{(\ln r - \ln \bar{r_\mathrm{k}})^2}{2\ln^2\sigma_\mathrm{k}}\right) \tag{2.6}$$

and each mode (k) being defined by the number concentration N_k, the number mean radius $\bar{r_\mathrm{k}}$, and the geometric standard deviation σ_k. Number and mass are calculated prognostically but the geometric standard deviations are fixed at $\sigma = 2.00$ for hydrophilic and hydrophobic coarse modes and $\sigma = 1.59$ for all other modes. Within the modes the following aerosol components are explicitly treated (also used in Chapter 7): sulfate (SO_4^{2-}), black carbon (BC), particulate organic matter (POM), nitrate (NO_3^-), ammonium (NH_4^+), dust (DU), sea spray (SS), chloride (Cl^-), sodium (Na^+), bisulfate (HSO_4^-), and aerosol water. However, it is possible to include more species, e.g., magnesium (Mg^{2+}), calcium (Ca^{2+}) or potassium (K^+). Emissions of the species are separately discussed in Chapter 7.

Nucleation is treated based on the approach of Vehkamaki et al. (2002) which relies on the following variables, temperature (T), relative humidity (RH), and the concentration of sulfuric acid (H_2SO_4) as is valid over the range $0.01\,\% < RH < 100\,\%$ and $190\,\mathrm{K} < T < 305.15\,\mathrm{K}$. Coagulation follows the approach of Vignati et al. (2004) with coagulation coefficients based on Brownian motion (Fuchs, 1964). Coagulation of particles follows three rules: 1) two particles from the same mode result in one particle from this mode, 2) smaller mode + larger mode leads to a particle in the larger mode, 3) hydrophilic + hydrophobic leads to a particle in the hydrophilic mode. Treatment of the gas-aerosol partitioning of the semi-volatile inorganic species is done through ISORROPIA-II (Fountoukis and Nenes, 2007) which is an inorganic equilibrium model for the $K^+ - Ca^{2+} - Mg^{2+} - NH_4^+ - Na^+ - SO_4^{2-} - NO_3^- - Cl^- - H_2O$ aerosol system. It solves the gas-aerosol-solid equilibrium partitioning by considering the chemical potential of the species (Nenes et al., 1998) and by choosing specific computational "regimes" it minimizes the number of equations and iterations to solve the set of equilibrium equations. Pre-calculated lookup tables are used to determine activity coefficients to reduce the computational expense (e.g., Pringle et al., 2010b; Pozzer et al., 2012a). The water uptake by inorganic aerosols is also treated in ISORROPIA-II in case of subsaturation ($RH < 95\,\%$) while it is generally permitted for organic species (Pringle et al., 2010b). The transfer between the modes is calculated twice, once after coagulation and once after gas-aerosol partitioning. In the latter case, five monolayers of hydrophilic material are needed to transfer mass from hydrophobic to hydrophilic modes which express the aging of hydrophobic particles (Vignati et al., 2004; Stier et al., 2005). Material is shifted from smaller to larger modes until the count median radii are within the fixed size boundaries. Finally, a mode merging algorithm (Vignati et al., 2004) is used to re-distribute aerosol mass between the size categories.

Aerosol optics (`AEROPT`)

Optical properties of aerosols are calculated in the diagnostic submodel `AEROPT` for the following aerosol types: water soluble compounds (WASO), i.e., all water soluble inorganic ions, aerosol water, black carbon, particulate organic matter, sea salt, and dust. The scheme is based on the one of Lauer et al. (2007) and makes use of pre-defined lognormal modes for which lookup tables are provided for the extinction coefficient σ_{sw}, the single scattering albedo ω_{sw}, and the asymmetry factor γ_{sw} for the shortwave (sw) and the extinction coefficient σ_{lw} for the longwave (lw) spectrum (Pozzer et al., 2012a).
The lookup tables are calculated with the help of LIBRADTRAN (Mayer and Kylling, 2005) for various aerosol types. Refractive indices for extensive Mie calculations are taken from several data bases, e.g., HITRAN2004 (Pozzer et al., 2012a).
During the simulation, the volume-weighted mean complex refractive index is determine for each mode. Moreover, the mode mean radius, and finally the Mie size parameter for each wavelength band is calculated. These three parameters provide the information for the lookup table for σ_{sw}, ω_{sw}, γ_{sw}, and σ_{lw}. These values are pre-defined for 16 bands in the shortwave and 16 bands in the longwave to cover the wavelength dependency. Since these bands do not need to match the bands in the radiation scheme of the GCM, a mapping between the pre-defined bands and those in the radiation scheme is performed. Finally, the aerosol optical depth (AOD) τ for each mode is assessed by calculating the extinction coefficient for a single particle and multiplying this value by the number of particles in one grid cell and consequent vertical integration (Pozzer et al., 2012a).

Gas phase mechanism (`MECCA`)

The Module Efficiently Calculating the Chemistry of the Atmosphere (MECCA, Sander et al., 2005) calculates the concentration of gas phase species by using the Kinetic PreProcessor (KPP, Sandu and Sander, 2006) to integrate the set of stiff differential equations with a third order Rosenbrock solver and automatic (chemical) time stepping. The selected mechanism consists of 104 gas phase species and 245 reactions (Jöckel et al., 2006). Ozone related chemistry is simulated in the troposphere, including non-methane-hydrocarbons (NMHCs) up to isoprene (C_5H_8) (von Kuhlmann et al., 2003). In the stratosphere, the main chlorine and bromine reactions are considered (Steil et al., 1998; Meilinger, 2000). Heterogeneous reaction rates are provided by the submodel `HETCHEM`, photolysis rates by the submodel `JVAL`. More details about the reactions, reaction kinetics and species included can be found in Jöckel et al. (2006) and on the organic chemistry in particular in Pozzer et al. (2007).

Heterogeneous reactions (`HETCHEM`)

Within the `HETCHEM` submodel the loss of gas phase species to the aerosol through heterogeneous reactions is treated (Jöckel et al., 2006). In this work, only a minimum configuration is applied to simulate reactions on liquid tropospheric sulfate aerosol (e.g., $N_2O_5\,(g) + H_2O\,(aq) \rightarrow 2HNO_3\,(aq)$).

Photolysis rate coefficients (`JVAL`)

The submodel `JVAL` provides on-line calculated photolysis rate coefficients (J-values) following (Landgraf and Crutzen, 1998). For this `JVAL` needs the cloud water and ice content, the cloud cover, and a climatological aerosol distribution. For O_3, either the prognostic tracer (default) or a prescribed climatology can be used.

Lightning produced NO_x *(LNOX)*

As mentioned before emissions are calculated in four different submodels. The production of NO_x from lightnings is parameterized as an individual process following the approach of Price and Rind (1994). Alternatively, the approach of Grewe et al. (2001) can be used. The total lightning-NO_x production scales with the flash frequency and the amount of produced NO_x per single flash (Jöckel et al., 2006).

Height of the planetary boundary layer and the tropopause (TROPOP)

Within the diagnostic submodel `TROPOP` (Jöckel et al., 2006) the height of the tropopause can be diagnosed according to various definitions: WMO definition based on temperature lapse rate (WMO, 1992) or as a potential vorticity iso-surface. Moreover, the height of the planetary boundary layer height can be determined for several applications.

As noted before, two different model setups have been used, one with a generic and one with a complex representation of aerosols which are briefly described in the last part of this section.

Model version ***A***

The first model version is based on the development cycle 1.9 of EMAC with updates in the representation of scavenging[4] compared to the standard release version. Furthermore, an additional emission scheme was included in `ONLEM` to add emissions in individual grid cells. Only generic tracers are initialized in this version. In the case of aerosols this means that radius, standard deviation, and density are prescribed and do not change during the simulation and that aerosols of various sizes do not interact with each other. However, aerosols are removed by dry and wet deposition. If applied, generic gas phase tracers are only removed by an exponential decay, while no chemical transformation is possible.
This model version is used to obtain results discussed in Chapters 4, 5, and 8 as well as for comparison in Chapter 6. Submodels included in this configuration are: `RAD4ALL`, `CLOUD`, `CONVECT`, `ONLEM`, `DRYDEP`, `SEDI`, `SCAV`,and `PTRAC`, see Table 2.2.

Model version ***B***

This model version is based on the development cycle 1.10 of EMAC with updates in the representation of scavenging and aerosol microphysics compared to the standard release. In the standard release, impaction nucleation is calculated before nucleation scavenging which is turned around here with the consequence that potentially more aerosols which previously had been efficiently removed from the atmosphere by impaction scavenging can participate in the nucleation process. This leads in general to higher aerosol burdens, especially of dust

---

[4] A mass imbalance was detected in the process of ice sedimentation. In the fixed version a satisfactory mass balance for model tracers is achieved with mass inconsistencies smaller than 1.0 % due to mass-wind inconsistencies (Jöckel et al., 2001).

aerosols. Since the aerosol microphysics scheme is still under development and constantly updated, several of the latest changes which also have been implemented in version 2.42 of EMAC have been adopted as far as they were useful and the implementation was feasible. Furthermore, the `GMXe` submodel was extended with the possibility to include passive aerosol tracers which can grow and become more hygroscopic but neither interact with ambient species nor change the overall aerosol size distribution (see Section 6.1.2).

Tropospheric aerosols are treated in an aerosol module including aerosol microphysics and gas-aerosol partitioning. Thus, interaction between aerosols and the environment is allowed requiring interaction with gas phase species. Furthermore, the size and density of the aerosol particles are not constant. Submodels included in this configuration are: `RAD4ALL`, `CLOUD`, `CONVECT`, `ONLEM`, `OFFLEM`, `DRYDEP`, `SEDI`, `SCAV`, `GMXe`, `AEROPT`, `HETCHEM`, `LNOX`, `MECCA1`, `JVAL`, and `TROPOP`, see Table 2.2.

Table 2.2: List of MESSy submodels used in model versions **A** and **B** together with a reference list. The last column shows the model configuration in which the submodel is used in this work. Further information on the various submodels and a complete list of all MESSy submodels can be found on the MESSy web page: www.messy-interface.org.

Submodel	Function	Reference	Version
`AEROPT`	Calculation of aerosol optical depth	Pozzer et al. (2012a)	**B**
`CLOUD`	Large-scale condensation	Jöckel et al. (2006)	**A,B**
`CONVECT`	Convective parameterization	Tost et al. (2006b, 2010)	**A,B**
`CVTRANS`	Convective tracer transport	Tost (2006)	**A,B**
`DRYDEP`	Dry deposition of gases and aerosols	Kerkweg et al. (2006a)	**A,B**
`GMXe`	Aerosol microphysics and gas-aerosol partitioning	Pringle et al. (2010a); Tost and Pringle (2012)	**B**
`HETCHEM`	Heterogeneous chemistry (reaction rates)	Jöckel et al. (2006)	**B**
`JVAL`	Calculation of photolysis rates	Jöckel et al. (2006)	**B**
`LNOX`	Production of NO_x from lightning	Tost et al. (2007b)	**B**
`MECCA`	Gas phase chemistry	Sander et al. (2005)	**B**
`OFFLEM`	Off-line (pre-scribed) emissions	Kerkweg et al. (2006b)	**B**
`ONLEM`	On-line (calculated) emissions	Kerkweg et al. (2006b)	**A,B**
`PTRAC`	Passive tracers	Jöckel et al. (2008)	**A**
`RAD4ALL`	Short- and longwave radiation	Jöckel et al. (2006)	**A,B**
`SCAV`	Scavenging and wet deposition of gases and aerosols	Tost et al. (2006a, 2007a)	**A,B**
`SEDI`	Gravitational settling of aerosols	Kerkweg et al. (2006a)	**A,B**
`TNUDGE`	Tracer nudging	Kerkweg et al. (2006b)	**B**
`TROPOP`	Diagnostic of tropopause and boundary layer height	Jöckel et al. (2006)	**B**

2.3 Data assimilation using reanalysis data of the European Centre for Medium-Range Weather Forecasts

In ECHAM5 it is possible to use a simplified type of data assimilation of four meteorological quantities, i.e., the temperature, the vorticity, the divergence, and the logarithm of the surface pressure. The goal of this so-called nudging is to push the model towards an observed state of the atmosphere. The model variables are altered during the model integration by adding a non-physical relaxation term $\partial X_{\mathrm{mod}}/\partial t$ to the respective variable by multiplying the difference between the observed state X_{obs} and the modeled value X_{mod} with a certain relaxation coefficient $G(X)$ that depends on the relaxation time which is a measure of the strength of the nudging for each variable and model layer:

$$\frac{\partial X_{\mathrm{mod}}}{\partial t} = G\left(X\right) \cdot \left(X_{\mathrm{obs}} - X_{\mathrm{mod}}\right) \qquad . \tag{2.7}$$

This technique is based on four-dimensional data assimilation first developed to insert satellite or aircraft measurements in numerical weather prediction models. Jeuken et al. (1996) implemented the nudging in ECHAM and it is also frequently used in EMAC (e.g., Jöckel et al., 2006; Lelieveld et al., 2007; Pozzer et al., 2012a), often to simulate shorter time periods with a general circulation model.

The observed state is commonly obtained from meteorological analysis or reanalysis data. In this work, observational data was taken from the ERA-INTERIM project of the European Centre for Medium-Range Weather Forecasts (Dee et al., 2011). The nudging is applied throughout the troposphere and for the entire simulation period at each time step.

If not stated differently, all simulations were initialized on 01 July 2004 and are integrated over one and a half years until 01 January 2006. The first six months were used as model spin up time to bring the tracer concentrations into quasi-equilibrium and the entire year 2005 is used for analysis. The year 2005 shows no strong signals in the El-Niño-Southern Oscillation (ENSO)[5] index or the North Atlantic Oscillation (NAO)[6]. However, in terms of global mean temperature, 2005 is the hottest year ever recorded[7]. In Appendix B meteorological variables and tracer burdens of the year 2005 are put in perspective to the years 2001-2010 to show that the results obtained in 2005 are representative.

---

[5] http://www.ncdc.noaa.gov/sotc/enso/2005/1, as of 17.09.2012

[6] http://www.cpc.ncep.noaa.gov/products/precip/CWlink/pna/nao.shtml, as of 17.09.2012

[7] http://en.wikipedia.org/wiki/Instrumental_temperature_record and http://www.ncdc.noaa.gov/sotc/global/2011/13, as of 27 June 2012

3

Quantification of atmospheric dispersion and subsequent deposition of pollutant emissions

3.1 Concept of pollution potentials

One of the primary goals of this work is to assess the differences in the dispersion and subsequent deposition of pollutants from anthropogenic emission source points. This approach was adopted from Lawrence et al. (2007) who also used metrics to quantify the dispersion of gas phase tracers with various but fixed atmospheric decay lifetimes. Here, generic tracers are applied to simulate aerosol particles and trace gases, which originate from various source points. These tracers are all continuously released with a constant rate at each emission source point. Thus, each tracer has the same source strength and the results depend only on meteorological conditions in the region of the release. Thus, the outflow from various source points can directly be compared and the source points can be ranked regarding their potential to pollute the environment.

Based on the analysis of Lawrence et al. (2007), I also used metrics to quantify the transport but added additional metrics to obtain more information on the deposition of the generic aerosol tracers. These metrics are introduced in the next section, followed by the Köppen-Geiger climate classification. This classification is used to group different source points for which similar ambient meteorological conditions prevail and is based on two main meteorological variables, i.e., temperature and precipitation. Moreover, the impact on ecosystems and humans is assessed by folding tracer densities and deposition fields with geographical distributions of cropland, pasture, and forests as well as with population numbers.

3.2 Quantifying pollutant dispersion and deposition - metrics

3.2.1 Transport

Four different metrics were defined to assess the atmospheric dispersion of the emissions: the city retention pollution potential RCL_{X}, the low-level remote pollution potential ELR_{Z}, the upper tropospheric pollution potential E_{UT}, and the area of tracer density threshold exceedance A_{Y}, which is the only metric which is not computed as a relative number. In detail, this means:

- City retention pollution potential: RCL_{X}
  This metric is a measure of the local pollution build-up around the emission source point and is calculated as the mass fraction, relative to the total atmospheric burden, which is

retained in a circular volume of height X (in km) around the source points. Generally, X was chosen to be 0.5 km, which is about the global average height of planetary boundary layer in the model simulations and the radius to be 500 km and the retention is labeled as $RCL_{0.5\text{km}}$. However, in principle it is possible to change the radius and the height of the circular volume.

- Low-level remote pollution potential: ELR_{Z}
  This metric describes the low-level long-range pollution export and is assessed as the mass fraction which has been transported beyond various distances away from the source point but is still below a certain altitude Z (in km). The common distance and altitude were chosen to be 1000 km and 1 km, respectively, denoted as $ELR_{1\text{km}}$. In some cases the height was also set 500 m.
- Upper tropospheric pollution potential: E_{UT}
  This metric describes the mass fraction in the free troposphere above 5 km. In this region the lifetime and properties of many trace species change compared to their source regions at or near the surface. 5 km were chosen as threshold value, since in most cases tracer mass above this altitude is located in the free troposphere.
- Area of tracer density threshold exceedance: A_{Y}
  The surface layer tracer density (in ng/m^3) is used to assess the area in which a certain threshold value Y is exceeded. In this study Y was chosen to be either 1, 10, or 100 ng/m^3. The size of the area can be used to characterize the near-source dilution of the outflow plume away from its release point.

For ELR_{Z} and RCL_{X} and later for DRT, equidistant points have to be calculated which are on a circle if the surface area is plane. On a sphere these points can be approximated by an ellipsoid for which the calculation of the coordinates in longitude and latitude are based on the radii of the WGS84 ellipsoid (National Imagery and Mapping Agency, http://earth-info.nga.mil/GandG/publications/tr8350.2/wgs84fin.pdf, 2000 and Lawrence et al., 2007). Only tracer burden in grid cells which are totally encircled by this ellipsoid is accounted for as well as the weighted fraction of the burden for grid cells which are on the boundaries of the ellipsoid. The difference between the area of this ellipsoid and an analytically derived area of a corresponding circle differs less than 8 % for the underlying horizontal base model resolutions used in this work.

3.2.2 Deposition

In addition, the deposition of the passive aerosol tracers is analyzed with certain metrics. In general, the model output allows to distinguish between dry and wet removal for which the fraction of dry deposition, DRY, is assessed and it can also be distinguished between the four individual deposition processes: 1) dry deposition due to the surface roughness and turbulent mixing in the lowest model layer (DED, from `DRYDEP`), 2) gravitational settling due to the weight of an aerosol particle (SED, from `SEDI`), and scavenging by nucleation or impaction in 3) large-scale (LSS, from `SCAV`) or 4) convective clouds (CVS, from `SCAV`). In general, I will refer to the sum of 1) and 2) as dry removal and to the sum of 3) and 4) as wet removal. DRY, DED, SED, LSS, and CVS can be assessed either as a scalar number, i.e., a fraction of the total global deposited mass or as a two dimensional field. In the latter case, the values are calculated in each grid box.

Further information about the spatial distribution of the deposition is obtained with four more metrics. CON returns the fraction of the total deposited mass which is removed over land surfaces. Similar to ELR_Z, a remote deposition potential, DRT, is calculated which is the mass fraction deposited beyond various distances away from the source. DRT is also a measure of the long-range transport potential. Additionally to DRT, the remote dry deposited mass fraction, DRD, is calculated which is the mass fraction of DRT which is dry removed from the atmosphere. Finally and in contrast to DRT, a metric is introduced which is used to focus on regions with high deposition mass fluxes. For this the ratio between the accumulated deposition mass flux DEP_accu (in kg/(m^{2}s)) and the mean global emission flux EM_total (in kg/(m^{2}s)) is computed in each grid box:

$$D_\mathrm{X} = \frac{DEP_\mathrm{accu}}{EM_\mathrm{total}} \times 100\,\% \quad . \tag{3.1}$$

Together with a threshold value X (in %), the emission normalized deposition field, D_X, can be utilized similar as A_Y before, to assess the area (in km^2) in which the deposition exceeds

Table 3.1: Summary of the metrics used in this work to quantify the transport and deposition of generic tracers.

Metric	Description	Unit
RCL_X	Fraction of mass retained within a circular volume around the source with height X, where $X = 0.5\,\mathrm{km}$	%
ELR_Z	Fraction of mass exported beyond certain distances and kept below an altitude Z, where $Z = 1.0\,\mathrm{km}$	%
E_UT	Fraction of mass above an altitude of 5 km	%
A_Y	Area in which the surface concentration exceeds a certain threshold value Y, where $Y = 1,\ 10,\ 100,\ \mathrm{ng/m^3}$	10^6 km^2
DRY	Mass fraction of the emission which is deposited by dry deposition or gravitational settling	%
DED	Mass fraction of the emission which is deposited by dry deposition	%
SED	Mass fraction of the emission which is deposited by gravitational settling	%
LSS	Mass fraction of the emission which is deposited by scavenging in large-scale clouds	%
CVS	Mass fraction of the emission which is deposited by scavenging in convective clouds	%
CON	Mass fraction of the emission which is deposited on land surfaces	%
DRT	Mass fraction of the emission which is deposited beyond various distances from the emission location	%
DRD	Mass fraction of DRT which is dry deposited	%
D_X	Area in which the emission normalized deposition field exceeds a threshold value X, where $X = 1,\ 5\,\%$	10^3 km^2

more than a certain fraction of the emission. The two dimensional field of D_X can further be folded with other surface properties like water or land area, cropland, pasture, or forest area to assess which ecosystems are heavily affected by emissions from certain source points. Table 3.1 summarizes all metrics used in this study.

3.3 Köppen-Geiger climate classification

In this thesis, either major population centers or nuclear power plants were chosen as anthropogenic emission source points. In the first case, 46 and in the second case, about 200 different locations are distributed around the world. In many examples, single emission hot spots are discussed individually, but often it is appropriate to group source points to larger clusters to facilitate the discussion of the results. Recall that the results should be discussed in light of the source location which leads to several possibilities to form the clusters. For example, it is possible to group the source points by latitude or altitude above sea level. However, to also include information on the prevailing meteorological parameters, clusters were built based on the Köppen-Geiger climate classification. This classification is based on two variables, namely temperature and precipitation, and thus offers the possibility to group source points which are in regions with -on a climatological basis- similar meteorological conditions. The Köppen-Geiger climate classification was first introduced in 1900 by Wladimir Köppen, based on the relation between vegetation and climate and later extended by Rudolf

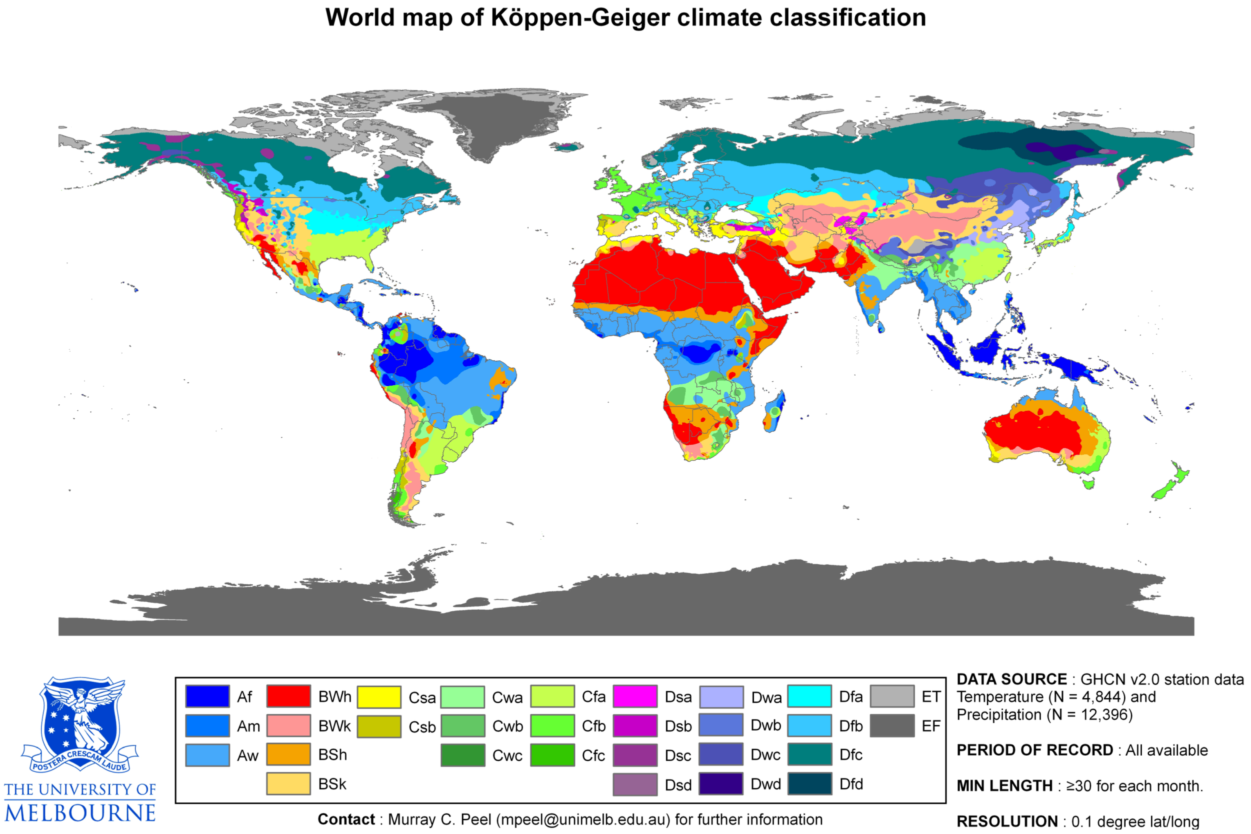

Figure 3.1: World map of Köppen-Geiger climate classification as provided by Peel et al. (2007). For explanation of important climate classes, see text and Table 3.2. Copyright by European Geophysical Union, 2007.

Table 3.2: Chosen climate classes and corresponding class names: A = tropical climate (defined by the mean temperature of the coldest month), B = arid climate (defined by the mean annual precipitation), C = temperate climate (defined by the mean temperature of the hottest and coldest month), and D = cold climate (defined by the mean temperature of the hottest and coldest month). Sub-classes are needed to define the C classes: w = dry winter (defined by the precipitation in the driest month in the winter and the wettest month in summer), s = dry summer (defined by the precipitation in the driest month in summer and the wettest month in winter), and f = no dry season (not w or s). Exact definitions are given for example in Peel et al. (2007).

Climate class	Class name
A	tropical
B	arid
Cf	temperate no dry season
Cw	temperate winter dry
Cs	temperate summer dry
D	cold

Geiger (Geiger, 1954, 1961). It comprises five different main climate classes, i.e., tropics (A), arid (B), temperate (C), cold (D), and polar (E) and several sub-classes. Updates on the spatial distribution of the climate class are published frequently by using either observational data of varying temporal coverage at each measurement site and an interpolation technique to obtain data in regions without measurements (e.g., Peel et al., 2007) or pre-compiled data sets for temperature and precipitation, e.g., from the Climate Research Unit (CRU) and the Global Precipitation Climatology Centre (GPCC, e.g., Kottek et al., 2006). Figure 3.1 shows the spatial distribution of the various climate classes as described by Peel et al. (2007). Furthermore, the climate classification was earlier used as a diagnostic tool in global climate modeling (e.g., Lohmann et al., 1993).

In this work, six climate clusters were defined which themselves comprise several climate classes: tropical regions include the entire tropical climate class (A), arid regions the entire arid climate class (B), and cold regions the entire cold climate class (D). However, since many anthropogenic sources are situated in temperate regions, three clusters originate from the temperate climate class (C): temperate no dry season (Cf), temperate winter dry (Cw), and temperate summer dry (Cs). An overview is presented in Table 3.2.

3.4 Agricultural and population data

In Chapter 4 aerosol surface densities and in Chapter 5 aerosol deposition fields are convolved with geographical distributions of population and ecosystems, respectively. Gridded population number for the year 2005 is used to determine the impact of aerosols on humans (see Figure 3.2d). Data is based on gridded population data of more than 300,000 national and sub-national administrative units to assign population values to grid cells (Socioeconomic Data and Applications Center (SEDAC), 2005).

Moreover, the fractions of three different land ecosystems, cropland, pasture, and forest data are used to determine the impact on land ecosystems (distributions are given in Figure 3.2a-

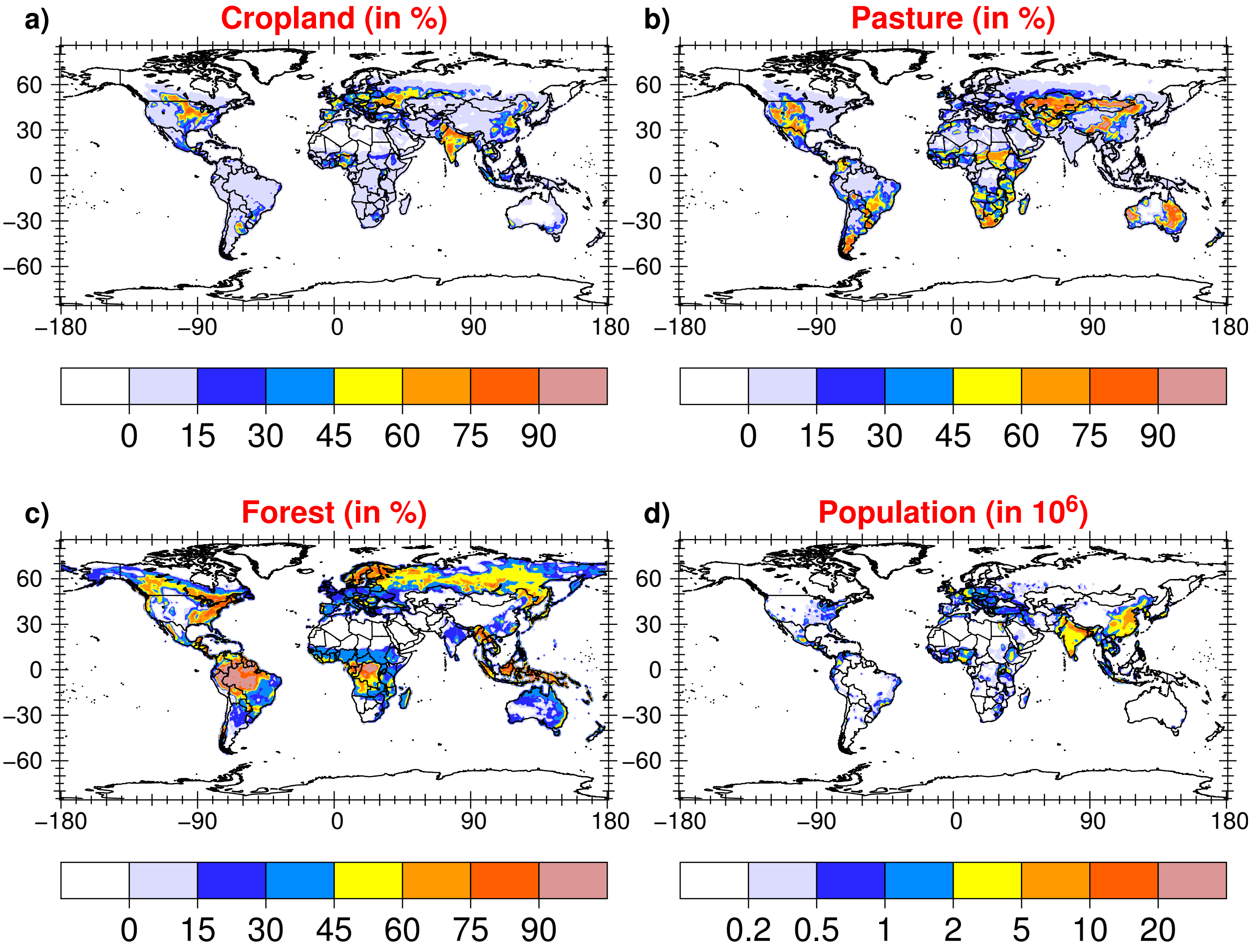

Figure 3.2: Fraction of the area covered with a) cropland, b) pasture, c) forest (in %) and absolute d) population number (in 10^6 person/box). Cropland and pasture data are taken from http://www.geog.mcgill.ca/landuse/pub/Data/, forest data from http://edc2.usgs.gov/glcc/fao/index.php, and population number for the year 2005 (Socioeconomic Data and Applications Center (SEDAC), 2005).

c). Cropland and pasture data are compiled using satellite-derived land cover data and agricultural inventory data for the year 2000 (Ramankutty et al., 2008). Data is originally available at about 10 km horizontal resolution (http://www.geog.mcgill.ca/landuse/pub/Data/, as of 08.06.2012). The forest data is based on US Geological Survey Global Forest Resource Assessment (FRA 2000) and is based on images from the Advanced Very High Resolution Radiometer (AVHRR) satellite at a resolution of about one kilometer (http://edc2.usgs.gov/glcc/fao/index.php, as of 08.06.2012). The data set originally comprises five classes: closed forest (40-100 % canopy cover), open or fragmented forest (10-40 % canopy cover), other wooded land, and water (lakes, rivers, etc.) which have been merged to one forest class for this study.

All these data sets have been regridded to the corresponding model resolution. Together with the metrics D_X and A_Y they are used to assess the human exposure, cropland deposition exposure, pasture deposition exposure, and forest deposition exposure.

Part II

Urban Emission Hot Spots

4

Aerosol pollution potentials: atmospheric dispersion

In this part of the thesis, large urban centers, so-called megacities or major population centers (MPCs) represent the release points of anthropogenic pollutants. On the global scale, these emission sources appear small, though their contribution to trace gas and aerosol concentrations is disproportionally large (see Section 1.1.2).

In this chapter, the atmospheric dispersion of aerosols from such urban source points is discussed. Only generic mono-modal aerosol tracers of different sizes and fixed standard deviations are applied which have varying atmospheric lifetimes. The aerosol tracers can undergo dry and wet deposition processes like all other aerosols which are treated in the model, though they are not affected by any microphysical processes. In Chapter 6 I show that these tracers can well represent atmospheric aerosols by comparing them to passive aerosol tracers which are treated within a comprehensive modal aerosol scheme. However, a model with a modal aerosol scheme and comprehensive representation of atmospheric chemistry is computational more expensive. Using generic aerosol tracers reduces this demand and gives the opportunity to apply the model at a higher horizontal model resolution and to perform a sensitivity analysis regarding the aerosol size.

The generic aerosol tracers are used to explore the outflow from the urban centers, similar to the analysis of Lawrence et al. (2007), there only for insoluble gas phase tracers, but focusing on aerosols and answering the following questions:

1. How does the aerosol from urban centers qualitatively disperse in the atmosphere?
2. In which regions is the emission retention strongest and which is the preferred export pathway?
3. How does the dispersion of the emission depend on the emission height?
4. What are the differences between the outflow of generic gas phase and aerosol tracers?
5. How many people are affected by strong air pollution which originates from major population centers?

To answer this question several metrics are applied, namely E_{UT}, $ELR_{1\mathrm{km}}$, A_{Y}, and $RCL_{0.5\mathrm{km}}$, which were defined in Section 3.2.1. The chapter is structured as follows: the urban emission centers and the model setup are presented first. Then the atmospheric dispersion is qualitatively discussed for small and large aerosol tracers, followed by a quantification of pollutant export and build-up. Finally, the results of a sensitivity study regarding the emission height are presented and the pollution potentials from aerosols are compared to those from gas phase tracers. Furthermore, in Appendix C it is shown that the results from

Lawrence et al. (2007) are reproducible with EMAC.
The content of this chapter, except for Sections 4.3 and 4.5, formed the basis for the following publication: Kunkel et al. (2012b).

4.1 Urban emission locations

In total, 46 major population centers represent the urban emission hot spots in this and the following chapters. The emission locations are distributed around the world, see Table 4.1 and Figure 4.1.

The term major population centers includes also areas which do not fulfill the criteria to be called a megacity for which, depending on definition, either more than five or ten million inhabitants are needed (UNFPA, 2007; Baklanov et al., 2010). However, several cities, e.g., Johannesburg, Sydney, Melbourne, Atlanta, Kinshasa, Khartoum, and Nairobi, have an exceptional standing in their region or are expected to become megacities in the near future. Additionally, three agglomerations of many cities and important industrial sites, i.e., the Rhine-Ruhr Area, the Po Valley, and the Szechuan Basin, are considered as source points but are also represented as small emission source point, so not the entire areas which historically represent these regions are used as urban hot spot. Moreover, Hong Kong includes also the Pearl River Delta (PRD) and Kinshasa in the Democratic Republic of the Congo is a representative for the agglomeration together with Brazzaville in the Republic of the Congo. All MPCs are taken as large emission point sources for generic tracers to study the dispersion in the atmosphere and subsequent deposition onto the surface in the case of aerosols.

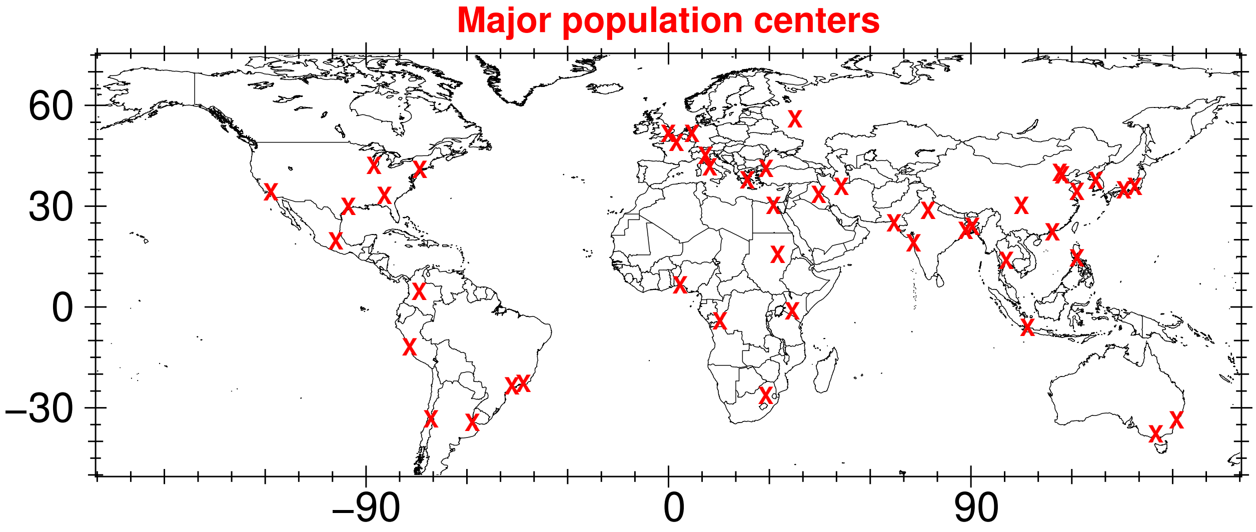

Figure 4.1: Global distribution of major population centers, based on the latitude and longitude information given in Table 4.1.

Table 4.1: Name, longitude, latitude, and climate class of all MPCs used as urban point sources. DRC = Democratic Rep. of the Congo, RC = Rep. of the Congo, PRC = People's Rep. of China, ROK = Rep. of Korea. Climate classes from Peel et al. (2007): Am = tropical, monsoon, Aw = tropical, savannah, BWh = arid, desert, hot, BSk = arid, steppe, cold, Csa = temperate, dry, hot summer, Csb = temperate, dry, warm summer, Cwa = temperate, dry winter, hot summer, Cwb = temperate, dry winter, warm summer, Cfa = temperate, no dry season, hot summer, Cfb = temperate, no dry season, warm summer, Dfa = cold, no dry season, hot summer, Dfb = cold, no dry season, warm summer, Dwa = cold, dry winter, hot summer. The longitude and latitude data for the Po Valley, the Rhine-Ruhr Area, and the Szechuan Basin represent the approximated center of these regions.

MPC	Longitude	Latitude	Climate class
Europe			
London, United Kingdom	0.12	51.50	Cfb
Paris, France	2.35	28.85	Cfb
Rhine-Ruhr, Germany	7.00	51.50	Cfb
Moscow, Russia	37.62	55.75	Dfb
Po Valley, Italy	11.00	45.00	Cfa
Rome, Italy	12.38	41.88	Csa
Athens, Greece	23.73	37.98	Csa
Istanbul, Turkey	28.95	41.00	Csa
Africa			
Cairo, Egypt	31.23	30.05	BWh
Khartoum, Sudan	32.52	15.58	BWh
Nairobi, Kenya	36.82	-1.28	Cwb
Kinshasa, DRC, Brazzaville, RC	15.32	-4.33	Aw
Lagos, Nigeria	3.40	6.45	Aw
Johannesburg, South Africa	28.07	-26.20	Cwb
West Asia			
Baghdad, Iraq	44.38	33.33	BWh
Teheran, Iran	51.42	35.70	BWh
South Asia			
Karachi, Pakistan	67.00	24.85	BWh
Mumbai, India	72.83	18.83	Aw
Delhi, India	77.22	28.67	Cwa
Kolkata, India	88.37	22.57	Aw
Dhaka, Bangladesh	90.40	23.73	Aw
East Asia			
Szechuan Basin, PRC	105.00	30.00	Cwa
Hong Kong, PRC	114.17	22.30	Cwa
Beijing, PRC	116.38	39.93	Dwa
Tianjin, PRC	117.18	39.13	Dwa
Shanghai, PRC	121.47	31.23	Cfa
Seoul, ROK	126.98	37.57	Cwa
Osaka, Japan	135.50	34.68	Cfa
Tokyo, Japan	139.77	35.68	Cfa
South-East Asia			
Bangkok, Thailand	100.52	13.75	Aw
Manila, Philippines	121.00	14.58	Aw
Jakarta, Indonesia	106.83	-6.18	Am
Oceania			
Melbourne, Australia	144.95	37.80	Cfb
Sydney, Australia	151.20	33.85	Cfa
North America			
Los Angeles, USA	-118.25	34.05	BSk
Chicago, USA	-87.63	41.88	Dfa
Houston, USA	-95.38	29.77	Cfa
Atlanta, USA	-84.38	33.75	Cfa
New York,USA	-74.00	40.72	Cfa
Mexico City, Mexico	-99.15	19.42	Cwb
South America			
Lima, Peru	-77.02	-12.03	BWk
Bogotá, Columbia	-74.08	4.60	Cfb
Santiago, Chile	-70.67	-33.45	Csb
Buenos Aires, Argentina	-58.38	-34.60	Cfa
São Paulo, Brazil	-46.62	-23.50	Cfa
Rio de Janeiro, Brazil	-43.20	-22.90	Aw

4.2 Model and simulation setup

4.2.1 Model setup

In this and the next chapter only model version **A** is used to study the fate of urban aerosols in the atmosphere. For the global studies, a relatively high horizontal model resolution of T106 was chosen (see Table 2.1). In the vertical, 31 hybrid sigma-pressure levels are used from the surface up to 10 hPa, which are mainly distributed in the troposphere (see mean midpoint pressures in Section 2.1). The model simulations were initialized in July 2004 and ended at the beginning of January 2006. The first six months are used as model spin up to bring the atmospheric tracer mass into quasi-steady state which takes about three to four months, while the analysis period comprises the last twelve months. Meteorological variables, namely temperature, divergence, vorticity, and the logarithm of the surface pressure are weakly nudged towards analysis data from the ECMWF (see Section 2.3).

4.2.2 Simulation setup

The model setup comprises the following physical processes: emission, atmospheric transport, and wet and dry deposition of generic aerosol tracers and emission, atmospheric transport, and an exponential decay of generic gas phase tracers equal to those used by Lawrence et al. (2007). Mono-modal aerosol tracers represent aerosols with ambient diameters of 0.1, 0.5, 1.0, 2.5, and 10.0 μm and a fixed standard deviation of 1.0. Instead of using a complex, computationally expensive aerosol module to explicitly treat for aerosol microphysics and thermodynamics, two different aerosol solubility states are used which differ in the treatment of scavenging by nucleation: in one case all aerosols can undergo this process (further denoted as $\mathrm{NS_{act}}$) which is tracer size dependent (see Section 2.2 and Tost et al., 2006a) and in the other case this process is completely inhibited and the aerosol tracers are considered to be insoluble (further denoted as $\mathrm{NS_{inact}}$). These two aerosol states are considered as extrema with respect to aerosol solubility, representing an upper and lower estimate of results with the range in between being representative for most of the real atmospheric aerosol particles. In Chapter 6, more complex passive aerosol tracers are introduced which explicitly treat for aerosol microphysics. There I will also show that the generic mono-modal aerosol tracers can well represent ambient aerosols in such a tracer transport study.

Ten aerosol tracers are released at each emission source point, one for each size and solubility state, all with the same source strength of $1\,\mathrm{kg\,s^{-1}\,gridbox^{-1}}$. Thus, the various aerosol tracer properties offer the possibility to obtain information on various parts of the aerosol size distribution. In total, 460 aerosol tracers (46 source points × 5 aerosol sizes × 2 aerosol solubility states) are used, which do not interact with each other and have no feedbacks on clouds or the radiative balance. The small aerosol tracers can be interpreted as primary solid aerosol particles, such as black carbon or soluble secondary organic or inorganic particles. The aerosol tracers with a diameter of $2.5\,\mu$m represent the largest aerosols that are still classified as fine particulate matter used for air quality regulations (cf. $\mathrm{PM_{2.5}}$ = aerosol mass of particles with an aerodynamic diameter smaller $2.5\,\mu$m). These aerosols are distinguished from larger particles, here the $10.0\,\mu$m tracers, which represent fractions of dust, sea-salt, and sometimes minor amounts of organic matter present in urban centers (Kunkel et al., 2012a).

Figure 4.2 shows the different annual atmospheric residence times of all generic aerosol tracers, ordered by the longest lifetime of the $\mathrm{NS_{inact}}$ $1.0\,\mu$m aerosol tracers. The aerosol residence time is calculated with a steady state approach by dividing the annual mean aerosol burden by the total annual emission (Seinfeld and Pandis, 1998). An upper limit for the residence times for each MPC is provided by $\mathrm{NS_{inact}}$ and a lower limit by $\mathrm{NS_{act}}$ aerosol tracers. Since the latter are more susceptible to wet deposition, they have shorter atmospheric residence

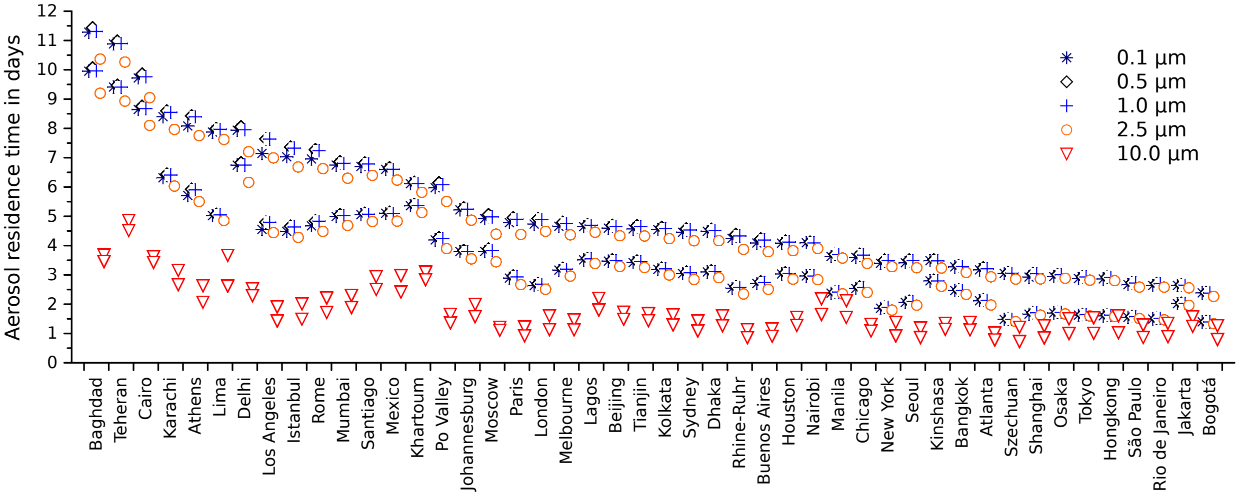

Figure 4.2: Aerosol residence times (in days) of all aerosol tracers from all MPCs. The upper value is determined by the $\mathrm{NS}_{\mathrm{inact}}$ tracers, the lower value by the $\mathrm{NS}_{\mathrm{act}}$ tracers. The MPCs are ordered by the lifetimes of the $\mathrm{NS}_{\mathrm{inact}}$ 1.0 μm aerosol tracers. This figure has been published in Kunkel et al. (2012b).

times. 80 % to 95 % of the mass of fine aerosols is wet deposited which is the main sink of fine aerosols in nature and in the model. For larger aerosols the difference in residence time with respect to aerosol solubility becomes smaller since dry and wet deposition contribute almost equally to the sink processes. Furthermore, the effect of nucleation scavenging is smaller for larger particles since they are removed very efficiently by impaction scavenging (see Section 2.2 and Tost et al., 2006a). In the following sections I will refer to aerosol tracers with diameters of 0.1, 0.5, 1.0, and 2.5 μm as small aerosol tracers, to those with diameters of 10.0 μm as large aerosol tracers.

4.3 Global dispersion of aerosols from major population centers

Before quantifying the transport of aerosols from major population centers with the help of the metrics defined in Section 3.2.1, the distribution of the aerosols in the atmosphere is qualitatively discussed on the basis of annual and seasonal means of total column, surface layer, and upper tropospheric (UT) column tracer densities.

The dispersion patterns deviate only little between the small aerosols, i.e., with diameter $d \leq 2.5\,\mu\mathrm{m}$, while the large differences are simulated between small and large aerosol tracers. Hence, I focus the discussion on generic aerosol tracers with diameters of 1.0 μm and 10.0 μm to represent small and coarse aerosols. $\mathrm{NS}_{\mathrm{inact}}$ aerosol tracer concentrations are more abundant almost everywhere in the atmosphere compared to their $\mathrm{NS}_{\mathrm{act}}$ counterparts, independent of whether the entire atmospheric or the UT column or the surface layer is considered (Figure 4.3). In source-remote areas both in horizontal directions, especially in the outflow regions over the ocean, and at higher altitudes, the $\mathrm{NS}_{\mathrm{act}}$ tracers have lower values compared to and thus the largest deviations to the $\mathrm{NS}_{\mathrm{inact}}$ tracers. This is in line with the longer atmospheric residence times of the $\mathrm{NS}_{\mathrm{inact}}$ aerosol tracers (see Figure 4.2) and a consequence of the lower wet removal rate due to the missing sink by nucleation scavenging.

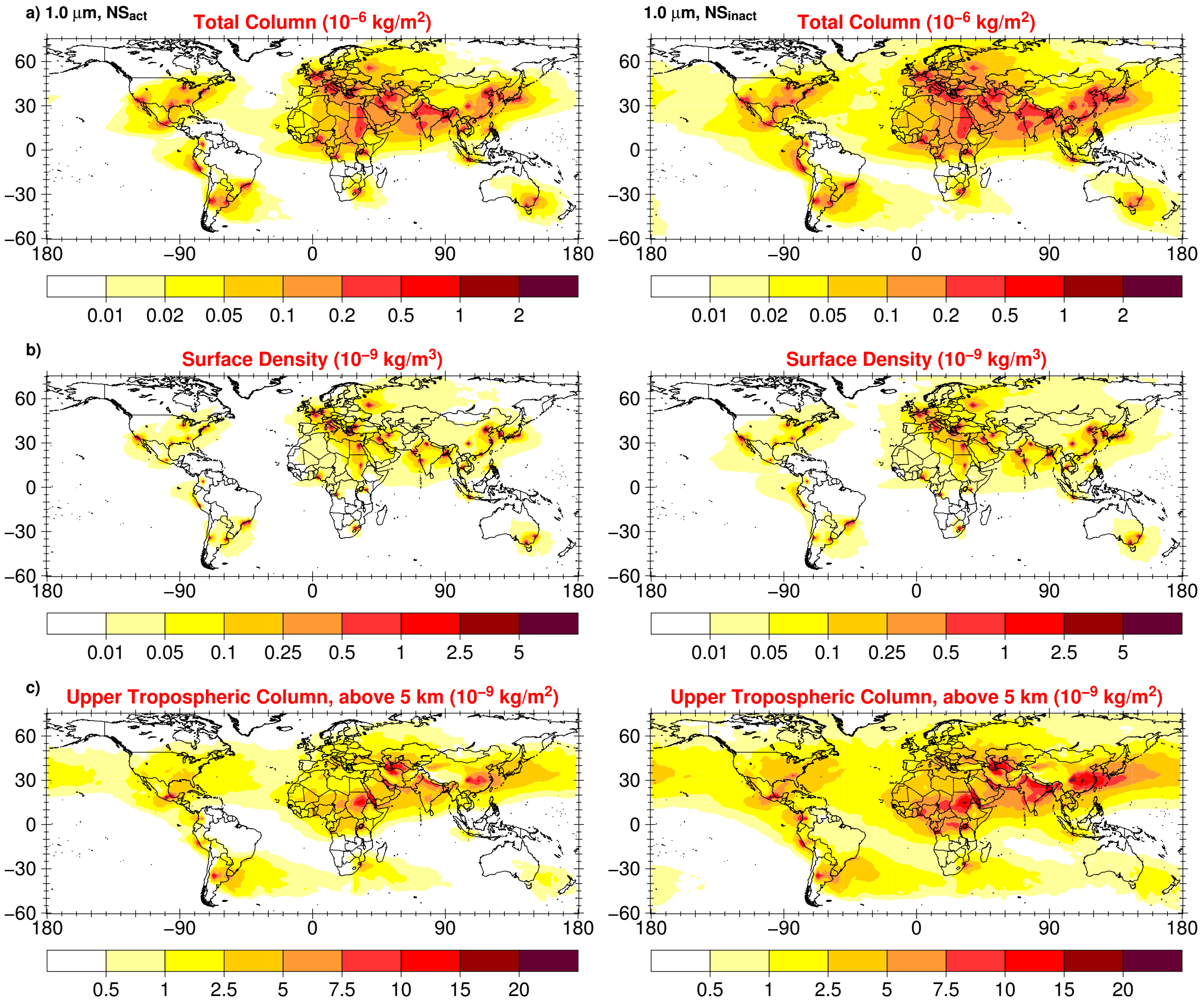

Figure 4.3: Annual mean of the sum of all 46 MPC aerosol tracers for a) the total column density (in 10^{-6} kg m^{-2}), b) the surface density (in 10^{-9} kg m^{-3}), and c) the upper tropospheric column density above 5 km (in 10^{-9} kg m^{-2}). On the left depicted for NS$_{\text{act}}$, on the right for NS$_{\text{inact}}$ 1.0 µm aerosol tracers.

In contrast, the difference between the two solubility states is less pronounced for the large aerosol tracers (see Figure 4.4). Mainly the transport above 5 km is slightly more efficient for large NS$_{\text{inact}}$ tracers, indicated by greater UT densities. As will be shown in Section 5.2, larger aerosols are removed more rapidly by gravitational settling. Thus, the difference is smaller between NS$_{\text{inact}}$ and NS$_{\text{act}}$ tracers since less mass is generally available for wet removal. The fast dry removal is also the main cause why the atmospheric burden of large aerosols is smaller compared to small aerosols, especially in source-remote areas. The long-range transport of large aerosols is less efficient but non-negligible as will be shown in Section 5.4.

Although the emissions are constant in time, the outflow of MPC tracers shows a seasonal cycle because of changing meteorological conditions in various regions. In course of this, the surface layer and the upper troposphere show opposing trends in the corresponding tracer densities. When more mass is retained in the surface layer, less mass is commonly transported to higher altitudes and vice versa. Figures 4.5 and 4.6 illustrate the seasonal cycle

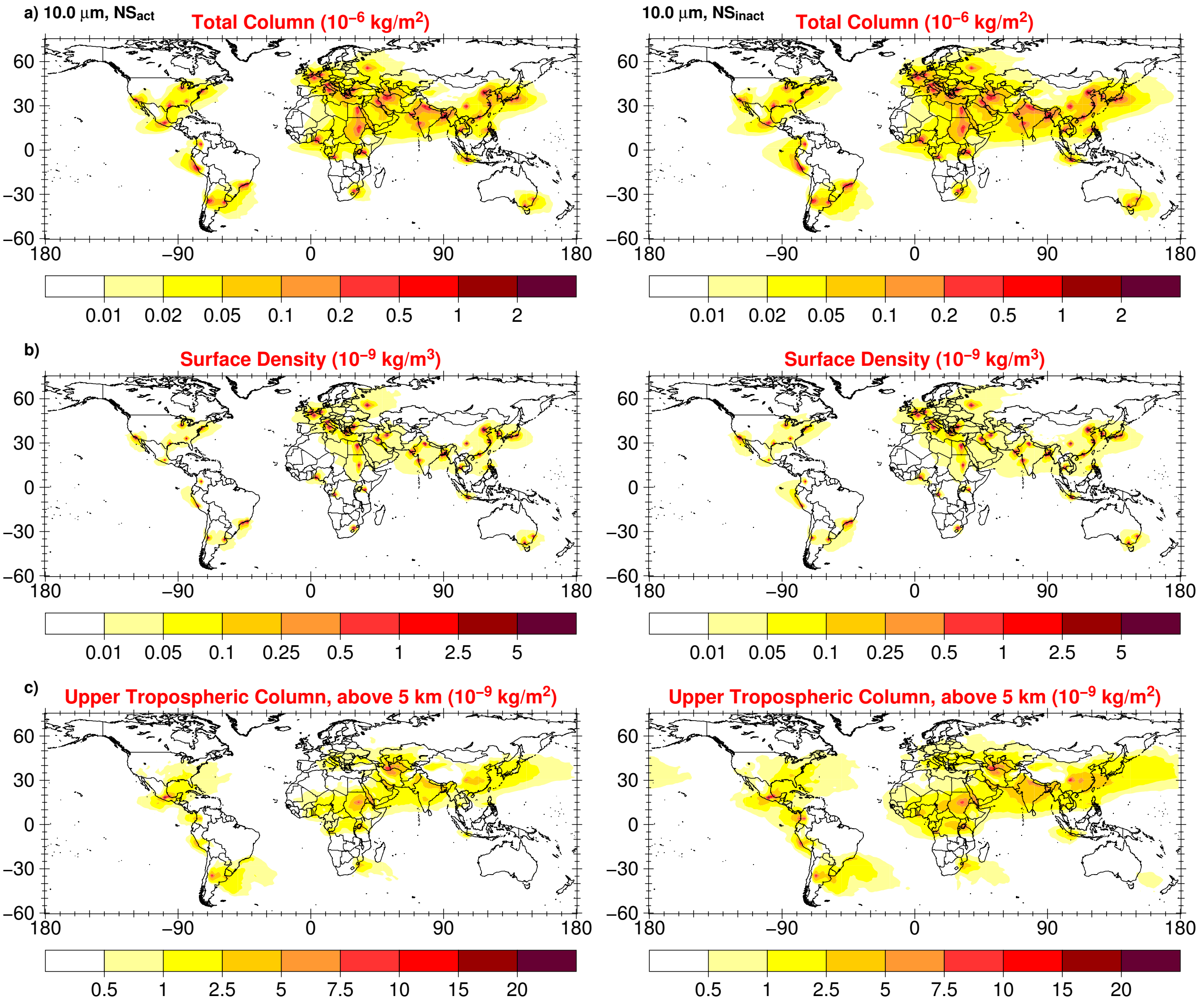

Figure 4.4: Same as Figure 4.3 for $\mathrm{NS}_{\mathrm{act}}$ and $\mathrm{NS}_{\mathrm{inact}}$ 10.0 µm aerosol tracers.

of small and large $\mathrm{NS}_{\mathrm{inact}}$ aerosol column densities in the upper troposphere. The amount of mass above 5 km is determined by the upward transport, either in convective cells or in warm conveyor belts. Hence, peaks in upper tropospheric column densities are found in regions where either one of these processes lifts aerosol mass in sufficiently large amounts. For example, from December until February (DJF) the UT mass burden peaks in Africa around the equator where the Intertropical Convergence Zone (ITCZ) is situated during this time of the year and in South America and eastern China. From March until May (MAM), aerosol tracers from Mexico City dominate the UT mass burden over North America. An immense peak occurs in the outflow from East Asia, originating from the emissions in South Asia (Indian sub-continent), which are lifted in the pre-Monsoon circulation. During boreal summer (June-August, JJA), convective activity in the middle latitudes lifts aerosol mass into the upper troposphere above the United States as well as in a region spanning from the eastern Sahel region to India. In the US, local summer storms mainly cause the lifting, whereas in the other region the lifting occurs in the ITCZ (Africa) or in the summer monsoon circulation (India). Another process to bring surface pollution into the upper troposphere occurs, for example, in Teheran: the development of a deep boundary layer. This

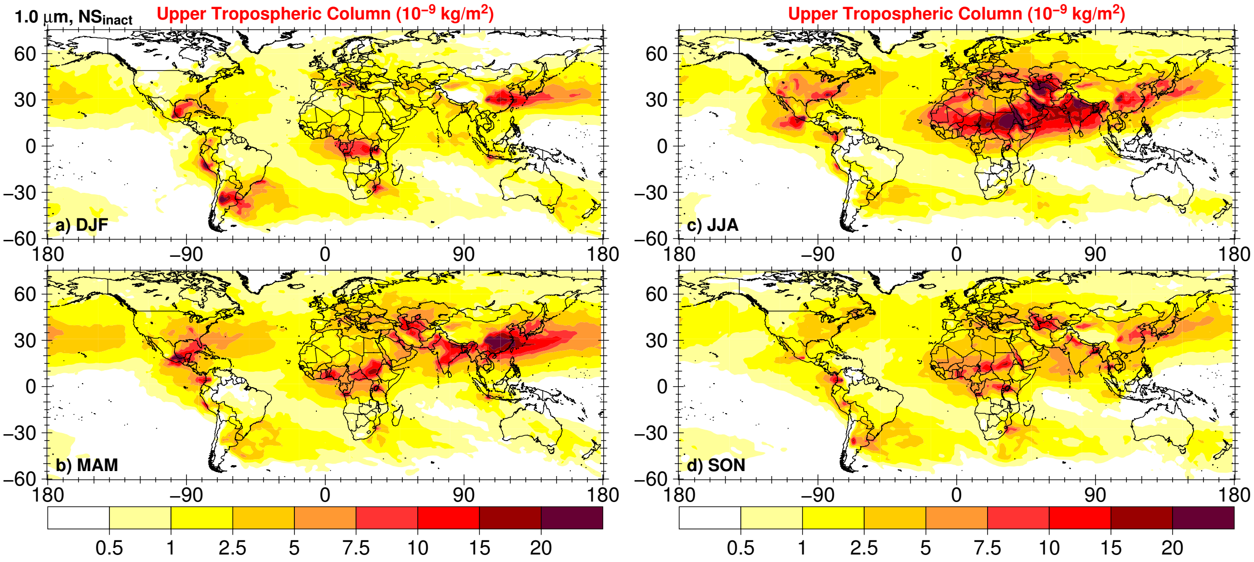

Figure 4.5: Seasonal means of the upper tropospheric column density (in $10^{-9}\,\mathrm{kg\,m^{-3}}$) of the sum of all 46 $\mathrm{NS_{inact}}$ 1.0 µm aerosol tracers for a) DJF, b) MAM, c) JJA, and d) SON.

is commonly observed in dry regions such as the Saharan dessert (Hall and Peyrillé, 2007), where the surface pollution becomes well mixed up to several kilometers. Furthermore, the elevation of Teheran (1191 m in reality, 1280 m in the model) reduces the distance between the emission altitude and the threshold altitude of 5 km. From September until November the peaks in the UT column densities are lower compared to MAM and JJA. Generally, the $\mathrm{NS_{act}}$ tracers (not shown) show the same spatial UT distribution but have lower UT column densities.

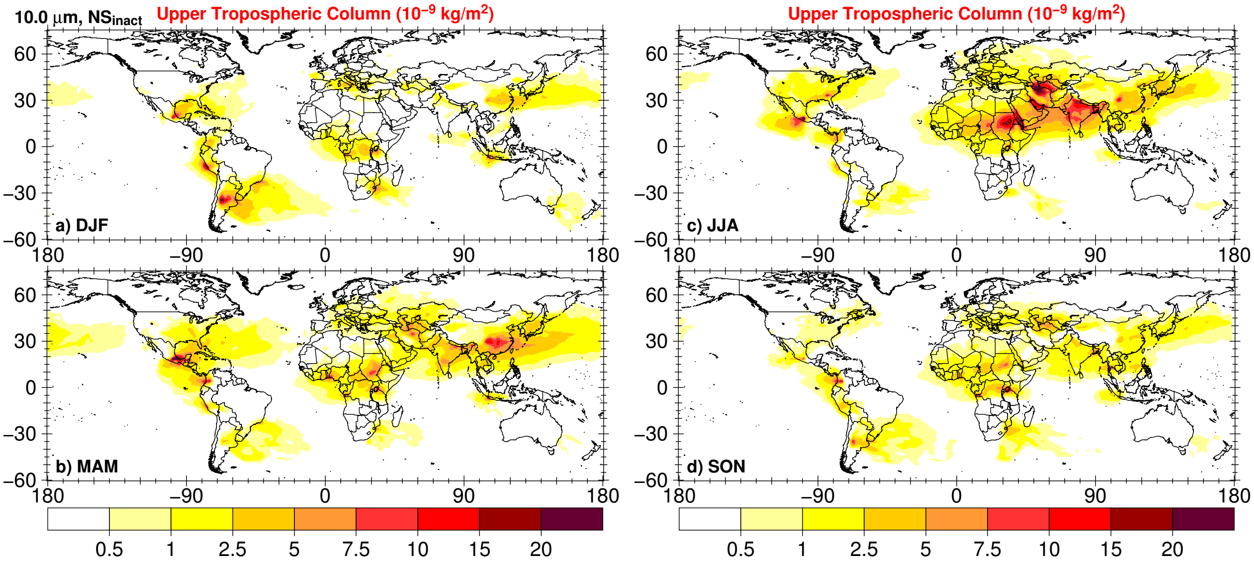

Figure 4.6: Same as Figure 4.5 for $\mathrm{NS_{inact}}$ 10.0 µm aerosol tracers.

4.4 Quantifying transport of aerosols from urban emission hot spots

4.4.1 Low-level retention of urban aerosol

Figure 4.7 shows annual means of the retention pollution potential, $RCL_{0.5\text{km}}$. The gray shaded area which is bounded by the solid and dashed black lines represents the MPC means for NS_{inact} and NS_{act} aerosol tracers. The light gray shaded areas contiguous to this area denote the standard deviation, each plotted one-sided for the upper and lower bound. The overall annual mean values range between 10 % and 14 % for small tracers and 15 % to 19 % for large tracers. The six climate classes introduced in Section 3.3 are used to provide more information about regional differences. The Köppen-Geiger climate class of each MPC is listed in the last column of Table 4.1 and the six climate clusters are as follows (with corresponding colors used in figures in parenthesis): tropical A (red), arid B (brown), temperate no dry season Cf (light green), temperate dry winter Cw (light blue), temperate dry summer Cs (dark green) and cold D (blue).

For small NS_{inact} aerosol tracers, minimum retention of tracer mass occurs in urban centers in arid (B) and temperate dry summer (Cs) regions with $RCL_{0.5\text{km}}$ about 7 %, and the maximum for MPCs in tropical (A) and cold (D) regions with values of about 11 % to 12 %. The same regions show the minima for NS_{act} aerosol tracers of about 9 %, while tropical and temperate no dry season (Cf) means are the maxima, with values of about 17 %. Large aerosol tracers from urban centers in arid regions reveal minimum values of 9 % (NS_{inact}) and 10 % (NS_{act}), respectively, while the maximum values are found for both solubility states in cold regions and also in the soluble case for temperate no dry season regions, with climate

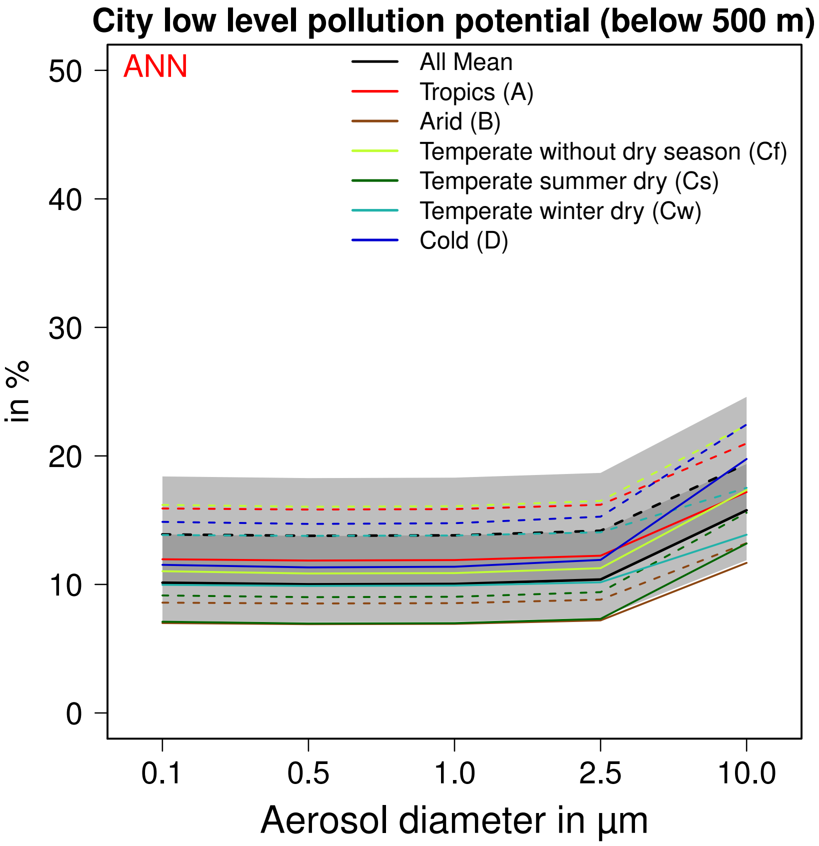

Figure 4.7: Annual overall and climate class means of $RCL_{0.5\text{km}}$ (in %). Dark gray shaded areas represent the area between the total means (black lines) of NS_{act} (dashed) and NS_{inact} (solid) MPC tracers. Light gray shaded areas show one standard deviation, plotted single sided for NS_{act} and NS_{inact} mean values. Each colored lines represent the mean values for different climate classes: tropical (red), arid (brown), temperate no dry season (light green), temperate summer dry (dark green), temperate winter dry (light blue) and cold (blue). No shading is used for climate classes to keep lucidity. This figure has been published in Kunkel et al. (2012b).

class means of 20 % ($\mathrm{NS}_{\mathrm{inact}}$) and 22 % ($\mathrm{NS}_{\mathrm{act}}$). Further, almost all mean values for arid and temperate dry summer regions show, independent of solubility state, smaller mean values than all other climate class means, which is also the case in almost every season of the year (Figure 4.10). Only in temperate dry winter regions such low $RCL_{0.5\mathrm{km}}$ values appear during winter months (DJF). Thus, the relative pollution build-up in these two regions is smaller than in all other climate classes. Furthermore, the pollution build-up in two contrary climate regions, tropical and cold, is highest, although meteorological conditions lead to different atmospheric dispersion. Please note that results from the Southern Hemisphere have been shifted by six months to be in accordance with the Northern Hemispheric seasonal cycle.

The retention of tracer mass is controlled by two mechanisms. On the one hand, $RCL_{0.5\mathrm{km}}$ anti-correlates with the atmospheric residence time of the tracers. As mentioned before, the residence time is mainly governed by wet removal, thus aerosol tracers with short residence times often originate in regions with high precipitation rates, i.e., tropical regions. In contrast, for tracers from arid regions the residence time is relatively long due to missing precipitation. Thus, the relative contribution of the emission to the global burden of a tracer is larger for those with short lifetimes since a large fraction of the burden is generally closer to the source with higher $RCL_{0.5\mathrm{km}}$ values. This accounts for about 50 % of the variance in the overall $RCL_{0.5\mathrm{km}}$ results (determined with the coefficient of determination, R^2). On the other hand, meteorological conditions that change the distribution of the tracer mass in the atmosphere, though not directly their residence time, are responsible for the missing variance. For example surface winds, turbulent mixing, or the depth of the boundary layer height can alter $RCL_{0.5\mathrm{km}}$ values without affecting the aerosol lifetime.

The influence of precipitation also plays a major role in the seasonal variations in $RCL_{0.5\mathrm{km}}$. The minimum climate means of $RCL_{0.5\mathrm{km}}$ are almost constant throughout the year since the minima are given by mean values from regions which are weakly affected by precipitation. In contrast, the maxima vary with the season, with the difference between $RCL_{0.5\mathrm{km}}$ minima and maxima being largest in summer (JJA) when precipitation rates are generally larger and consequently the aerosol residence times shorter.

4.4.2 Low-level long-range export of urban aerosol

In contrast to local pollution build-up, the emissions from urban centers also undergo transport which can either be horizontal or vertical. At first the horizontal transport is investigated by focusing on the mass which is transported near the surface or which was first lifted and subsequently descended again to lower altitudes, e.g., in a dry intrusion or simply by aerosol sedimentation. Overall annual means of the low-level remote pollution potential $ELR_{1\mathrm{km}}$ vary between 16 % and 20 % for small and 12 % and 15 % for large tracers, with larger values now given by $\mathrm{NS}_{\mathrm{inact}}$ aerosol tracers (see Figure 4.8). Including climate class averages, the diversity increases with values ranging from 11 % to 27 % for small and from 8 % to 19 % for large aerosol diameters. Aerosol tracers from cold regions possess the largest remote low-level mass fraction with more than 25 % of their total mass (averaged over $\mathrm{NS}_{\mathrm{inact}}$ and $\mathrm{NS}_{\mathrm{act}}$ tracers) located in the near-surface layer downwind of the source. In contrast to the local build-up, aerosols from temperate dry summer regions show a large downwind

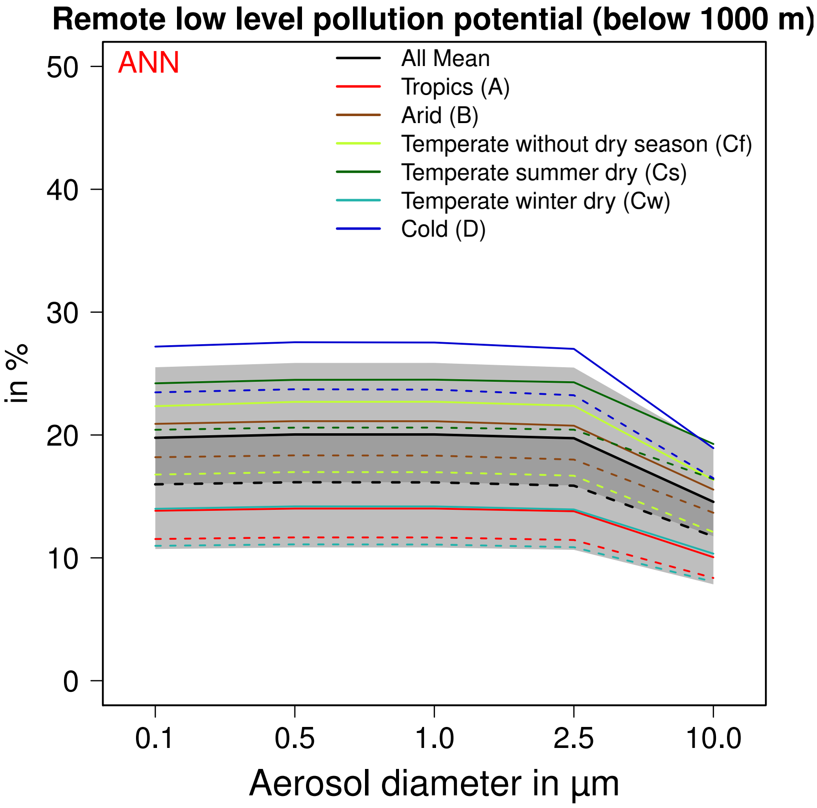

Figure 4.8: Same as Figure 4.7 for $ELR_{1\mathrm{km}}$. This figure has been published in Kunkel et al. (2012b).

pollution potential. The least low-level export occurs in temperate dry winter and tropical regions since upper level export is favored in these regions (see following Section 4.4.3). Similarly, the smallest seasonal means appear for aerosol tracers from tropical regions, except during winter when those from temperate dry winter regions show least downwind pollution potential due to relatively enhanced transport into the upper troposphere. $ELR_{1\mathrm{km}}$ means peak either for aerosol tracers from cold or temperate dry summer regions. In general, the highest downwind pollution potential is found during winter months (DJF) with overall means between 21 % and 25 % and the least during summer (JJA) with overall means of about 10 % to 12 %.

In winter, atmospheric low-level inversions occur more frequently and aerosol tracer mass is kept more efficiently within the boundary layer which is commonly shallower during this time of the year. Together with less convective activity, the $ELR_{1\mathrm{km}}$ seems to be dominated by the atmospheric stability. Higher stability leads to greater remote low-level transport (see Figure 4.10).

Similar to Lawrence et al. (2007) the response of a change in the depth of the near-surface layer is analyzed and a metric height of 500 m is considered. They found that the remote low-level export decreased almost linearly with the volume, i.e., only a tenth of the $ELR_{1\mathrm{km}}$ numbers are found in a layer which is 100 m deep. For aerosols, on average about 50 % of the $ERL_{1\mathrm{km}}$ mass is present in a volume half as deep as the original volume, thus the same relationship is found for aerosols like for gases in Lawrence et al. (2007). This number shows a small seasonal variation with a maximum in winter (on average 53 %) and a minimum in summer (on average 47 %) due to the same reason as for the seasonal variation in $ELR_{1\mathrm{km}}$.

Additionally, the ratio is slightly dependent on aerosol solubility with higher ratios for soluble aerosol tracers but with almost no dependence on aerosol size.

4.4.3 Export of urban aerosol into the upper troposphere

Aerosol mass is also lifted out of the source region into the upper troposphere (see Figure 4.9). Overall annual means of E_{UT} are between 3 % and 4 % for small and 2.5 % and 3.5 % for large aerosol tracers and thus much smaller than for the other two metrics and especially much smaller than E_{UT} values for gas phase tracers reported by Lawrence et al. (2007). The order of the climate means is reversed compared to the order found for $ELR_{1\mathrm{km}}$, now with maximum pollution for aerosol tracers from temperate dry winter and tropical regions and minimum pollution for those from cold regions.

These findings rely on several facts which need to be discussed. First, the difference between $\mathrm{NS}_{\mathrm{inact}}$ and $\mathrm{NS}_{\mathrm{act}}$ means strongly varies between climate classes. For tropical regions which are heavily and regularly affected by convection, the different treatment of nucleation scavenging leads to strong differences in the UT pollution with $\mathrm{NS}_{\mathrm{act}}$ means accounting for only about 60 % of the $\mathrm{NS}_{\mathrm{inact}}$ means. In contrast, for aerosols from cold regions this ratio is about 90 %, thus the difference is almost negligible caused by an inefficient nucleation scavenging of snow and ice crystals according to the model formulation. Second, for gas phase tracers the strongest vertical tracer displacement occurred in tropical regions (Lawrence et al., 2007), contrary to the aerosol tracer results with maximum vertical aerosol transport in temperate dry winter regions, especially in the case of $\mathrm{NS}_{\mathrm{act}}$ means. The input of mass into the upper troposphere occurs in most cases by convective or conveyor belt lifting. Both processes are

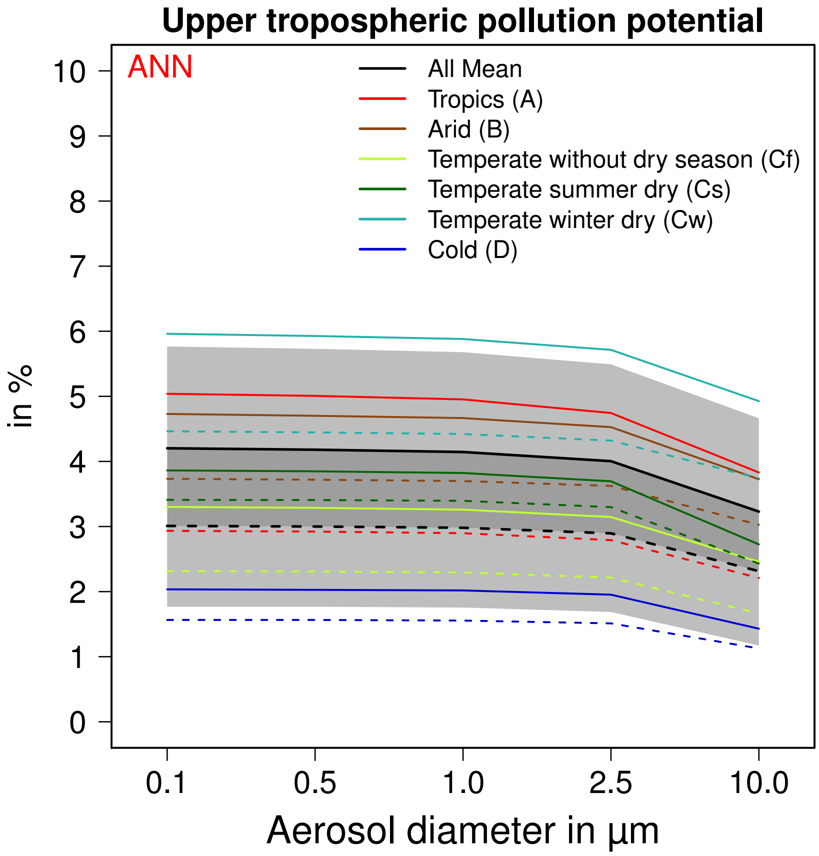

Figure 4.9: Same as Figure 4.7 for E_{UT}. This figure has been published in Kunkel et al. (2012b).

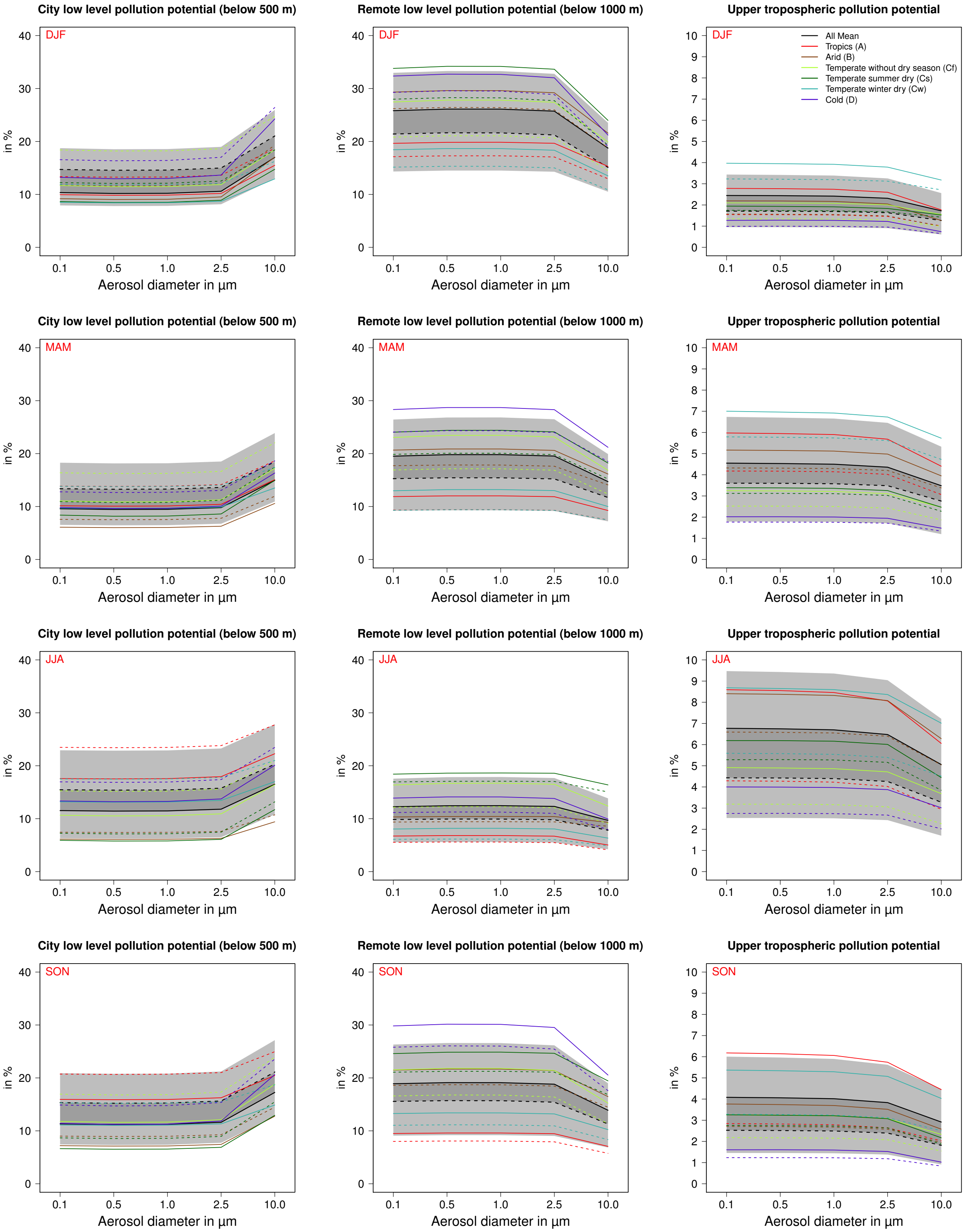

Figure 4.10: Seasonal means (in %) of $RCL_{0.5\mathrm{km}}$ (left panels), $ELR_{1\mathrm{km}}$ (middle panels), and E_{UT} (right panels) for winter (DJF), spring (MAM), summer (JJA) and autumn (SON) from top to bottom. Results from the Southern Hemisphere have been shifted by six months to be in accordance with the Northern Hemispheric seasonal cycle. The color-scaling is the same as in Figure 4.7. This figure has been published in the appendix of Kunkel et al. (2012b).

commonly associated with cloud formation and subsequent precipitation which both remove aerosol particles efficiently. Nucleation scavenging during cloud formation is the dominant scavenging process for aerosol particles with diameters larger than $0.2\,\mu\mathrm{m}$, while impaction scavenging becomes important for large aerosol particles (diameter $d \geq 2.5\,\mu\mathrm{m}$). With sufficient lifting activity the E_{UT} mass fraction strongly depends on the liquid and/or ice water content of the clouds and their extension, which in turn determine the scavenged mass. From the pure gas phase tracer simulations it is known that the upward transport is strongest in the tropics though the moisture present there limits the upward transport of aerosols so strongly that less mass than in the temperate dry winter regions reaches the upper troposphere. In arid regions precipitation hardly affects lifting processes. As mentioned before, the tracer distribution is affected by the development of a very deep, well mixed air layer which can reach altitudes up to 5 km such as the Saharan Air Layer (Hall and Peyrillé, 2007). The aerosols emitted at the surface are already mixed to altitudes of several kilometers in this layer and consequent lifting above 5 km can occur faster and is often associated with little or no precipitation. Third, the seasonal cycle is also reversed compared to what was reported for ELR_{1km}, with minimum values during winter, with overall means of about 1.5 % and 2.5 %, and maximum values during summer, with overall means of about 4.5 % and 6.5 % (Figure 4.10). Furthermore, the variability, indicated by the standard deviation and also by the differences between various climate classes, is largest in summer and smallest in winter. This is again attributed to the convective activity, which is stronger in summer, but also shows strong differences between different regions of the world and thus also between different climate classes.

Thus, the interplay of atmospheric moisture and lifting activity and their effect on aerosol tracers is the controlling factor for transport to the upper troposphere, with relatively small aerosol mass fractions in this domain.

4.4.4 Relation between near surface and vertical transport

As mentioned before in Section 4.3, pollutant export and retention are not distinct from each other. Now it is assessed whether there are significant correlations in the outflow of aerosols from MPCs. Lawrence et al. (2007) reported that for gas phase tracers a significant relation was found, and that the upward transport, rather than the low-level transport, is mainly responsible for ventilating surface pollution. Moreover, they found that the trade-off between long-range low-level export and dilution of pollutants in the region surrounding the MPCs becomes more evident for regions with similar vertical transport.

In general, an anti-correlation is computed between the horizontal and vertical export (see Table 4.2). This relationship is expected since aerosol mass is either lifted to higher altitudes or kept at lower levels, being advected rather horizontally. However, the overall anti-correlation is weakened since this anti-correlation breaks down in the tropics. An ambiguous situation is found there for different MPCs. For instance in Jakarta and Manila, the opposing relationship between the two export pathways is still assessed, while it breaks down in other MPCs, for instance in Rio de Janeiro, Kolkata, or Lagos. A possible interpretation might be that in the first case, convective scavenging dominates the wet deposition and in the second case more aerosols are scavenged in large-scale clouds. In regions with dominant

Table 4.2: Pearson correlation coefficients for correlations between E_{UT}, ELR_{1km}, and $RCL_{\mathrm{0.5km}}$, climate class resolved and for all MPCs (row All) for small (1.0 µm) and large (10.0 µm) aerosol tracers. This table has been published in Kunkel et al. (2012b).

	E_{UT}: ELR_{1km}	ELR_{1km}: $RCL_{\mathrm{0.5km}}$	E_{UT}: $RCL_{\mathrm{0.5km}}$	E_{UT}: ELR_{1km}	ELR_{1km}: $RCL_{\mathrm{0.5km}}$	E_{UT}: $RCL_{\mathrm{0.5km}}$
1.0 µm	$\mathrm{NS_{inact}}$			$\mathrm{NS_{act}}$		
A	0.00	-0.26	-0.04	0.43	-0.31	-0.30
B	-0.97	0.43	-0.43	-0.76	-0.12	-0.36
Cf	-0.75	-0.38	-0.18	-0.61	-0.43	-0.31
Cs	-0.90	0.72	-0.88	-0.96	0.73	-0.84
Cw	-0.84	0.13	-0.60	-0.58	0.02	-0.70
D	-0.98	-0.92	0.84	-0.98	-0.95	0.86
All	-0.77	-0.19	-0.27	-0.51	-0.28	-0.49
10.0 µm	$\mathrm{NS_{inact}}$			$\mathrm{NS_{act}}$		
A	0.05	-0.31	-0.05	0.15	-0.38	-0.21
B	-0.92	0.39	-0.64	-0.59	-0.17	-0.63
Cf	-0.75	0.08	-0.53	-0.66	-0.09	-0.52
Cs	-0.96	0.89	-0.95	-0.97	0.90	-0.95
Cw	-0.70	0.22	-0.75	-0.49	0.09	-0.78
D	-0.97	0.45	-0.66	-0.92	0.01	-0.38
All	-0.74	0.13	-0.58	-0.50	-0.07	-0.66

convective scavenging more aerosol mass is effectively lifted to higher altitudes but also efficiently removed by scavenging. Less mass is then left over to participate in any long-range transport, especially at low levels. This could result in an opposing relationship between vertical and near-surface long-range transport. Oppositely, more large-scale scavenging indicates that a larger proportion of aerosol mass has possibly undergone farther transport before removal. A correlation between vertical and near-surface long-range transport would then suggest that the outflow occurs at high and low levels.

Between low-level export and low-level retention, the correlation coefficients show a very ambivalent behavior with most values in the range of $[-0.5, 0.5]$. The sign varies between various climate classes and also between aerosol size and solubility. Only in two cases higher correlations are assessed: a positive one in temperate dry summer regions for small and large aerosol tracers and a negative one for small aerosol tracers from cold regions. In the first region, the mass fraction is rather small for $RCL_{\mathrm{0.5km}}$ but high for ELR_{1km}. The positive correlation indicates that the low level export forms an important path to accumulate mass in the near-surface region downwind. A positive correlation might be expected for the cold regions with high ELR_{1km} and $RCL_{\mathrm{0.5km}}$ mass fraction. However, since the vertical export is low in this climate region, the strength of surface wind and turbulent mixing within the boundary layer determines whether more of the mass is retained close to the source or advected downwind.

As expected, the correlation coefficients between low-level retention and vertical export reveal a negative sign in most cases. For small aerosol tracers the correlations are rather weak, only in temperate dry summer regions a strong anti-correlation is assessed and in cold regions a strong correlation. The positive correlation coefficients for cold regions indicate that if lifting takes place it occurs close to the emission source at low levels. On the other hand, an anti-correlation points more to lifting that either takes place farther away from the source or has its origin above 500 m altitude. For most climate regions this is true for the large aerosol tracers since they show stronger anti-correlations, even in cold regions. However, the sampling statistics are small and not equally distributed over the climate classes, thus the results should only be interpreted as a first indication.

4.4.5 Surface pollution impact on humans

$ELR_{1\text{km}}$ and $RCL_{0.5\text{km}}$ have been used so far to determine the low-level pollution, in the first case in remote regions and in the second case the pollution around the source near the surface. Complementary to $RCL_{0.5\text{km}}$, the dense part of the outflow plume around the emission sources can be described by the area of surface tracer density threshold exceedance (A_{Y}). Figure 4.11 shows an example for A_1, A_{10}, and A_{100} for Paris. The annual mean surface layer tracer densities of four different tracers are depicted such that A_{100} is represented by the red areas, A_{10} by red and orange areas, and A_1 by red, orange, and yellow areas. The geographical distributions of the surface densities reflect the general expectation that small aerosols are more widely dispersed than large aerosols. In Table 4.3 A_1, A_{10}, and A_{100} are listed as annual means, averaged over all MPC values, and the corresponding standard

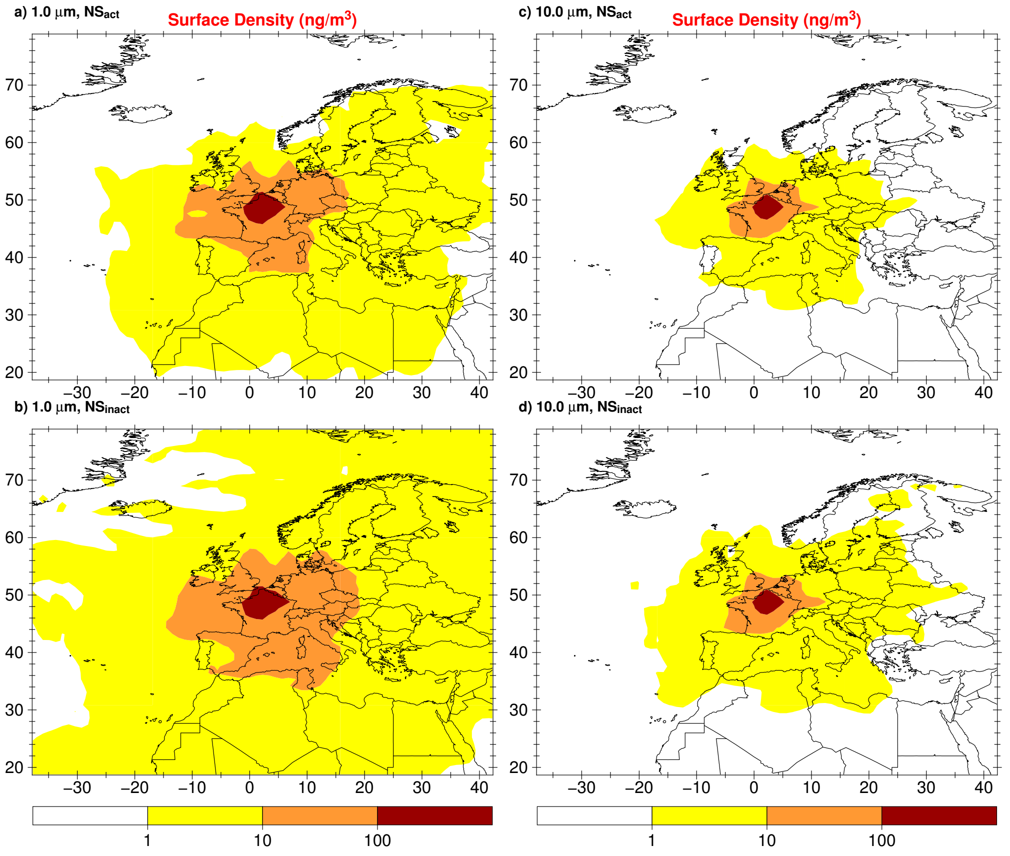

Figure 4.11: Annual mean surface layer density (in ng m^{-3}) for a) NS$_{\text{act}}$ 1.0 μm, b) NS$_{\text{inact}}$ 1.0 μm, c) NS$_{\text{act}}$ 10.0 μm, and d) NS$_{\text{inact}}$ 10.0 μm, released from the location of Paris. The color bar is chosen to represent the tracer density thresholds.

Table 4.3: Annual means of MPC-averaged areas (in $10^6\,\mathrm{km}^2$) and corresponding standard deviations of tracer density threshold exceedance for threshold concentrations of $100\,\mathrm{ng/m}^3$ (A_{100}), $10\,\mathrm{ng/m}^3$ (A_{10}), and $1\,\mathrm{ng/m}^3$ (A_1).

		A_{100}	A_{10}	A_1
$d = 0.1\,\mu\mathrm{m}$	$\mathrm{NS}_{\mathrm{act}}$	0.235±0.118	2.479±1.607	14.247± 9.424
	$\mathrm{NS}_{\mathrm{inact}}$	0.279±0.144	3.293±2.013	21.977±13.384
$d = 0.5\,\mu\mathrm{m}$	$\mathrm{NS}_{\mathrm{act}}$	0.240±0.123	2.542±1.643	14.575± 9.614
	$\mathrm{NS}_{\mathrm{inact}}$	0.288±0.150	3.413±2.089	22.800±13.920
$d = 1.0\,\mu\mathrm{m}$	$\mathrm{NS}_{\mathrm{act}}$	0.238±0.121	2.528±1.629	14.500± 9.544
	$\mathrm{NS}_{\mathrm{inact}}$	0.287±0.150	3.391±2.068	22.668±13.794
$d = 2.5\,\mu\mathrm{m}$	$\mathrm{NS}_{\mathrm{act}}$	0.226±0.112	2.358±1.482	13.657± 8.814
	$\mathrm{NS}_{\mathrm{inact}}$	0.267±0.141	3.130±1.881	20.984±12.561
$d = 10.0\,\mu\mathrm{m}$	$\mathrm{NS}_{\mathrm{act}}$	0.128±0.049	1.025±0.538	6.199± 3.146
	$\mathrm{NS}_{\mathrm{inact}}$	0.139±0.055	1.194±0.623	7.908± 3.693

deviations to account for the variation among the MPCs. The numbers indicate that close to the source the dilution is almost linear, while this relationship is lost the longer the pollutant is in the atmosphere. Mean values of A_{10} are about ten times larger than for A_{100} but larger than a tenth of A_1. The area of the tracer density threshold exceedance is larger for the small aerosols by a factor of two ($\mathrm{NS}_{\mathrm{act}}$) to three ($\mathrm{NS}_{\mathrm{inact}}$) than for the large aerosols in all three cases.

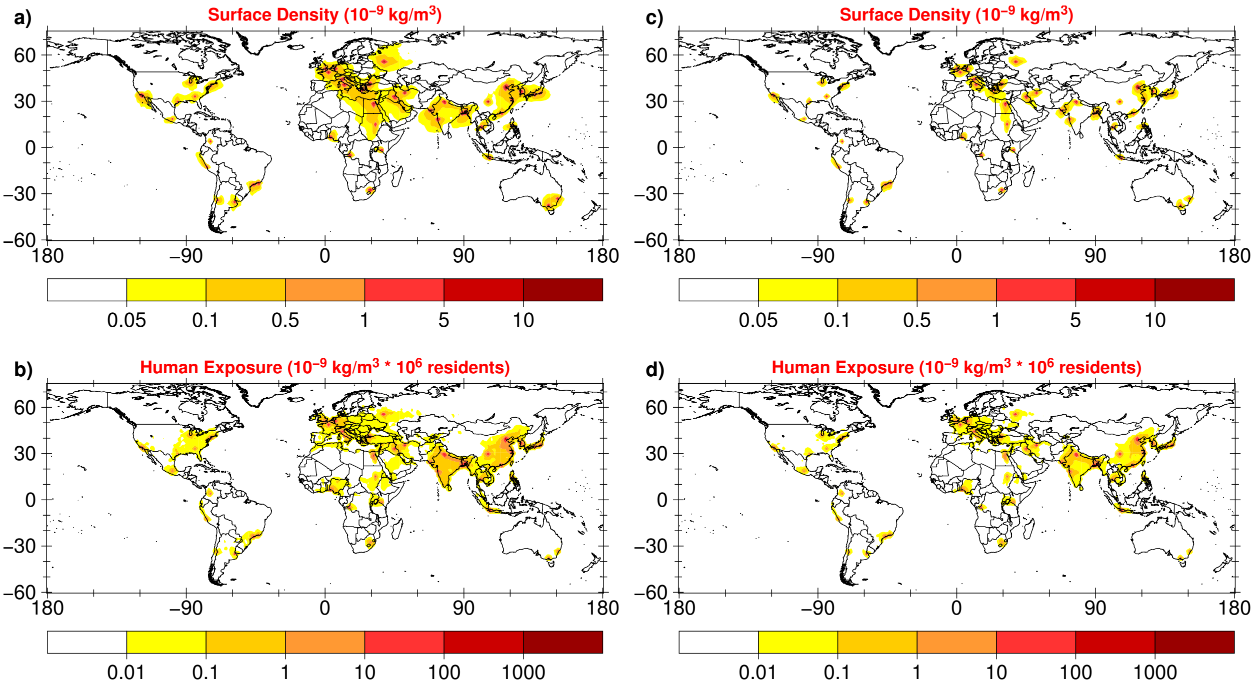

Figure 4.12: Sum of all MPC surface densities (in $10^{-9}\,\mathrm{kg\,m^{-3}}$, upper panels), and convolved with the geographical population distribution (in $10^{-9}\,\mathrm{kg\,m^{-3}} \cdot 10^6$ residents, lower panel). On the left side for the $\mathrm{NS}_{\mathrm{act}}$ $1.0\,\mu\mathrm{m}$, on the right side for the $\mathrm{NS}_{\mathrm{act}}$ $10.0\,\mu\mathrm{m}$ aerosol tracers. This figure has been published in Kunkel et al. (2012b).

In addition, aerosol particles have the ability to potentially influence their environment when they are airborne in several ways. For instance, humans can breathe in small aerosol particles into the lungs and it is certain that this affects the life expectancy of humans (e.g., Dockery et al., 1993; Pope et al., 2009), since the small aerosols penetrate the membranes and enter the blood circulation or are transported along olfactory nerves into the brain (Pöschl, 2005). However, it is not clear which physical or chemical property of the aerosol particle (size, structure, number or mass concentration, solubility, chemical components, etc.) determines the adverse health effects (for review it is referred to Stanek et al., 2011). In light of this, surface densities of small and large aerosols, represented by the 1.0 µm and 10.0 µm aerosol tracers, are convolved with a geographical population distribution (see Section 3.4) to study the regions where emissions from megacities have the largest effects on humans. Furthermore, A_{10} is used to determine the number of people that is exposed to strong air pollution.

In Figure 4.12a and c, surface tracer densities for small and large $\mathrm{NS_{act}}$ tracers are displayed. In the surface layer the differences between $\mathrm{NS_{act}}$ and $\mathrm{NS_{inact}}$ are almost negligible, especially in regions close to the MPCs, thus the focus of the discussion is on the $\mathrm{NS_{act}}$ aerosols tracers. MPCs are easily detectable by the red dots in the figure, even when the surface tracer densities are convolved with the geographical population distribution (Figure 4.12b and d). However, two large domains are additionally more accentuated: India and (East) China. Together these two countries host about one third of the global human population and thus

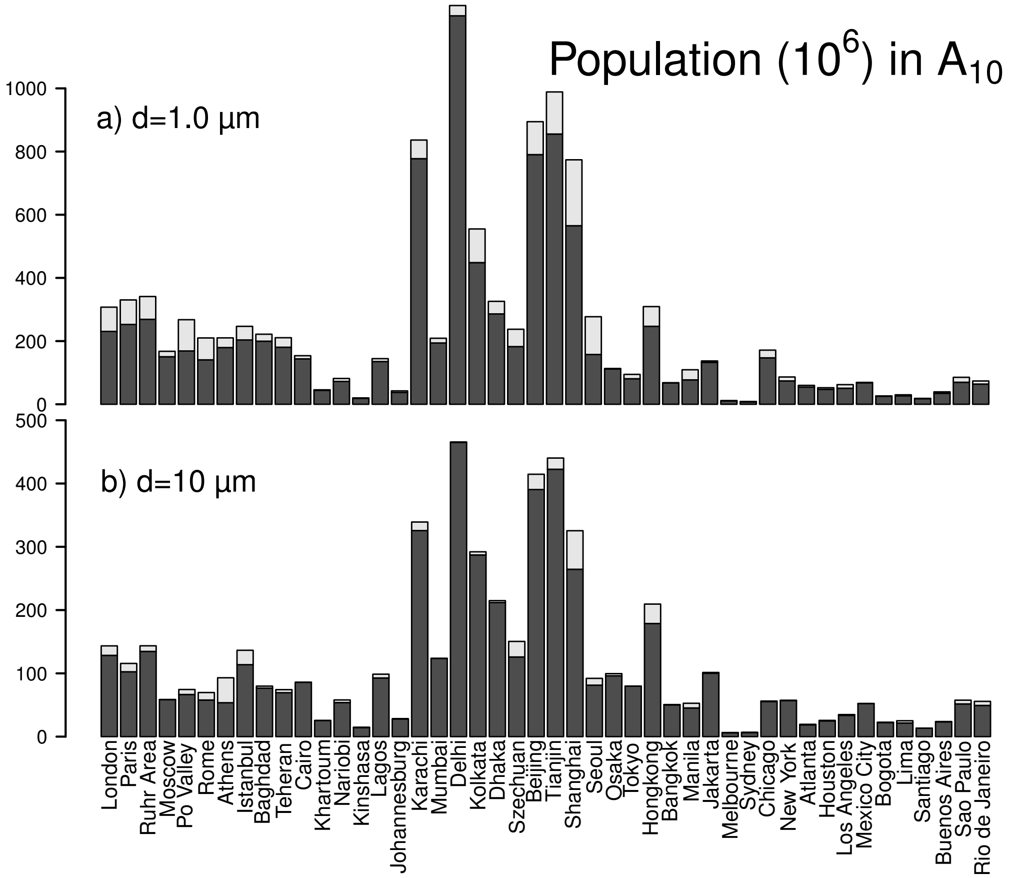

Figure 4.13: Human population (in 10^6) which is exposed to more than $10.0\,\mathrm{ng\,m^{-3}}$ (A_{10}) for a) 1.0 µm and b) 10.0 µm aerosol tracers. Dark and light gray bars are used to show the differences between $\mathrm{NS_{act}}$ and $\mathrm{NS_{inact}}$. This figure has been published in Kunkel et al. (2012b).

the high population densities ensure that the highest numbers in the convolved variable of surface density and population number are found there. Other densely populated regions like Europe, Japan, or eastern US show similar tracer surface densities but lower convolved numbers over large areas.

To further investigate and quantify how many people are affected by each MPC, the number of people is added up in the area with a tracer density threshold exceedance (A_Y). In Figure 4.13 this is shown for the 1.0 µm and 10.0 µm aerosol tracers and a threshold Y of $10\,\mathrm{ng\,m^{-3}}$. Highest values are found independently of aerosol size or solubility in Delhi, Beijing, Tianjin, Karachi, and Shanghai with more than 1.3 billion people being exposed to more than $10\,\mathrm{ng\,m^{-3}}$ in and around Delhi. For other MPCs such as Sydney, Melbourne, Santiago, or Kinshasa, the lowest population numbers are found simply due to the relatively sparse population density around these cities.

In conclusion, the area A_Y is a measure of the distribution of aerosol mass in the surface layer, especially of the dense part of the outflow plume. However, A_Y does not seem to determine how many people are exposed to a certain aerosol mass. Instead, this is more dependent on the population in and around an MPC. This is also underlined when computing the coefficients of determination to see how much of the variance of the exposed population number is explicable by the area itself. For A_{10} only weak correlations are assessed for small ($R^2 < 0.2$) and large ($R^2 < 0.06$) aerosol tracers, and also by changing the threshold value to $1\,\mathrm{ng\,m^{-3}}$ and $100\,\mathrm{ng\,m^{-3}}$ no substantially higher correlations are ascertained.

4.5 Sensitivity of the emission height on atmospheric dispersion and surface deposition

So far, all results are based on emissions that are introduced into the surface model layer. This layer is on average about 60 m deep and varies between 45 m and 75 m (global monthly means).

However, pollutants from MPCs may be emitted either at higher altitudes by the release from industrial chimneys or have a higher effective release height due to an initial transformation processes (e.g., Pregger and Friedrich, 2009). Furthermore, the development of an urban heat island (UHI) can lead to a temperature increase in the cities relative to their rural environment which potentially increases the effective emission heights in the cities,

Table 4.4: Scenarios to test the dependence on the emission height of the MPC tracer outflow along with height of the upper boundary and depth of the first five layers.

Scenario	Emission into model layer	Annual mean top height of model layer	Annual mean depth of layer
L1	1	63 m	63 m
L2	2	223 m	160 m
L3	3	461 m	208 m
L4	4	761 m	300 m
L5	5	1114 m	353 m

which however cannot be resolved in global models (e.g., Arnfield, 2003; Zhang et al., 2009; Parker, 2010). However, the impact of the vertical distribution of trace gas emissions on tropospheric chemistry was discussed by Pozzer et al. (2009) and they found that substantial deviations can occur close to the source but the overall effect on the chemical composition is rather low. By neglecting elevated emissions, a conservative estimate is expected regarding long-range transport. To at least obtain some information on the magnitude of this effect, four additional simulations (L2-L5) have been conducted, in which the emissions are not placed in the surface layer but in the four consecutive layers above the bottom layer (see Table 4.4).

The model configuration is the same in all five simulations, except of the model layer in which the emissions are introduced. The five first model layers cover the first kilometer in the atmosphere (see Table 4.4). In regional air quality models anthropogenic emissions are vertically distributed up to this altitude, for example in the EMEP model[1]. Only $\mathrm{NS_{act}}$ $1.0\,\mu\mathrm{m}$ aerosol tracers are released at the 46 urban centers, all with the same source strength of $1\ \mathrm{kg\,s^{-1}}$ per box in each simulation. Consequently, the emissions are already more diluted when placed in grid boxes at a higher altitude since the depth of the grid boxes increases with altitude (see Table 4.4 and Figure 4.14 depicting the emission layer densities in each case). More important for rapid dilution is the increase of the horizontal wind speeds with altitude in the planetary boundary layer (cf. Stull, 1988) since the effect of surface friction becomes smaller. Consequently, the aerosols are faster transported away from their source when introduced at higher levels.

Thus, the question remains how the pollution potentials change compared to the reference scenario (L1). The most interesting changes are simulated for the retention pollution potential $RCL_{0.5\mathrm{km}}$ since it increases in L2 and L3 but decreases in L4 and L5 (Figure 4.15). The increase in L2 and L3 results from a lower dry deposition rate, indicated by the simultaneous decrease in DED (sedimentation, SED, is in general to low and shows no difference between the simulations) because the aerosols have to be in the surface layer to be dry removed. In L4 and L5, the emissions are placed above 500 m from the ground at many source locations and thus are already above the upper boundary of the metric leading to a decrease in $RCL_{0.5\mathrm{km}}$. The wet deposition fractions (LSS and CVS) change accordingly to balance the decrease in DED. While $ELR_{1\mathrm{km}}$ and A_{10} show no substantial change, DRT (remote deposition potential) increases with increasing emissions height, hence indicating an increase in long-range transport. However, this increase occurs at levels below 5 km since the upper tropospheric mass fraction E_{UT} is almost equal in all five scenarios, although an increased emission height reduces the distance between the altitude of emission and 5 km. Larger wind speeds at higher altitudes increase the horizontal transport, with consequently more mass being diluted in the background air.

In conclusion, the surface emissions result in conservative estimates with respect to long-range transport but have no substantial effect on upper tropospheric pollution and on the low-level remote pollution compared to emissions at higher altitudes.

---

[1] http://www.emep.int/UniDoc/report.html, Chapter 4.1, as of 11.09.2012

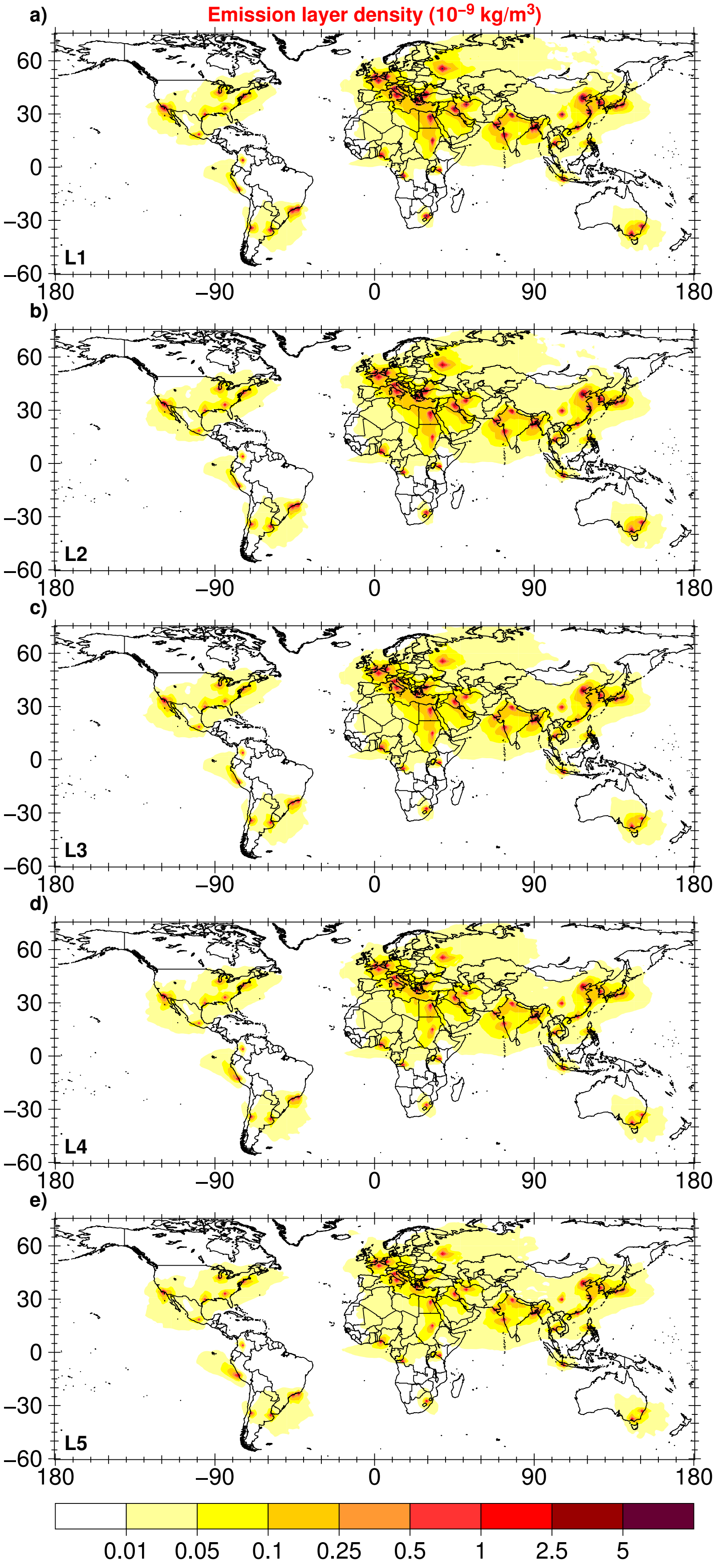

Figure 4.14: Annual means of the emission layer density (in $10^{-9}\mathrm{kg\,m^{-3}}$) for the five different emission heights. The emissions are introduced in one of the lowest five model layers, here indicated by L1-L5 (a-e) with L1 being the surface model layer.

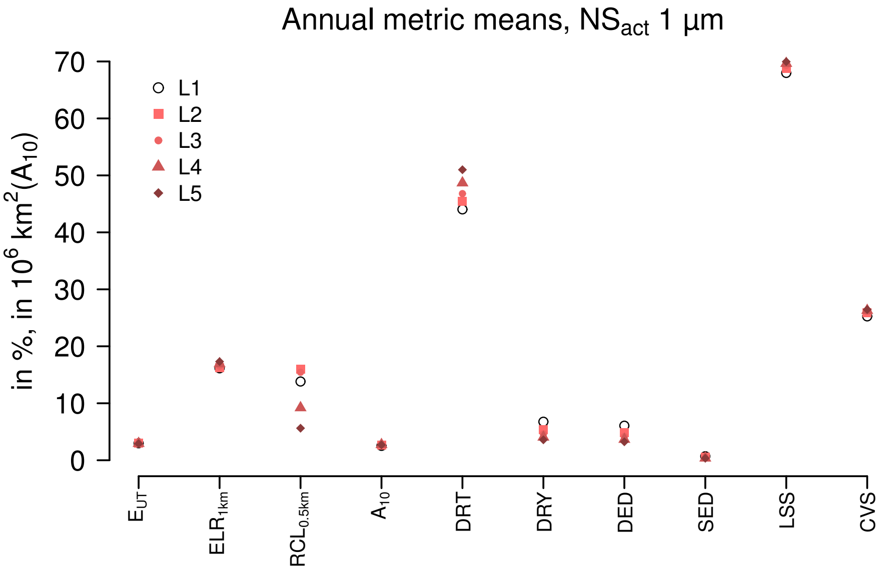

Figure 4.15: Annual means of the transport and deposition metrics for the five emission scenarios (L1-L5).

4.6 Comparison between aerosol and gas phase tracer transport

Finally to conclude the analysis of atmospheric dispersion from urban emission sources, similarities and differences between gas phase tracers with fixed atmospheric lifetime and aerosol tracers with variable atmospheric residence times are discussed. Here, the focus is on aerosol tracers with a diameter of 1.0 µm which have a lifetime comparable to, though generally shorter than the lifetime of, the gas phase tracers for which an exponential decay lifetime of ten days is applied. In parts of the discussion, aerosol tracers with a diameter of 10 µm are also included. Therefore, the aerosol results discussed in the sections before are compared with gas phase tracer results from an EMAC simulation using the same configuration as used for the aerosol simulation.

Figure 4.16 gives a qualitative overview of how the atmospheric dispersion patterns change with respect to the removal of an atmospheric tracer. The amount of various removal processes acting on the individual tracers decreases from left to right in Figure 4.16. In general, the gas phase tracers in the right column are wider spread from the source due to their longer lifetime. Close to the source points, similar values are found for gas phase and aerosol tracers but farther away the discrepancies between the various tracer types become more apparent. The total column densities reveal higher values in the direct outflow regions of the MPCs in the case of the gas phase tracers and also in remote areas such as the southern Pacific with no significant tracer burden present for aerosol tracers. Tracer distributions in the surface layer vary strongly and the transport to higher latitudes is not strongest for the gas phase tracers, but rather for NS$_{inact}$ tracers, especially in northern Europe. In contrast, the gas phase tracers predominate in the northern latitude storm tracks where almost no aerosol mass is present anymore. The largest differences between aerosol and gas phase tracers are found for the column densities in the upper troposphere above 5 km. The absolute aerosol tracer peak values are about the magnitude of the background levels of the gas phase tracers in remote areas. Moreover, location and strength of peak values differ, for instance for

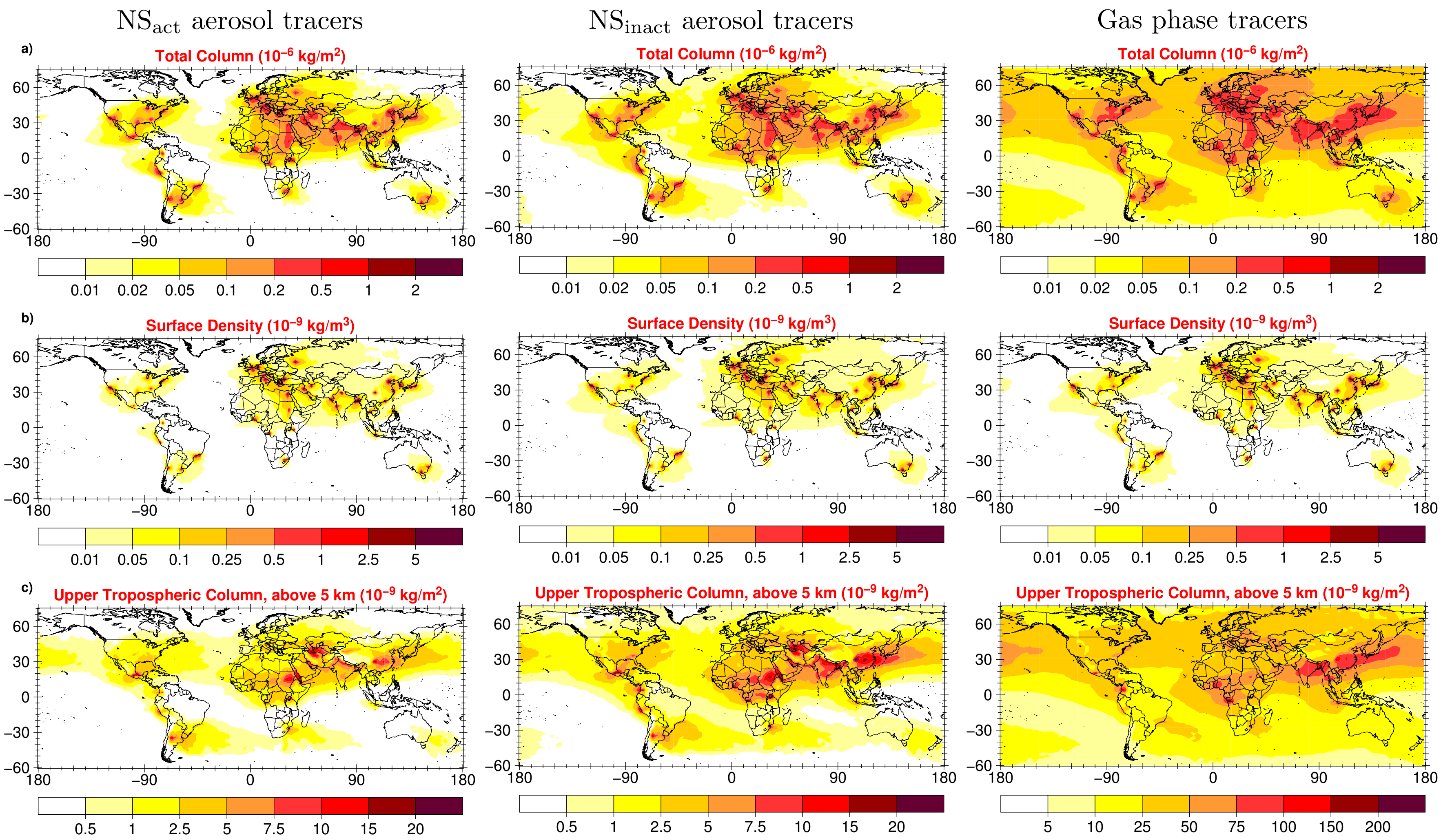

Figure 4.16: Annual mean of the sum of all 46 MPC tracer sources for a) total column density (in 10^{-6} kg m^{-2}), b) surface density (in 10^{-9} kg m^{-3}), and c) upper tropospheric column density (in 10^{-9} kg m^{-2}) from the EMAC simulations. Left and central columns depict the 1.0 µm NS_{act} and NS_{inact} aerosol tracers and the right column the gas phase tracers with the 10 day decay lifetime. This figure has been published in Kunkel et al. (2012b).

a) Remote low-level pollution potential

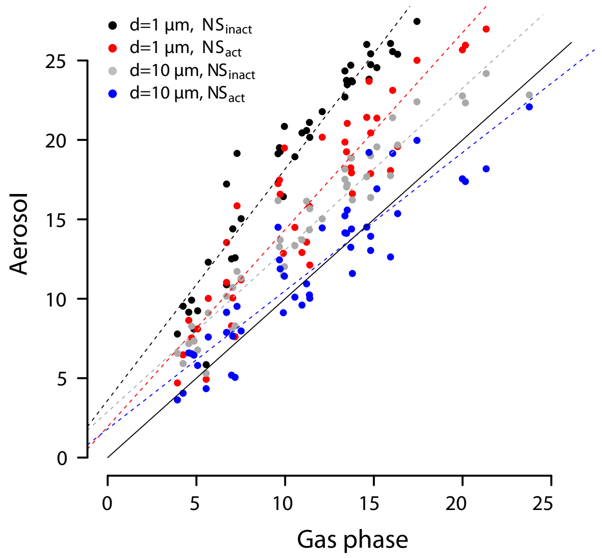

b) Upper tropospheric pollution potential

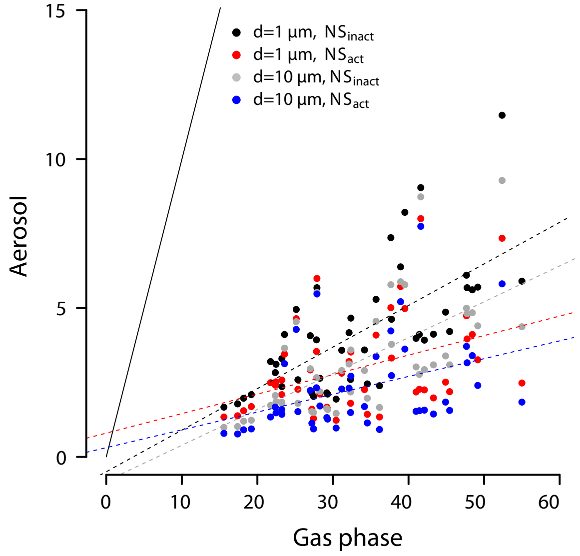

c) Area of mass threshold exceedance

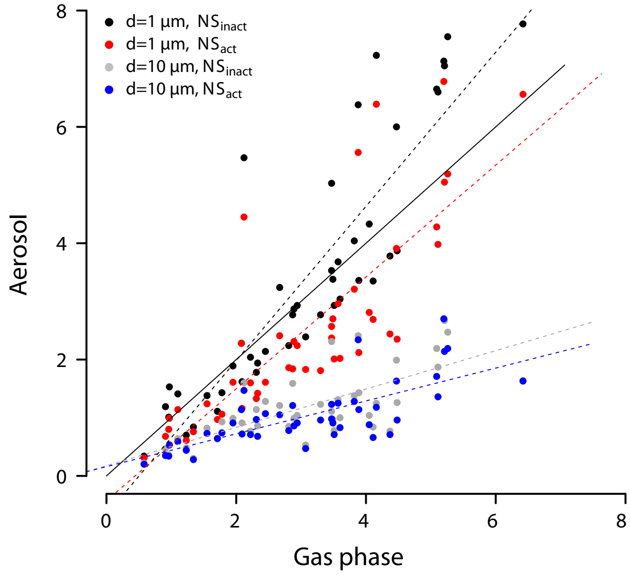

Figure 4.17: Comparison between gas phase and aerosol pollution potentials: a) $ELR_{1\mathrm{km}}$ (in %), b) E_{UT} (in %), and c) A_{10} (in 10^6 km^2). Colored dots represent different aerosol properties: black = NS$_{\mathrm{inact}}$ 1.0 µm, red = NS$_{\mathrm{act}}$ 1.0 µm, gray = NS$_{\mathrm{inact}}$ 10.0 µm, and blue = NS$_{\mathrm{act}}$ 10.0 µm. These aerosol tracers are considered to cover the aerosol spectrum of this study and other tracers are neglected to keep lucidity. The solid black lines represent the bisecting line, the colored dashed lines the regression lines. These regression lines are based on the following equations. x values are representatives of gas phase results, y values of aerosol results:
For E_{UT}:
NS$_{\mathrm{inact}}$ 1.0 µm: $y = 0.139\,x - 0.499$;
NS$_{\mathrm{act}}$ 1.0 µm: $y = 0.065\,x + 0.798$;
NS$_{\mathrm{inact}}$ 10.0 µm: $y = 0.121\,x - 0.813$;
NS$_{\mathrm{act}}$ 10.0 µm: $y = 0.060\,x + 0.311$.
For $ELR_{1\mathrm{km}}$:
NS$_{\mathrm{inact}}$ 1.0 µm: $y = 1.443\,x + 3.592$;
NS$_{\mathrm{act}}$ 1.0 µm: $y = 1.245\,x + 1.195$;
NS$_{\mathrm{inact}}$ 10.0 µm: $y = 1.023\,x + 2.885$;
NS$_{\mathrm{act}}$ 10.0 µm: $y = 0.872\,x + 1.800$.
For A_{10}:
NS$_{\mathrm{inact}}$ 1.0 µm: $y = 1.352\,x - 0.667$;
NS$_{\mathrm{act}}$ 1.0 µm: $y = 0.964\,x - 0.425$;
NS$_{\mathrm{inact}}$ 10.0 µm: $y = 0.333\,x + 0.176$;
NS$_{\mathrm{act}}$ 10.0 µm: $y = 0.283\,x + 0.159$.
This figure has been published in Kunkel et al. (2012b).

Khartoum and Teheran, which both have a much weaker signal in the gas phase compared to the background than for the aerosol tracers. Furthermore, Santiago and Lima are clearly discernible in the aerosol phase but not in the gas phase, and also the outflow from East Asia extends farther northward for the gas phase tracers.

The question arises then how the pollution potentials differ between gas phase and aerosol tracers. Figure 4.17 shows the three pollution potentials used to investigate the similarities and differences in the local pollution build-up and pollution export: ELR_{1km} (top panel), E_{UT} (middle panel), and A_{10} (bottom panel). Generally, the accordance between aerosol and gas phase tracer is higher when using the $\mathrm{NS}_{\mathrm{inact}}$ aerosols. The greatest similarity in pollution potential is found for the low-level pollution potentials. Aerosol tracers show slightly higher ELR_{1km} values than gas phase tracers, with coefficients of determination (R^2) higher than 0.9 ($\mathrm{NS}_{\mathrm{inact}}$) and 0.8 ($\mathrm{NS}_{\mathrm{act}}$), respectively. Since R^2 is a measure of how much of the variance in the correlation can be explained by the source location, the tracer properties seem to be less important to determine the mass fraction found in the lowest layers downwind of the source. Instead, the location of the source along with the prevailing meteorology account for the mass transported downwind. In contrast, the vertical transport shows gas phase mass fractions up to ten times greater than aerosol mass fractions. The correlation between gases and aerosols is still positive but weak, with an R^2 of about 0.4 ($\mathrm{NS}_{\mathrm{inact}}$) and about 0.15 ($\mathrm{NS}_{\mathrm{act}}$), respectively. The source location is in this case of minor importance compared to the tracer properties, especially the solubility of a tracer which determines to a great extent the mass fractions above 5 km. In the case of the area density threshold exceedance, both the source location and tracer properties need to be considered more equally to explain the relation between gases and aerosols. Positive correlations are found with $R^2 = 0.78$ ($\mathrm{NS}_{\mathrm{inact}}$) and $R^2 = 0.67$ ($\mathrm{NS}_{\mathrm{act}}$) for small aerosols and an averaged R^2 of about 0.53 for large aerosols. Hence, the source location determines the A_{10} more in case of small aerosols while the size of the aerosol becomes more important for larger aerosols.

In summary, the findings of Section 4.4 are further supported by the comparison of gas phase and aerosol tracers, especially that the source location is most important in determining the low-level pollution, while tracer properties have a substantial impact on the vertical transport.

4.7 Summary

The main intention in this chapter was to extend the study of Lawrence et al. (2007) by exploring the dispersion and the balance between pollution export and pollution build-up of aerosol tracers from 46 individual major population centers. The results contribute significantly to the understanding of the dispersion of aerosols from major population centers. The results in this chapter depend only on the location of the emission sources and on the tracer properties, since all tracers were continuously released with the same constant emission rate at each emission source point.

One conclusion is that high mass fractions of pollutants are found around the source points in regions where pollutants have short atmospheric residence times. The lifetimes are generally constrained by meteorological conditions, especially by scavenging in and below clouds.

Export from the cities, either by vertical or low-level long-range transport is found to be strongly determined by the stability of the atmosphere. The low-level export is found to dominate in cold regions, where inversions and thus high stability conditions occur more frequent. In contrast, the vertical export is strongest in regions with a high lifting potential, i.e., high instability. Furthermore, the export to higher altitudes is shown to be also contingent upon the moisture in the atmosphere and therefore on cloud formation and subsequent wet removal processes. For aerosol particles it is found that the strongest vertical export occurs in temperate dry winter regions and not in tropical regions, where insoluble gas phase tracers are most efficiently lifted. However, on average the mass fraction of insoluble gas phase tracers above 5 km is about a factor of ten higher than the mass fraction of aerosol tracers.

The low-level export is found to be similar for aerosol and gas phase tracers. Moreover, on average the low-level export ($\sim 12 - 20\,\%$) is about a factor of five stronger for aerosols than the export into the upper troposphere ($\sim 2.5 - 4\,\%$). This ratio has a strong regional dependence and varies from two in temperate winter dry regions to ten in cold regions.

Furthermore, a tracer density threshold in the surface layer is used to determine the number of people that lives in an area which is strongly polluted in and around MPCs. This area is assessed by defining a threshold for the surface tracer density. It is found that the population density rather than the size of the area determines how many people are affected by strong pollution. Thus, most people are likely to be affected in East and South Asia, where about one third of the human population lives.

Since all results are assessed from tracer experiments with surface emissions, the influence of emissions at higher altitudes was studied. It is found that the long-range transport is more efficient when the tracers are released at higher altitudes, indicated by a larger mass fraction that is deposited beyond 1000 km away from the source points, and that the export at low levels and into the upper troposphere are hardly affected. Moreover, since dry removal occurs only near the surface, an increased emission altitude leads to more a larger mass fraction that is wet deposited.

5

Aerosol pollution potentials: surface deposition

Chapter 4 summarizes the findings of the atmospheric dispersion of aerosols from major population centers (MPCs), which is the direct continuation of the work of Lawrence et al. (2007). Now the focus turns to the surface deposition of the aerosols. For aerosol particles this is just as important to discuss since the particles have not only environmental effects when they are airborne. Besides their effects on humans discussed in Section 4.4.5, the aerosol composition may be such that they have substantial impacts on soils and the flora(e.g., Wiman et al., 1990; Burkhardt, 2010). Anthropogenic aerosol particles can change the rain pH and consequently the soil pH because of their acidic nature (acid rain, e.g., Galloway et al., 1982; Seinfeld and Pandis, 1998) or potentially damage crops when they contain toxins (e.g., Schroeder and Munthe, 1998). Aerosol particles can also contain micro-nutrients such as iron and phosphorus, which constitute a major fertilizer in several regions (e.g., Okin et al., 2004; Mahowald et al., 2005; Bristow et al., 2010).

Aerosol particles are removed by dry and wet deposition and the deposition fields can be used to identify long-range transport when the source is known. The following sections are dedicated to analyze the deposition of aerosols from MPCs and answer the following questions:

1. What does the geographical distribution of urban aerosol deposition look like, how is its temporal variation and which is the dominant removal process?
2. How much of the emission from urban centers is remotely deposited beyond various distances away from the source?
3. How strongly are individual ecosystems affected by concentrated urban aerosol deposition?

For this, an overview on the global deposition patterns is given. Then the focus is on regions close to the source points which are exposed to high deposition mass fluxes before the remote deposition is discussed. Sections 5.2 and 5.4 formed the basis for the publication of Kunkel et al. (2012a), Section 5.3 laid the groundwork for a part of the results published by Kunkel et al. (2012b).

5.1 Model and simulation setup

The results presented in this chapter are based on the same model simulations as the results in Chapter 4. Thus, I will not repeat the details here for which I refer to Section 4.2.

5.2 Global deposition patterns

Figure 5.1 shows annually accumulated total deposition mass fluxes (DMFs) for all 46 major population centers (MPCs) for small and large aerosol tracers. Total DMFs are focused over regions with high concentrations of MPCs, like eastern USA, Europe, South and East Asia, parts of South America and Africa. Maximum values are found near the emission sources, where both dry and wet deposition processes contribute to the total deposition. Aerosol tracers with a diameter of 1.0 μm show significant deposition values over large parts

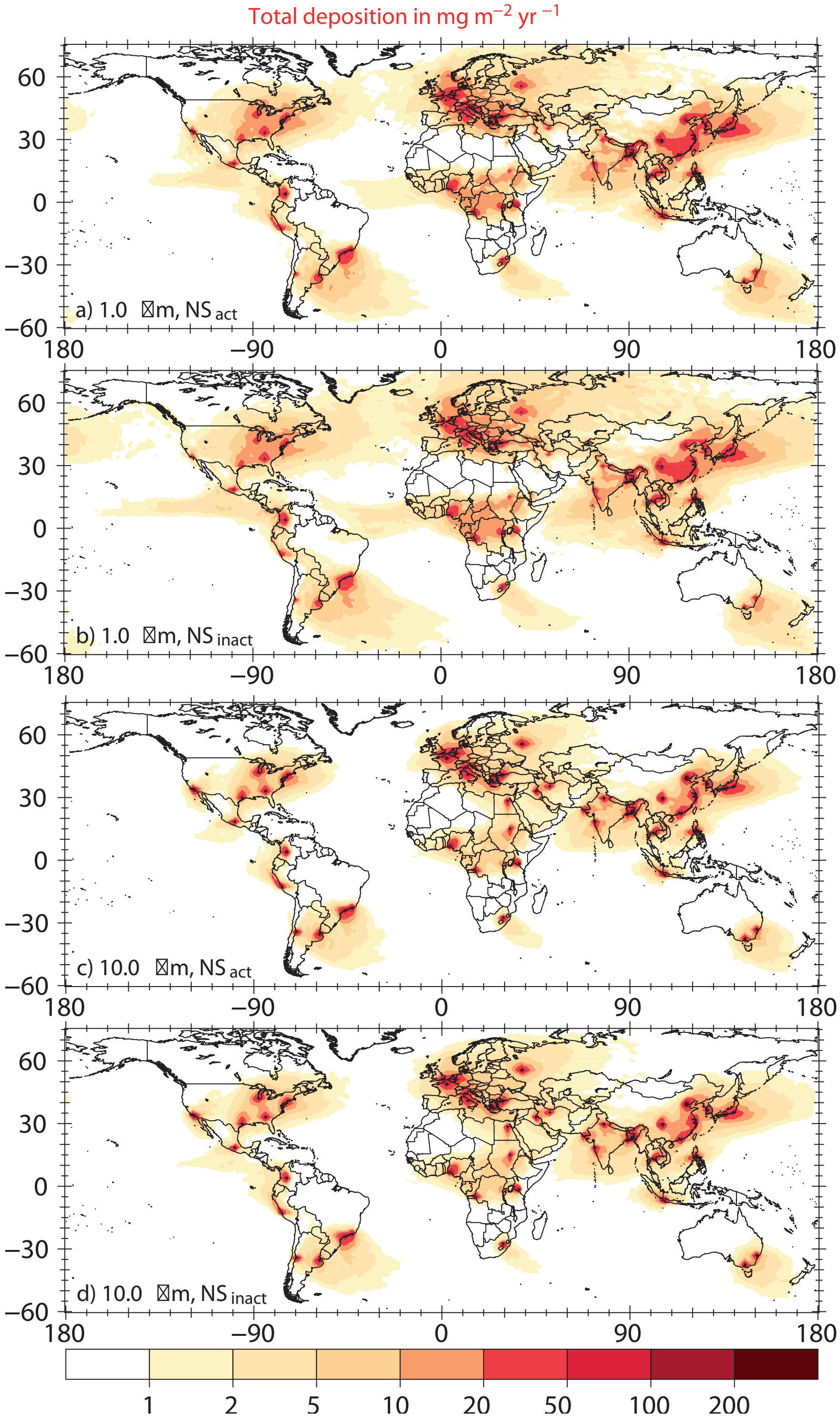

Figure 5.1: Annually accumulated deposition mass flux (in mg $\mathrm{m}^{-2}\,\mathrm{yr}^{-1}$) for the sum of all 46 MPCs for a) $\mathrm{NS}_{\mathrm{act}}$ 1.0 μm, b) $\mathrm{NS}_{\mathrm{inact}}$ 1.0 μm, c) $\mathrm{NS}_{\mathrm{act}}$ 10.0 μm, and d) $\mathrm{NS}_{\mathrm{inact}}$ 10.0 μm aerosol tracers.

of the Atlantic Ocean. In some regions, notable DMFs are seen for tracers with a diameter of 10.0 μm where no deposition is evident for tracers with 1.0 μm diameter. An example is the Eastern Sahara, which experiences the main southward outflow of the Cairo tracer. The aerosol tracers have to travel through the hot and dry Sahara before they reach the humid region of the Intertropical Convergence Zone (ITCZ), where small aerosol tracers are effectively washed out. In contrast, large aerosol tracers are removed via sedimentation in larger amounts during the transport through the Sahara due to their higher gravitational

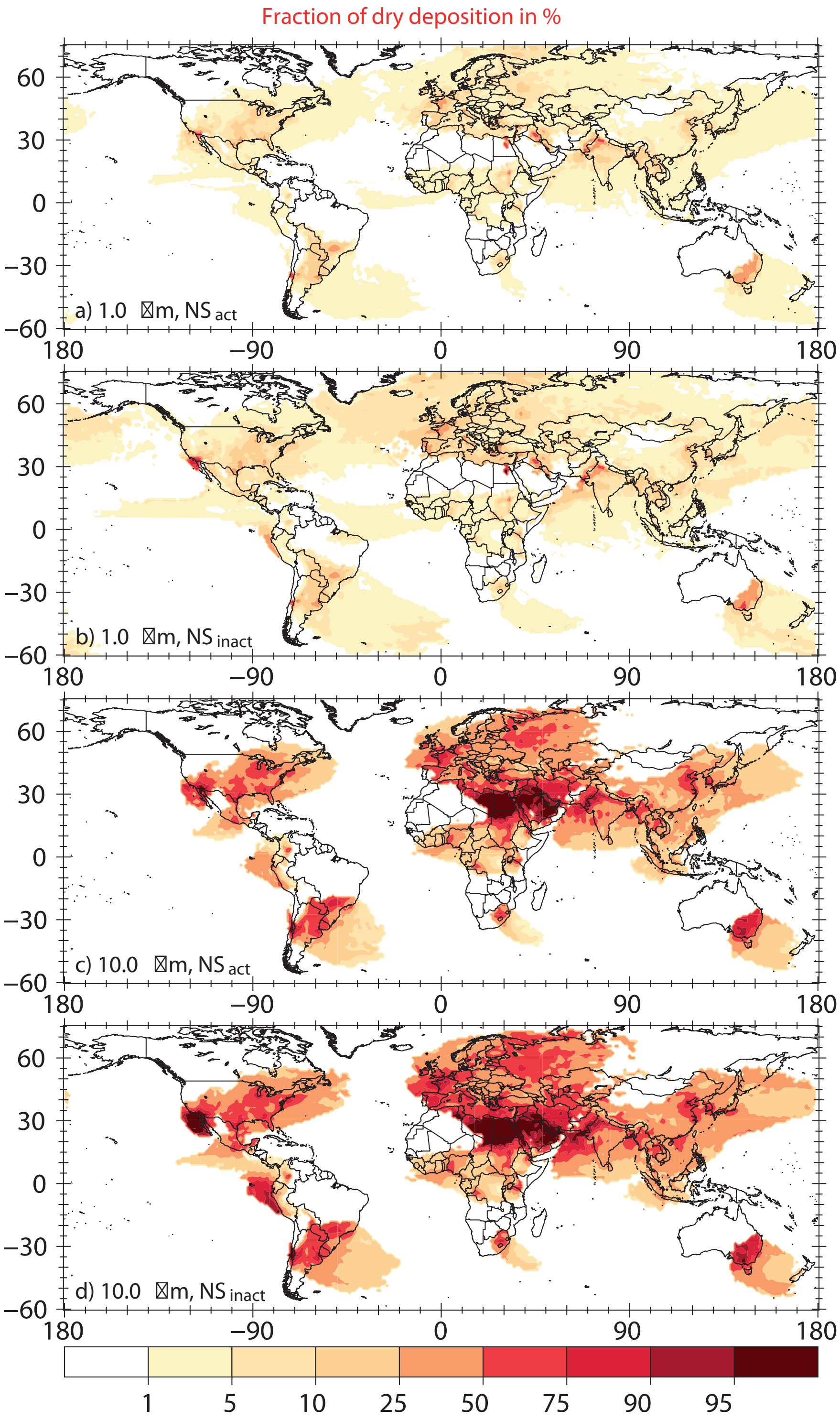

Figure 5.2: Dry deposited mass fraction of total annually accumulated deposition (in %) for a) $\mathrm{NS}_{\mathrm{act}}$ 1.0 μm, b) $\mathrm{NS}_{\mathrm{inact}}$ 1.0 μm, c) $\mathrm{NS}_{\mathrm{act}}$ 10.0 μm, and d) $\mathrm{NS}_{\mathrm{inact}}$ 10.0 μm aerosol tracers.

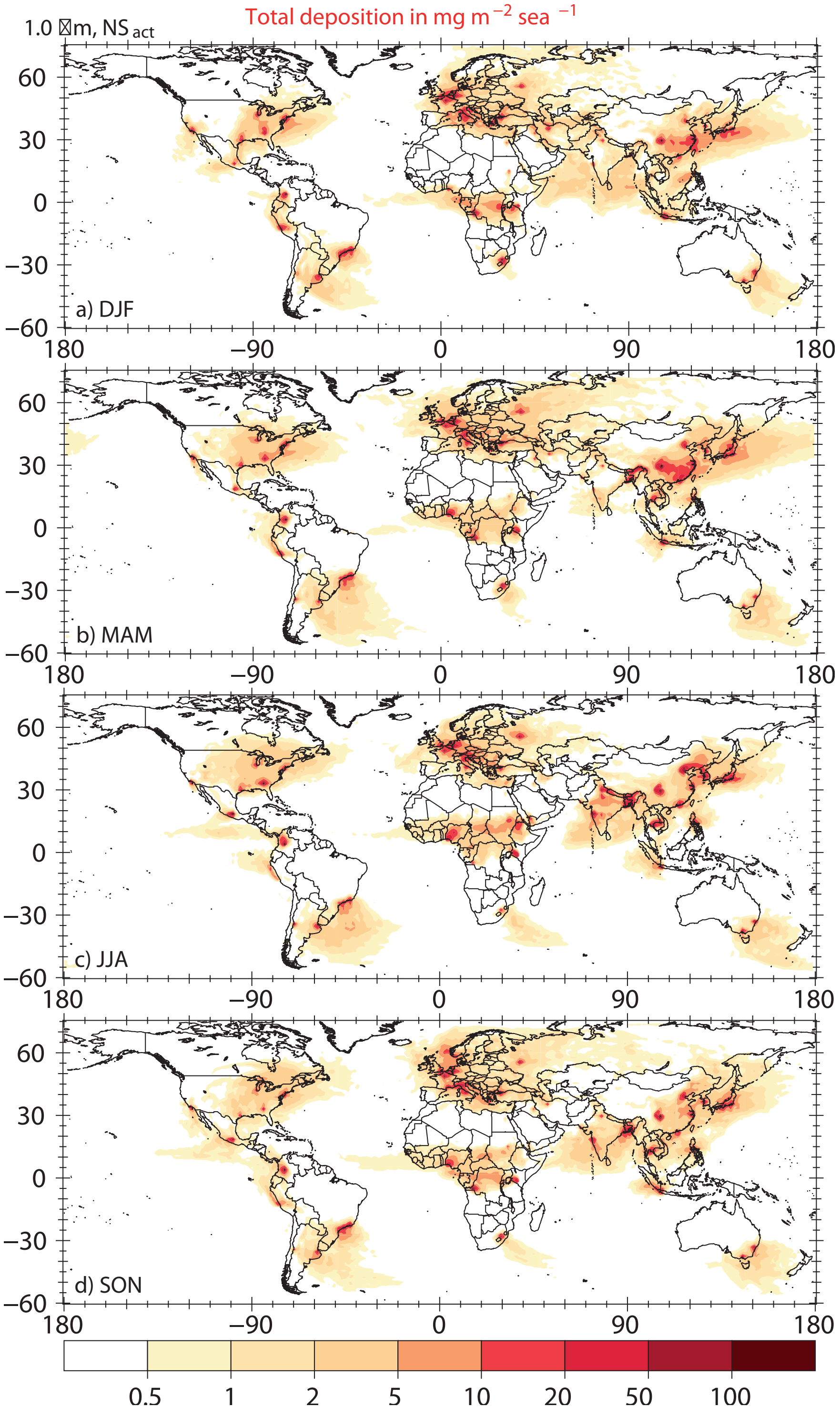

Figure 5.3: Seasonally accumulated deposition mass flux (in mg m^{-2} sea^{-1}) for the sum of all 46 MPCs for the NS$_{\text{act}}$ 1.0 µm aerosol tracers for a) DJF, b) MAM, c) JJA, and d) SON.

settling velocities.

In Figure 5.2, the percentage of total DMFs due to dry removal (dry deposition and sedimentation) is shown for small and large aerosol tracers. When comparing both sizes, a shift in the ratio between dry and wet deposition is observed. Deposition of small tracers mainly occurs via wet removal. On average more than 90 % of the total emitted mass is removed by wet deposition, regardless of the nucleation scavenging activation. In contrast, only 38 % (NS$_{\text{inact}}$) to 45 % (NS$_{\text{act}}$) of the total emissions are wet deposited for 10.0 µm tracers. Wet removal of the tracers depends on the presence of clouds and precipitation and can occur in large parts of the troposphere. Dry removal is limited to the lowest model layer and depends on parameters like surface roughness for dry deposition or the mass of the aerosol particle in the case of sedimentation. About 34 % of the emissions of large particles sediment onto the ground due to their weight, in contrast to less than 1 % for small tracers, both numbers averaged over the nucleation scavenging activation state and for all MPCs. Regions near the emission sources show a large aerosol tracer abundance at low levels. Consequently, large aerosol tracers show higher dry DMFs near their source. In turn, small tracers are rapidly vertically mixed or directly lifted into regions with a higher potential for long-range transport. The small tracers are then primarily wet removed in regions farther away from their source points. $\mathrm{NS}_{\mathrm{inact}}$ tracers have slightly higher dry removal fractions since their wet deposition is reduced. Thus, the characteristics of the deposition potential vary mainly with the aerosol size and also slightly with the activation regime for different regions.

Furthermore, meteorological conditions are responsible for inter-seasonal differences in total DMFs. The influence of precipitation on DMFs is evident in many regions in Figure 5.3. For instance, the shift of the African and Southern Asian ITCZ from its southernmost position during DJF to its northernmost position during JJA is clearly marked by the location of the maximum of the DMFs. DMFs over the Indian Peninsula are also strongly affected by the seasonal reversal in the monsoon wind direction, with deposition primarily to the south over the Indian Ocean in DJF and over the continent in the rainiest and most polluted regions (e.g. Western Ghats and Indo-Gangetic Plain) in JJA.

5.3 Regions of concentrated deposition – MPC impact on ecosystems

In this section the potential impact of the urban emitted aerosol particles on the environment is assessed by using the emission normalized deposition fraction D_{X}. This is the ratio of the total mean (= dry and wet) deposition flux to the global mean emission flux (defined in Section 3.2.2). Threshold values X of 1 % and 5 % are applied and D_1 and D_5 are referred to as high relative deposition. Although I am aware of the different impacts of dry and wet deposited particles, only the total deposition is discussed here and further investigation is left open for following studies.

5.3.1 Deposition on land and sea surfaces

First, the total surface area of the model grid cells is assessed which fulfills the criterion of D_{X}. In Figure 5.4 the total surface area is illustrated for each MPC and for two aerosol diameters, 1.0 µm and 10.0 µm. On the left D_1 is shown, i.e., more than 1 % of the emissions, and on the right D_5, i.e.,more than 5 % of the emissions. The solubility states are displayed by different gray shadings with the light gray bar representing the additional area between the two solubility states. In contrast to the atmospheric metrics, the smaller area, indicated by the dark gray bar, is not always determined by the same solubility state for each MPC but most commonly by the $\mathrm{NS}_{\mathrm{inact}}$ tracers. If only a dark gray bar is drawn, then there is no difference between the two states, while a single light gray bar indicates that no area is

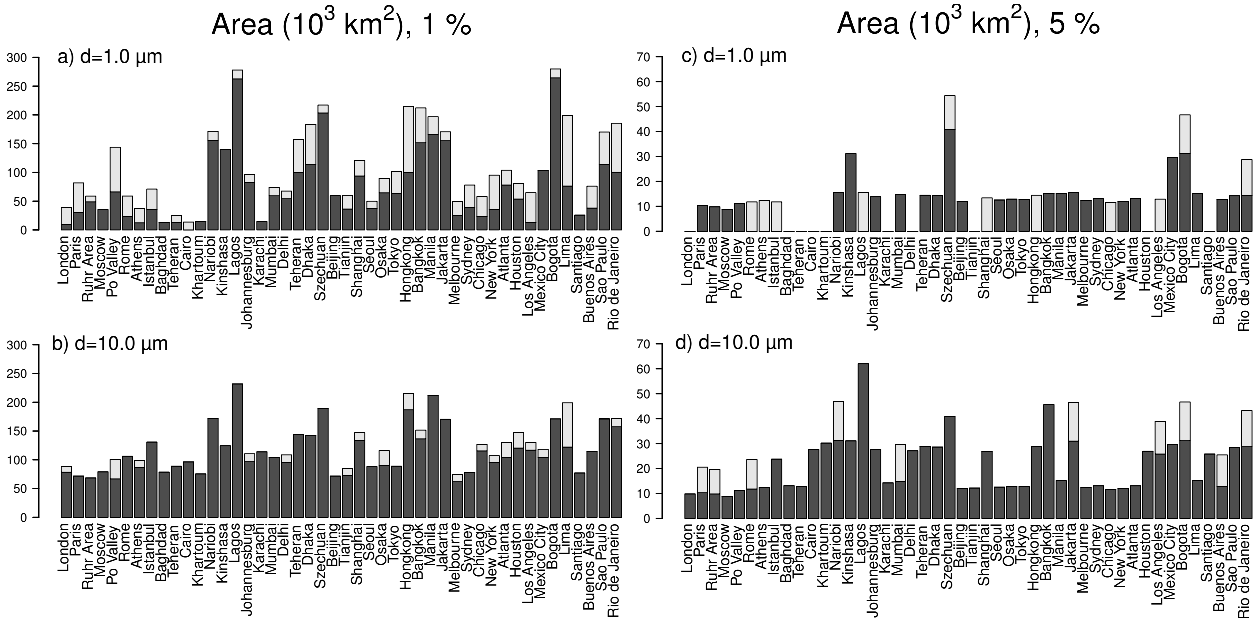

Figure 5.4: Total surface area (in $10^3\,\mathrm{km}^2$) covered with more than 1 % (D_1, a) 1 µm, b) 10 µm) and 5 % (D_5, c) 1 µm, d) 10 µm) of the global mean annual emission. The dark gray shaded bars show the minimum area covered by either the $\mathrm{NS_{act}}$ or $\mathrm{NS_{inact}}$ tracers, the light gray shaded bars on top the additional area covered by the tracers with the other nucleation scavenging state. This figure has been published in Kunkel et al. (2012b).

covered at all for one state. By definition areas which are covered with at least 5 % are also covered with at least 1 % of the emissions.

In the case of D_1, each MPC covers at least a small area, independent of aerosol size, which is not the case for D_5. Aerosol tracers from MPCs which are known to undergo substantial long-range transport, e.g., Baghdad, Teheran, Cairo, or Khartoum, are more widely spread in the atmosphere and thus aerosol mass is deposited in lower concentrations in each grid cell. However, other MPCs, e.g., London or Tianjin, show also zero area covered, thus long-range transport is not the only limiting factor for high relative deposition. In contrast, the maximum is found for MPCs which are either influenced by heavy precipitation rates, e.g., Lagos or MPCs in South-East Asia, or located in a basin with low ventilation, e.g., Bogotá or Szechuan. On average large aerosol tracers cover larger areas because of their shorter travel distances and the subsequent smaller total overall area which is affected by deposition. This in turn leads to higher removal rates on the area where deposition occurs. Furthermore, the faster deposition rates for large aerosols lead to smaller differences between the areas covered by the two solubility states.

The total surface area is furthermore divided into land and sea fractions to obtain more detailed information over the location of high relative deposition. Generally, the low-level outflow of aerosols is similar to the gas phase outflow reported by Lawrence et al. (2007) with more low-level long-range transport over oceans. Nevertheless, the total deposition still occurs more over continents with about 55 % of the small tracer emissions and 68 % of the large tracer emissions being deposited on land surfaces. For the high relative deposition, the focus is only on D_1 since not all of the MPCs cover a surface area in case of D_5. Since the land-sea fractionation is very similar for all aerosol tracers, independent of size or solubility,

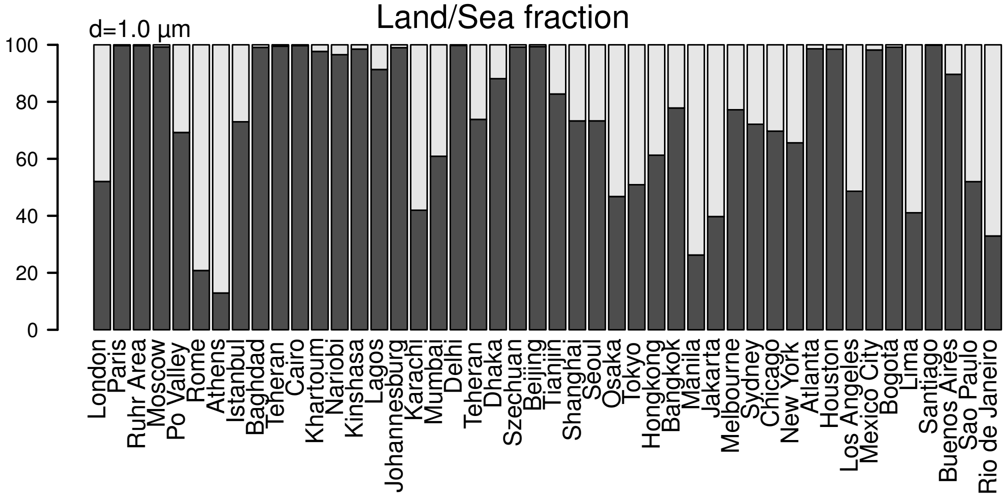

Figure 5.5: Example for land-sea fractionation (in %) of D_1 for the $\mathrm{NS}_{\mathrm{act}}$ 1.0 µm aerosol tracers. Dark bars represent the land fractions, light bars the sea fractions. This figure has been published in Kunkel et al. (2012b).

D_1 is only shown for the $\mathrm{NS}_{\mathrm{act}}$ 1.0 µm aerosol tracers in Figure 5.5. The dark gray bars represent the land fraction which outweighs the sea fraction in the light gray color bars, although almost 50 % of the MPCs are located at coastlines and several more close to the coast. In several cases the land fraction is close to 100 %, mainly for MPCs with a dominant outflow over continental regions, e.g., Moscow, Rhine-Ruhr Area, Teheran, Delhi, Szechuan. However, there are also some MPCs close to coastlines which do not have high relative deposition over seas, e.g., Santiago or Beijing. The highest marine D_1 values appear for Athens and Rome, with about 80 % sea fraction, but not surprisingly Jakarta and Manila show the highest sea fractions in terms of absolute area as each of these cities is located on a small island in a maritime environment.

5.3.2 Impact on ecosystems – cropland, pasture, and forest

To answer the question which of the three ecosystem introduced in Section 3.4 –cropland, pasture, or forest– is most exposed to deposition from MPCs, the sum of all annually accumulated MPC deposition fields is initially convolved with the relative fractions for cropland, pasture, and forest (see Figure 3.2 in Section 3.4). The differences between small aerosol tracers ($d \leq 1.0$ µm) are minor as well as between the two solubility states. Thus, the focus of the discussion is again on the $\mathrm{NS}_{\mathrm{act}}$ 1.0 µm and 10.0 µm aerosol tracers which are shown in Figure 5.6 and it is recalled that the pure deposition patterns have their maximum around to the source location (see Section 5.2). In Figure 5.6 MPCs are in most cases well detectable by the red areas in the six panels. For several MPCs these red areas exceed the MPC size since these are surrounded by large areas of an ecosystem, e.g., for cropland the corn-belt around Chicago, the region between Paris and east of the Rhine-Ruhr Area, the region north of Lagos or large areas on the Indian subcontinent and in eastern China. In the case of pasture land, only a few hot spots are detected, for instance the region around Bogotá, the Sahel region in Africa, and again large areas in eastern China. Forests seem to be widely exposed to deposition from MPCs, e.g., in the USA in a belt from New England

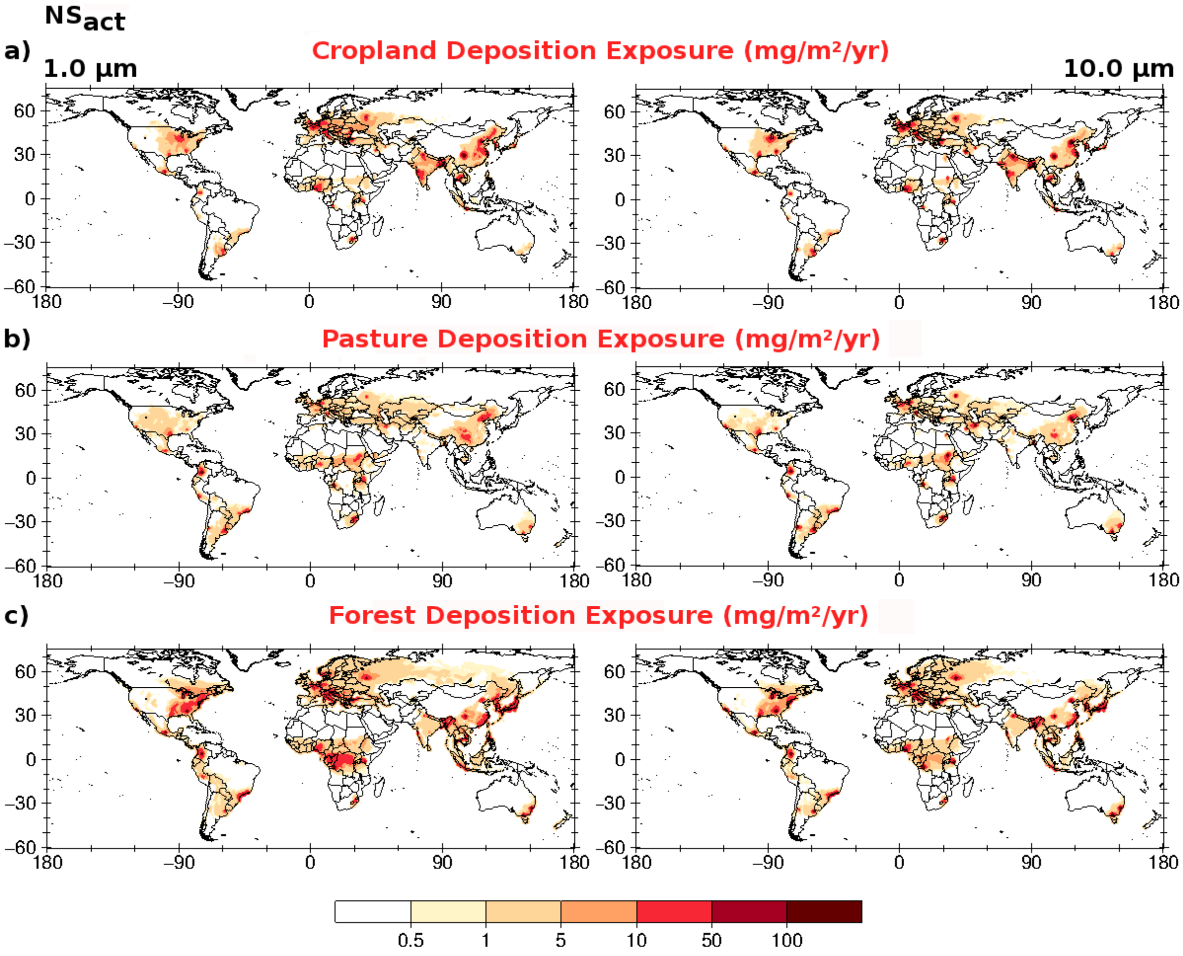

Figure 5.6: Folded maps of the sum of the annually accumulated deposition fields of all MPCs (in $\mathrm{mg\,m^{-2}\,yr^{-1}}$) and the relative fractions of the three ecosystems, a) cropland, b) pasture, and c) forest (see also Figure 3.2). On the left side for the $\mathrm{NS_{act}}$ $1.0\,\mu\mathrm{m}$, on the right side for the $\mathrm{NS_{act}}$ $10.0\,\mu\mathrm{m}$ aerosol tracers. This figure has been published in Kunkel et al. (2012b).

down to Atlanta, high forest deposition exposure is simulated as well as in Bogotá and in the region between Rio de Janeiro and São Paulo. In central Africa the Congo basin with

Table 5.1: Mean ecosystem area (in $10^3\,\mathrm{km}^2$) covered with high relative deposition, D_1 and D_5 for four aerosol tracers and averaged over all MPCs.

D_1		Cropland	Pasture	Forest
$d = 1.0\,\mu\mathrm{m}$	$\mathrm{NS_{act}}$	20.26	12.61	33.21
	$\mathrm{NS_{inact}}$	16.37	10.74	31.23
$d = 10.0\,\mu\mathrm{m}$	$\mathrm{NS_{act}}$	25.29	15.87	32.26
	$\mathrm{NS_{inact}}$	24.48	15.12	24.56
D_5				
$d = 1.0\,\mu\mathrm{m}$	$\mathrm{NS_{act}}$	2.28	1.51	4.25
	$\mathrm{NS_{inact}}$	1.88	1.25	3.28
$d = 10.0\,\mu\mathrm{m}$	$\mathrm{NS_{act}}$	5.29	3.14	6.54
	$\mathrm{NS_{inact}}$	4.69	2.60	5.85

the African rainforest and in Asia regions in eastern China and also in Japan reveal high exposure. In Europe, the high northern latitudes are affected due to the vast appearance of boreal forest. For the same reason the deposition of Moscow can still be detected north of Mongolia far away from its source. In contrast, one of the most forested areas, the Amazon basin, seems not to be affected by the high relative deposition of the MPC tracers used in this study because it is not located downwind of one or several MPCs.

Using D_1 and D_5, the area of each ecosystem is assessed for each MPC individually which is exposed to more than 1 % or 5 % of the emission of the corresponding MPC. Table 5.1 shows the means of small and large aerosol tracers for each ecosystem. Generally, larger areas are found for the soluble tracers and, as discussed before for the total surface area, for larger aerosol tracers with one exception in the case of forests for D_1 ($\mathrm{NS}_{\mathrm{act}}$ 1.0 µm). The results for the two aerosol solubility states differ by less than 25 %, in most cases even less than 20 %. Maximum means are found for forests, followed by croplands with up to 40 % less and pasture with about 50 % less area exposed to high relative deposition compared to forests.

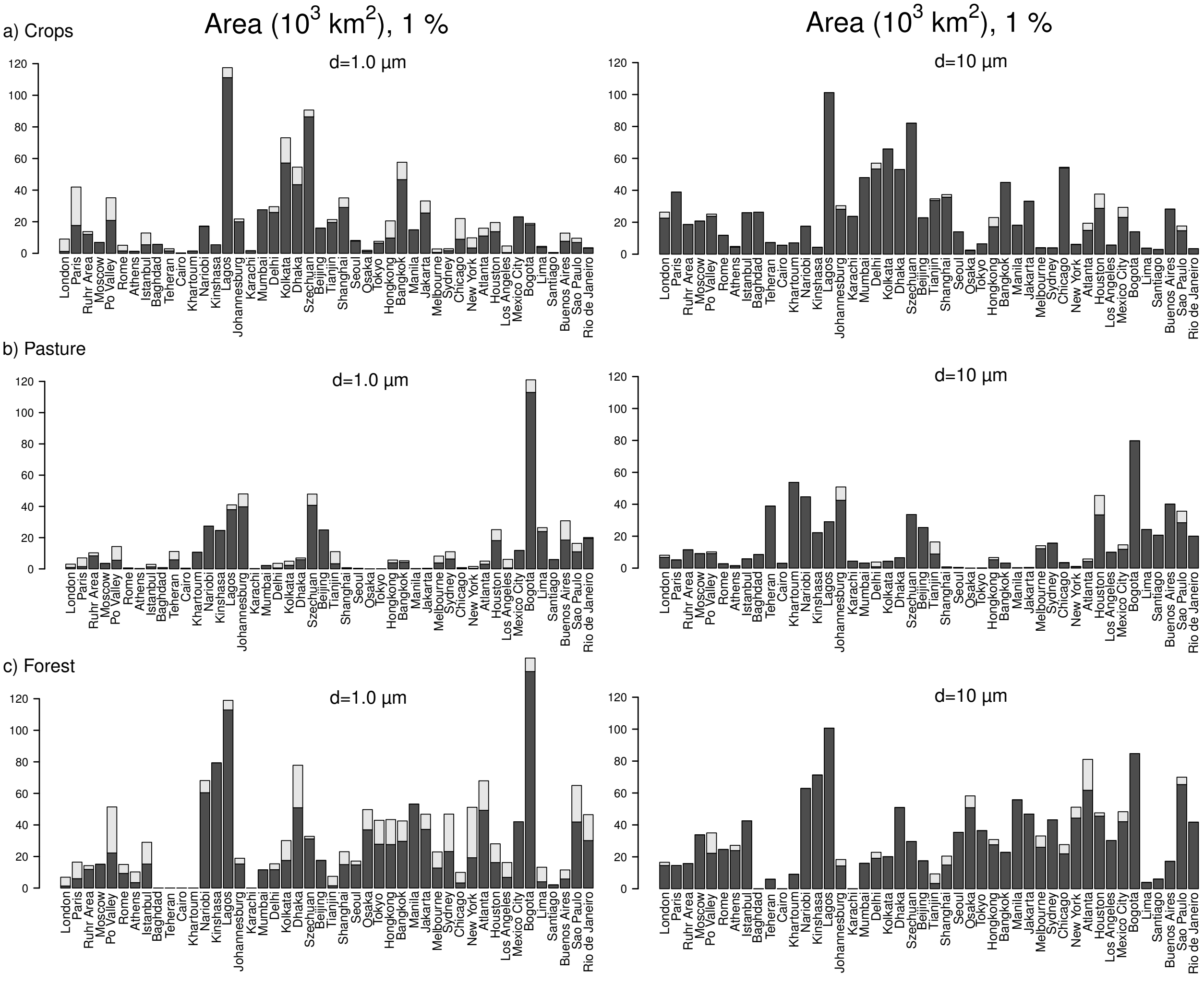

Figure 5.7: a) Cropland, b) pasture, and c) forest areas (in $10^3\,\mathrm{km}^2$) covered with at least 1 % of the emission of an MPC (D_1) for 1.0 µm (left) and 10.0 µm (right) aerosol tracers. Dark gray bars show the minimum area covered by either the $\mathrm{NS}_{\mathrm{act}}$ or $\mathrm{NS}_{\mathrm{inact}}$ tracers, light gray bars show the additional area by the tracer with the other NS state. This figure has been published in Kunkel et al. (2012b).

More detailed information for each MPC and ecosystem is depicted in Figure 5.7. The size of an ecosystem area which is affected by D_1 strongly varies from city to city, independent on the ecosystem or the size of the aerosol tracer. All three ecosystems are heavily affected around Lagos, especially cropland and forest. For pasture Bogotá shows by far the largest impact, with more than twice the area affected in the case of small aerosol tracers compared to all other MPCs. The least effects are assessed for several cities in all cases. Only in the case of large aerosol tracers and croplands an area for D_1 can be assessed for each MPC. In all other cases there are at least two MPCs for which no area fulfills the criterion of D_1.
Taken together, forests which cover large areas on each continent are most affected by the MPC deposition. In contrast, pasture areas are also widespread though they are less affected by the MPC deposition than croplands, which are mainly present in a few concentrated regions. However, these regions are nearly all close to or in the outflow regions of MPCs.

5.4 Remote deposition characteristics

In contrast to the last section, the focus is now on the fraction of remotely deposited mass, i.e. the mass removed from the atmosphere after traveling for a certain distance through the atmosphere for which the remote deposition potential (DRT) is assessed. The main outcome is presented in Table 5.2, which lists annually accumulated remote deposition mass fractions and the corresponding standard deviations. The numbers represent MPC averaged annual means, given for four circles with radii of 50, 500, 1000, and 2000 km and for each aerosol diameter and activation state. They give the fraction of the emission which is deposited outside of the corresponding circle. The single emitting grid cells correspond to a radius of approximately 50 km. The remote deposition fractions for $\mathrm{NS}_{\mathrm{inact}}$ tracers is always larger than for $\mathrm{NS}_{\mathrm{act}}$ tracers because of the missing removal by nucleation scavenging and consequently longer lifetime. The difference between the two nucleation scavenging activation states generally increases with increasing radius of the circles, except for aerosol tracers with diameter of 10.0 µm, showing almost constant differences. For a given radius of a circle, the small tracers ($d \leq 1\,\mu\mathrm{m}$) show similar results in their remote deposition mass fractions, while these numbers are smaller and decrease faster for increasing radii for the large aerosol tracers.
The dark gray shaded area in Figure 5.8 shows the fractional deposition beyond 1000 km, averaged over all MPCs (with individual lines for averages of various climate classes, see below). For small tracers, on average about 50 % of the MPC emissions are deposited in regions more than 1000 km away from the source. Nearly the same result is found for the 2.5 µm aerosol tracers, while the amount deposited beyond 1000 km away is still about 25 % for large aerosol tracers.
Furthermore, regional means are assessed with the help of the Köppen-Geiger climate classification, like it has been done in Chapter 4[1]. Differences in remote deposition fractions

---

[1] For better readability, the six classes are repeated here: one for tropical regions, i.e. tracers from cities which are classified with A in the climate classification, one for arid regions (class B), one for cold regions (class D), and three for tracers from temperate regions (class C) with dry summer (subclass Cs), dry winter (subclass Cw), or without a dry season (subclass Cf). No MPCs are located in Arctic regions (class E)

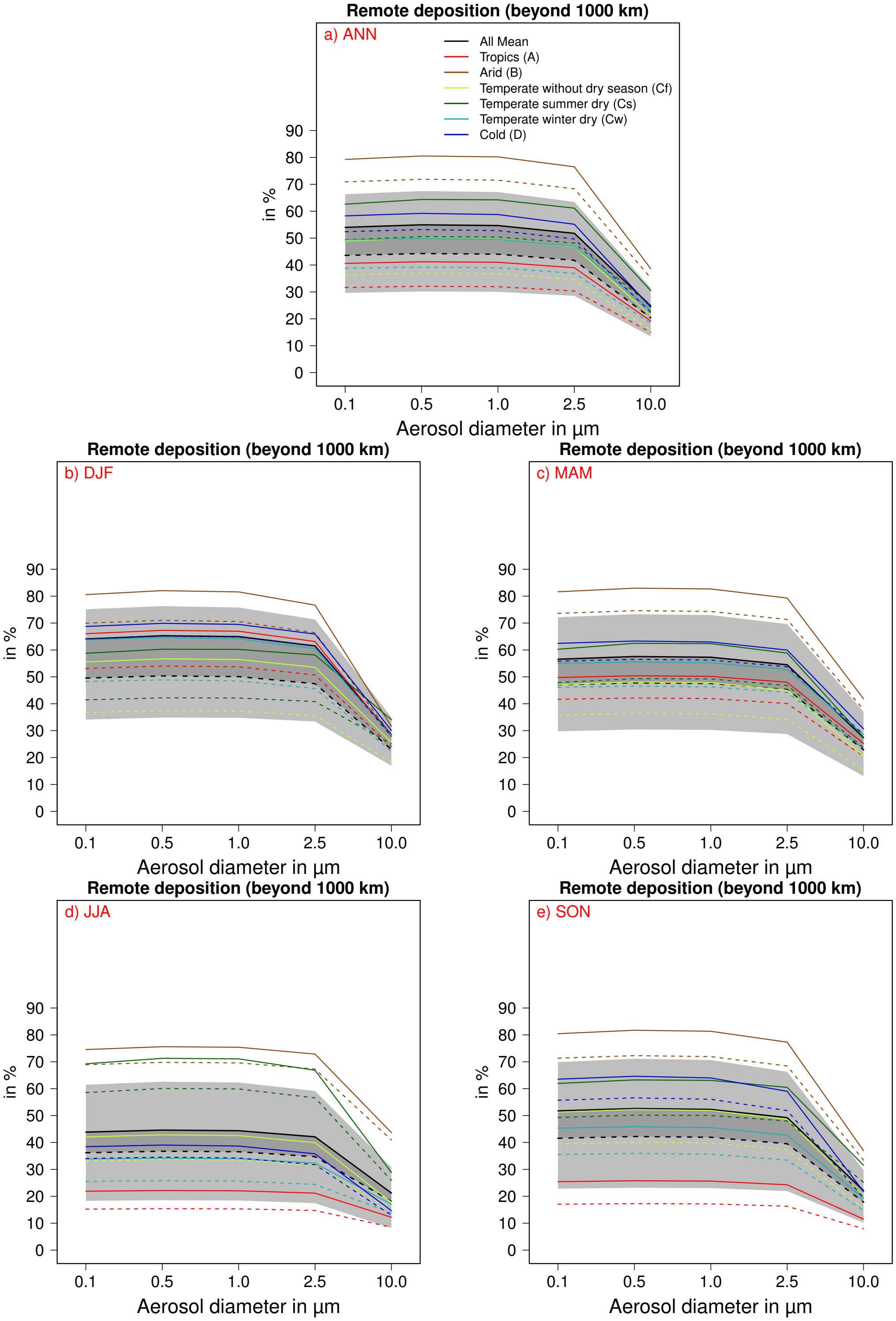

Figure 5.8: Remote deposition mass fraction (in %) which is removed outside of a circle centered at the source with a radius of 1000 km, shown for the a) the annual means and the seasonal means (b) DJF, c) MAM, d) JJA, and e) SON). Each line consists of five data points for each size simulated with one standard deviation plotted one-sided indicated by the light gray area. Dashed lines are drawn for NS_{act} tracers, solid lines for NS_{inact} tracers. The gray shaded area represents the overall mean results bounded by the mean results for NS_{inact} tracers at the top and the mean results for NS_{act} tracers at the bottom. Each colored line represents a climate class. No shading is used for climate classes to keep lucidity.

Table 5.2: Annual mean remote deposition mass fractions (DRT, in %) and the standard deviations shown for the five aerosol sizes and two nucleation scavenging activation regimes in regions outside of circles with radii given in the first row: 50, 500, 1000, 2000 km around the MPCs.

Size		50	500	1000	2000
$d = 0.1\,\mu\text{m}$	NS_{act}	89.1 ± 4.8	61.3 ± 11.7	43.6 ± 13.9	23.8 ± 11.7
	NS_{inact}	92.5 ± 3.3	70.1 ± 9.9	53.9 ± 12.3	33.8 ± 12.3
$d = 0.5\,\mu\text{m}$	NS_{act}	89.5 ± 4.7	62.0 ± 11.8	44.3 ± 14.1	24.3 ± 11.9
	NS_{inact}	93.0 ± 3.4	71.0 ± 10.1	55.0 ± 12.6	34.7 ± 12.4
$d = 1.0\,\mu\text{m}$	NS_{act}	89.4 ± 4.7	61.8 ± 11.8	44.0 ± 14.0	24.1 ± 11.8
	NS_{inact}	92.8 ± 3.5	70.7 ± 10.1	54.7 ± 12.4	34.4 ± 12.3
$d = 2.5\,\mu\text{m}$	NS_{act}	87.8 ± 4.7	59.2 ± 11.2	41.8 ± 13.2	22.6 ± 11.0
	NS_{inact}	91.1 ± 3.6	67.7 ± 9.7	51.8 ± 11.7	32.1 ± 11.5
$d = 10.0\,\mu\text{m}$	NS_{act}	69.1 ± 6.9	33.7 ± 7.6	20.4 ± 6.9	9.0 ± 4.8
	NS_{inact}	71.1 ± 7.3	38.0 ± 7.4	24.8 ± 6.7	12.4 ± 4.8

between MPCs in one climate class are always less than 10 %, while the differences for the mean values of remote deposition fractions vary strongly between the classes, with the smallest differences for large aerosol tracers in all classes (2.8 % − 7.5 %) and for all tracers in the cold regions (about 3.8 %). Small differences in mean remote deposition mass fractions are found for classes Cf and Cw as well as for Cs and D. Between class B and all other classes large differences occur, with a maximum difference between arid (class B) and tropical (class A) classes of about 40 %.

This classification of MPCs highlights two points. First, the difference between NS_{inact} and NS_{act} aerosol tracers is rather constant for DRT for each climate class, about 10 % for small tracers and about 4 % for large tracers. Second, it is well known that wet deposition is the dominant removal process for small aerosols. The differing results for the climate classes might suggest that wet removal contributes in different amounts to the overall deposition in each climate class. However, in both cases, for minimal (class A) and for maximal (class B) remote deposition mass fraction, about 95 % of the emissions are removed by wet deposition. For a circle with a 1000 km radius, aerosol tracers from arid regions (class B) have a remote deposition mass fraction of about 75 %, while for tracers from tropical regions (class A) this is less than half as much (about 36 %). This reflects the general difference in the transport distances from source to sink regions for the two classes, with MPCs in arid regions (e.g. Cairo, Teheran, Baghdad) experiencing substantially less wet removal near their source and thus more transport into regions with precipitation farther downwind, while for tracers from tropical regions, the main sink regions are the same as the source regions. Thus, source and sink regions seem to play an important role in characterizing the remote pollution potential for aerosols of the same size.

The remote deposition mass fractions can again be split into their dry and wet removal components. Considering deposition beyond circles of 1000 km radius, dry removal (DRD) accounts for only 3.8 % of the remote deposition mass fraction of the small tracers, while this number increases to about 30 % for the large tracers. In fact, no single climate class exceeds a dry remote removal mass fraction of more than 6 % for the small tracers. In contrast, maximum values for large tracers amount to about 40 % dry remote removal in cold (class D) and temperate regions with dry summer (class Cs) and to about 25 % in tropical (class A) and temperate regions with dry winter (class Cw).

Remote deposition mass fractions also show seasonal variations (see Figure 5.8). During winter (DJF) the range between climate classes is smallest, with generally higher values for the remote deposition mass fractions, while the range is largest during summer (JJA). Furthermore, the order of the climate classes changes with season. Tracers from tropical and cold regions show rather high remote deposition mass fractions in the winter season, but low *DRT* in the summer season because of the different meteorological conditions, especially the convective activity and precipitation (see also discussions in Section 4.4)).

5.5 Summary

In this chapter the main focus was on the removal of aerosol emissions from major population centers (MPCs), based on the same tracer experiments as in Chapter 4.

A major result is that large amounts of fine particulate matter (with ambient diameter $\leq 2.5\,\mu$m) from urban point sources travel long distances in the atmosphere, with consequent substantial remote deposition. About 50 % of the emissions are deposited outside of a circle with a radius of 1000 km which is centered at the emission point for aerosol tracers with ambient diameter $\leq 1.0\,\mu$m and still 46 % for aerosol tracers with ambient diameter of 2.5 µm. The largest remote deposition potential is found for aerosol tracers from MPCs located in arid regions (75 %), the lowest for those in tropical regions (36 %). The main processes determining the remote deposition mass fractions are the prevailing circulation patterns along with precipitation. Seasonal changes of these meteorological characteristics lead to inter-seasonal variations in the remote deposition potential of MPCs.

Furthermore, it was found that more than 90 % of the emissions of small aerosol tracers are deposited by scavenging in and below clouds whereas the dry deposited mass fraction exceeds 50 % in the case of large aerosol tracers. Locally, the dry deposition mass fraction can exceed 75 %, especially close to the source region or in dry regions such as deserts.

In contrast to the diluted remote deposition, areas around the emission points are exposed to high deposition rates. A normalized deposition field was used to assess the size of areas on which more than 1 % or 5 % of the total annual emissions are deposited. In doing so, it is found that these areas are generally larger for large aerosol particles and also show less variation between the individual major population centers. Smaller particles have longer lifetimes and therefore undergo stronger dilution in the atmosphere and the dispersion varies more strongly between different regions than for large aerosols (see Chapter 4). The areas are largest for MPCs in regions which are either frequently affected by heavy precipitation or in poorly ventilated geographic locations. Most of the MPC aerosol emissions are removed over land surfaces, although about half of the MPCs are directly located along and several more are close to the coast. Moreover, it is found that forests are more substantially exposed to aerosols from MPCs than croplands or pasture.

6

Impact of aerosol microphysics and horizontal model resolution

Generic aerosol tracers of various sizes were used until now to simulate the transport and deposition of aerosols from urban centers. Except for the aerosol lifetimes which generally agree with observations no proof has been given whether the generic aerosol tracers are good representatives of ambient aerosols. This issue will however be discussed in this chapter. For this the generic aerosol tracers are tested against more complex aerosol tracers which undergo microphysical transformations and have not yet been available in the model. The new tracers are implemented in the aerosol module `GMXe` and are treated in most parts like all other aerosol species. The complexity of the new tracers increases and consequently also the computational expense, which is counteracted by reducing the horizontal model resolution. In doing so, the following questions arise and will be answered in this chapter:

1. What are the differences in the dispersion and deposition between passive aerosol tracers which have properties of a primary anthropogenic aerosol (like black carbon or particulate organic matter) and generic aerosol tracers which have a fixed size and solubility?
2. To which degree can microphysical processes such as coagulation and coating influence the aerosol transport and deposition?
3. The more sophisticated representation of the passive aerosol tracers favors the usage of a low resolution model to allow a reasonable CPU time. Consequently, the question arises: how does the chosen model resolution influence aerosol transport and deposition?

These questions are answered in detail after a description of the model and simulation setup are given in the first section. In the second part I compare the results of model simulations with different horizontal model resolutions and in the third part the new passive tracers are compared to the generic tracers used before. Finally, the influence of coagulation and coating on the aerosol dispersion is discussed.

6.1 Model and simulation setup

6.1.1 Model setup

In this chapter both model versions, **A** and **B**, are used to study the dispersion of aerosols. Results from model version **A** are obtained in two different horizontal resolutions, 1.1° × 1.1° in longitude and latitude (T106) and 2.8° × 2.8° in longitude and latitude (T42). The results for T106 have already been discussed in Chapters 4 and 5 and those for the low resolution are put in perspective here to see whether the results show a dependence on the chosen model resolution. The change to the low horizontal resolution and thus the decrease in computational expense is necessary since model version **B** requires more CPU time due to the comprehensive representation of atmospheric chemistry (Jöckel et al., 2006) and the aerosol microphysics (Pringle et al., 2010b,a). A detailed description of the model setup regarding emissions and boundary conditions for trace gases and aerosols will be given in Chapter 7 since only results of the passive tracers are presented in this chapter.

6.1.2 Passive aerosol tracers and aerosol microphysics

Together with Holger Tost, I implemented a new possibility to add passive aerosol tracers in the MESSy submodel `GMXe`. In contrast to the generic aerosol tracers, those in `GMXe` can grow and shrink in size and increase their solubility through coagulation, cloud processing as well as coating with soluble mass. However, the passive tracers are implemented in `GMXe` such that they do not influence other species; all other species give identical results in simulations with and without the passive tracers. Thus, the passive tracers represent a simplified tagging method.

The passive aerosol tracers are initialized according to the tracer implementation in MESSy (Jöckel et al., 2008). `GMXe` has in total seven modes to represent the aerosol size distribution. The passive tracers can be emitted in one or more modes which are set in the `GMXe` FORTRAN namelist. Furthermore, the total number of passive tracers and also the modes in which these are represented are set in the namelist. The additional number of tracers which have to be treated in the model is assessed by multiplying the number of passive tracers with the number of modes in which the tracers are defined. For example, in this study 46 passive tracers are initialized, each being treated in four of the seven modes, which implies a total of 184 additional tracers. This number should be kept in mind since each tracer is individually treated within the transport and aerosol schemes, which in turn increases the CPU and memory requirements.

6.1.3 Simulation setup

To obtain results corresponding to those discussed in the chapters before, the model simulations have been initialized in July 2004 and the model integration ended in January 2006. The last twelve months are used for the analysis and all simulations are weakly nudged towards meteorological data of ECMWF. Since no feedbacks between atmospheric species (trace gases and aerosols) and meteorology are considered, all simulations have the same meteorology, except for differences introduced due to different horizontal resolutions. Model version **A** (no microphysics) is run in T106 (1.1° × 1.1° in longitude and latitude, high resolution model) and T42 (2.8° × 2.8°, low resolution model) resolutions with 31 hybrid sigma-pressure levels in the vertical. Model version **B** (with microphysics) is only run in T42.

Mono-modal passive tracers with a diameter of 1.0 µm are applied with two different solubilities, $\mathrm{NS_{inact}}$ and $\mathrm{NS_{act}}$, in model version **A**. These tracers were extensively discussed in Chapters 4 and 5 and had been chosen to represent fine aerosol particles. In model version **B**, two types of passive aerosols are emitted; in the first case, the entire emitted mass is

Table 6.1: Overview of simulations to assess the impact of aerosol microphysics and model resolution. The first column gives an abbreviation for the corresponding simulation: T42 means truncation of the base model at wavenumber 42, T106 at wavenumber 106, respectively. PA means passive aerosol, ins stands for emission only in the hydrophobic Aitken mode, sol for 75 % in the hydrophobic Aitken mode and 25 % in the hydrophilic Aitken mode. d is the fixed aerosol diameter, d_e is the diameter at emission. REF is the reference simulation for the two sensitivity studies NOCOAG (no coagulation) and NOCOAT (no coating).

Simulation	Passive aerosol	Aerosol size	Hor. resolution
T42-NS$_\mathrm{act}$	`PTRAC`	$d = 1.0\ \mu\mathrm{m}$	2.8° × 2.8°
T42-NS$_\mathrm{inact}$	`PTRAC`	$d = 1.0\ \mu\mathrm{m}$	2.8° × 2.8°
T106-NS$_\mathrm{act}$	`PTRAC`	$d = 1.0\ \mu\mathrm{m}$	1.1° × 1.1°
T106-NS$_\mathrm{inact}$	`PTRAC`	$d = 1.0\ \mu\mathrm{m}$	1.1° × 1.1°
PA$_\mathrm{ins}$/REF	`GMXe`	$d_\mathrm{e} = 100$ nm	2.8° × 2.8°
PA$_\mathrm{sol}$	`GMXe`	$d_\mathrm{e} = 100$ nm	2.8° × 2.8°
NOCOAT	`GMXe`	$d_\mathrm{e} = 100$ nm	2.8° × 2.8°
NOCOAG	`GMXe`	$d_\mathrm{e} = 100$ nm	2.8° × 2.8°

introduced into the insoluble Aitken mode (KI), for example representing an initially fully insoluble primary aerosol like black carbon, in the other case 25 % of the emitted mass is added to the soluble Aitken mode (KS) and the rest to the KI mode, for example an initially slightly soluble primary aerosol like organic carbon. The passive tracers in model version **B** can subsequently be transferred into the soluble Aitken (KS), accumulation (AS), and coarse mode (CS). The emission flux has again arbitrarily been chosen to be $1\,\mathrm{kg\,s^{-1}}$, placed in the middle of each grid box hosting an emission source point for which the same 46 MPCs are used as in Chapters 4 and 5 (see Table 4.1).

Two more simulations were performed with model version **B**. In one case the coagulation and in the other case the coating of the aerosol tracers was switched off to assess the contribution of each of the microphysical processes during the dispersion of (passive) aerosols in different regions around the world (see Table 6.1).

6.2 Sensitivity of aerosol dispersion on horizontal model resolution

EMAC has been run in several model configurations with respect to the model resolution, from T42L19 up to T106L31 (e.g, Burrows et al., 2009; Tost et al., 2006b; Pringle et al., 2010b,a; Kunkel et al., 2012a; Pozzer et al., 2012b) and also in a middle atmosphere configuration with substantially more vertical levels, T42L90 (e.g., Jöckel et al., 2006). The standard procedure to investigate the differences between two different model configurations would be to start to compare results from the base model, i.e., the meteorology, before comparing the results from the atmospheric chemistry part, i.e., the aerosols. Here, the focus is on the latter part and refer to Roeckner et al. (2006) and Hagemann et al. (2006) who both evaluated the performance of the model at different resolutions.

A first check whether the passive aerosols in two different simulations behave similarly is to compare the aerosol residence times in the atmosphere. The lifetime of the generic aerosol tracers is however longer in the low resolution model, independent of the solubility state of

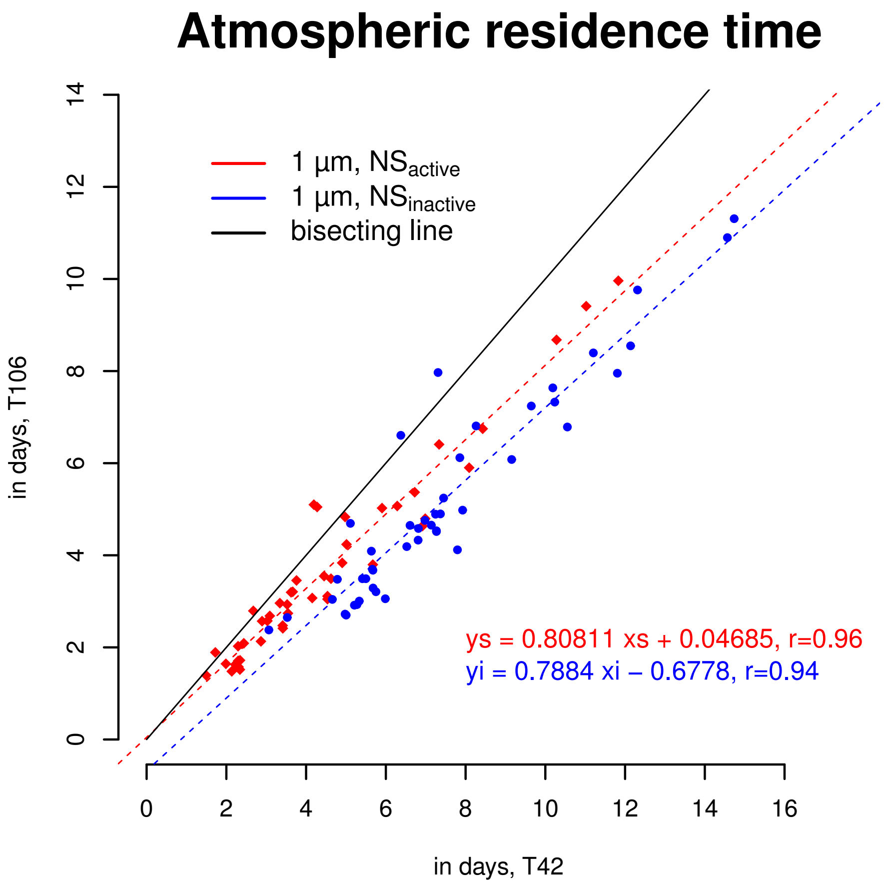

Figure 6.1: Scatter plot of atmospheric residence times (in days) for $\mathrm{NS}_{\mathrm{inact}}$ (blue) and $\mathrm{NS}_{\mathrm{act}}$ (red) 1.0 µm aerosol tracers simulated with two different horizontal resolutions, T42 (abscissa) and T106 (ordinate). Dashed lines represent regression lines with equations provided as legends. The black solid line represents the bisecting line.

the aerosol and for most of the emission sources (Figure 6.1). The emission fluxes are the same in both simulations and thus more mass has to be present in the T42 simulations to obtain the longer lifetimes. This results either from a less effective removal of aerosols in the low resolution model or from differences in the transport.

As a next step, the total column, the surface, and the upper tropospheric column densities are plotted to test the latter hypothesis (Figure 6.2). It is apparent that in all three cases more mass is present in the low resolution simulations, here only shown for the $\mathrm{NS}_{\mathrm{inact}}$ aerosol tracers in the left panels of Figure 6.2 but the same is evident for the $\mathrm{NS}_{\mathrm{act}}$ aerosol. However, the largest difference occurs in the upper tropospheric column density. The high resolution model maximum values hardly reach the upper end of the color bar ($20 \times 10^{-9}\,\mathrm{kg\,m^{-3}}$), while this value is exceeded over large regions in the low resolution model. Two additional aspects are of interest in this discussion. First, pure gas phase tracers which only undergo an exponential decay as sink process, i.e., their atmospheric dispersion is mainly determined by transport, do not show such a difference with respect to model resolution (see Appendix D). Second, using an intermediate resolution (T63, 1.9° × 1.9°, see Appendix D) gives results which are intermediate between the T42 and T106 results, so that it seems that the results follow a linear trend.

The metrics to determine the transport and deposition potentials can further help to identify

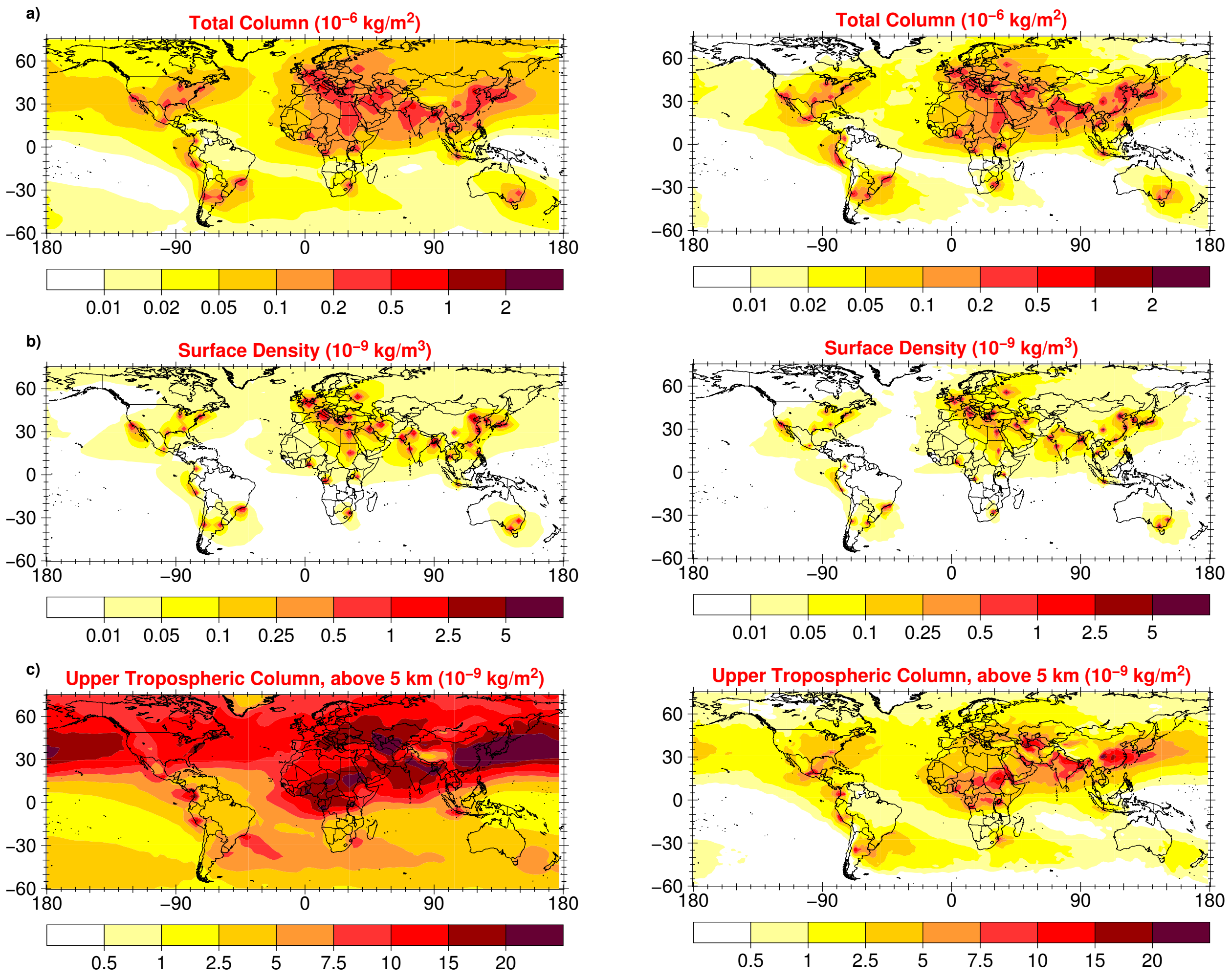

Figure 6.2: Sum of all 46 MPC tracers for a) total column density (in 10^{-6} kgm^{-2}), b) surface density (in 10^{-9} kgm^{-3}), and c) upper tropospheric column density (in 10^{-9} kgm^{-2}) from the EMAC simulations. Shown are NS$_{\text{inact}}$ 1.0 µm aerosol tracers, on the left for a horizontal resolution of T42, on the right for T106.

the differences between the low and the high resolution model. The largest deviations in annual mean values appear for E_{UT}, CVS, and LSS. The first two are larger in the low resolution model and the latter in the high resolution model (Figure 6.3). Thus, the question emerges why more aerosol mass is transported to higher altitudes in the low resolution model. The answer is implied in the differences for CVS and LSS and in findings from Hagemann et al. (2006). They reported that although the total precipitation flux (sum of large-scale and convective precipitation flux) is essentially independent of the model resolution of ECHAM5, the fraction of large-scale precipitation increases with increasing resolution at the expense of the convective precipitation. This is reflected in CVS and LSS, which both depend on the cloud cover and liquid water path in convective and large-scale clouds, respectively. Furthermore, although convective precipitation is more effective in removing aerosol particles compared to large-scale precipitation, more aerosols are removed in total by large-scale precipitation due to the more frequent appearance and extended coverage of large-scale clouds (see also Appendix D).

In the model it is no trivial task to overcome this behavior, since the rain formation depends

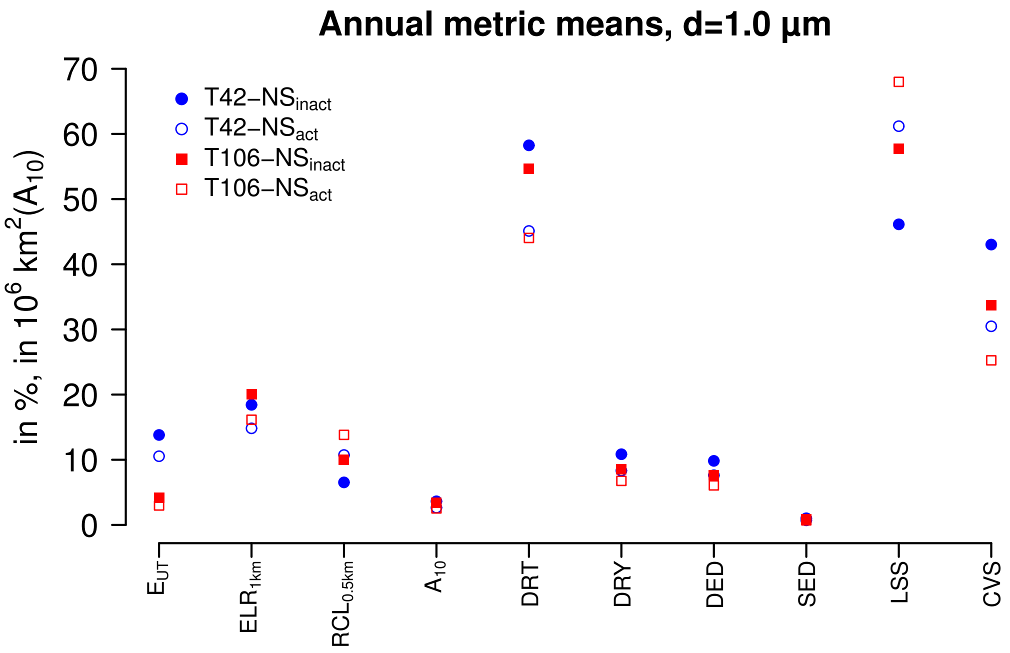

Figure 6.3: Overall annual means of the transport and deposition metrics to characterize the difference between the dispersion and deposition of 1.0 µm NS_{inact} and NS_{act} aerosol tracers. Annual means for T42 means are depicted by blue circles, for T106 in red squares, for NS_{inact} in filled signs, and for NS_{act} in open signs.

on the auto-conversion rate which is a resolution-dependent parameter for both cloud types. Changing this parameter would not only be expected to lead to a different rain formation rate and thus to a potentially wrong total precipitation flux, but also to an imbalance in the radiative forcing which would then result in a different climate state. Hence, I do not focus on correcting this model feature, but consider it in the discussion of the results. Especially for the results in Chapter 5, it is important to emphasize that the long-range transport is greater in the low resolution model, indicated for example by the greater *DRT* values.

6.3 Impact of microphysical aerosol properties on aerosol dispersion

The results in Chapters 4 and 5 rely on the assumption that passive aerosol tracers with fixed sizes and solubility properties can be used to represent the ambient aerosol tracers with the advantage of CPU requirements which allow simulations at a high model resolution. The nature of the generic tracers in Chapter 4 only allowed the conclusion that the modeled aerosols have lifetimes which are of the order of magnitude of reported values (see Figure 4.2 and Seinfeld and Pandis, 1998). However, the passive tracers implemented in `GMXe` provide the possibility of further verifying this assumption since a comparison to the generic tracers is feasible. For this I will first compare results from the generic and the more complex passive tracers by using the following simulations (see Table 6.1): T42-NS_{act}, T42-NS_{inact}, PA_{sol}, and PA_{ins}. After this I use simulation PA_{ins} as a reference simulation (REF) and compare the results to those from two sensitivity simulations, NOCOAG and NOCOAT, to identify the impact of coagulation and coating on the aerosol dispersion.

6.3.1 Differences in atmospheric dispersion and surface deposition between generic and more complex passive aerosol tracers

The aerosol lifetime serves again as a first measure for the comparison between the PAm tracers (passive aerosols in simulations PA_{sol} and PA_{ins}, PAm = passive aerosols with microphysics) and PAs (passive aerosols in simulations $T42\text{-}NS_{inact}$ and $T42\text{-}NS_{act}$, PAs = "simple" passive aerosols/generic aerosol tracers). For most MPC tracers the lifetimes do not differ much, with slightly longer lifetimes of the PAs tracers. The largest differences are about two days and occur for those tracers with the longest lifetimes. Thus, since the emissions are equal, the quasi-steady state mass burden is larger for PAs tracers.

This becomes also apparent when comparing annual mean column densities (Figure 6.4). The PAs tracers have larger values in the total column, surface, and upper tropospheric column densities, but the regional patterns of high and low values are very similar distributed for PAm and PAs tracers. This in turn results in moderately different annually accumulated deposition fields which give the impression that PAs tracers undergo slightly more long-range transport than PAm tracers because of the higher deposition mass fluxes in the outflow re-

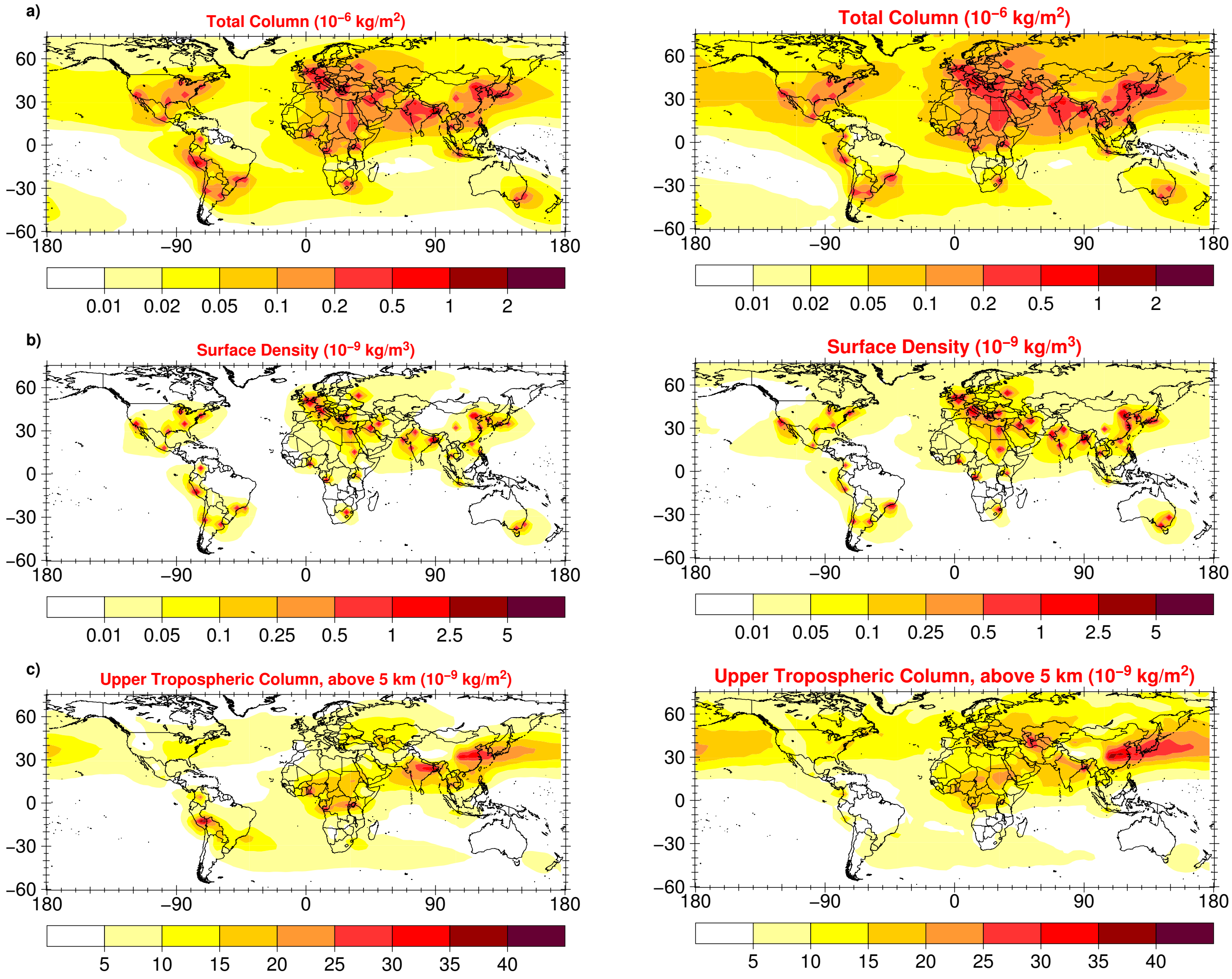

Figure 6.4: Sum of all 46 MPC tracers for a) total column density (in 10^{-6} kg m^{-2}), b) surface density (in 10^{-9} kg m^{-3}), and c) upper tropospheric column density (in 10^{-9} kg m^{-2}); on the left for PA_{ins} tracers and on the right for $T42\text{-}NS_{inact}$ tracers.

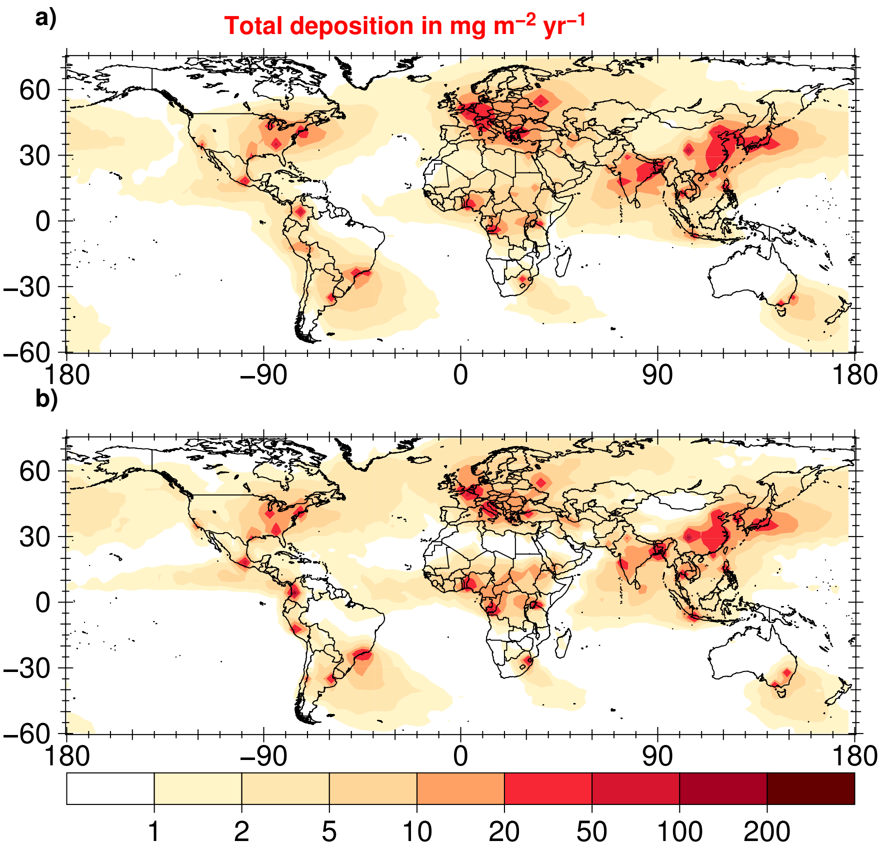

Figure 6.5: Annually accumulated deposition fields (in $\mathrm{mg\,m^{-2}\,yr^{-1}}$) for the sum of all 46 MPCs for a) $\mathrm{PA_{ins}}$ and b) T42-$\mathrm{NS_{inact}}$ tracers.

gions of East Asia and North America (Figure 6.5).

However, no significant deviation is assessed for *DRT* (deposited mass fraction beyond 1000 km) between T42-$\mathrm{NS_{inact}}$ and $\mathrm{PA_{ins}}$ tracers, while the smallest *DRT* value is computed for T42-$\mathrm{NS_{act}}$ aerosol tracers (Figure 6.6). In general, the difference between annual metric means of PAm and PAs is in all cases smaller than the difference between annual metric means of T42-$\mathrm{NS_{inact}}$ and T42-$\mathrm{NS_{act}}$ tracers. This means that the difference resulting from one process, namely scavenging by nucleation, is larger than the difference from aerosol microphysics. Only for *SED*, and consequently for *DRY*, larger metric means are assessed for PAm tracers, resulting from different aerosol densities. While the aerosol density of the PAs tracers had been chosen to be $1\,\mathrm{g\,cm^{-3}}$, a density of $2\,\mathrm{g\,cm^{-3}}$ was used for the PAm tracers, equal to the density applied for black carbon and particulate organic matter in `GMXe`, which leads to a faster gravitational settling.

As a first conclusion: the transport and deposition potentials agree well between the PAs and PAm tracers. This further justifies the use of the PAs tracers (here with a diameter of $1.0\,\mu\mathrm{m}$) to represent the ambient aerosols from the emission hot spots with the benefit of less demanding CPU requirements regarding the aerosol scheme, and thus the benefit of being able to use a possible higher model resolution.

In addition, the implementation of the PAm tracers allows further analysis. In Figure 6.7 an example is provided by illustrating mode-resolved annual mean total column densities and the fractions of the annually accumulated total deposition mass flux in each mode. Each

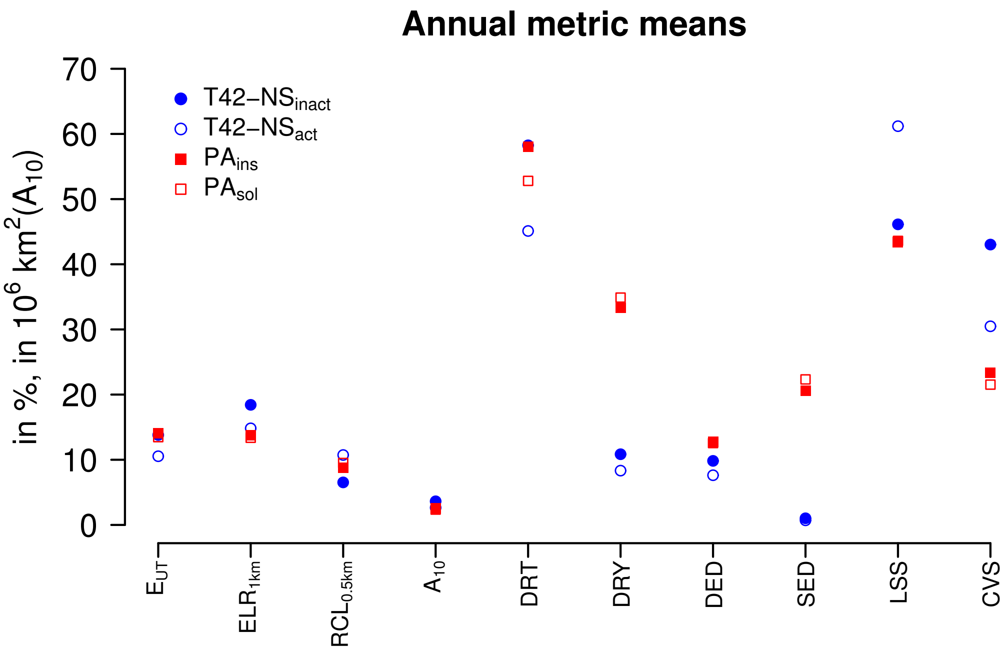

Figure 6.6: Annual means of the transport and deposition metrics of the PAm (red) and PAs (blue) tracers.

row shows information about one of the four modes in which PAm tracers are represented. Largest mass densities are found around the source points in the mode in which the emission takes place (KI). In contrast, almost no mass is present in the soluble Aitken mode (KS) since coagulation transfers particles quickly into the soluble accumulation mode (AS). In some regions the source points can still be distinguished from the background indicating that the aging of the aerosols is fast compared to the transport away from the source. In the soluble coarse mode, the source points cannot be identified anymore. Generally, aerosol mass in AS and CS represents the aged MPC aerosol which has grown in size and solubility and in many cases has already been transported away from its source. The deposition fractions show that only in the KI mode a substantial deposition occurs directly around the emission hot spots. In some cases, more than 50 % of the emitted mass are deposited in the KI mode, while most mass is removed farther away from the source in the AS and especially in the CS mode.

Furthermore, the pollution potentials (metrics) can also be extended to track the aging process of the aerosol (see Table 6.2). Recall that aerosol aging is usually an indicator for the time the aerosol was airborne; and that the longer the aerosol is in the atmosphere the more the aerosol particles are transported over long distances. Instead of only assessing, for example, the mass fraction above 5 km (E_{UT}, $m_{\mathrm{t}}/M_{\mathrm{t}}$), it is possible to determine the insoluble (soluble) mass fraction of the global total insoluble (soluble) burden ($m_{\mathrm{i}}/M_{\mathrm{i}}$, $m_{\mathrm{s}}/M_{\mathrm{s}}$) as well as the total insoluble mass fraction above 5 km, either relative to the global total burden ($m_{\mathrm{i}}/M_{\mathrm{t}}$), i.e., the mass fraction that has not been transformed during transport, or relative to the total mass above 5 km ($m_{\mathrm{i}}/m_{\mathrm{t}}$). Using this additional information, some of the conclusions from Chapter 4 can be refined. In particular, although soluble aerosols are much more susceptible to be removed from the atmosphere (by nucleation scavenging) and have consequently a shorter lifetime, more than 90 % of the aerosol mass above 5 km is soluble.

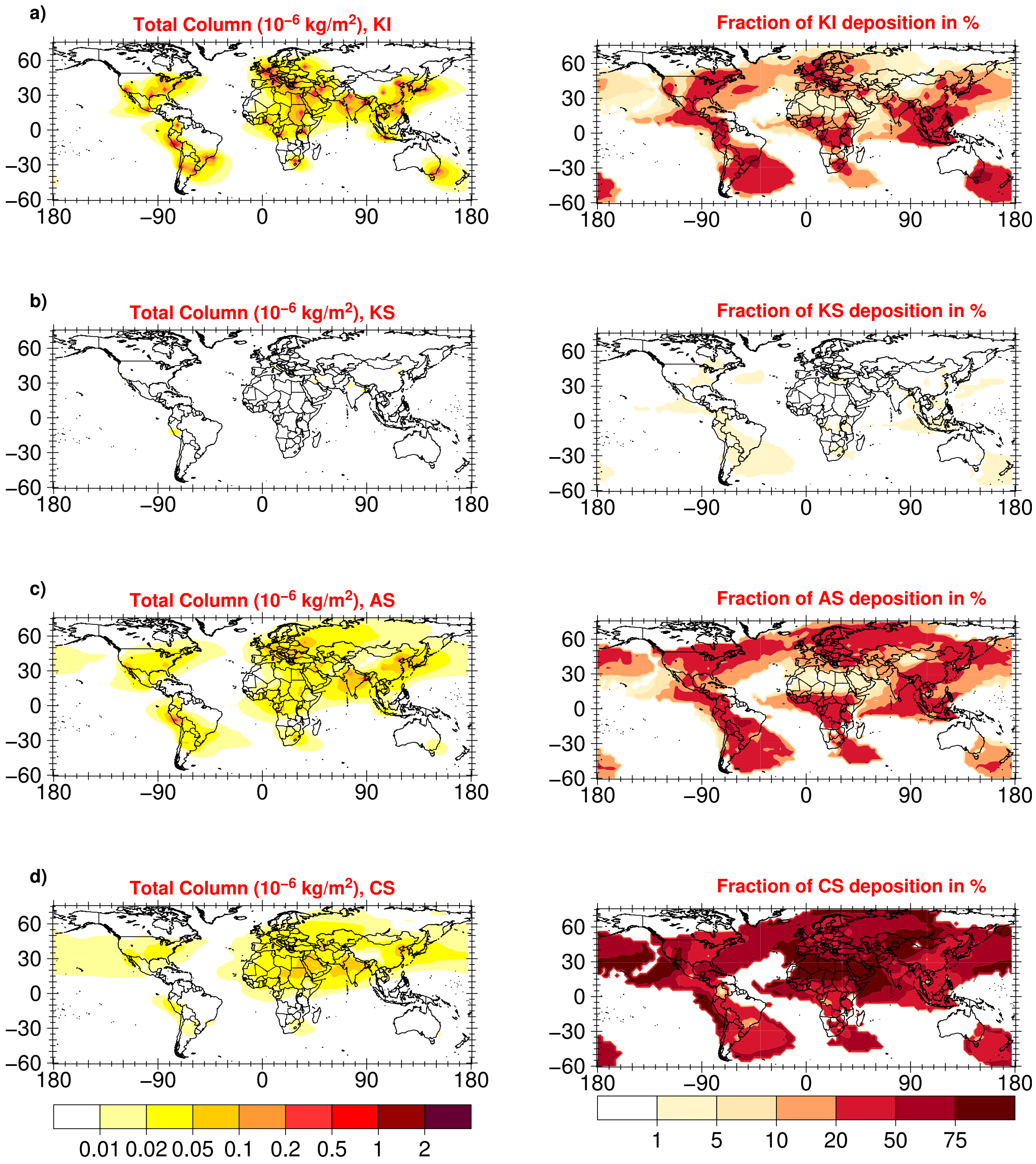

Figure 6.7: Annual mean total column densities (left, in 10^{-6} kg m^{-2}) and fractions of annually accumulated total deposited mass (right, in %) for the sum of all 46 MPCs of the a) insoluble (KI), b) soluble (KS) Aitken mode, c) soluble accumulation mode (AS), and d) soluble coarse mode (CS).

At low levels this is reversed: only about one quarter of the retained mass ($RCL_{0.5\mathrm{km}}$) has already turned hydrophilic and still about 40 % of the low-level export has not accumulated enough hydrophilic material to be moved into a soluble mode.

Table 6.2: Annual means (in %) of extended metric values of E_{UT}, ELR_{1km}, and $RCL_{\mathrm{0.5km}}$ for the $\mathrm{PA_{ins}}$ tracers. M_{t}=total atmospheric burden in all modes, M_{i}=total atmospheric burden in the insoluble mode, M_{s}=total atmospheric burden in the soluble modes, m_{t}, m_{i}, m_{s} atmospheric burden of all, all insoluble, and all soluble modes fulfilling the criteria of the metric.

	$m_{\mathrm{t}}/M_{\mathrm{t}}$	$m_{\mathrm{i}}/M_{\mathrm{i}}$	$m_{\mathrm{s}}/M_{\mathrm{s}}$	$m_{\mathrm{i}}/M_{\mathrm{t}}$	$m_{\mathrm{i}}/m_{\mathrm{t}}$
E_{UT}	14.06 ± 6.47	3.28 ± 1.93	21.97 ± 10.25	1.31 ± 0.66	8.73 ± 2.34
ELR_{1km}	13.79 ± 6.01	12.70 ± 6.59	14.17 ± 5.32	5.51 ± 3.50	38.87 ± 9.99
$RCL_{\mathrm{0.5km}}$	8.76 ± 2.21	16.31 ± 4.12	3.50 ± 1.40	6.66 ± 7.30	77.43 ± 1.33

6.3.2 Impact of coagulation and coating

In `GMXe` microphysical processes are simulated one after another, with the possibility of switching them off in the FORTRAN namelist. Hence, the contribution of each process to the overall evolution of the aerosol population can be almost fully assessed. A full quantification is surely not possible since processes can have feedbacks on each other. However, using the passive tracers in `GMXe` and the possibility to turn off coagulation and coating processes offers the potential for quantifying their impact on the evolution of fine aerosol particles. Coagulation is known to reduce the particle number and to increase the mean diameter of an aerosol population as well as shifting particles from the nucleation and Aitken mode into the accumulation mode, while transfer into the coarse mode mainly occurs through cloud processing. Furthermore, coagulation can lead to a transfer of aerosol particles from hydrophobic to hydrophilic modes. Coating mainly increases the hygroscopicity of the aerosol population and affects the diameter of particles in the smaller modes (e.g., Seinfeld and Pandis, 1998). From this, it can be expected that both processes reduce the aerosol lifetime and therefore

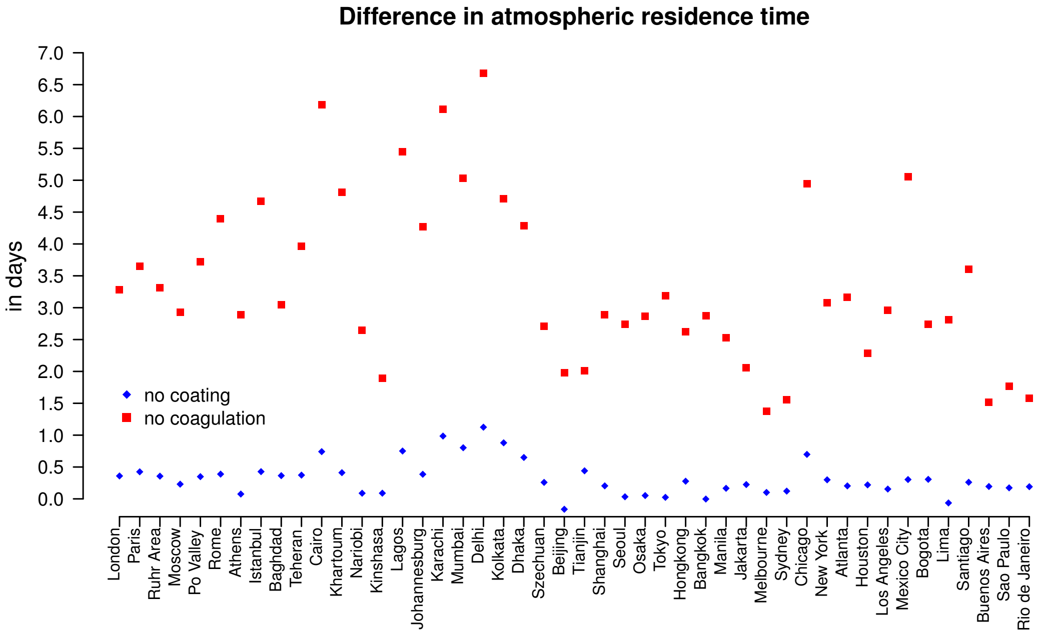

Figure 6.8: Absolute changes in the aerosol lifetimes (in days) in the simulations NOCOAG (red) and NOCOAT (blue) compared to the reference simulation.

also the long-range transport potential. To assess the magnitude of the contribution, two simulations have been conducted: NOCOAG (no coagulation) and NOCOAT (no coating). Both have been compared to the reference simulation which is the PA_{ins} simulation. All three simulations were executed with the same binary and namelist settings, except for the coagulation and coating, respectively.

Coagulation generally has a larger effect on the aerosol residence time than coating (Figure 6.8). The annual mean lifetime is longer for all MPCs in the case of no coagulation with an increase between 1.3 days for Melbourne and more than 6.5 days for Delhi. In contrast, the increase in aerosol lifetime is confined to less than a day for coating. Furthermore, for several MPCs (e.g., Beijing and Lima) a decrease in lifetime is simulated which is, however, only of a few hours. Thus, the impact of coagulation on the lifetime and as such on the atmospheric mass burden is much larger than that of coating, with increases of more than 50 %.

The change in aerosol lifetimes is further reflected in the annual metric means, with almost equal means in the REF and NOCOAT simulations but apparent differences between means in the REF and NOCOAG simulations (see Figure 6.9). In particular, the long-range transport increases, which is indicated by the differences in the metrics E_{UT}, $ELR_{1\mathrm{km}}$, $RCL_{0.5\mathrm{km}}$, and DRT, with DRT being increased by almost 10 % in the NOCOAG simulation. This is caused by the slower particle growth and transfer into hydrophilic modes, which in turn slows down the aging of the aerosol particles. This also leads to an interesting artifact in the deposition. Not surprisingly, the smaller particles sediment more slowly to the ground. It could be expected that this leads to higher wet deposition (see the decrease in DRY for NOCOAG), but the compensation occurs only by scavenging in convective clouds (CVS).

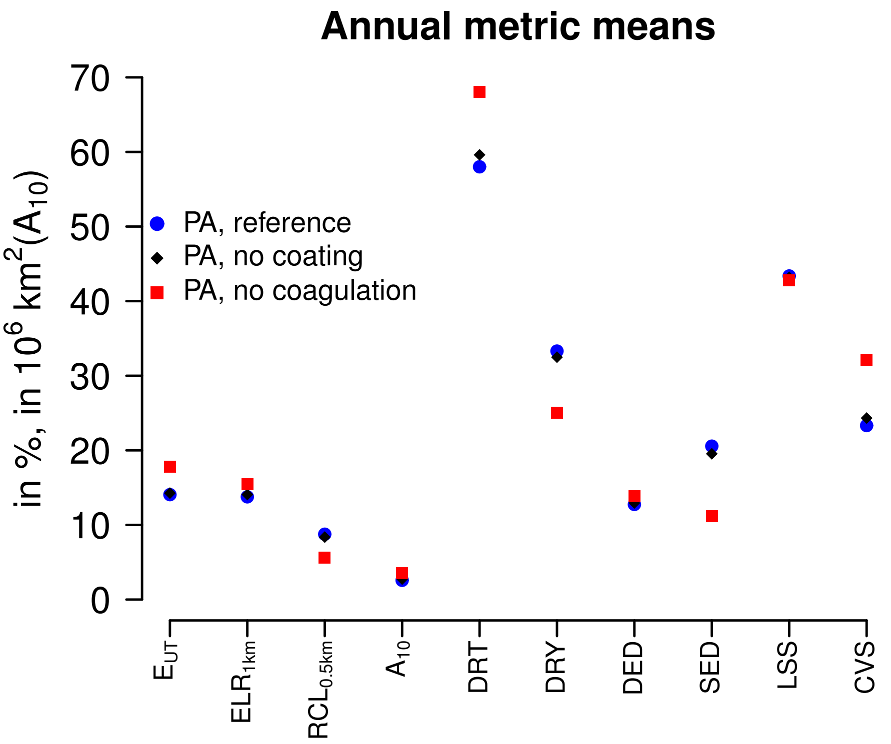

Figure 6.9: Annual means of the transport and deposition metrics for REF, NOCOAG, and NOCOAT.

Table 6.3: MPC-averaged annual mean atmospheric burden (in Tg) for the sum of all modes, the hydrophobic mode, and the sum of the hydrophilic modes for the reference simulation (REF) and the simulation without coagulation (NOCOAG).

Simulation	All modes	Hydrophobic mode	Hydrophilic modes
REF	462.2	190.4	271.8
NOCOAG	752.9	512.7	240.2

The atmospheric burdens in the REF and NOCOAG simulations can help to explain this change. On average the total mass burden increases (expressed as MPC mean) by more than 60 % in the NOCOAG simulation (first column in Table 6.3). The second and third column of this table reveal further that the mass increase is limited to the hydrophobic mode (increase of 169 %), while there is even less mass in the hydrophilic modes. Furthermore, nucleation scavenging is the dominant removal process for particles between 0.2 and 2.5 μm. However, insoluble particles are not removed by nucleation scavenging but can be scavenged by falling raindrops, i.e., by impaction scavenging. This process has a minimum efficiency for particles with diameters of several hundred nanometers (Greenfield gap) and further depends on the rain rates. In large-scale clouds, the rain rates are not high enough to effectively remove the small, insoluble particles; only in convective clouds can sufficiently high rain rates occur to wash out the particles. Moreover, this further increases the lifetime since convective clouds have a much smaller coverage in time and space compared to large-scale clouds which can be present on a longer time scale during a frontal passage.

To conclude this section and the chapter, I make a bridge from passive aerosols to the aerosol species included in `GMXe` and briefly discuss how the size distribution of ambient aerosols would change when either coagulation or coating are prohibited. For a detailed description of the emissions and boundary conditions of these aerosols I refer to the next chapter (in

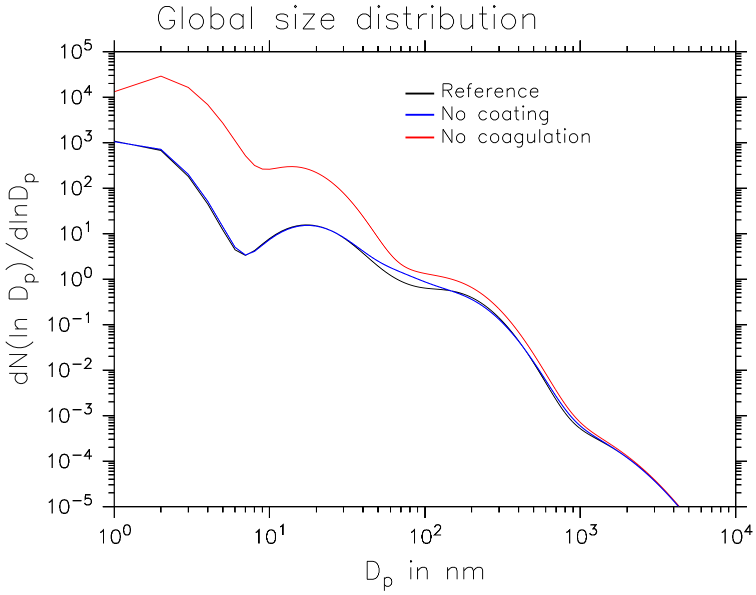

Figure 6.10: Global tropospheric size distribution (in 1/cm^3) representing all species present in the `GMXe` submodel except the passive tracers.

particular Section 7.1). Similar to what was found for the passive tracers, coating hardly changes the size distribution, whereas coagulation substantially decreases the number of particles in each mode and shifts the modal diameter (see Figure 6.10). While the modal diameter becomes smaller in the nucleation mode, it is always larger in all other modes when coagulation is turned on. The smallest deviations occur in the two coarse modes which show the least changes in the size distribution with respect to coagulation and coating. Only a slightly higher particle number density is simulated in the hydrophobic coarse mode since the transfer of insoluble dust, which is the main constituent of this mode, is slowed down when either coating or coagulation is missing.

6.4 Summary

In this chapter several rather technical questions regarding the transport and deposition of passive aerosol tracers are discussed. More complex passive aerosol tracers were introduced and compared to the generic aerosol tracers which had been used before. In doing so, and to keep the computational expense on a reasonable level, the horizontal resolution was decreased from T106 to T42. The major results of this chapters are summarized in the following:

1. The choice of horizontal resolution has a significant impact on the amount of mass which is transported into the upper troposphere. This is most probably the consequence of a shift from more convective to large-scale precipitation with increasing horizontal model resolution. This effect was first described by Hagemann et al. (2006) and here the consequences are shown and quantified for soluble trace species. It is shown that the aerosol lifetime is simulated to be longer in low resolution simulations due to less effective removal. Moreover, the potential of long-range transport increases in the low resolution model.
2. Generic aerosol tracers of a given size are shown to well represent ambient aerosols in transport studies. The differences between passive aerosol tracers which can undergo microphysical changes and generic aerosol tracers which do not share this ability are generally smaller than the difference between generic aerosol tracers (no microphysics) which can be removed by nucleation scavenging to those which cannot. Hence, the different treatment in one process which can affect both types of passive aerosol tracers (with and without microphysical treatment) is found to be at least as large than the difference due to aerosol microphysics.
3. Coagulation is shown to be the dominant process to alter the properties of a primary emitted aerosol tracer. The atmospheric burden substantially increases when coagulation is prohibited, especially in the hydrophobic mode, resulting in a much longer lifetime (up to 50 % increase) and more long-range transport. Moreover, the removal of the aerosol tracers changes: gravitational settling becomes less important due to a greater number density of smaller particles which is almost entirely balanced by more scavenging in convective clouds due to the high liquid and ice water abundance and the high precipitation rates removing also initially small, hydrophobic particles in these clouds compared to large-scale clouds. In contrast, the effect of coating is rather small. The annual mean metrics hardly change due to coating and the annual mean lifetime is only slightly modi-

fied, with a modest increase for most tracers (maximum one day) but also a decrease for tracers from some source regions.

Taken together, several assumptions, which were made to conduct the tracer experiments, were tested and their influence was quantified. In Section 4.5, the transport was already re-examined regarding the emission altitude, which mainly revealed that the long-range transport is more efficient the higher the emission is introduced in the model. In this chapter, on the one hand the generic representation of aerosols was explored in more detail, which showed no major influence on the results. On the other hand the results were discussed for different horizontal model resolutions, which revealed that the vertical transport of soluble species is stronger for larger grid cell sizes.

7

Megacity aerosol emission impact on the global aerosol budget

Until now the emissions from major population centers (MPCs) have been investigated more in light of potential outflow and how aerosol properties may influence the dispersion from strong localized sources. Since passive tracers were used, no chemical or microphysical interactions between the outflow plume and constituents in the background atmosphere were considered; the experiments were designed such that mainly meteorological conditions determined the distribution of the tracers in the atmosphere. However, it is known that physico-chemical interactions can have a substantial influence on the evolution of aerosols, especially in polluted regions and thus the question arises how strong these interactions may be. Chemical reactions and microphysical processes can be highly non-linear and depend on many trace species and therefore are difficult to assess. To fully capture all MPC emissions on the global scale, a large set of additional tracers would be required (even more than the passive tracers used in Chapter 6) to track all relevant species. Another possibility arises when the question is posed slightly different which requires no additional tracers and follows the approach of Butler and Lawrence (2009) and Butler et al. (2012). They assessed the impact of megacity trace gas emissions on gas phase atmospheric chemistry by modifying the MPC emissions. Following this approach I will assess the impact of megacities on the global aerosol budget by changing the emissions from MPCs to answer the following question in this chapter:

1. To what extent do anthropogenically released pollutants from megacities influence the global aerosol budget?
2. How do the changes in various species lead to modified concentrations in other species, and are these changes significant?
3. Do changes in emissions lead to a proportional change in concentrations?

To answer these questions the emissions of primary anthropogenic aerosols, black carbon (BC) and particulate organic matter (POM), as well as the emissions of secondary aerosol precursors of sulfate (SO_4^{2-}) and nitrate (NO_3^-) are changed individually and all at once. The four species were chosen since they represent the major anthropogenic emissions for both, primary and secondary aerosol species. Not considered in this study are for example secondary organic aerosols which can also be formed from anthropogenic emissions.

The section is structured as follows: the model specifications are introduced along with the emission scenarios. Then the results of four simulations are presented, in which only the emission of one species is reduced. In this context I will show the effects on the atmospheric burden of the species itself and also the consequent effects on other species. Finally, the emissions of all four species are changed at once to assess whether and to which extent there are non-linearities in the system before the chapter is finished with a summary.

7.1 Model description and simulation setup

7.1.1 Model setup

For this study, I use model version **B** with the comprehensive chemical mechanism of atmospheric chemistry (`MECCA`) and the extended aerosol scheme (`GMXe`). More details about the submodels in version **B** and in particular on `MECCA` and `GMXe` are found in Section 2.2. No passive tracers are employed in this analysis. To proper simulate aerosols and trace gases boundary conditions are required, especially at the lower boundary as emissions. Either emissions are solely surface emissions or, as done for some species, distributed within the first hundred meters of the atmosphere. Since the focus was not to test which emission inventory is best to simulate megacity emissions, the standard emission inventories in EMAC were chosen to obtain a first idea on how megacities' emissions may alter the aerosol budget. Model version **B** is based on MESSy version 1.10 and thus I use the chemical setup from the evaluation simulation (Jöckel et al., 2006) for the first MESSy development cycle and the emissions from the evaluation of the `GMXe` submodel (Pringle et al., 2010a), which are briefly summarized in the following paragraphs:

Aerosol bulk emissions

Bulk emissions for black carbon, organic carbon, dust, and sea salt were taken from the AEROCOM initiative (Dentener et al., 2006; Textor et al., 2006, and the AEROCOM web page[1]) as discussed in Pringle et al. (2010b,a). Black and organic carbon emissions were completely introduced into the hydrophobic Aitken mode (KI) and it is distinguished between anthropogenic and natural, i.e., biomass burning, emissions. In the model organic carbon (OC) was treated as particulate organic matter (POM). For this the OC emissions were multiplied by 1.4 to account for chemical species in the organic matter, i.e., oxygen, hydrogen, and nitrogen, additional to carbon (Seinfeld and Pandis, 1998). Natural emissions of dust (DU) were also considered as hydrophobic but with much larger diameters at the time of emission so that the main emission is introduced into coarse mode (95 % in CI) and a minor part of the total emission is added to the hydrophobic accumulation mode (AI). Furthermore, the emissions for sea salt were introduced in the hydrophilic accumulation (AS) and coarse (CS) mode and are distributed between sodium (Na^+), chloride (Cl^-), and a bulk sea salt (SS), which comprises all other species present in sea spray, according to the ratios of their molar masses. All aerosol emissions were prescribed as surface boundary conditions and added to the tracer tendency in the lowest model layer.

---

[1] http://aerocom.met.no, as of 20.10.2012

Gas phase emissions

Anthropogenic trace gas emissions were taken from the EDGAR3.2FT 2000 ("fast track") database (van Aardenne et al., 2005, and the EDGAR web page[2]). SO_2 and NO_x[3] emissions were distributed as multi-layer emissions onto six levels (45, 140, 240, 400, 600, 800 m) provided as off-line emissions. Other off-line emissions included those for CO, C_2H_4, C_2H_6, C_3H_6, C_3H_8, C_4H_{10}, CH_3CHO, CH_3COCH_3, CH_3COOH, CH_3OH, HCHO, HCOOH, methyl ethyl ketone (MEK), and NH_3, and on-line calculated emissions for dimethyl sulfide (DMS) and NO from soils. The biogenic emissions of organic species were compiled following Guenther et al. (1995) and were prescribed off-line with the unique exception of isoprene, for which the emission was calculated on-line (Pozzer et al., 2007; Kerkweg et al., 2006b). Aircraft NO emissions were taken from Schmitt and Brunner (1997), SO_2 ship emissions from AEROCOM, and additional lower boundary conditions (treated in the submodel `TNUDGE`) were provided for N_2O, CH_4, $CFCl_3$, CF_2Cl_2, CH_3CCl_3, CCl_4, CH_3Cl, CH_3Br, CF_2ClBr, CF_3Br, H_2, CO_2, and SF_6 as time-dependent mixing ratios using the AGAGE database (Prinn et al., 2000). More information on the chemical mechanism is provided in Jöckel et al. (2006) and Pozzer et al. (2007).

7.1.2 Simulation setup

In total eight simulations have been conducted (see Table 7.1), all initialized in July 2004 and ending at the beginning of January 2006, with the first six months as model spin-up and the last twelve months for model analysis. As a result of the more comprehensive model setup the horizontal model resolution was chosen to be T42 (approximately 2.8° × 2.8° in latitude and longitude, see Table 2.1) with 31 hybrid sigma-pressure levels in the vertical from the surface up to 10 hPa. The model time step is 1200 seconds and output has been archived for every five hours to capture a full daily cycle within five days of model integration. The

Table 7.1: Overview of MPC emission study simulations to assess the impact of changes in the emission fluxes of anthropogenic black carbon (BC), particulate organic matter (POM), sulfur dioxide (SO_2), and nitrogen oxides (NO_x).

Simulation	Description
REF	Reference simulation, no changes in emissions
EMS1	−100 % reduction of anthropogenic MPC BC emissions
EMS2	−100 % reduction of anthropogenic MPC OC (POM) emissions
EMS3	−100 % reduction of anthropogenic MPC SO_2 emissions
EMS4	−100 % reduction of anthropogenic MPC NO_x emissions
EMSM100	−100 % reduction of anthropogenic MPC BC, POM, SO_2, and NO_x emissions
EMSM20	−20 % reduction of anthropogenic MPC BC, POM, SO_2, and NO_x emissions
EMSP20	+20 % increase of anthropogenic MPC BC, POM, SO_2, and NO_x emissions

---

[2] http://themasites.pbl.nl/tridion/en/themasites/edgar/emission_data/edgar_32ft2000/index-2.html, as of 20.10.2012

[3] In the model the NO_x, i.e., NO and NO_2, emissions were solely added to NO. However, since NO is rapidly converted to NO_2, it is always referred to NO_x emissions in the text.

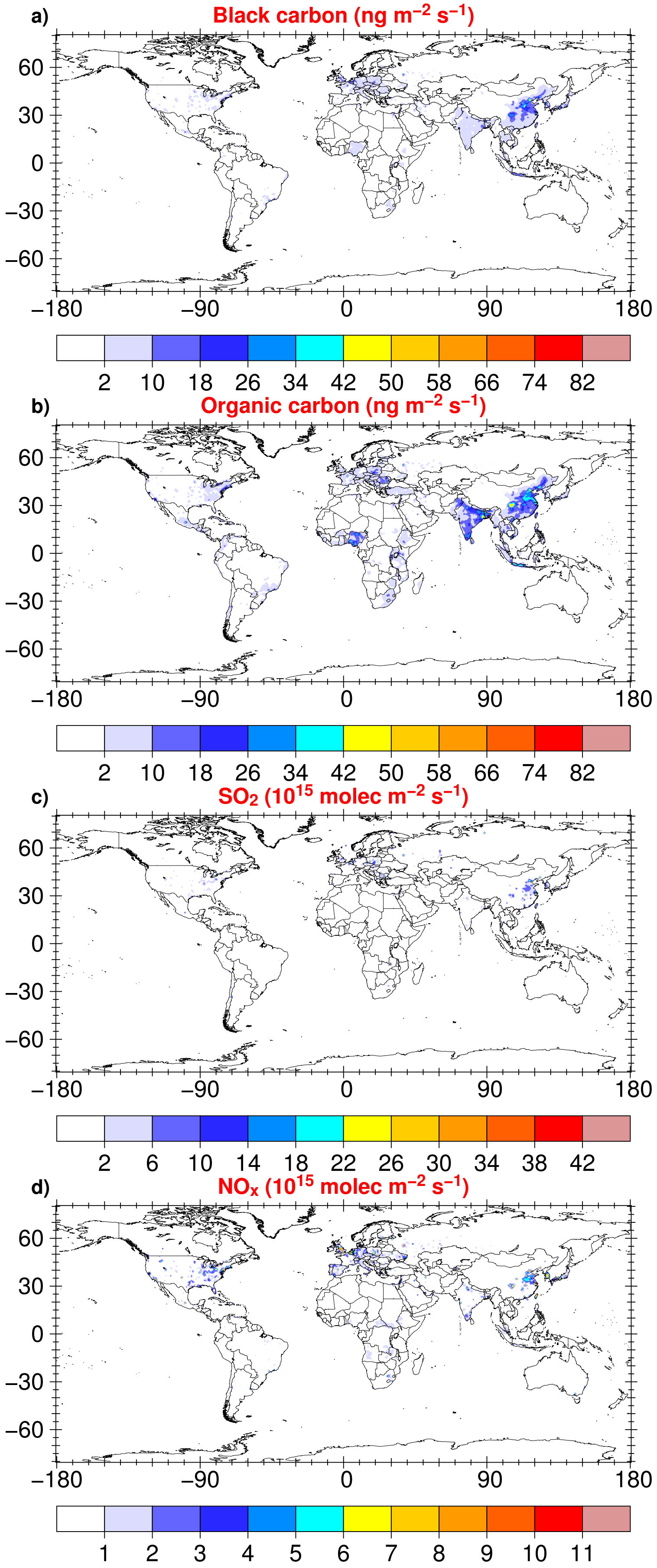

Figure 7.1: Annual mean anthropogenic emissions of a) BC, b) OC, c) SO_2, and d) NO_x on the original grid (1° × 1°). BC and OC are originally provided from AEROCOM, SO_2 and NO_x from the EDGAR database.

meteorology was weakly nudged with data from ECMWF (see Section 2.3). To only account for feedbacks of changed emissions on tracer concentrations with no interference by different meteorological fields, no feedbacks from chemical constituents on meteorological variables have been allowed. Thus, the meteorology is the same in all simulations and except for the differences introduced by the different horizontal resolutions the same meteorology is computed as for the passive tracer studies in Chapters 4 and 5.

In the reference simulation (REF), all emissions are used as described above. The annual means of the original emissions of anthropogenic BC, OC, SO_2, and NO_x are shown in Figure 7.1 on a 1° × 1° grid. Fossil and biomass fuel black carbon emissions peak in eastern Asia and India on a larger area, while additionally small singular emission hot spots are situated at the locations of urban centers around the world. Organic carbon has a similar spatial appearance to BC but the emission fluxes are generally larger. The original BC and OC AEROCOM emissions are provided as annually constant fields. However, to account for domestic heating the emission fields are altered on the Northern Hemisphere in `ONLEM`, which leads to slightly larger emissions during boreal winter than in boreal summer. In the case of SO_2 and NO_x an annual cycle is already included in the original emissions from the EDGAR database. The SO_2 and NO_x emissions have been summed over the six emission layers. Emission patterns are similar for both precursor gases, with peaks in the eastern US, western Europe, and East China. Furthermore, singular points in other regions around the world often mark the location of MPCs or large industrial sites.

For the sensitivity studies the emissions were altered on the original 1° × 1° grid at the location of the MPCs, based on the longitude and latitude information, which is provided

Table 7.2: Anthropogenic (ANTH) and total (TOTAL) emissions of BC, POM, SO_2, NO_x in Tg/yr and changes relative to the ANTH ($\%_{\mathrm{ANTH}}$) and the total ($\%_{\mathrm{TOTAL}}$) emissions in % due to reduced and increased emissions at the MPC locations in %. Emission reductions are either by 20 % or 100 %, the increase by 20 %.

Emissions		BC	POM	SO_2	NO_x[a]
Standard	ANTH	4.66	12.26	151.20	42.85
	TOTAL	7.74[b]	65.98[c]	195.65[d]	51.71[e]
−100 %	ANTH	4.36	11.73	138.93	40.00
	$\%_{\mathrm{ANTH}}$	−6.4	−4.3	−8.1	−6.6
	$\%_{\mathrm{TOTAL}}$	−4.3	−0.8	−6.3	−5.5
−20 %	ANTH	4.60	12.16	148.75	42.28
	$\%_{\mathrm{ANTH}}$	−1.3	−0.8	−1.6	−1.3
	$\%_{\mathrm{TOTAL}}$	−0.8	−0.2	−1.3	−1.1
+20 %	ANTH	4.72	12.36	153.65	43.55
	$\%_{\mathrm{ANTH}}$	+1.3	+0.8	+1.6	+1.3
	$\%_{\mathrm{TOTAL}}$	+0.8	+0.2	+1.31	+1.1

[a] Absolute numbers of the NO_x emissions are given in Tg N/yr.

[b] Total BC emissions comprise anthropogenic, biomass burning, and agricultural waste burning emissions.

[c] Total POM emissions include anthropogenic, biomass burning, agricultural waste burning as well as biogenic emissions.

[d] Total SO_2 emissions include anthropogenic, ship, and volcanic emissions.

[e] Total NO_x emissions comprise anthropogenic, soil, aircraft, and lighting emissions.

in Table 4.1. In some cases the largest emissions fluxes were located in a grid cell next to the given location or had a greater spatial extension than one grid cell, because the area of the real emission is divided by the overlying 1° × 1° grid. For these MPCs, namely Rome, Athens, Istanbul, Mumbai, Szechuan Basin, New York, and Bogotá, it was assumed that the neighboring grid cells are also attributed to the corresponding MPC and were consequently also considered in the emission reduction. In the Rhine-Ruhr and the Po Valley only the grid cells with the strongest emission points have been changed.

The annual anthropogenic and total, i.e., natural and anthropogenic, emission flux of the reference simulation is listed in Table 7.2 (first two lines) along with the annual anthropogenic emission fluxes from the sensitivity simulations. Additionally, the relative changes are presented in relation to the anthropogenic and total emissions of the reference simulation. SO_2 is by far the largest anthropogenic source with 151.2 Tg/yr, followed by NO_x with 42.85 Tg N/yr. Anthropogenic emissions of black carbon are much smaller with 4.66 Tg/yr and those for primary organic matter sum up to be 12.26 Tg/yr. Reducing now the emissions by 100 % in the megacities decreases the total anthropogenic emissions by 6.4 %, 4.3 %, 8.1 %, and 6.6 % for BC, POM, SO_2, and NO_x, respectively and the total emissions by 4.3 %, 0.8 %, 6.3 %, and 5.5 %. Changing the MPC emissions only by 20 % leads to changes which are one fifth of the changes for a 100 % change.

7.2 Reduction of anthropogenic emissions

Reduced emissions of a species, independent of phase, lead to a reduced atmospheric burden, less dry and wet deposited mass, and often a changed atmospheric residence time. The emissions are only changed in their anthropogenic fraction but with consequences for the total (anthropogenic plus natural) burden of a species, since species are not treated individually in the model because of their emission source. Moreover, changing one species may influence other species which are connected in atmospheric cycles (e.g., sulfur cycle, carbon cycle, nitrogen cycle) by changing gas phase equilibria or gas-particle partitioning. Since the concentration of a species contributes to the calculation of the aerosol optical depth (AOD), which is an integral measure of the extinction of solar radiation by aerosol scattering and absorption, a change in emission also affects this variable. For some species the AOD changes are also discussed. However, it is noted here that the AOD is too high over the industrial centers on the Northern Hemisphere (the eastern US, Europe, and East China) by about a factor of two compared to measurements from the MODIS instrument on-board of the NASA A-TRAIN satellites Terra and Aqua (not shown). The emission fluxes of anthropogenic SO_2 and NO_x are larger in the EDGAR database compared to, for example, the IPCC-AR5 emission inventory (Lamarque et al., 2010).

7.2.1 Primary aerosol emission: black carbon (BC)

For the first sensitivity simulation, EMS1, only the black carbon emissions in the MPCs are reduced by 100 %. The main source of black carbon in cities is the incomplete combustion from fossil and bio fuels. The emission reductions in the MPCs lead to a decrease of 4.3 % in the total and of 6.4 % in the anthropogenic BC emissions (see Table 7.2). The atmospheric

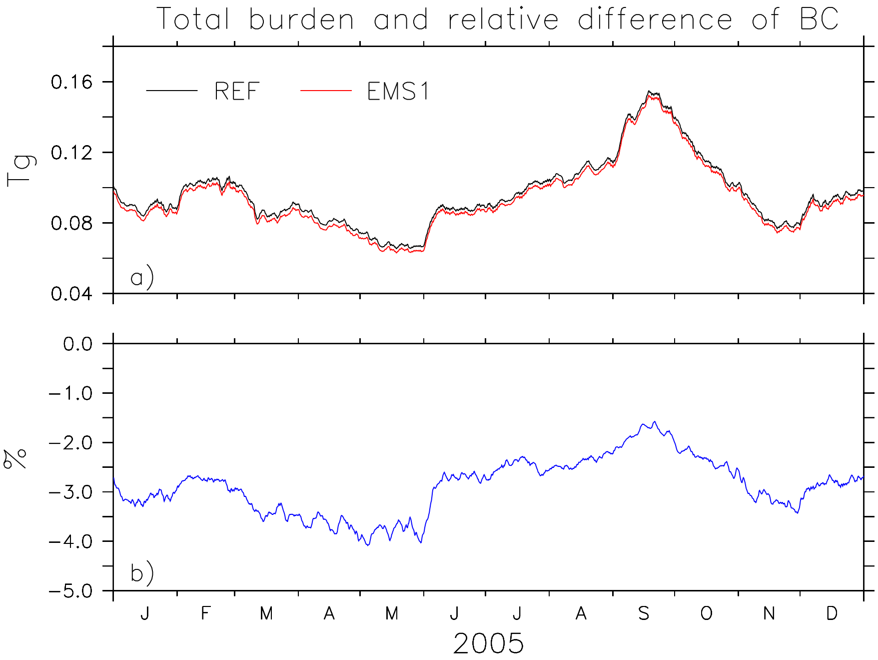

Figure 7.2: Time series of a) total burden (in Tg) and b) relative difference (in %) for black carbon. The burden of the reference simulation is indicated by the black line, for the emission reduction scenario (EMS1) by the red line. The blue line in the lower panel shows the relative difference between the two scenarios $(\frac{\mathrm{EMS1-REF}}{\mathrm{REF}})$.

BC burdens in REF and EMS1 show the same time evolution over the analysis year, with a mean reduction in total burden of 2.8 % in EMS1 compared to REF (Figure 7.2b). The minimum burden in BC is simulated at the end of May when also the maximum reduction is apparent. Conversely, the maximum in atmospheric burden coincides with the minimum in the relative change in September. Remember that the anthropogenic BC emissions are almost constant in time but that the natural emissions undergo an annual cycle which in large parts determines the annual cycle of the BC burden. The natural emissions are lowest at the end of May and largest in September. Thus, the anthropogenic contribution to the total burden is larger in May and lower in September, which causes the variation in the relative change.

Both natural, especially in equatorial regions, and anthropogenic, especially in industrial regions on the Northern Hemisphere, e.g., China, emissions lead to peak values in the surface and tropospheric column densities (Figure 7.3). The relative changes are large in the close vicinity of the MPCs. However, depending on the background concentration, the area where a change shows statistical significance is larger when background values are smaller and vice versa. Furthermore, in the surface layer relative changes on the order of 50 % appear in the outflow regions of several regions, while these changes still lead to changes larger than 10 % in the tropospheric column density in the same regions. Although the outflow regions often reveal low absolute concentrations, the changes are substantial since they show statistical significance which is obtained from a Student's t-test on a 90 % significance level (description of the test is given in Appendix A and in Schönwiese, 2000). Thus, the BC emissions from MPCs have a substantial impact on regions around the MPCs and on regions downwind.

Black carbon concentrations rapidly decrease with altitude, with the main mass being lo-

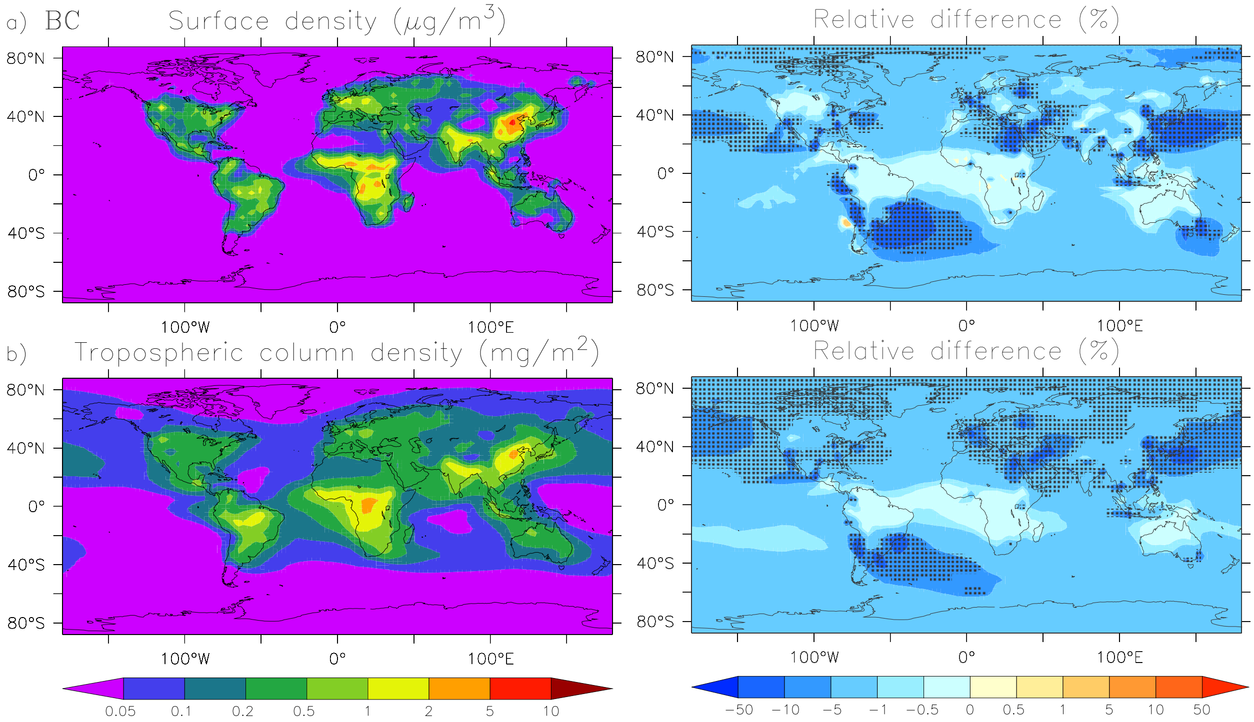

Figure 7.3: a) Surface (in μg m^{-3}) and b) tropospheric column (in mg m^{-2}) density of black carbon for REF and the corresponding relative difference ($\frac{\text{EMS1}-\text{REF}}{\text{REF}}$, in %) to black carbon in EMS1 (right panels). Black dots mark regions with statistical significance on a 90 % confidence level.

cated below 2.5 km. However, differences between the zonal means reveal that in particular north of 10° N concentrations show statistically significant changes in the entire troposphere (not shown). Thus, the changes in the MPC emissions affect not only the source regions themselves but have impacts which are much more far reaching in the horizontal and vertical. In contrast, in regions with large natural emissions such as the tropics no significant changes are assessed and south of the equator mainly the outflow region of Rio de Janeiro and São Paulo shows non-negligible differences, which, however, are confined to the first 2 km in the atmosphere.

Finally, the total AOD hardly differs between REF and EMS1. The initially small and hydrophobic BC particles contribute relatively little to the total AOD, especially in contrast to other aerosol species such as dessert dust or aerosol water. The only noticeable difference occurs in East Asia, with a maximum relative change of 3 % (not shown) but no statistical significance. The AOD is also assessed for each contributing species individually. When comparing only the AOD due to BC, significant differences occur in the regions of the MPCs or in regions downwind. However, since the contribution of BC to the total AOD is too small, these changes have no substantial influence on the total AOD.

7.2.2 Primary aerosol emission: primary organic matter (POM)

Anthropogenic primary organic matter (POM) originates from combustion, car exhaust, or residential housing. The total removal of anthropogenic POM emissions in the MPCs (scenario EMS2) leads to an annual mean decrease in the total organic burden of about 0.7 % (Figure 7.4b) which is lower compared to the relative mass reduction of BC but on

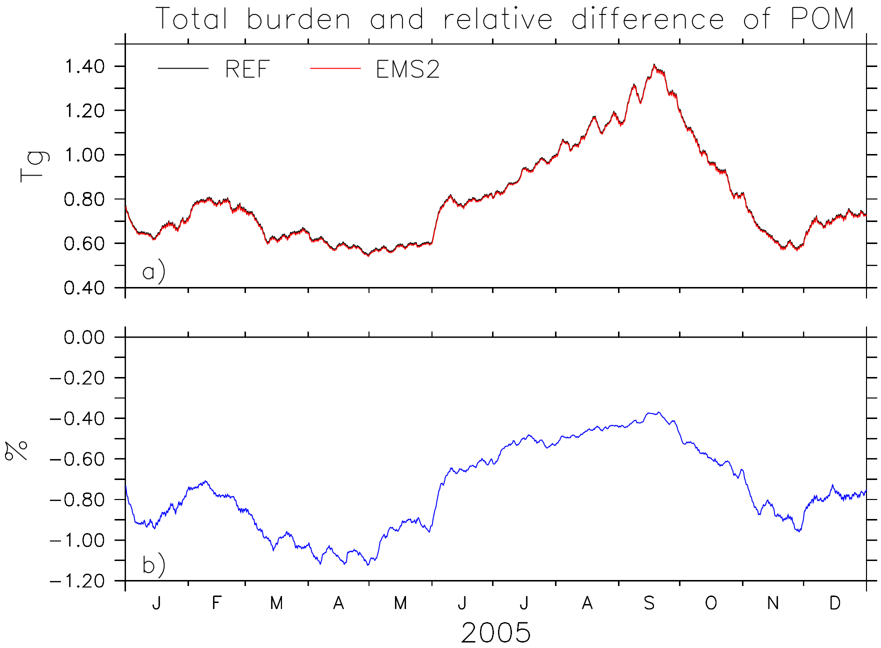

Figure 7.4: Time series of a) total atmospheric burden (in Tg) and b) relative difference (in %) for particulate organic matter. The burden of the reference simulation is indicated by the black line, for the emission reduction scenario (EMS2) by the red line. The blue line in the lower panel shows the relative difference between the two scenarios $\left(\frac{\text{EMS2}-\text{REF}}{\text{REF}}\right)$.

the order of the total POM emission reduction (see Table 7.2). The temporal evolution of the POM burdens in REF and EMS2 shows no substantial difference and the evolution is mainly determined by the natural emissions which, like for BC before, cause the different

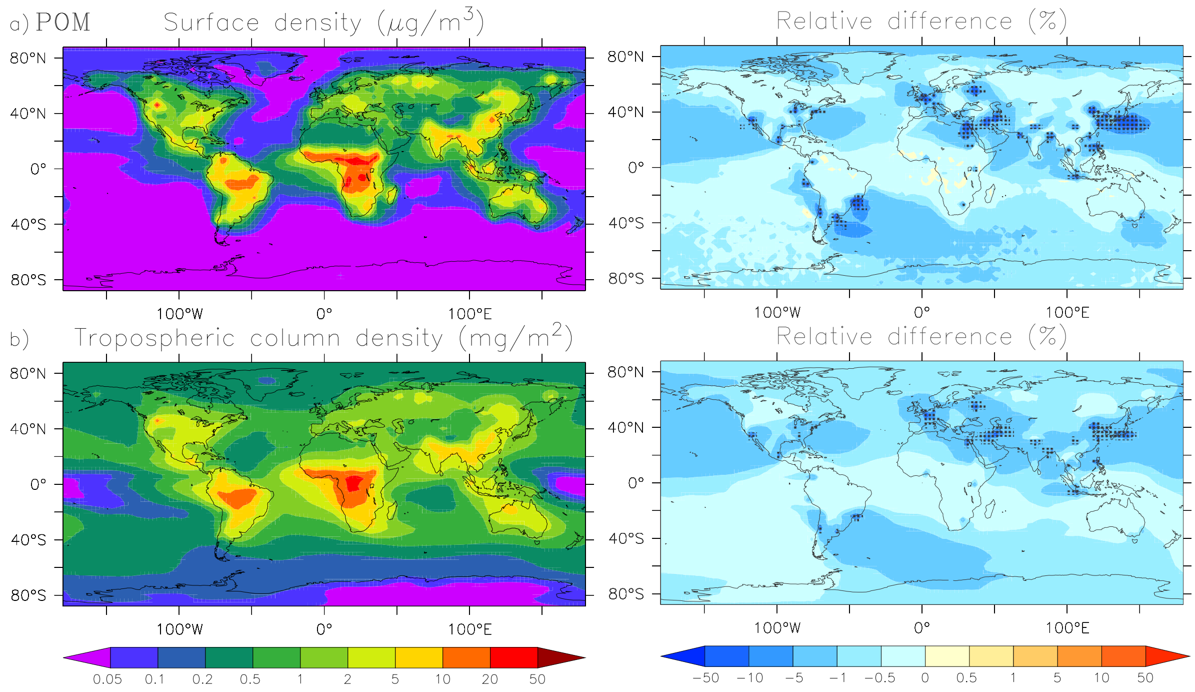

Figure 7.5: a) Surface (in $\mu g\,m^{-3}$) and b) tropospheric column (in $mg\,m^{-2}$) density of particulate organic matter for REF and the corresponding relative differences ($\frac{\text{EMS2}-\text{REF}}{\text{REF}}$, in %) to particulate organic matter in EMS2 (right panels). Black dots mark regions with statistical significance on a 90 % confidence level.

contribution of the –almost constant– anthropogenic emissions to the total burden. Moreover, natural emissions dominate the spatial distribution of POM. In general, relative changes in surface and tropospheric column densities are small and hardly exceed 10 % (Figure 7.5). Changes are only statistically significant for some MPCs; most of them are located farther away from the main natural POM emission sources. The only region which shows an impact on a larger scale is the one in the outflow from MPCs in East Asia because of the cumulative impact of several cities, namely Beijing, Tianjin, Seoul, Osaka, and Tokyo. Moreover, significant differences in the zonal mean are confined to the lowest levels between 30° N and 40° N (not shown). The effects on the AOD have a similar order of magnitude as those from BC because of the same reasons and thus are negligibly small.

7.2.3 Aerosol precursor gas emission: sulfur dioxide (SO_2) and particulate sulfate (SO_4^{2-})

In contrast to the primary emissions of BC and POM, most sulfate SO_4^{2-} originates from gaseous SO_2 or other gaseous sulfur containing constituents. In the model, only a small fraction (2.5 %) of the sulfur dioxide emission directly enters the particulate phase, while SO_4^{2-} mainly results from the oxidation of sulfur containing gases to gaseous sulfuric acid in the aqueous or gaseous phase (e.g., Seinfeld and Pandis, 1998; Tost et al., 2007b). Moreover, anthropogenically emitted SO_2 forms the major source of the particulate sulfate (see also Table 7.2). Thus, the reduction in megacity SO_2 emissions causes a relatively stronger reduction in the anthropogenic (−8.1 %) and total (−6.3 %) emissions compared to BC or POM. The global atmospheric burden of SO_2 decrease about 7.0 % on average, while the global burden of aerosol sulfate shows a reduction of about 4.5 %. This decrease is larger than the decrease in the burdens of the primary aerosols BC and POM (see Figure 7.6).

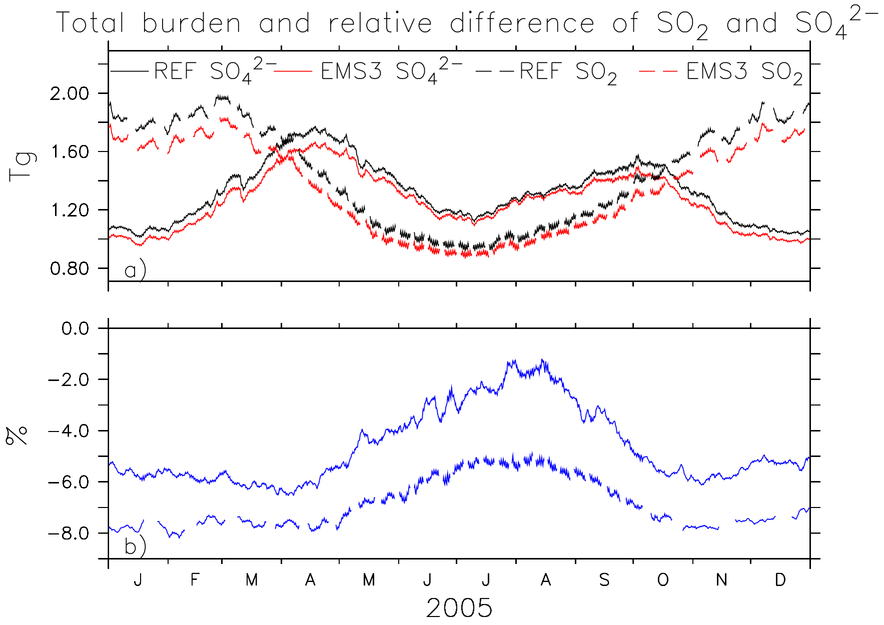

Figure 7.6: Time series of a) total burdens (in Tg) and b) relative differences (in %) for sulfate (solid lines) and sulfur dioxide (dashed lines). Burdens of the reference simulation are indicated by the black line, for the emission reduction scenario (EMS3) by the red lines. The blue lines in the lower panel show the relative difference between the two scenarios ($\frac{\text{EMS3}-\text{REF}}{\text{REF}}$).

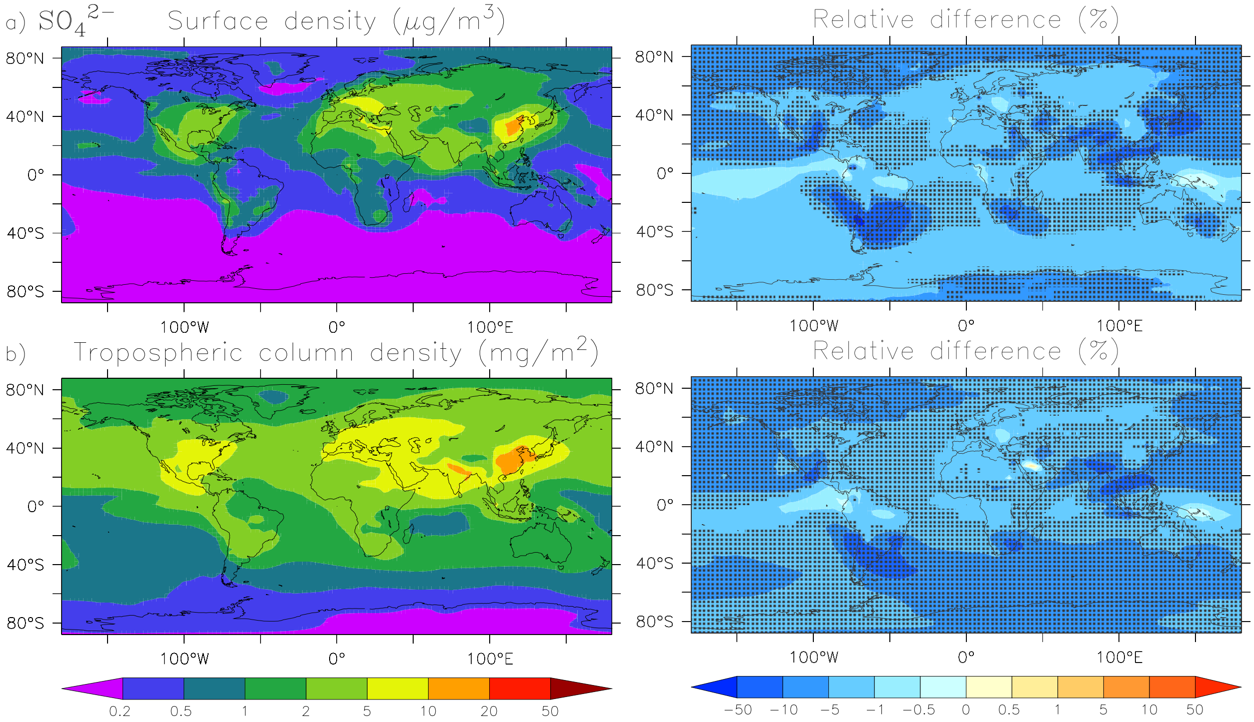

Figure 7.7: a) Surface (in µg m^{-3}) and b) tropospheric (in mg m^{-2}) density of sulfate for REF and the corresponding relative differences $\left(\frac{\mathrm{EMS3-REF}}{\mathrm{REF}}, \text{ in } \%\right)$ to sulfate in EMS3 (right panels). Black dots mark regions with statistical significance on a 90 % confidence level.

Furthermore, the relative change of both species follows an annual cycle, which relies on anthropogenic and not natural emissions. For SO_2 the maximum in atmospheric burden coincides with the maximum in relative change, which is another indicator that the MPC emissions significantly contribute to the gaseous sulfur dioxide burden. For aerosol sulfate the situation is bit more complicated, especially in boreal winter since the oxidation of SO_2 to sulfuric acid depends on other species, e.g., OH or H_2O_2, and environmental conditions influencing, e.g., the photolysis rates. Conversely, the minimum in SO_4^{2-} burden coincides with the minimum relative change in boreal summer. This emphasizes that the MPC emissions have a stronger influence on atmospheric sulfate than on black carbon or particulate organic matter.

This is further reflected in the significant reduction of the aerosol sulfate in the surface layer and in the troposphere (Figure 7.7). The reduction in aerosol sulfate is not only confined to the source and downwind regions. Even source-remote regions show a decrease of more than 10 %, which is also statistically significant. In particular, the changes in the tropospheric column density are significant almost everywhere, except for some equatorial regions (Pacific, South America, and Africa) and for some industrialized regions on the Northern Hemisphere where other anthropogenic sources outside of the MPCs contribute substantially to the sulfate burden, i.e., the region between the Great Lakes and the northeastern US coast as well as eastern Europe).

Sulfate is part of the water soluble compounds (WASO). WASO compounds contribute more to the total AOD than BC or POM but their overall contribution is still small. However, the change in total AOD is disproportionately large since the concentration of WASO com-

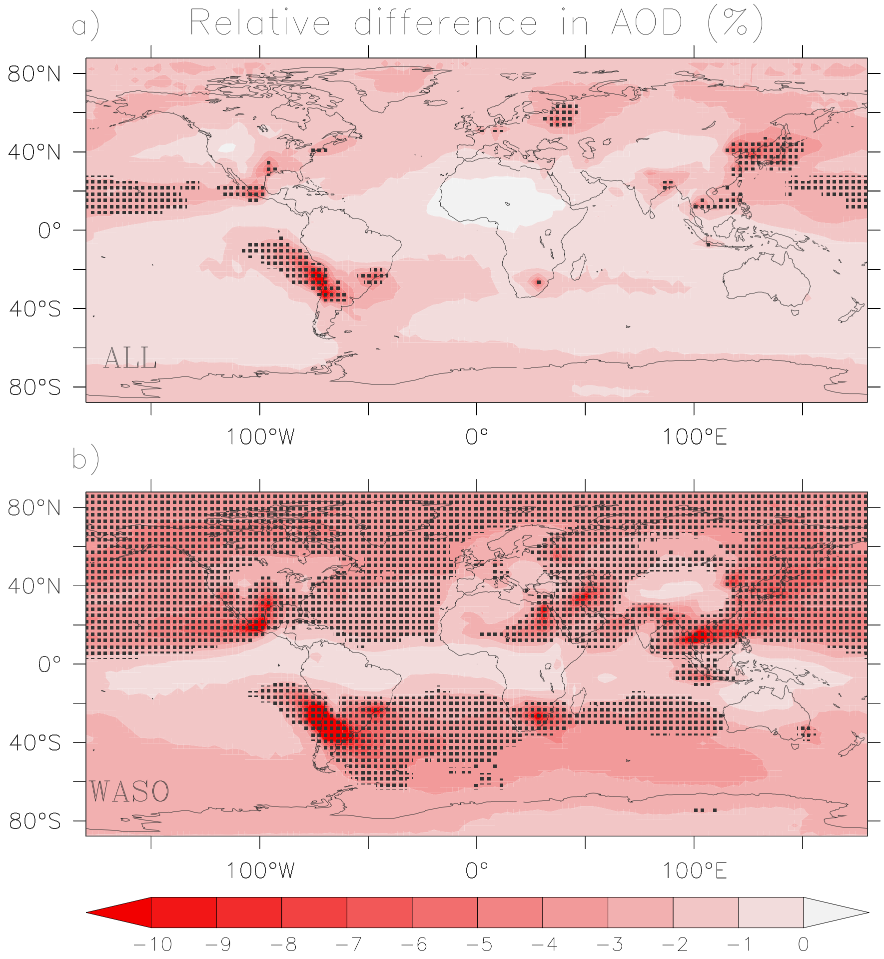

Figure 7.8: Relative difference (in %) in annual mean aerosol optical depth between a) the total and b) the water soluble fraction of the AOD $\left(\frac{\text{EMS3}-\text{REF}}{\text{REF}}\right)$. Black dots mark regions with statistical significance on a 90 % level.

pounds in the aerosol is strongly coupled to the amount of water that is in the aerosol. Aerosol water in turn is one of the major contributors to total AOD. Thus, a reduction in WASO compounds, here sulfate, leads also to less incorporation of aerosol water and to a stronger impact on the total AOD. Consequently, the total AOD shows areas with signifi-

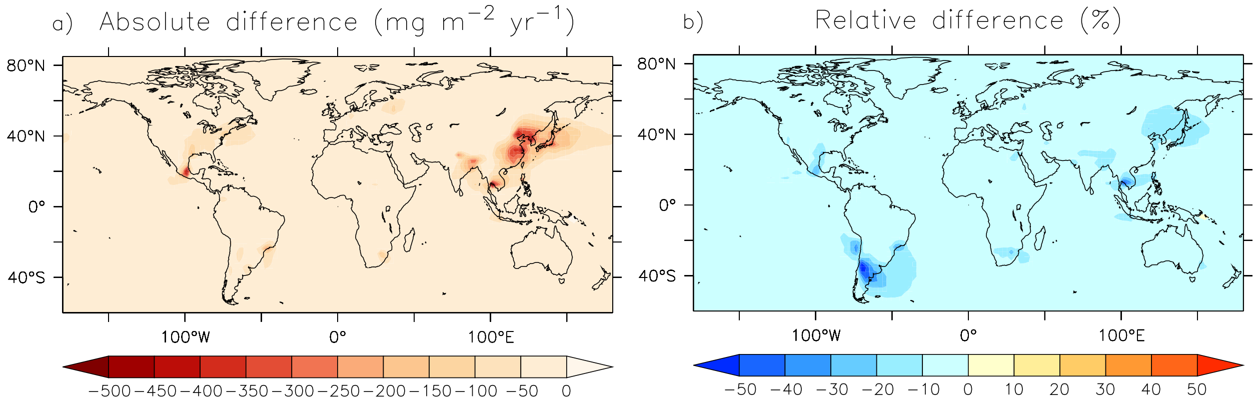

Figure 7.9: a) Absolute $\left(\text{in mg m}^{-2}\,\text{yr}^{-1},\ \text{EMS3}-\text{REF}\right)$ and b) relative $\left(\text{in \%},\ \frac{\text{EMS3}-\text{REF}}{\text{REF}}\right)$ difference in annually accumulated wet deposition of sulfate.

cant reductions, e.g., about 10 % on the western coast of South America (see upper panel in Figure 7.8). The emission of Santiago as well as those in Mexico City and Moscow dominate the SO_2 emissions in their regions and thus have relatively stronger impacts on the regional sulfate burden. Furthermore, other AOD contributing species have low emissions in these regions. The AOD due to WASO compounds changes in large parts of the Northern and Southern Hemisphere (lower panel in Figure 7.8). However, in regions which are not mainly influenced by the MPC-emissions, no significant change is assessed for the WASO-AOD.

Furthermore, the deposition of sulfate aerosols is of interest due to their acidic nature. The absolute difference in annually accumulated wet deposition flux is largest in regions which have also the large deposition fluxes, i.e., over China (Figure 7.9). However, in these regions the relative changes are not strongest since MPCs in these regions represent only one of many sources. In contrast, the largest relative change occurs in the downwind region of Santiago which is an important source of SO_2 on the South American continent.

7.2.4 Aerosol precursor gas emission: nitrogen oxides (NO_x) and particulate nitrate (NO_3^-)

Aerosol nitrate is formed solely from gas phase species. NO_2 is first converted to nitric acid (HNO_3) either by reaction with the hydroxyl radical (OH) or by reaction with ozone and dinitrogen pentoxide (N_2O_5). Nitric acid is in equilibrium with aerosol nitrate, which is formed when neutralizing cations, e.g., NH_4^+, Na^+, are already present in the particulate phase. The formation further depends on the mass of water in the aerosol phase. Nitrate is commonly present in the coarse mode particles since more total aerosol water is present in the coarse than in the accumulation mode particles. Moreover, nitrate can also displace chloride in sea spray (sea-spray acidification, Jacobson, 2002), which occurs mainly in the coarse mode. Nitric acid can dissolve in accumulation mode particles under certain conditions. The ambient sulfuric acid has to be dissolved in the aerosol phase, which is usually the case when particles are present due to its low water vapor. Moreover, the sulfuric acid should not have neutralized all cations in the aerosol phase. Their presence facilitates the phase transition of nitric acid into nitrate (Jacobson, 2002; Seinfeld and Pandis, 1998).

In contrast to SO_2, the reduction of MPC NO_x emissions have only a small influence on the gaseous NO_x burden, with reductions smaller than one per cent, and a larger influence on the aerosol nitrate, with a mean reduction of the global burden of 3.6 % (see Figure 7.10) which is most probably an effect of the short lifetime of NO_x. The annual cycle of aerosol nitrate indicates lower values during summer because of the temperature dependence of the nitrate formation, with nitric acid following an opposing annual cycle (not shown). Furthermore, the minimum in burden coincides with the minimum relative change due to the reduced MPC emissions. Thus, similar to the MPC SO_2 emissions for aerosol sulfate, the MPC NO_x emissions significantly contribute to the total aerosol nitrate.

The maximum relative changes of aerosol nitrate occur in regions with maximum surface and tropospheric column densities, e.g., China. However, the statistically significant changes (see Figure 7.11) are not limited to these regions since differences in the NO_3^- at high latitudes are also significant. In the Arctic, the remnants of the long-range transport from the emission source regions accumulate. Especially, the MPCs in East Asia contribute substantially to the changes in the Arctic and also to the change in the outflow further south over the Pacific Ocean towards North America.

The changes in total AOD are smaller than for sulfate, with a maximum decrease of about 5 %. However, the spatial distribution of the changes is similar to what was found for sulfate. Nitrate aerosol is part of the water soluble compounds but contributes less due to its lower burden compared to sulfate (not shown) and has thus a smaller impact on the WASO and total AOD.

Similar to aerosol sulfate, the aerosol nitrate can affect the soil pH when being deposited (e.g., Seinfeld and Pandis, 1998). The spatial distribution and the magnitude of the nitrate wet deposition field shows similiarties to the sulfate wet deposition field; even the main absolute reduction occurs over eastern Asia. Contrary to sulfate, this is also the region where the largest relative change is assessed (Figure 7.12) which means that the MPC NO_x emissions in eastern Asia contribute significantly to the nitrate which is wet deposited in this region. The same is simulated for cities in North America (New York, Houston, and Mexico City). However, in Europe the MPC emissions are small compared to other sources and thus the effect on the nitrate deposition is negligible.

7.2.5 Feedback of anthropogenic aerosol and aerosol precursor emission changes on black carbon, particulate organic matter, sulfate, and nitrate

Changing the emission of a species or its precursor will not only affect the species itself but also impacts the concentrations of other atmospheric constituents. First the discussion focus on how the emission change of one of the four aerosol species affects the atmospheric burdens of the other species considered so far. In the next section the focus is then on the major implications for other atmospheric trace gases and aerosols.

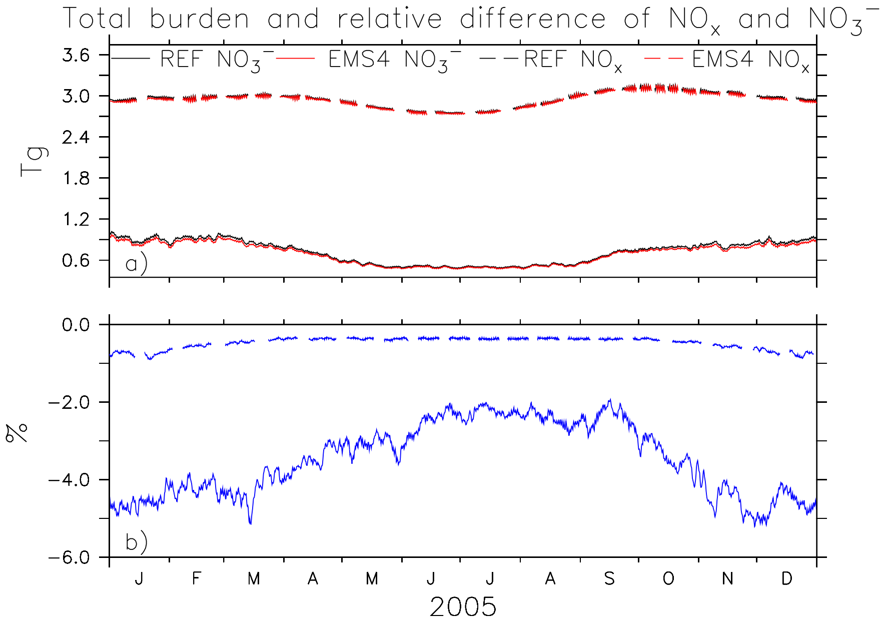

Figure 7.10: Time series of a) total burdens (in Tg) and b) relative differences (in %) for nitrate and nitrogen oxides. The burden of the reference simulation is indicated by the black line, for the emission reduction scenario (EMS4) by the red line. The blue lines in the lower panel show the relative differences between the two scenarios ($\frac{\text{EMS4}-\text{REF}}{\text{REF}}$).

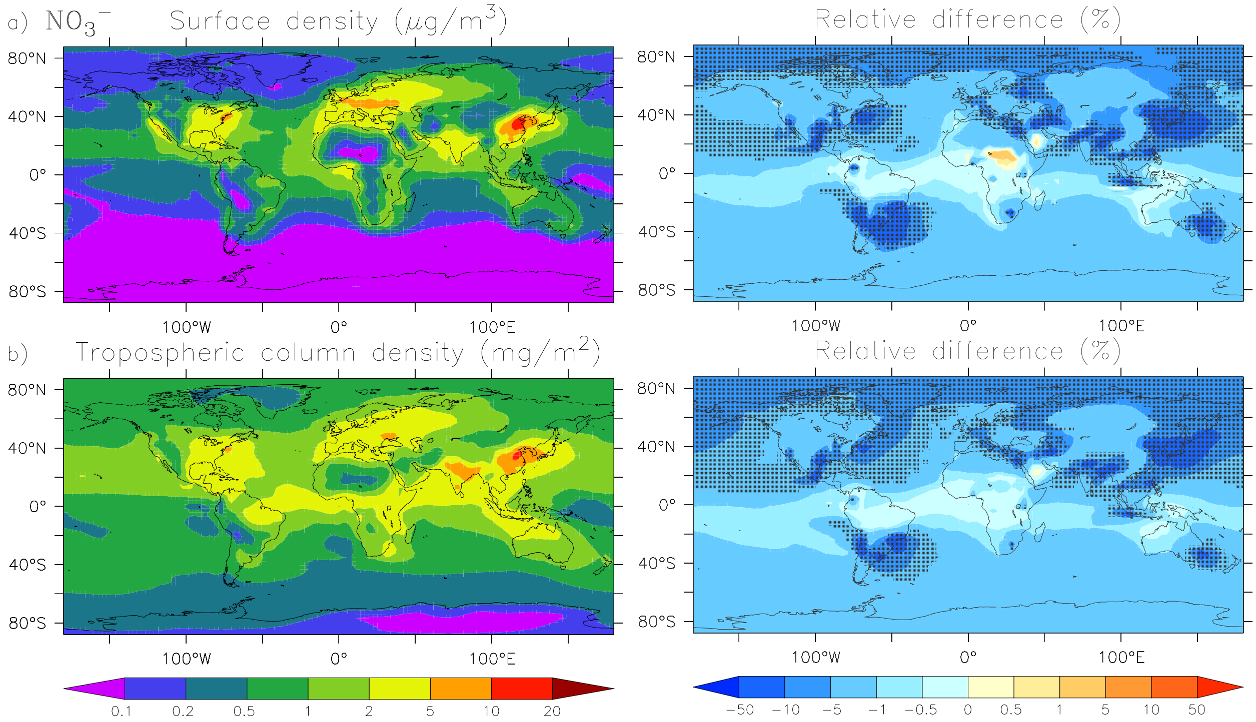

Figure 7.11: a) Surface (in $\mu g/m^3$) and b) tropospheric (in mg/m^2) density of aerosol nitrate for the reference scenario. Corresponding relative changes for EMS4 are depicted on the right side ($\frac{\text{EMS4}-\text{REF}}{\text{REF}}$, in %). Black dots mark regions where the difference is statistically significant on a 90 % confidence level.

For this the temporal evolution of the relative changes of BC, POM, SO_4^{2-}, and NO_3^- burdens are shown for the four simulations, EMS1 (– MPC BC emissions), EMS2 (– MPC POM emissions), EMS3 (– MPC SO_2 emissions), and EMS4 (– MPC NO_x emissions). The red lines in Figure 7.13 mark the simulation in which the emission of the species was reduced, while the dashed blue, light blue, and black lines show the relative change of the species in one of the other simulations. The global burdens of BC, POM, and SO_4^{2-} mainly differ from the respective burden in the reference simulation when only their own emission is reduced. However, there are a few exceptions to this worth discussing. For example, the two primary aerosols show slight increases in the case of reduced SO_2 and NO_x emissions

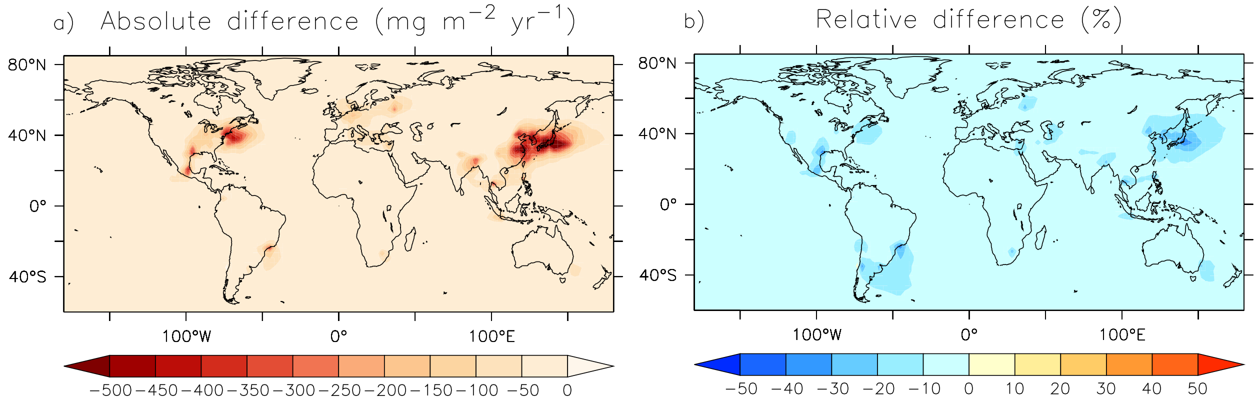

Figure 7.12: a) Absolute (in $mg\,m^{-2}\,yr^{-1}$, EMS3 – REF) and b) relative (in %, $\frac{\text{EMS3}-\text{REF}}{\text{REF}}$) difference in annual accumulated wet deposition of nitrate.

due to reduced amount of potentially available coating material. Furthermore, the aerosol nitrate is not only reduced when its precursor emission is reduced but shows an increase in global burden in EMS3 when SO_2 is reduced. On average this results in an increase of 2.5 % in aerosol nitrate, with maximum changes of almost six per cent in April. At that time the decrease is largest for aerosol sulfate and thus less sulfate is present in the atmosphere. In turn, more nitric acid can dissolve in the particulate phase and increase the nitrate burden.

7.2.6 Feedback of anthropogenic aerosol and aerosol precursor emission changes on other trace species

After analysing the direct causality of the reduction of anthropogenic emissions on the atmospheric burden of the selected species, the feedback on other species is subject of the next paragraphs. However, since BC and POM have only a negligible influence on other species, these impacts are not discussed here in again and the focus is more on feedbacks from changes of SO_2 and NO_x MPC emissions.

As shown before, reduced sulfur dioxide emissions (EMS3) result in reduced SO_2 concentrations and thus in lower concentrations of gaseous H_2SO_4 and aerosol sulfate. Moreover, less sulfur dioxide and less aerosol sulfate disturb the equilibirum between several gas phase and aerosol species. Since there is less competing aerosol sulfate, nitric acid can more easily dissolve in aerosol particles (see Figure 7.14). However, the statistically significant decrease of nitric acid covers a smaller area compared to the area of statistically significant increase in aerosol nitrate. Additionally, when a single negatively charged ion, nitrate, is present in the aerosol particles instead of a twice negatively charged ion, sulfate, the charge balance

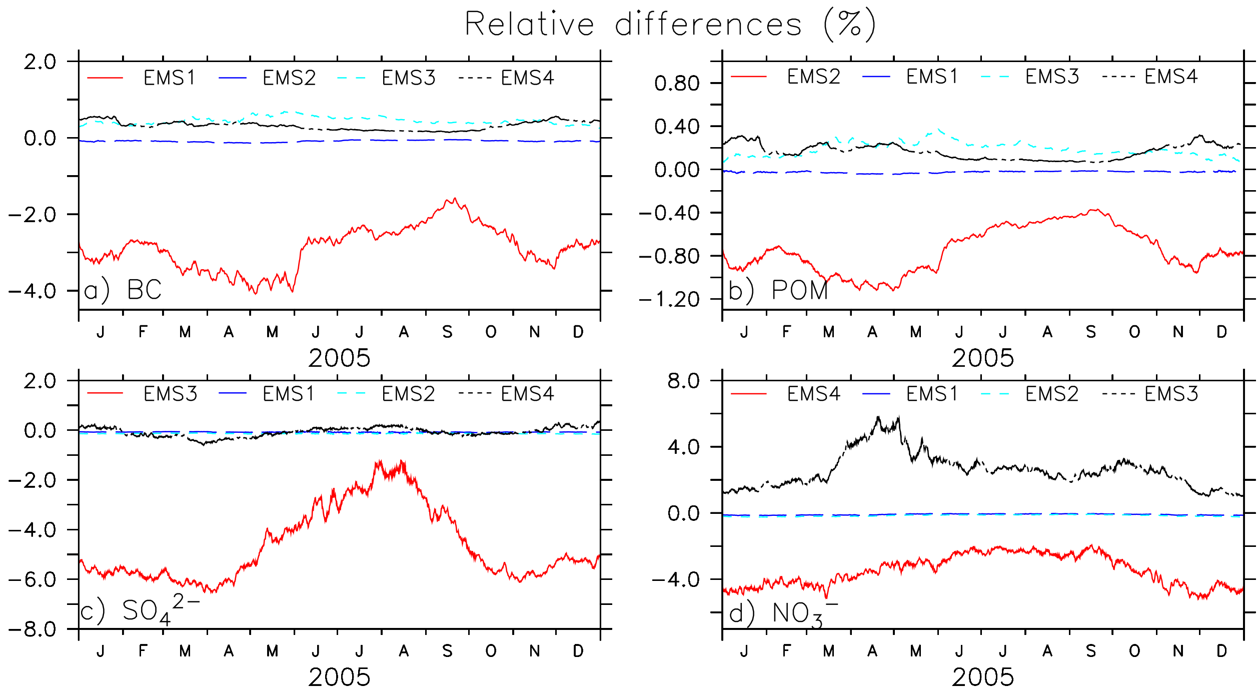

Figure 7.13: Relative differences (in %) of a) BC, b) POM, c) SO_4^{2-}, and d) NO_3^- in EMS1, EMS2, EMS3, and EMS4. The red lines indicate the sensitivity simulation where the species is reduced by 100 % in the megacities, blue, light blue, and black dashed lines show the relative change in the other simulations.

has to adopt accordingly, with consequences for the major species which is responsible to restore charge balance. Therefore, less particulate ammonium (NH_4^+) but more ammonia (NH_3) is abundant in the atmosphere (see middle panel of Figure 7.14, shown is the surface layer density, but the same trend is apparent in the tropospheric column density). A last interesting change is simulated for the $HCl - Cl^-$ equilibrium as a result of changed sulfate and nitrate concentrations in the atmosphere. The concentration of the gaseous HCl shows substantial, global decreases, except for the region around the equator. The increase is due

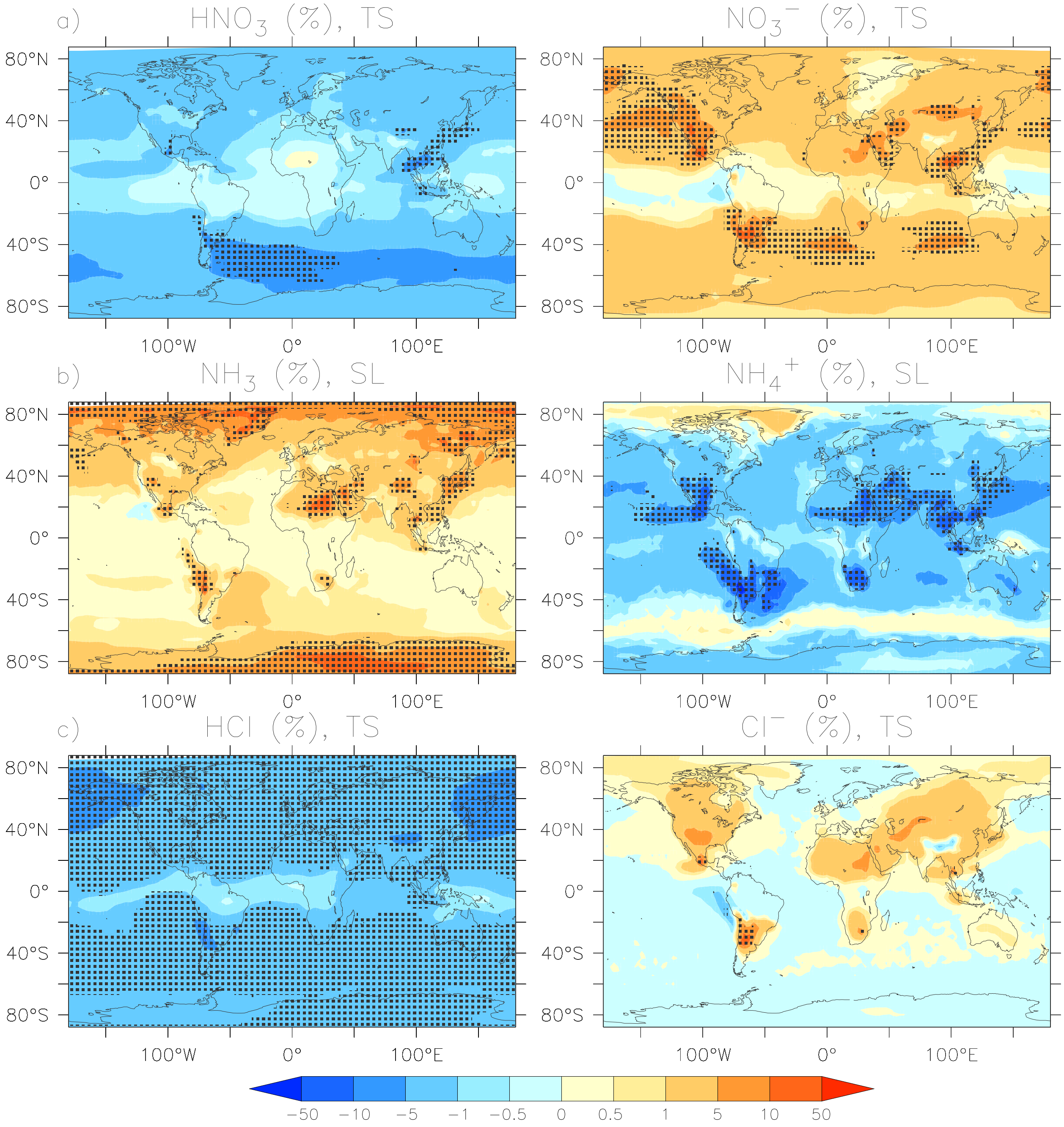

Figure 7.14: Relative changes (in %) in the gas-aerosol equilibria for reduced MPC SO_2 emissions. Relative changes are shown for a) the tropospheric (TS) column densities of the $HNO_3 - NO_3^-$ equilibrium, for b) the surface layer (SL) densities of the $NH_3 - NH_4^+$ equilibrium, and for c) the tropospheric column densities of the $HCl - Cl^-$ equilibrium. Black dots mark regions where the difference is significant on a 90 % confidence level.

to less sea-spray acidification since less sulfate is generally present and nitrate can also enter into accumulation mode particles. However, the changes in aerosol chloride are negligible, only over regions with low sea spray abundances, i.e., continents, an increase is simulated. Over the oceans the changes range from −0.5 % to 0.5 % due to the high abundance of chloride in the sea spray particles.

By far the most widespread consequences are simulated in the case of reduced NO_x emissions. Lower NO_x, and thus lower HNO_3 and NO_3^- levels influence the gas-aerosol equilibria between NH_3 and NH_4^+ as well as between gaseous HCl and particulate Cl^-. The changes show similar tendencies to those just discussed for reduced SO_2 emissions, but the changes

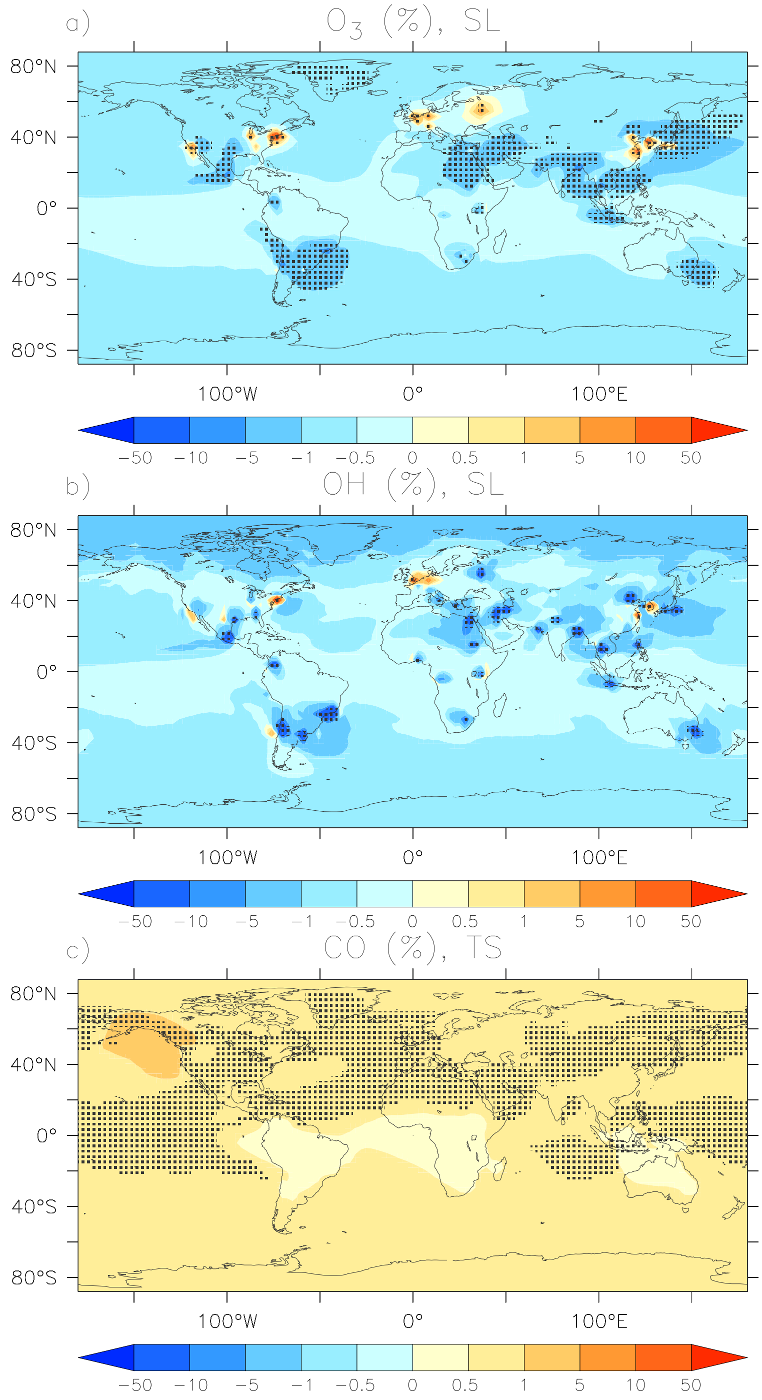

Figure 7.15: Relative changes (in %) in a) O_3 (surface layer, SL), b) OH (SL), and c) CO (tropospheric column, TS) for reduced MPC NO_x emissions in %. Black dots mark regions where the difference is significant on a 90 % confidence level.

are more confined to areas around the MPCs.

However, more far reaching consequences emerge in EMS4 because of the strong connections between NO_x, O_3, and OH. Ozone production and destruction directly depend on NO and HO_2 concentrations which are crucial in the oxidations of carbon monoxide and methane[4] (Seinfeld and Pandis, 1998). Depending on the ratio of NO to O_3, ozone is either produced or destroyed. In most MPCs more ozone is destroyed in EMS4 due to lower NO levels. Exceptions are several MPCs on the Northern Hemisphere where an increase in the annual mean surface ozone concentration is assessed (Figure 7.15). Butler and Lawrence (2009) showed that MPCs on the Northern Hemisphere are generally in an ozone removal regime. They claim that the potential of pollution build-up is larger in extra-tropical cities than in tropical cities where surface layer pollution is more rapidly removed by convective transport. The reaction of NO and O_3 to form NO_2 and O_2, which is a slow reaction under natural conditions, usually contributes significantly to destroy ozone in extra-tropical cities. However, if NO is decreased, less ozone is destroyed. Thus, reduced NO_x emissions in the extra-tropical MPCs potentially decrease the titration. Furthermore, ozone concentrations depend also on the concentrations of VOCs (volatile organic compounds) from which ozone can be produced. Reducing the NO_x levels in this comprehensive chemical system can directly lead to an increase in O_3 concentrations (for reference see the ozone isopleth plot, for example in Sillman and He, 2002). Moreover, OH shows the same spatial changes as ozone and the impacts on the short-lived species also affect the relatively long-lived carbon monoxide (Figure 7.15). Reduced MPC NO_x emissions affect the oxidation capacity of the atmosphere, indicated by a global increase in the tropospheric CO column density. The

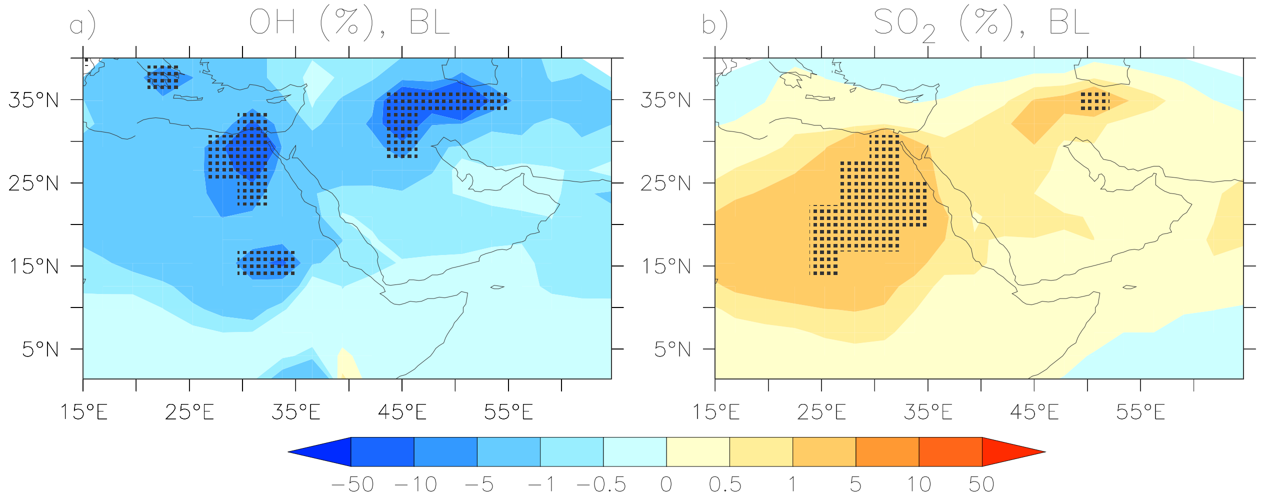

Figure 7.16: Relative changes (in %) of a) OH and b) SO_2 in the boundary layer (BL) for reduced MPC NO_x emissions in the Middle East. Black dots mark regions where the difference is significant on a 90 % confidence level.

---

[4] In particular, two reactions are of major interest in these cases (Seinfeld and Pandis, 1998, see equations (5.25) and (5.46)):

$$\begin{aligned} HO_2\cdot + NO &\rightarrow NO_2 + OH\cdot && \Rightarrow O_3 \text{ production} \\ HO_2\cdot + O_3 &\rightarrow OH\cdot + 2O_2 && \Rightarrow O_3 \text{ destruction} \end{aligned}$$

changes in CO show statistical significance in most regions over the Northern Hemisphere. Finally, a local feedback is discussed regarding the oxidation of SO_2 by OH. Usually, the pre-dominant oxidation pathway of SO_2 is in the aqueous phase. For this, enough water vapor, e.g., in clouds or fogs, has to be present in the atmosphere. In contrast, the oxidation in the gas phase is also non-negligible in dry regions like the Saharan dessert or the Middle East. In MPCs in these regions, the OH levels are lower when the NO_x emissions are reduced (see middle panel in Figure 7.15). In the case of Cairo, the outflow is directed southward into the Sahara, now carrying air with lower OH concentration. Consequently, less sulfur dioxide is oxidized to sulfuric acid in the outflow of Cairo (Figure 7.16). In principle, this is also evident in Teheran and Baghdad where similar ambient meteorological conditions prevail.

7.3 Cumulative impact of anthropogenic megacity emissions

So far, the emissions have only been reduced for a single species which, nevertheless, resulted in substantial changes in the concentration of the species and also in other species when aerosol precursor gases had been changed. A remaining question is now what happens when the MPC emissions of all four species are changed at once? To study this the MPC emissions of BC, POM, SO_2, and NO_x were simultaneously reduced once by 100 % (EMSM100) and once by 20 % (EMSM20) as well as increased by 20 % (EMSP20).
Hence, two questions will be answered in this section:

1. Do the atmospheric burdens of BC, POM, SO_4^-, and NO_3^- change differently in EMSM100 compared to EMS1, EMS2, EMS3, EMS4, respectively?
2. Do changes in emissions lead to responses in the atmospheric burden of species which are linear, i.e., which are proportional to the order of magnitude of the changed emissions?

The initially hydrophobic species black carbon and particulate organic matter respond differently in EMSM100 than in EMS1 and EMS2 (compare black and red solid lines in Figure 7.17). In EMSM100, the emissions of SO_2 and NO_x are additionally reduced which leads to a decrease in the mass which is potentially available to coat the hydrophobic aerosol particles. Thus, the growth and the mass transfer into hydrophilic modes is slower, resulting in a smaller decrease of BC and POM in EMSM100. In contrast, the reduction in SO_4^{2-} is of the same magnitude in EMSM100 and EMS3. This can already be anticipate from the sulfate burdens shown in Figure 7.13 which did not change when the emission of another species was reduced. The largest difference between EMSM100 and the single emission reduction scenarios is assessed for aerosol nitrate. The annual cycles of the relative changes of BC, POM, and SO_4^{2-} follow the same tendencies in EMSM100 and the respective scenarios, which is not the case for NO_3^-. Although the MPC NO_x emissions are reduced by 100 % in EMSM100, the relative change shows that the NO_3^- burden is often larger than in the reference simulation between March and August. This results from the competition between sulfuric and nitric acid to enter the aerosol phase. When both acids are present, nitric acid only dissolves when several prerequisites are fulfilled, i.e., sulfuric acid fully consumed, enough cations and aerosol water in the particulate phase. This effect has been discussed before, when only the sulfur dioxide emissions were removed. Interestingly, the aerosol nitrate can reach total burdens, which are higher than in the reference simulation, even when the emission of its

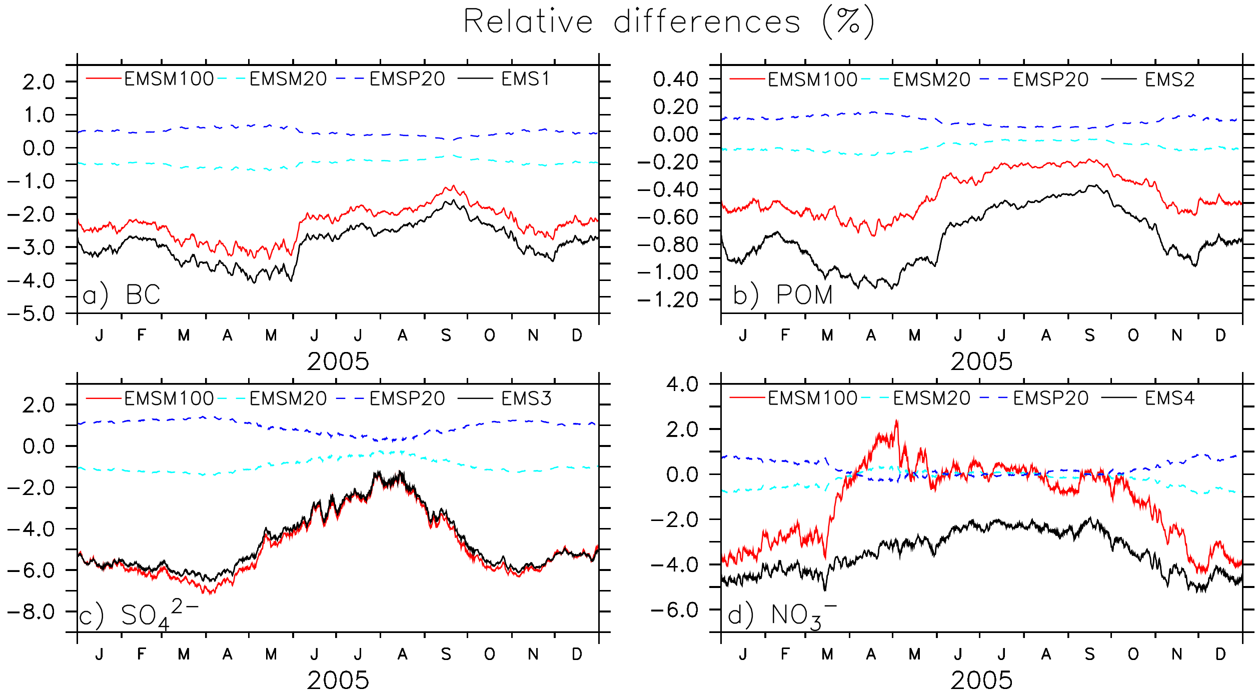

Figure 7.17: Time series of relative changes (in %) of a) BC, b) POM, c) SO_4^{2-}, and d) NO_3^- burdens for EMSM100 (red solid lines), EMSM20 (light blue dashed lines), EMSP20 (dark-blue dashed lines), and the changes when only the species considered is reduced (black solid lines).

precursor gas is reduced.

In Figure 7.17, the relative changes for EMSM20 (−20 %, light blue line) and for EMSP20 (+20 %, blue line) are included. For BC, POM, and SO_4^{2-} these lines look like they are mirrored at the horizontal zero line. This is confirmed by computing the ratio of the burden changes. In the case of EMSM20 and EMSP20 the ratios are assessed to be close to −1 for these species, with mean values: −0.98 for BC, −0.95 for POM, and −1.00 for SO_4^{2-} and minimum and maximum values: [−1.04, −0.94] for BC, [−1.21, −0.76] for POM, and [−1.44, −0.80] for SO_4^{2-}. Moreover, the ratio between the burden changes in EMSM100 and EMSM20 is computed to be close to 5, with mean values: 4.92 for BC, 4.75 for POM, and 5.12 for SO_4^{2-} and minimum and maximum values: [4.76, 5.14] for BC, [4.28, 5.42] for POM, and [4.46, 6.43] for SO_4^{2-}. Thus, the changes in the atmospheric burden are almost directly proportional to the emission changes. In contrast, the ratios for NO_3^- differ substantially from −1 and 5 (see Figure 7.18), especially from March to September. Remember that this partly coincides with time range when the nitrate burden is more abundant in EMSM100 than in the reference simulation. Thus, there is a great potential that the competition between sulfuric and nitric acid contributes to this non-linear behavior. Furthermore, the thermal instability of ammonium nitrate has to be considered to explain this strong variation in the ratios. Most of the NO_x is emitted over the Northern Hemisphere where temperatures large enough to shift the gas-aerosol equilibrium more towards the gas phase occur between March and September. In contrast, during the boreal winter months the ratios stabilize around −1 and 5.

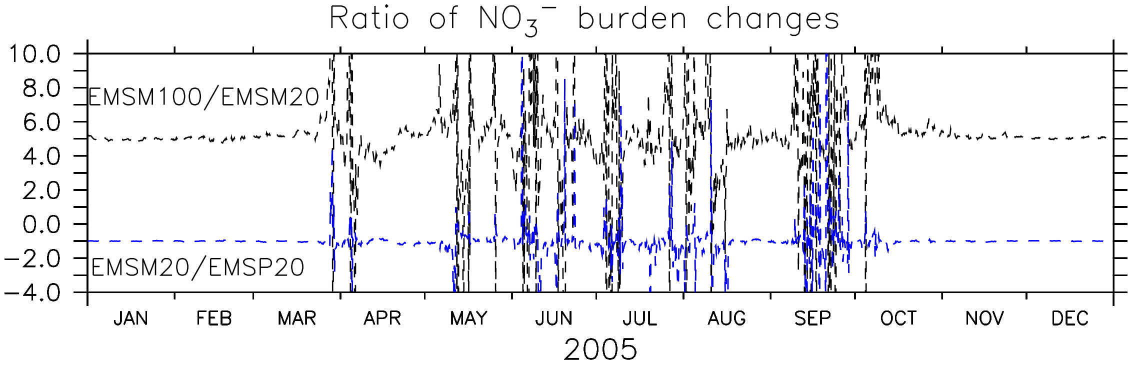

Figure 7.18: Ratio of atmospheric burden changes $\Delta m_{\mathrm{EMSM100}}/\Delta m_{\mathrm{EMSM20}}$ (black line) and $\Delta m_{\mathrm{EMSM100}}/\Delta m_{\mathrm{EMSM20}}$ (blue line).

7.4 Summary

In this chapter, the main objective went beyond the analysis of transport pathways and deposition patterns of individual tracers from major population centers. It focused more on the contribution of anthropogenic emissions from major population centers (MPCs) on key trace species on regional and global scales. The anthropogenic emissions of four species, black carbon, particulate organic matter, sulfur dioxide, and nitrogen oxides, were changed at the locations of the 46 MPCs, similar to the approach of Butler and Lawrence (2009) who focused on gaseous species. The main findings of this chapter are summarized in the following:

1. Annihilation of BC and POM at all MPCs results in a decrease in total emission of 4.3 % and 0.8 % and a decrease in the annual mean atmospheric burden of 2.8 % and 0.8 %, respectively. Total reduction in SO_2 (−6.3 %) as precursor gas of SO_4^{2-} and NO_x (−5.5 %) as precursor gas of NO_3^- leads to a reduction of about 4.5 % and 3.6 % in the global burden of the aerosol species. The main changes occur around the cities and in the downwind regions with maximum reductions up to 50 % in the tropospheric column compared to the reference scenario. The most widespread changes were calculated for sulfate, with reductions in the tropospheric burden assessed almost for the entire Northern Hemisphere.
2. While almost no feedback of BC and POM on other species is simulated, there are several trace species affected when emissions of SO_2 and in particular, when emissions of NO_x are reduced. In the case of SO_2, mainly those species are affected, which are involved in the oxidation of SO_2 to H_2SO_4. Additional feedbacks emerge in gas-aerosol equilibria of $HNO_3 - NO_3^-$, $NH_3 - NH_4^+$, and $HCl - Cl^-$. By reducing the emissions of NO_x, many species participating in the $NO_x - O_3$ chemistry show a response in their concentrations. In particular, ozone changes differently in extra-tropical and tropical cities, which is in accordance with findings of Butler and Lawrence (2009). Moreover, the oxidation capacity of the atmosphere is changed. OH changes similarly to O_3, which leads to an increase in the tropospheric CO concentration and to locally greater SO_2 concentrations.
3. Emission changes for BC, POM, and SO_2/SO_4^{2-} result in almost linear response of the atmospheric burden. However, for NO_x/NO_3^- this is only the case during boreal winter but not during summer when the (ammonium-) nitrate burden does not only depend on

the NO_x emissions but also on the ambient temperature and the available sulfuric acid concentration.

The results show that MPC emissions of BC, POM, SO_4^{2-}, and NO_3^- can have wide implications on many key species in the atmosphere. The effects are assessed to be larger for secondary aerosols than for primary aerosols. Although primary species have no substantial feedbacks on other species, the changes, in particular of absorbing black carbon, may be relevant in assessing the direct effect of MPC aerosols, which has not been done here and is left open for following studies.
Considering that the number of MPCs will increase in the future, these impacts may increase and more regions will be influenced by the urban centers. Especially, when a region is downwind of several MPCs, the cumulative impacts might lead to severe air quality problems.

Part III

Nuclear Power Plants

8

Dispersion of and radioactive contamination by radionuclides from nuclear reactor accidents

The purpose of this chapter is to show an application of the passive tracers which is beyond pure transport and deposition from different source points. The deposition fields are used in a global risk assessment to study the radioactive contamination after major nuclear reactor accidents. Such studies are challenging since a large number of factors have to be taken into account which influence the release of radionuclides and their subsequent dispersion in and removal from the atmosphere.

Empirical data is used to estimate the probability of a major nuclear accident. Transport and deposition of radionuclides, in particular of cesium-137 (^{137}Cs) and iodine-131 (^{131}I), are simulated to identify regions which are more vulnerable to becoming contaminated with high doses of radioactivity. Additionally, a deposition threshold value is applied in order to obtain the risk of contamination. In doing so the following questions are answered in this chapter:

1. What does the geographical distribution of the risk of contamination after nuclear accidents look like? What are the major uncertainties and are generic tracers good representatives of radionuclides in a risk assessment study?
2. The Chernobyl accident is the best documented nuclear reactor accident, with estimates available on the emission source function as well as on the spatial distribution of deposited ^{137}Cs. Using this data the following question is answered: how well can EMAC simulated the dispersion of ^{137}Cs after the Chernobyl accident?
3. How well do the pollution potentials from nuclear power plants agree with those from major population centers?

For this, the distribution of the nuclear power plants is introduced first, before the model configuration and the performance of EMAC in simulating the dispersion of radionuclides after the Chernobyl accident are presented. Thereafter, the pollution potentials are discussed for the NPP sources and compared to those from major population centers. The Chernobyl source term for ^{137}Cs and ^{131}I are then used as the basis for a discussion about severe nuclear reactor accidents and the global risk of contamination after such accidents.

The work in this chapter laid the groundwork for the publications of Lelieveld et al. (2012a) and Lelieveld et al. (2012b), and Sections 8.2.1 and 8.4 largely follow the arguments in those papers.

8.1 Nuclear power plants as emission source points

Currently, there are about 440 nuclear reactors operating in about 191 different nuclear power plants. The number varies due to maintenance of operating reactors as well as due to shutting down old reactors and putting new reactors into operation. The first civilian nuclear reactor went operational in 1954 in Obninsk. Since then the total number of nuclear reactors has increased rather steadily. A full list of all nuclear power plants with at least one operating reactor unit is given in Table 8.1. Additional information is provided for the total number of reactor units at each site, how many of those reactors are currently in use, and the total gross and total net power of all operating reactors. Furthermore, it is shown that there is a large diversity of reactor types.

Table 8.1: List of all nuclear power plants which were operational in April 2011. Additionally, the records for Chernobyl and Windscale (Sellafield) are listed. Columns are: country, name of NPP, reactor type, number of reactors in use, total number of reactors, total gross power (TGB) in 10^6 W (all reactors in use), total net power (TNP) in 10^6 W (all reactors in use), longitude, and latitude in degrees. Reactor type abbreviations are: ABWR=Advanced Boiling Water Reactor, AGR=Advanced Gas Cooled Graphite Reactor, BN=Russian Fast Neutron Reactor, BWR=Boiling Water Reactor, CANDU=Canada Deuterium Uranium Reactor, CPR=Chinese Pressurized Reactor, EPR=European Pressurized Reactor, FBR=Fast Breeder Reactor, GBWR=Russian Graphite Moderated Reactor, Magnox=Gas Cooled Reactor, PHWR=Pressurized High Water Reactor, PWR=Pressurized Water Reactor, RBMK=Russian Light Water Cooled Reactors, WWER=Water-Water Energetic Reactor. List adopted from Wikipedia: http://de.wikipedia.org/wiki/Liste_der_Kernkraftwerke, as of 27.03.2011, in German. This list is also published as supplementary information to Lelieveld et al. (2012a).

Country	Name	Reactor type	# blocks in use	Total # blocks	TGP (MW)	TNP (MW)	Lon (°)	Lat (°)
South Africa	Koeberg	PWR	2	2	1888	1800	18.42	-33.67
Armenia	Mezamor	WWER	1	2	816	752	44.13	40.17
China	Daya Bay	PWR	2	2	1968	1888	114.53	22.58
	Ling'ao	PWR	3	4	3067	2876	114.55	22.60
	Qinshan	PWR/CANDU	6	7	3660	3418	120.95	30.43
	Tianwan	CPR	2	2	2000	1866	119.45	34.68
India	Kaiga	PHWR	4	4	880	808	74.43	14.87
	Kakrapar	PHWR	2	4	440	404	73.35	21.23
	Madras	PHWR/FBR	2	3	440	410	80.17	12.55
	Narora	PHWR	2	2	440	404	78.40	28.15
	Rajasthan	PHWR	6	6	1180	1085	75.60	24.87
	Tarapur	BWR/PHWR	4	4	1400	1280	72.65	19.82
Japan	Fukushima-Dai-ichi	BWR	2	6	1884	1827	141.02	37.42
	Fukushima-Dai-ni	BWR	4	4	4400	4268	141.02	37.32
	Genkai	PWR	3	4	3478	3312	129.83	33.50
	Hamaoka	BWR/ABWR	3	5	3617	3473	138.13	34.62
	Higashidori	BWR	1	1	1100	1067	141.18	41.18
	Ikata	PWR	3	3	2022	1922	132.30	33.48
	Kashiwazaki-Kariwa	BWR/ABWR	7	7	8212	7970	138.58	37.42
	Mihama	PWR	3	3	1666	1570	135.70	35.70
	Ohi	BWR	4	4	4710	4494	135.65	35.53
	Onagawa	BWR	3	3	2174	2090	141.48	38.40
	Sendai	PWR	2	2	1780	1692	130.18	31.83
	Shika	BWR/ABWR	2	2	1898	1809	136.72	37.05
	Shimane	BWR	2	3	1280	1228	132.98	35.53
	Takahama	BWR	4	4	3392	3220	135.50	35.52
	Tokai	AGR/BWR	1	2	1100	1060	140.60	36.45
	Tomari	BWR/PWR	3	3	2070	1966	140.50	43.03
	Tsuruga	BWR/PWR	2	2	1517	1450	136.02	35.75
Pakistan	Chashma	PWR	1	2	325	300	71.45	32.38
	Karachi	CANDU	1	1	137	125	66.78	24.83
South Corea	Gori	PWR	4	4	3288	3136	129.30	35.32
	Singori	PWR	1	4	1000	960	129.28	35.32
	Uljin	PWR	6	6	6157	5553	129.38	37.10
	Wolseong	CANDU	4	4	2786	2582	129.47	35.70
	Yeonggwang	PWR	6	6	6137	5835	126.42	35.40

Table 8.1: continued.

Country	Name	Reactor type	# blocks in use	Total # blocks	TGP (MW)	TNP (MW)	Lon (°)	Lat (°)
Taiwan	Chin Shan	BWR	2	2	1272	1208	121.57	25.28
	Kuosheng	BWR	2	2	2004	1933	121.65	25.20
	Maanshan	PWR	2	2	1902	1780	120.75	21.95
Belgium	Doel	PWR	4	4	2963	2839	4.25	51.32
	Tihange	PWR	3	3	3129	2985	5.27	50.53
Bulgaria	Kosloduj	WWER	2	6	2000	1906	23.77	43.73
Germany	Biblis	PWR	2	2	2525	2407	8.40	49.70
	Brokdorf	PWR	1	1	1480	1410	9.33	53.85
	Brunsbüttel	BWR	1	1	806	771	9.20	53.88
	Emsland	PWR	1	1	1400	1329	7.32	52.47
	Grafenrheinfeld	PWR	1	1	1345	1275	10.18	49.98
	Grohnde	PWR	1	1	1430	1360	9.40	52.03
	Gundremmingen	BWR	2	2	2688	2572	10.40	48.50
	Isar	BWR/PWR	2	2	2387	2278	12.28	48.60
	Krümmel	BWR	1	1	1402	1346	10.40	53.40
	Neckarwestheim	PWR	2	2	2240	2095	9.17	49.03
	Philippsburg	BWR/PWR	2	2	2384	2282	8.43	49.25
	Unterweser	PWR	1	1	1410	1345	8.47	53.42
Finland	Loviisa	WWER	2	2	1020	976	26.33	60.37
	Olkiluoto	BWR/EPR	2	3	1780	1720	21.43	61.23
France	Belleville	PWR	2	2	2726	2620	2.87	47.50
	Blayais	PWR	4	4	3804	3640	0.68	45.25
	Bugey	PWR	4	5	3724	2580	5.27	45.78
	Cattenom	PWR	4	4	5448	5200	6.22	49.40
	Chinon	PWR	4	7	3816	3620	0.17	47.22
	Chooz	PWR	2	3	3120	3000	4.78	50.08
	Civeaux	PWR	2	2	3122	2900	0.65	46.45
	Cruas	PWR	4	4	3824	3660	4.75	44.63
	Dampierre	PWR	4	4	3748	3560	2.52	47.73
	Fessenheim	PWR	2	2	1840	1760	7.55	47.90
	Flamanville	PWR/EPR	2	3	2764	2660	1.87	49.53
	Golfech	PWR	2	2	2726	2620	0.83	44.10
	Gravelines	PWR	6	6	5706	5460	2.13	51.00
	Nogent	PWR	2	2	2726	2620	3.52	48.50
	Paluel	PWR	4	4	5528	5240	0.63	49.85
	Penly	PWR	2	2	2764	2620	1.20	49.97
	Saint-Alban	PWR	2	2	2762	2630	4.75	45.40
	Saint-Laurent	PWR	2	4	1912	1830	1.57	47.72
	Tricastin	PWR	4	4	7640	3660	4.72	44.32
The Netherlands	Borssele	PWR	1	1	515	482	3.72	51.42
Romania	Cernavoda	CANDU-6	2	2	1412	1300	28.05	44.32
Russia	Balakowo	WWER	4	4	4000	2800	47.95	52.08
	Belojarsk	BN	1	4	600	560	61.32	56.85
	Bilibino	GBWR	4	4	48	44	166.53	68.05
	Kalinin	WWER	3	4	3000	2850	35.05	57.90
	Kola	WWER	4	4	1760	1644	32.47	67.47
	Kursk	RBMK	4	5	4000	3700	35.60	51.67
	Leningrad	RBMK	4	4	4000	3700	29.05	59.85
	Nowoworonesch	WWER	3	5	1834	1720	39.20	51.27
	Rostow	WWER	2	4	2000	1900	42.58	47.58
	Smolensk	RBMK	3	3	3000	2725	33.23	54.17
Sweden	Forsmark	BWR	3	3	3275	3157	18.17	60.40
	Oskarshamn	BWR	3	3	2307	2209	16.67	57.40
	Ringhals	BWR/PWR	4	4	3820	3642	12.10	57.25
Switzerland	Beznau	PWR	2	2	760	730	8.22	47.55
	Gösgen	PWR	1	1	1020	970	7.97	47.35
	Leibstadt	BWR	1	1	1220	1165	8.18	47.60
	Mühleberg	BWR	1	1	372	355	7.27	46.97
Slovakia	Bohunice	WWER	2	5	904	839	17.67	48.48
	Mochovce	WWER	2	4	940	872	18.45	48.25
Slovenia	Krsko	PWR	1	1	730	666	15.50	45.93
Spain	Almaraz	PWR	2	2	1957	1900	-5.68	39.80
	Ascó	PWR	2	2	2060	1992	0.57	41.20
	Cofrentes	BWR	1	1	1092	1064	-1.05	39.22
	Santa María de Garoña	PWR	1	1	466	446	-3.20	42.77
	Trillo	PWR	1	1	1066	1003	-2.62	40.70
	Vandellòs	PWR	1	2	1087	1045	0.87	40.95
Czech Republic	Dukovany	WWER	4	4	1824	1708	16.13	49.08
	Temelín	WWER	2	2	2026	1926	14.37	49.17
Ukraine	Chmelnyzkyj	WWER	2	4	2000	1900	26.63	50.30
	Riwne	WWER	4	4	2835	2657	25.88	51.32
	Saporischschja	WWER	6	6	6000	5700	34.92	47.50
	South-Ukraine	WWER	3	3	3000	2850	31.22	47.82
	Chernobyl	RBMK	0	4	3800	3515	30.08	51.38
Hungary	Paks	WWER	4	4	1940	1829	18.85	46.57
UK	Dungeness	AGR	2	4	1230	1090	0.95	50.90
	Hartlepool	AGR	2	2	1310	1190	-1.17	54.63
	Heysham	AGR	4	4	2610	2390	-2.90	54.03
	Hinkley Point	AGR	2	4	1310	860	-3.12	51.20
	Hunterston	AGR	2	2	1288	840	-4.88	55.72
	Oldbury	Magnox	2	2	460	434	-2.57	51.63
	Sizewell	PWR	1	3	1250	1188	1.62	52.22
	Torness	AGR	2	2	1364	1250	-2.40	55.97
	Windscale AGR	AGR	0	1	41	32	-3.48	54.42
	Wylfa	Magnox	2	2	1080	980	-4.48	53.42

Table 8.1: continued.

Country	Name	Reactor type	# blocks in use	Total # blocks	TGP (MW)	TNP (MW)	Lon (°)	Lat (°)
Canada	Bruce	CANDU	6	8	5090	4745	-81.58	44.32
	Darlington	CANDU	4	4	3736	3512	-78.72	43.87
	Gentilly	CANDU	1	2	675	635	-72.35	46.38
	Pickering	CANDU	6	8	3244	3094	-79.05	43.80
	Point Lepreau	CANDU	1	1	680	635	-66.45	45.07
Mexico	Laguna Verde	BWR	2	2	1264	1260	-96.40	19.72
USA	Arkansas One	PWR	2	2	1920	1834	-93.22	35.30
	Beaver Valley	PWR	2	2	1846	1736	-80.42	40.62
	Braidwood	PWR	2	2	2453	2330	-88.22	41.23
	Browns Ferry	BWR	3	3	3497	3297	-87.12	34.70
	Brunswick	BWR	2	2	1979	1875	-78.00	33.95
	Byron	PWR	2	2	2421	2300	-89.27	42.07
	Callaway	PWR	1	1	1236	1190	-91.78	38.75
	Calvert Cliffs	PWR	2	2	1829	1735	-76.43	38.43
	Catawba	PWR	2	2	2376	2285	-81.07	35.05
	Clinton	BWR	1	1	1098	1052	-88.82	40.17
	Columbia	BWR	1	1	1200	1131	-119.33	46.47
	Comanche Peak	PWR	2	2	2378	2300	-97.78	32.28
	Cooper	BWR	1	1	801	760	-95.63	40.35
	Crystal River	PWR	1	1	890	838	-82.68	28.95
	Davis Besse	PWR	1	1	925	891	-83.08	41.58
	Diablo Canyon	PWR	2	2	2300	2209	-120.85	35.20
	Donald Cook	PWR	2	2	2200	2093	-86.55	41.97
	Dresden	BWR	2	3	1826	1754	-88.27	41.38
	Duane Arnold	BWR	1	1	614	581	-91.77	42.10
	Enrico Fermi	BWR	1	2	1154	1111	-83.25	41.95
	Farley	PWR	2	2	1800	1711	-85.10	31.22
	Fitzpatrick	PWR	1	1	882	852	-76.40	43.52
	Fort Calhoun	PWR	1	1	512	478	-96.07	41.52
	Grand Gulf	BWR	1	1	1333	1266	-91.05	32.00
	H.B. Robinson	PWR	1	1	745	710	-80.15	34.40
	Hatch	BWR	2	2	1819	1759	-82.33	31.93
	Hope Creek	BWR	1	1	1139	1059	-75.53	39.47
	Indian Point	PWR	2	3	2127	2045	-73.95	41.27
	Kewaunee	PWR	1	1	581	556	-87.53	44.33
	Lasalle	BWR	2	2	2356	2238	-88.67	41.23
	Limerick	BWR	2	2	2388	2268	-75.58	40.22
	McGuire	PWR	2	2	2316	2200	-80.93	35.42
	Millstone	PWR	2	3	2163	2037	-72.17	41.30
	Monticello	BWR	1	1	600	572	-93.83	45.32
	Nine Mile Point	BWR	2	2	1847	1756	-76.40	43.52
	North Anna	PWR	2	2	1931	1834	-77.78	38.05
	Oconee	PWR	3	3	2673	2538	-82.88	34.78
	Oyster Greek	BWR	1	1	652	619	-74.20	39.80
	Palisades	PWR	1	1	842	778	-86.30	42.32
	Palo Verde	PWR	3	3	4174	3875	-112.85	33.38
	Peach Bottom	BWR	2	3	2342	2224	-76.27	39.75
	Perry	BWR	1	1	1303	1235	-81.13	41.80
	Pilgrim	BWR	1	1	711	685	-70.57	41.93
	Point Beach	PWR	2	2	1088	1026	-87.53	44.27
	Prairie Island	PWR	2	2	1110	1055	-92.62	44.62
	Quad Cities	BWR	2	2	1826	1734	-90.30	41.72
	R.E. Ginna	PWR	1	1	608	560	-77.30	43.27
	River Bend	BWR	1	1	1036	966	-91.33	30.75
	Saint Lucie	PWR	2	2	1766	1678	-80.23	27.33
	Salem	PWR	2	2	2398	2304	-75.53	39.45
	San Onofre	PWR	2	3	2254	2150	-117.55	33.37
	Seabrook	PWR	1	1	1296	1244	-70.85	42.88
	Sequoyah	PWR	2	2	2442	2277	-85.08	35.22
	Shearon Harris	PWR	1	1	960	900	-78.95	35.63
	South Texas	PWR	2	2	2708	2560	-96.05	28.78
	Surry	PWR	2	2	1696	1598	-76.68	37.15
	Susquehanna	BWR	2	2	2403	2275	-76.13	41.08
	Three Mile Island	PWR	1	2	837	786	-76.72	40.15
	Turkey Point	PWR	2	2	1458	1386	-80.32	25.43
	Vermont Yankee	BWR	1	1	650	605	-72.50	42.77
	Virgil C. Summer	PWR	1	1	1003	966	-81.32	34.25
	Vogtle	PWR	2	2	2405	2301	-81.75	33.13
	Waterford	PWR	1	1	1200	1158	-90.47	29.98
	Watts Bar	PWR	1	2	1202	1121	-84.78	35.60
	Wolf Creek	PWR	1	1	1213	1166	-95.68	38.23
Argentina	Atucha	PWHR	1	2	357	335	-59.18	-33.95
	Embalse	CANDU	1	1	648	600	-64.43	-32.22
Brazil	Angra	PWR	2	3	2007	1795	-44.45	-23.00

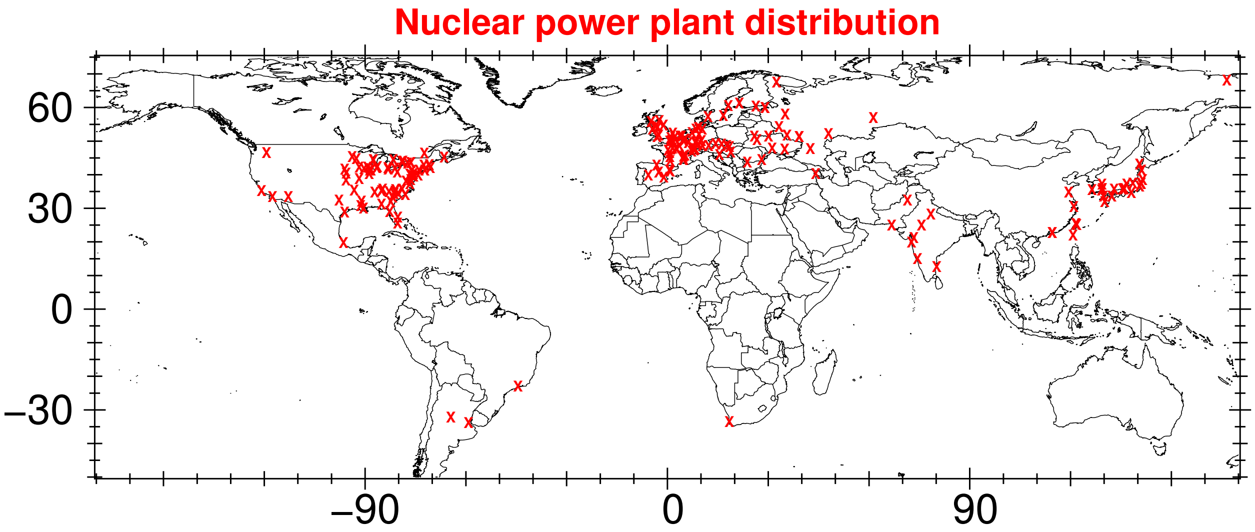

Figure 8.1: Spatial distribution of all nuclear power plants based on the latitude and longitude information provided in Table 8.1.

The spatial distribution of the nuclear power plants is shown in Figure 8.1. Three regions show a high density of nuclear power plants. These are located in the highly industrialized regions of the Northern Hemisphere, where the population density is also large (see Figure 3.2). The most reactors per country are in the United States (104), followed by France (58). The number of power plants was expected to increase further. However, since the Fukushima accident occurred, several countries declared that they will either phase out of nuclear energy production or will not start to build new reactors. Thus, the future development of the number of active nuclear reactors is difficult to predict.

NPPs have maximum horizontal extensions of several kilometers and are thus much smaller then major population centers. However, in the model no difference between the two emission source types is assumed; both are treated equally, since with both the focus is on the regional to global scale transport and deposition patterns rather than small-scale variability.

8.2 Model and simulation setup

8.2.1 The Chernobyl accident as an aerosol transport test case

The Chernobyl accident is the best documented major accident (e.g., Persson et al., 1986; Anspaugh et al., 1988; Hass et al., 1990; De Cort et al., 1998; Brandt et al., 2002; Smith and Beresford, 2005; IAEA, 2006; EU, 2011), although more data from the Fukushima accident are becoming available in scientific literature, which reduces the uncertainties related to the release of radionuclides (e.g., Chino et al., 2011; Leon et al., 2011; Yasunari et al., 2011; Kinoshita et al., 2011; Stohl et al., 2012; Buesseler et al., 2012). Given the present uncertainty, the Chernobyl accident is chosen for use as a basis in this chapter in two ways: 1) the total emission terms of cesium-137 and iodine-131 are the basis for the risk assessment in Section 8.4 and 2) the Chernobyl accident provides the possibility of evaluating the simulated transport of aerosols from an anthropogenic surface source point which has a much smaller extension than the grid cells in the model.

Table 8.2: List of largest nuclear reactor accidents (INES 4-7) and total released radioactivity (in PBq). INES 0-3 events are indicated as "deviations", "anomalies", and "incidents". INES 4 is an "accident with local consequences", INES 5 an "accidents with wider consequences", INES 6 a "serious accident". INES 7 is a "major accident with widespread health and environmental effects requiring implementation of planned and extended countermeasures". This table has also been published in Lelieveld et al. (2012a).

Location	Country	INES	Date	Total	^{131}I	^{137}Cs
Chernobyl	USSR	7	26 April 1986	> 12000	1760	85
Fukushima Dai-ichi	Japan	7	11 March 2011	> 630	190 – 380	12 – 37
Mayak	USSR	6	29 September 1957	74 – 1850	nda[a]	nda
Chalk River	Canada	5	12 December 1952	> 0.3	nda	nda
Windscale	UK	5	10 October 1957	1.6	0.7	0.2
Simi Valley	USA	5–6	26 July 1959	> 200[b]	[c]	nda
Belojarsk	USSR	5	1977	nda	nda	nda
Three Mile Island	USA	5	28 March 1979	1.6[d]	< 0.0007	nda
Chernobyl	USSR	5	1 September 1982	nda	nda	nda
Idaho Falls	USA	4	29 November 1955	[e]	[e]	[e]
Idaho Falls	USA	4	03 January 1961	nda	nda	nda
Monroe	USA	4	05 October 1966	[e]	[e]	[e]
Lucens	Switzerland	4-5	21 January 1969	[e]	[e]	[e]
Windscale	UK	4	1973	nda	nda	nda
Leningrad	USSR	4–5	06 February 1974	[f]	nda	nda
Leningrad	USSR	4–5	October 1974	55	nda	nda
Jaslovské Bohunice	CSSR	4	22 February 1977	nda	nda	nda
Saint-Laurent	France	4	13 March 1980	nda	nda	nda
Buenos Aires	Argentina	4	23 September 1983	nda	[c]	nda
Tokaimura	Japan	4	30 September 1999	nda	nda	nda

[a] nda = no data available
[b] substantial emission of ^{85}Kr
[c] substantial ^{131}I emissions assumed, though nda
[d] mainly ^{85}Kr emitted
[e] no strong source of radioactivity to the atmosphere
[f] release of radioactivity sludge from filter powder to the environment

On 26 April 1986, reactor unit four of the Chernobyl nuclear power plant was dedicated for a system test. A sudden power excursion led to a reactor vessel rupture and a series of explosions. From this the reactor was damaged and the graphite moderator of the reactor was exposed to air, igniting a fire which lasted for ten days. During this time large amounts of fuel particles were released, the so-called "hot particles", carrying isotopes of cerium, zirconium, molybdenum, neptunium, and plutonium (Smith and Beresford, 2005; IAEA, 2006). The relatively large size of these particles caused them to settle quickly back onto the surface, mainly within an area of about 30 km around the reactor. However, the release of these particles was strongly dependent on the reactor type, which is now obsolete. More interesting also for newer reactor technologies is the release of the radionuclides that were emitted as gases which can attach to ambient aerosol particles, e.g., the semi-volatile isotopes of iodine, strontium, cesium, tellurium, ruthenium, and barium (^{131}I, ^{133}I, ^{89}Sr, ^{90}Sr, ^{134}Cs, ^{137}Cs, ^{132}Te , ^{103}Ru, ^{106}Ru, and ^{140}Ba). These radionuclides were mostly found on small particles with a radius of $r \leq 1\,\mu$m. Further information about the size distribution of radioactive aerosols is reported by Dorrian (1997).

In total more than 12,000 PBq[1] were released during the initial explosions and the fire. Anspaugh et al. (1988) estimated that the collective dose to humans was about 930,000 Gray[2]. A small fraction of the total emission was released as cesium-137, i.e., 85 PBq (about

---

[1] P is peta=10^{15}; radioactivity from radionuclides (unstable atoms) is measured in becquerel (Bq) where 1 Bq = 1 disintegration per second.

[2] Dose of ionizing radiation, expressed by 1 Gray, is equivalent to 1 Sievert (Sv) for gamma and beta radiation, which represents the absorption of 1 Joule by one kilogram of (generally living) matter.

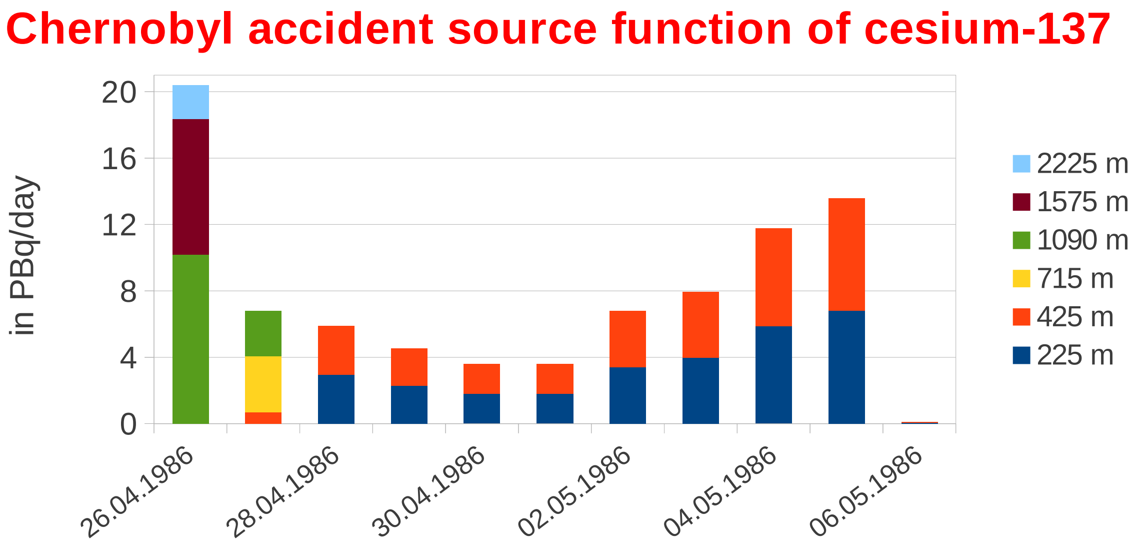

Figure 8.2: Chernobyl source function for cesium-137 for the first eleven days after the start of the accident. For each day the total release is plotted in 10^{15} Bq. The color-scaling indicates different effective emission heights between 225 m and 2225 m. The data were adopted from Brandt et al. (2002).

27 kg), which, however, is useful to track the long-range deposition, since it is easy to measure and radiologically important due to its long half-lifetime of 30 years (Smith and Beresford, 2005). A larger amount was released as iodine-131, i.e., 1760 PBq, but since it has a half-lifetime of only eight days its long-term consequences are less significant. In particular, in the first weeks after the release, the high levels of ^{131}I and consequently high radioactivity doses pose a potential threat to living beings since it can rapidly enter the food chain (IAEA, 2006; WHO, 2006; Christodouleas et al., 2011).

In Table 8.2, publicly available information[3] on the most severe accidents, following the International Nuclear Event Scale (INES)[4], is listed. This puts the emissions from Chernobyl into the perspective of other accidents. Only accidents which are classified as INES 4 or higher have been taken into account. The table shows that besides Chernobyl and Fukushima there is little reliable data available. However, the uncertainties in the data regarding Chernobyl and Fukushima are non-negligible.

The Chernobyl accident in 1986 provides an opportunity to test the transport from a small scale source point. The modeled ^{137}Cs deposition can be compared with a compilation-interpolation of measurement data first presented by De Cort et al. (1998) and further used by Smith and Beresford (2005). Passive aerosol tracers were released in EMAC simulations at the location of Chernobyl, with a source function see Figure (8.2), which varies in height and time and which had been presented first by Persson et al. (1986) and was adopted for regional modeling studies from Hass et al. (1990) and Brandt et al. (2002). The latest estimates using inverse modeling techniques confirmed the temporal release of radioactivity (Davoine and Bocquet, 2007). Since the final deposition data could not be made available upon request

---

[3] The data has been collected from Smith and Beresford (2005) and IAEA (2006) and also from (partly non-official) web pages: http://de.wikipedia.org/wiki/Liste_der_Kernkraftwerke, http://en.wikipedia.org/wiki/List_of_nuclear_reactors, http://www.iaea.org/programmes/a2/ and references therein, all last accessed on 25.09.2012.

[4] More information: http://www-ns.iaea.org/tech-areas/emergency/ines.asp, as of 26.09.2012.

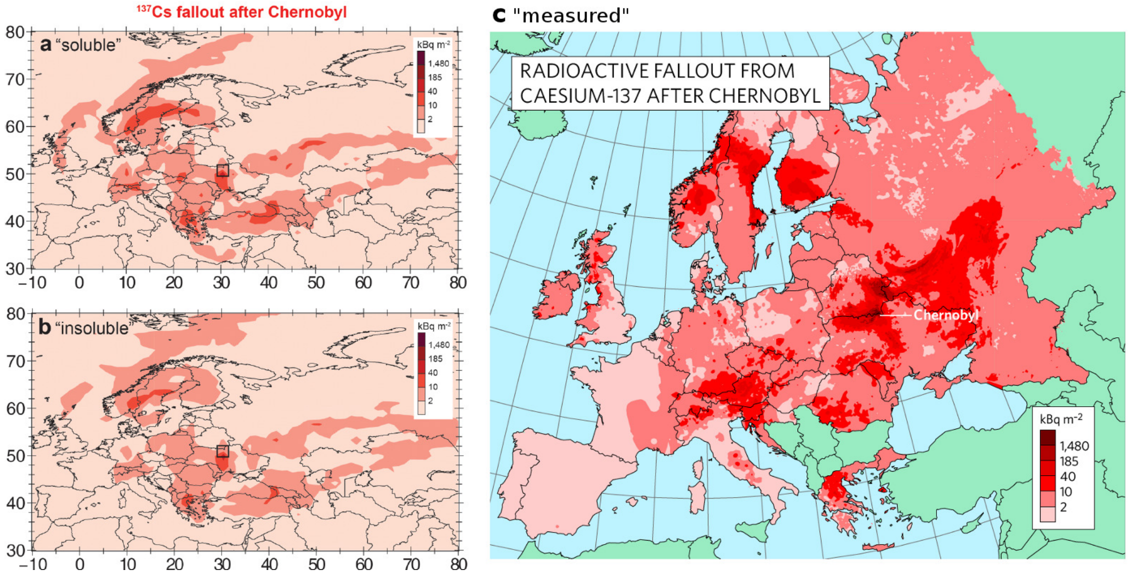

Figure 8.3: Cesium-137 deposition (in kBq m^{-2}) after Chernobyl from model output for a) the NS_{act} and b) the NS_{inact} tracer (Lelieveld et al., 2012a) as well as from c) compilation-interpolation of measurement data, originally published by De Cort et al. (1998), reprinted by Smith and Beresford (2005) and here adopted from Peplow (2006).

from the Radioactivity Environmental Monitoring Action of the European Commission, the model output was evaluated based on all available data (Smith and Beresford, 2005; Peplow, 2006), applying the same color scaling (compare left and right side of Figure 8.3). Since the chemical composition of the aerosols is not known, two simulations have been conducted like for the urban hot spots. In one case the tracers can be removed from the atmosphere by nucleation scavenging (NS_{act}) and in the other case they are not (NS_{inact}), while the mono-modal passive aerosol tracers have a diameter of 0.5 μm. Especially for the NS_{act} tracer, the model results show a qualitatively good agreement with the map of Peplow (2006), indicating largest ^{137}Cs deposition values in the Ukraine, Scandinavia, Northern Greece, southern Germany, and Austria. Quantitative agreement cannot be expected, since large particles are neglected and due to the difficulty of accurately simulating the emission time and height profiles. Considering the better agreement for the NS_{act} tracer, and since most airborne particles are soluble (Pruppacher and Klett, 2000), it is henceforth (in Section 8.4) assumed that 75 % of the aerosols are removed by nucleation scavenging, i.e., a mixture of 75 % soluble and 25 % insoluble aerosol particles. The modeled ^{137}Cs deposition distribution also compares favorably with the high-resolution regional model results of Brandt et al. (2002), which is notably the map for which the most sophisticated deposition method was applied.

8.2.2 Model configuration

Model version **A** is used to simulate the transport and deposition of the two radionuclides cesium-137 and iodine-131. Since cesium-137 attaches to the ambient aerosol, it is represented by passive aerosol tracers which have a diameter of 0.5 μm, a standard deviation of 1.0, and are removed from the atmosphere by dry and wet deposition like the passive aerosol tracers used in Chapters 4 and 5. The mean atmospheric residence times of such tracers is about one week, which is much shorter than the half-lifetime of 30 years for ^{137}Cs, and thus the aerosol deposition processes determine the atmospheric fate of cesium-137. In contrast, iodine-131 is assumed to travel in the gas phase as $^{131}I_2$. It is removed from the atmosphere by its radioactive decay (half-lifetime of 8 days) and by dry deposition for gases (see Section 2.2 Kerkweg et al. (2006a), and Ganzeveld et al. (1998)). A Henry's law coefficient for iodine of 3.1 $\mathrm{mol\,l^{-1}\,atm^{-1}}$ indicates its low solubility (Crutzen and Lawrence, 2000). A small fraction of the released iodine will also be present in other gas molecules and in the particulate phase, which is, however, not considered here, since this fraction is not known and thus is assumed to be removed just like the gas phase iodine.

For each reactor unit an emission is placed in the model grid box in which the reactor is located. The horizontal model resolution has been chosen to be T106 with 31 hybrid sigma-pressure levels in the vertical (for more details see Sections 2.2 and 4.2.1). In T106, 171 surface grid cells represent the 440 individual reactors as emission source points. All reactors within a grid cell are treated equally. To account for all reactors within these grid cells the deposition from the one representative tracer is multiplied by the number of reactors in the grid cell. The emission is released gradually so that the integrated emissions over one year are equal to the emission of ^{137}Cs (85 PBq) and ^{131}I (1760 PBq) from Chernobyl. The focus is then on the accumulated deposition field. By releasing the radionuclides gradually, different meteorological situations are captured throughout an entire year. In Section 8.4.4 it is demonstrated that annual accumulated deposition fields from the continuous emissions are comparable to the mean value of short-term emissions occurring during any single week of the year.

Furthermore, the emission from each reactor is scaled according to its gross capacity relative to the Chernobyl reactor unit four. Thus, a reactor with half the gross capacity of Chernobyl is assumed to emit half of the amount mentioned above. The emission is only placed in the lowest model layer, which results in lower estimates regarding long-range transport (compare Section 4.5). This is not entirely representative, since nuclear accidents are often attributed to rather explosive release of radionuclides or a release during fires, which increases the effective emission altitude. In Fukushima, however, substantial release of radioactivity occurred not only during the hydrogen explosions but also in the time thereafter. Nevertheless, there is no generally applicable source function for the release, thus this conservative approach is applied. Implications following from a release at higher altitudes are discussed in Section 4.5.

The model integration starts in July 2004 and ends in January 2006. The last twelve months are used for the analysis and the meteorology is weakly nudged towards ECMWF reanalysis data. Thus, the model configuration is equal to that one used for the urban emission hot spots, except for the number of tracers, the gas phase tracer properties, and the locations of the emissions. This offers the potential to compute the metrics defined in Section 3.2 for the NPPs and compare the regional pollution potentials between NPP and MPC tracers.

8.3 Pollution potentials from nuclear power plants

The outflow of pollutants from NPPs has been analyzed in the same way as was done in the previous chapters for major population centers and the results are compared to the re-

Table 8.3: Annual mean pollution potentials (averaged over all source points) from NPPs and MPCs for $\mathrm{NS}_{\mathrm{act}}$ and $\mathrm{NS}_{\mathrm{inact}}$ 0.5 µm tracers. Units are in % for all pollution potentials except for A_{10} (in $10^6\,\mathrm{km}^2$).

	$\mathrm{NS}_{\mathrm{act}}$		$\mathrm{NS}_{\mathrm{inact}}$	
	MPC	NPP	MPC	NPP
E_{UT}	3.00	1.91	4.18	2.56
ELR_{1km}	16.15	21.40	20.04	26.44
$RCL_{\mathrm{0.5km}}$	13.76	13.84	10.00	9.78
A_{10}	2.54	2.70	3.41	3.83
DRT	44.27	44.91	54.95	57.07

sults for the MPCs. For this the pollution potentials have been calculated for the upper troposphere (E_{UT}), the low-level remote outflow (ELR_{1km}), the local retention ($RCL_{\mathrm{0.5km}}$), and the remote deposition (DRT) as well as the area of tracer density threshold exceedance (A_{10}). The simulations have been performed with emissions of $1\,\mathrm{kg\,s^{-1}}$, released at the 171 different NPP source locations on the T106 grid. Mono-modal aerosol tracers with a diameter of 0.5 µm are used, the same as used for the MPCs.

Table 8.3 shows the annual means of NPP- and MPC-averaged pollution potentials. The emissions from NPPs are exported more at low levels and less in the vertical direction, while the pollution build-up around the sources is similar for both source types. The higher low-level pollution, indicated by ELR_{1km} and A_{10}, results from an over-proportional number of NPPs at mid-latitudes in either a temperate no dry season (Cf, 60 % of the source points) or a cold (D, 27 % of the source points) climate. In contrast, among the MPC emission sources only 35 % (Cf) and 8.5 % (D) are located in these two climate classes, respectively. Each of the other climate classes contains only $3-4$ % of the NPP sources, while the MPCs are more evenly distributed over all climate classes: 19.5 % in tropical regions, 15 % in arid regions, 13 % in temperate dry summer regions, and 8.5 % in temperate dry winter regions. Interestingly, although the vertical export is weaker and additionally a relatively small number of NPPs are in arid regions, the remote deposition potentials are very similar with a difference less than 5 %. This is, however, due to several balancing effects as seen in Table 8.4.

The influence of local conditions, especially surface winds and the height of the boundary layer, can cause large deviations between climate class means when the sources are distributed differently within the climate classes (see Table 8.4). Recall that the climate classes are solely based on temperature and precipitation (see also the discussion about the variation in the climate class means in Section 5.4). Thus, the emission source locations determine to a large extent the means in each climate class. For example, in tropical regions the vertical transport is stronger for the MPCs and the low-level export stronger for NPPs, in both cases the difference being about a factor of two. The NPPs attributed to the tropical climate class are located in Mexico, Florida, and in South India. These regions are not as intensely influenced by tropical convection and precipitation, as is the case throughout the entire year for the MPCs Lagos, Manila, and Jakarta.

Table 8.4: Annual mean pollution potentials (averaged over all source points) for NPPs and MPCs for $\mathrm{NS_{act}}$ and $\mathrm{NS_{inact}}$ 0.5 µm tracers for all climate class: A (tropics), B (arid), Cf (temperate no dry season), Cs (temperate dry summer), Cw (temperate dry winter), and D (cold). Units are in % for all pollution potentials except for A_{10} (in $10^6\,\mathrm{km}^2$).

$\mathrm{NS_{act}}$		E_{UT}	ELR_{1km}	$RCL_{\mathrm{0.5km}}$	A_{10}	DRT
A	MPC	2.92	11.66	15.83	1.65	32.10
	NPP	1.77	25.61	11.54	2.57	46.87
B	MPC	3.72	18.34	8.52	4.39	71.88
	NPP	1.28	27.40	14.15	2.00	45.37
Cf	MPC	2.31	16.98	16.05	1.89	37.00
	NPP	1.38	27.15	13.69	2.05	45.33
Cs	MPC	3.41	20.60	9.01	3.56	50.56
	NPP	1.49	26.74	13.39	2.16	46.19
Cw	MPC	4.45	11.10	13.78	1.88	39.23
	NPP	1.82	25.33	11.23	2.49	45.55
D	MPC	1.57	23.72	14.71	3.90	53.18
	NPP	2.03	24.89	10.74	2.87	45.00
$\mathrm{NS_{inact}}$		E_{UT}	ELR_{1km}	$RCL_{\mathrm{0.5km}}$	A_{10}	DRT
A	MPC	5.00	14.01	11.86	2.16	41.21
	NPP	2.23	31.55	7.75	4.20	61.83
B	MPC	4.70	21.13	6.91	5.81	80.53
	NPP	1.71	34.49	8.58	3.22	64.44
Cf	MPC	3.29	22.70	10.85	2.66	49.98
	NPP	1.80	33.91	8.63	3.18	64.63
Cs	MPC	3.85	24.49	6.96	5.31	64.37
	NPP	1.92	33.14	8.69	3.28	62.15
Cw	MPC	5.93	14.19	9.89	2.35	49.89
	NPP	2.28	31.15	7.69	3.85	59.65
D	MPC	2.03	27.55	11.33	4.80	59.20
	NPP	2.51	30.08	7.55	4.27	58.58

8.4 Global and regional risk of nuclear reactor accidents

8.4.1 Major accidents

Table 8.2 lists the most severe accidents according to the International Nuclear Event Scale (INES). In total there have been about 20 core melts (total or partial) worldwide in civilian and military reactors (Burns et al., 2012). INES ranges from 0 (no safety significance) to 7 (major accidents). So far, nuclear accidents have been classified as major accidents when the reactor unit was damaged associated with a total core melt and destruction of the containment (if present). In total four reactor units, one in Chernobyl and three in Fukushima, have been classified as INES 7 accidents.

The probability of a core melt was estimated from different institutions in the last 40 years. In 1975 the US Nuclear Regulatory Commission (NRC) estimated the probability of a core melt at 1 in 20,000 per year for a single reactor (NRC, 1975). In a follow-up report in 1990 they stated that the core damage frequency is nothing which can be calculated with certainty, although a number for the core melt probability of 1 in 10,000 per year per reactor was given in the appendix of NRC (1990). Moreover, probabilities of containment failure (1 in 100), unfavorable wind direction (1 in 10), meteorological inversion (1 in 10), and evacuation failure (1 in 10) are listed in the appendix. Following NRC (1990), these probabilities indicate the likelihood of a catastrophic accident, which is assessed to be 1 in 1 billion per year for a single reactor since they assume that the probabilities are independent. However, this is not the case in reality. Another study by the German Gesellschaft für Reaktorsicherheit (GRS) assessed the probability of a core melt to be about 1 in 3.6 million per year (GRS, 1990). These probabilities are low compared to the frequency with which core melts occurred so far.

The probabilities of a core melt can be put into perspective using empirical data. Taking into account only civilian used nuclear power plants and major accidents, i.e., INES 7, four full core melts occurred. The total number of full operational reactor years of all reactors which produced energy between 1954 and 2011 sums up to 14,500 years. This indicates that in reality a core melt occurred once every 3625 active reactor years. This is about three times higher than the last estimate of a core melt probability in NRC (1990). However, since 2011 was at a junction in time with impacts of the last major accident still unfolding, this estimate will be high-biased, and therefore the probability is rounded off to 1 in 5000 per year for a single reactor. This value is then only a factor of two larger than the estimated value in NRC (1990).

Moreover, the Chernobyl reactor type had no containment and the containments in Fukushima failed. Based on the past evidence, this principally assumes that if a major accident occurs, the probability of containment before substantial release of radioactivity is very small. Thus, any probability about the failure of the containment is further neglected, since it does not fit to the historical data. The same is considered for probabilities about unfavorable wind directions or meteorological inversions. Using numerical models results in better representation of these factors, with several approaches applicable, e.g., deterministic approaches (http://flexrisk.boku.ac.at) or probabilistic approaches (Baklanov and Mahura, 2004). A last point which has to be accounted for to call an accident a catastrophic event is the evacuation of humans in the affected areas around an NPP. Although the evacuation can be successful in saving human lives by reducing direct health effects (e.g., radiation exposition, leukemia, tumors, see Christodouleas et al., 2011), large areas around the reactors are made uninhabitable for decades afterwards. Bromet et al. (2011) reviews psychological consequences for humans who have been affected by the Chernobyl accident. They report that mental health effects were the most significant public health consequence of the accident. Therefore, contrary to NRC (1990), the probability of evacuation is excluded in computing the probability of a major accident, since for the existing NPPs, all near populated regions, it seems very unlikely based on historical experience that an accident which releases significant amounts of radioactivity will not have major affects on humans.

The probability of a major accident in the past thus depends only on the full reactor years (14,500) and the number of core melts in civilian nuclear reactors which have been classified as INES 7; as a first estimate, this is also applied to the probability of future major accidents, recognizing that there are many uncertainties that may make this an overestimate or underestimate, such as improvements in safety standards, the growing NPP fleet, and terrorist attacks. The rounded estimate implies that with 440 reactors worldwide a major accident can be expected to occur about every few decades, depending on whether Fukushima is counted as a triple or a single event. Note that with Fukushima counted as a single event, the probability of a major accident is about the same as the core melt frequency reported by NRC (1990).

8.4.2 Risk of contamination

After the Chernobyl accident, large areas have been declared to be contaminated. For this the surface deposition of ^{137}Cs had to exceed $37\,\mathrm{kBq}\,^{137}\mathrm{Cs}\,\mathrm{m}^{-2}$, or $40\,\mathrm{kBq}\,\mathrm{m}^{-2}$ for beta- and gamma-emitters (IAEA, 2005, 2006). Two reasons for this threshold are given by IAEA (2006):

- This level was about ten times higher than the ^{137}Cs deposition in Europe from global fallout.
- At this level the human dose during the first year after the major accident was about 1 mSv and was considered to be radiologically important.

Following this, regions with accumulated deposition $\geq 40\,\mathrm{kBq}\,\mathrm{m}^{-2}$ are defined as contaminated. The cumulative, time-integrated risk of contamination for fallout from ^{137}Cs is consequently computed based on the following expression:

$$\begin{aligned}\text{Risk of Contamination} \;=\; & \frac{\text{modeled total } ^{137}\text{Cs deposition in kBq}\,\mathrm{m}^{-2}\,\mathrm{yr}^{-1}}{40\,\mathrm{kBq}\,\mathrm{m}^{-2}} \\ & \times \text{ probability of a major accident} \quad . \qquad (8.1)\end{aligned}$$

Consequently, the presented cumulative risk maps are directly proportional to the original modeled deposition fields of ^{137}Cs from all nuclear reactors.

Figure 8.4 shows the modeled annual risk of contamination by ^{137}Cs, which varies from less than 0.01 %/yr in regions of the Northern Hemisphere (Alaska, western China, northern Africa) to more than 2 %/yr in the areas with high NPP densities in the north-eastern US, western Europe, and Japan. These numbers signify the expected value, defined as the weighted average (first moment) of an independent variable of all possible values it can take. The weights correspond to the probabilities of these values. This means, for example, that on average in the Northeast US, West Europe, and Japan, contamination by major accidents is expected at least every 50 years, which is roughly in accord with the frequency of the past events in Europe and Japan. In Figure 8.5, zooms of the regions with high NPP density show that large areas have a risk of > 0.1 %/yr (orange color scale).

For ^{131}I no level of contamination is specified. However, if $40\,\mathrm{kBq}\,\mathrm{m}^{-2}$ is applied to define contamination, then the deposition patterns over land and the risks of contamination are quite comparable to ^{137}Cs (see Figures 8.6 and 8.7). Although the release of radioactivity in Chernobyl was ~20 times higher for ^{131}I than for ^{137}Cs, the low solubility of iodine and the much shorter lifetime limit deposition, in particular over water surfaces. The two radionuclides are used as proxies for the total release of radionuclides. The risks scale with

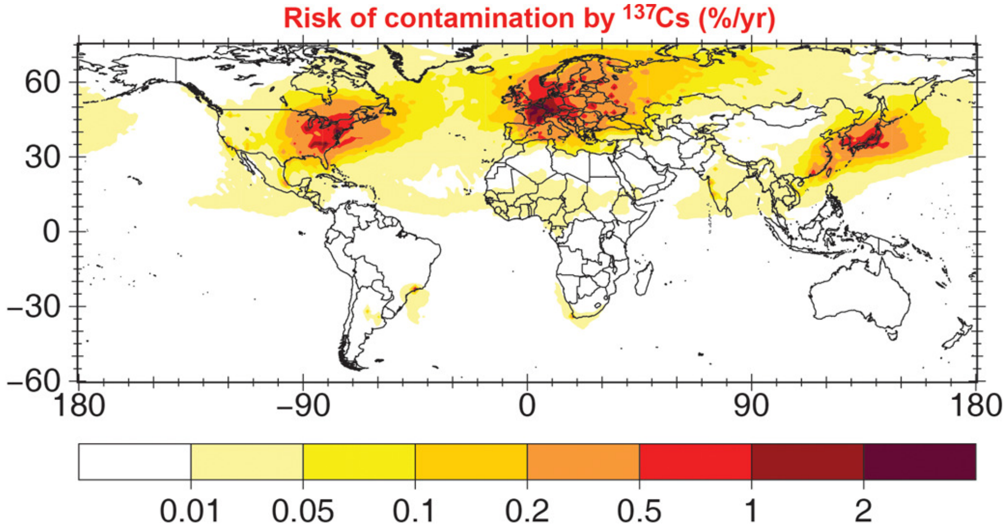

Figure 8.4: Global risk of radioactive contamination by ^{137}Cs based on the annually accumulated, modeled deposition of ^{137}Cs (in %/yr). The risk is the expected value normalized by 40 kBq m^{-2}. This figure has also been published in Lelieveld et al. (2012a).

the addition of other tracers such as ^{134}Cs and ^{90}Sr. However, then the half-lifetime has to be considered, since the different radionuclides have different effects on various timescales. For example, with a half-life of eight days, ^{131}I is of great concern in the initial phase after accidents, since it is then present in large amounts and deposits on agricultural crops, contaminating fruits, herbs, and vegetables, and on grasslands where dairy cows graze (IAEA, 2006; Christodouleas et al., 2011). Once it has entered the food chain, it can concentrate in the thyroid and potentially increase the long-term cancer risks (WHO, 2006; Christodouleas et al., 2011). In contrast, due to its longer half-lifetime of 30 years, ^{137}Cs poses an enduring threat to the fauna through forage and to humans through meat, milk, and to a lesser extent vegetables (IAEA, 2006; WHO, 2006).

Using the emissions from Chernobyl may cause the estimated risk of contamination to be high-biased and be less representative due to the design of the RBMK reactor in Chernobyl. First estimates of the release of radioactivity during the weeks after the Fukushima accident are substantially lower than for Chernobyl. Chino et al. (2011) estimated the emissions to be ~ 140 PBq for ^{131}I and ~ 10 PBq for ^{137}Cs, Winiarek et al. (2012) estimated them to be a factor of $5-10$ less than of Chernobyl. Stohl et al. (2012) calculated that during a period of 40 days after the accident ~ 37 PBq ^{137}Cs were released, about 43 % of the emission by

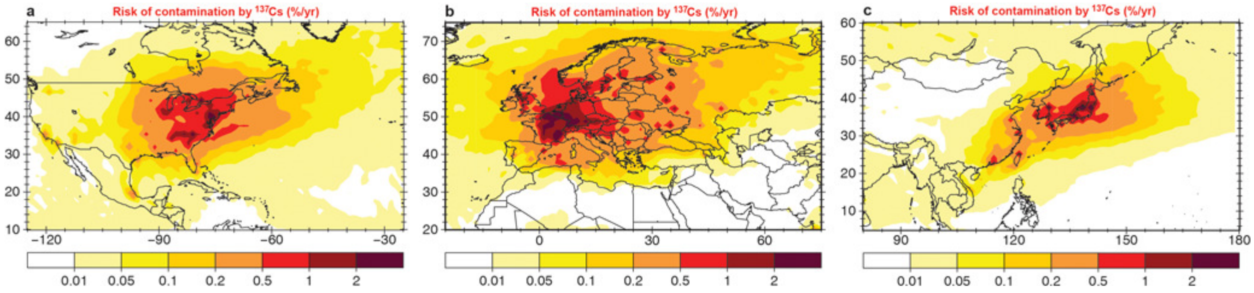

Figure 8.5: Regional risk of contamination by ^{137}Cs. Same as Figure 8.4 for selected regions. This figure has also been published in Lelieveld et al. (2012a).

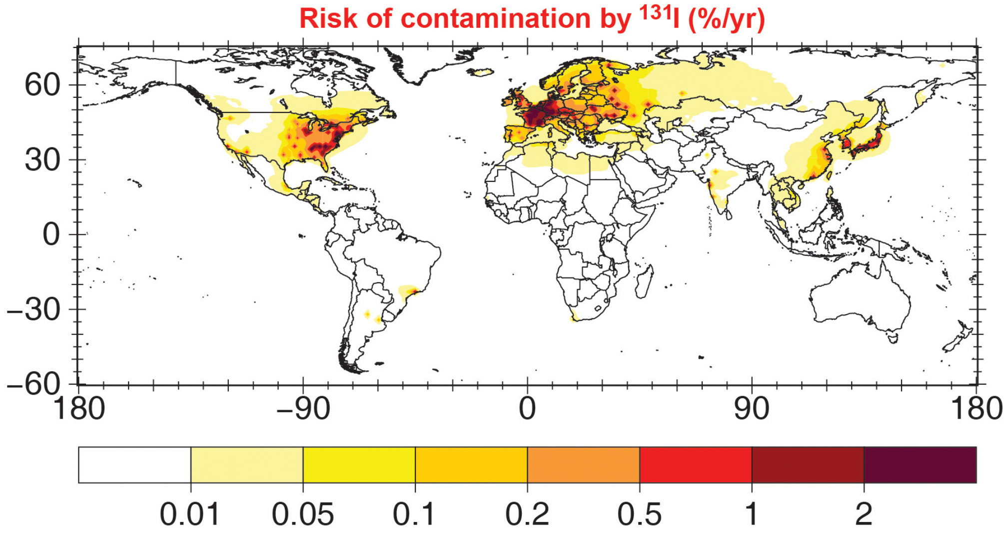

Figure 8.6: Global risk of radioactive contamination by ^{131}I based on the annually accumulated, modeled deposition of ^{131}I (in %/yr). The risk is the expected value normalized by 40 kBq m^{-2}. This figure has also been published in Lelieveld et al. (2012a).

Chernobyl. If the latter would be more representative of contemporary and future accidents associated with core melts than Chernobyl, the numbers in Figures 8.4 – 8.7 would decrease by about a factor of seven (recall that three reactors experienced a core melt). However, as noted above, there are many other uncertainty factors acting in both directions.

These results represent a probabilistic assessment that is representative for an entire year and the accumulated deposition fields are integrated over the annual range of weather conditions, thus accounting for the temporal and spatial variability of transport and removal processes (Baklanov and Mahura, 2004). The major accidents in Chernobyl and Fukushima demonstrated that most of the radioactivity emissions occur within the first month after the accident. To gain an impression of the seasonal cycle of the risks of ^{137}Cs, more simulations have been performed in which the emission was condensed into one month. Hence, the total deposition in one month is approximately the same as in Figure 8.4, but the distribution differs depending on the meteorological conditions specific to the month of release (see Figure 8.8). On the Northern Hemisphere, in particular at middle latitudes, the risk is lowest in winter in the USA, Europe, and Japan. In Europe it is highest in late spring and summer, in Japan from June to September, and in Northeast America during late summer to November. In winter the outflow in the westerlies from the North America and East Asia is

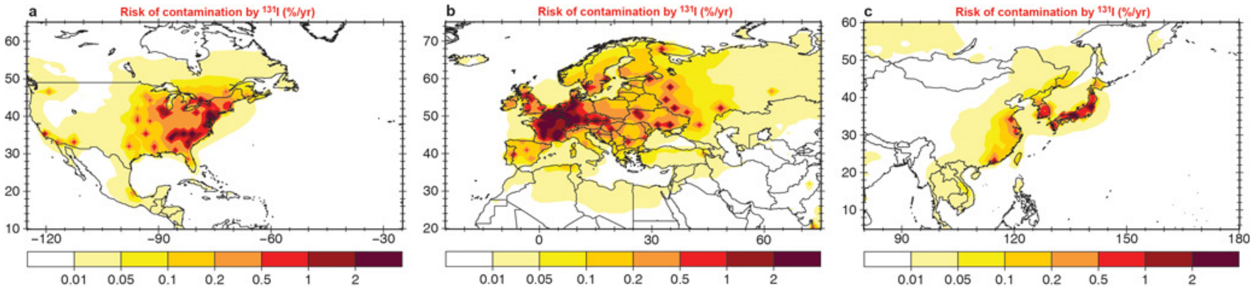

Figure 8.7: Regional risk of contamination by ^{131}I. Same as Figure 8.6 for selected regions. This figure has also been published in Lelieveld et al. (2012a).

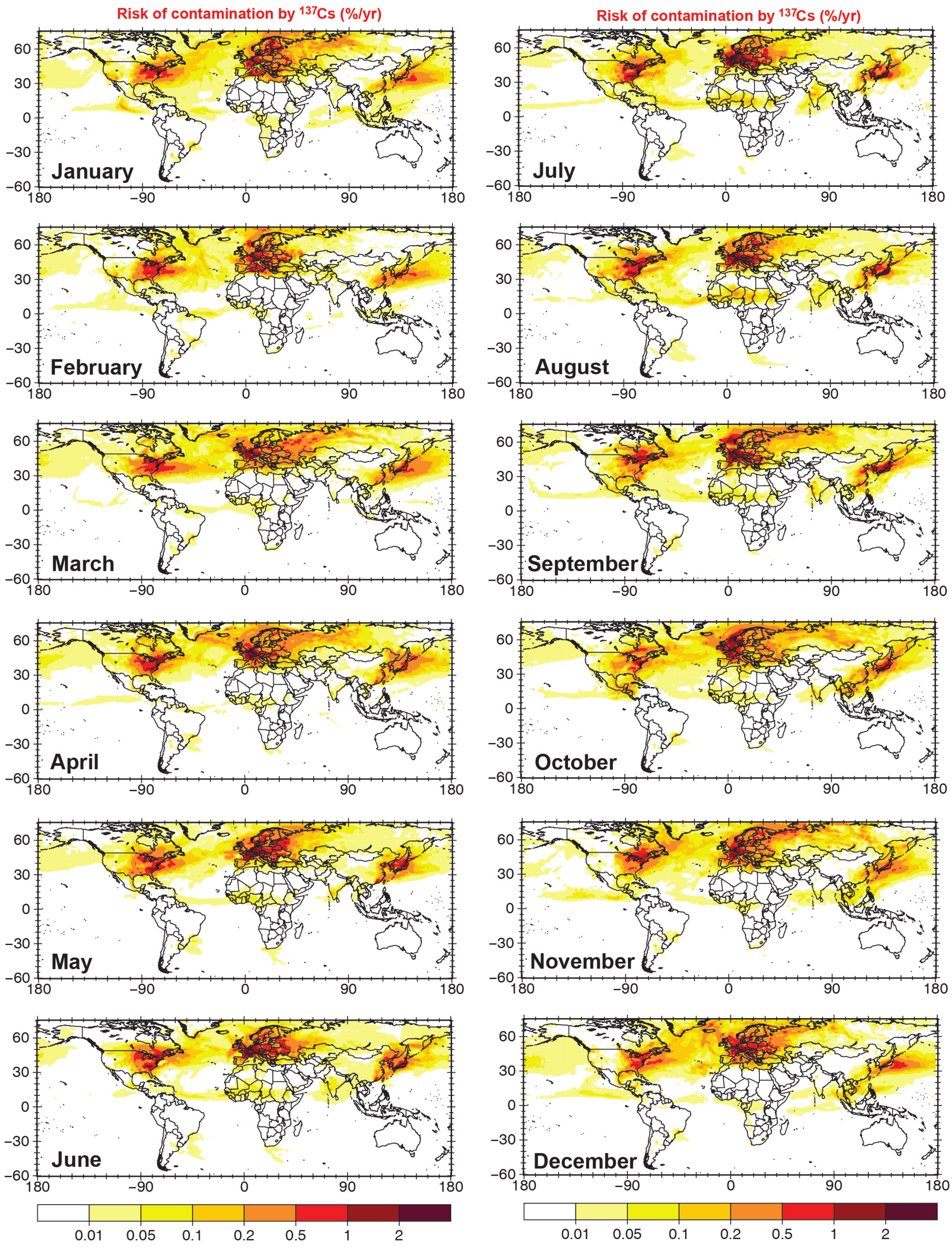

Figure 8.8: Global risk of radioactive contamination by ^{137}Cs based on the monthly accumulated, modeled deposition of ^{137}Cs, applying the same emission as in Figure 8.4, though monthly instead of annually. This figure has also been published in Lelieveld et al. (2012a).

strongest, thus diverting the risk over the Atlantic and Pacific Oceans; in Europe the outflow is directed towards the Arctic region and across Russia. In summer the westerlies are weaker at mid-latitudes, the flow is more stagnant in predominating high pressure systems.

8.4.3 Footprint of major accidents

The footprint of major accidents is calculated next for the annual deposition. For this the area around a nuclear reactor onto which more than $40\,\mathrm{kBq}\,{}^{137}\mathrm{Cs}\,\mathrm{m}^{-2}$ are deposited after an accident is calculated, as well as the number of people living in this area. On average a region of $138,000\,\mathrm{km}^2$ is affected with a range of about $\pm 20\,\%$. The largest area affected by a single reactor accident is found in West Europe with about $168,000\,\mathrm{km}^2$, followed by East Asia with $153,000\,\mathrm{km}^2$, East USA with $148,000\,\mathrm{km}^2$, $140,000\,\mathrm{km}^2$ in Midwest USA, $129,000\,\mathrm{km}^2$ in North Europe, and $102,000\,\mathrm{km}^2$ in South Asia.

The variability is mainly related to differences in the ventilation of the surface layer, especially by vertical lifting in convective storms and by removal in precipitation, which is consistent with finding of Lawrence et al. (2007) and findings in Chapter 4. There it is shown that the venting of pollutants is strongest in the tropics (e.g., South Asia) and in temperate dry winter regions, whereas radionuclides emitted by NPPs in the middle latitudes tend to remain more in the boundary layer over longer low-level transport distances. To compute the number of people affected by a single reactor accident, the population distribution described in Section 3.4 (Socioeconomic Data and Applications Center (SEDAC), 2005) is used. The average number of people that would be affected varies strongly by region, depending on the regional population density. In North Europe about 3 million people live in the area that would be affected by more than $40\,\mathrm{kBq}\,{}^{137}\mathrm{Cs}\,\mathrm{m}^{-2}$, 8 million in the Midwest USA and in East Europe, 14 million in East USA, 21 million in East Asia, 28 million in West Europe, and 34 million in South Asia.

To put these numbers in perspective, it is possible to compare them to the corresponding numbers from Chernobyl. In 1986 an area of about $200,000\,\mathrm{km}^2$ was contaminated, and more than 5 million people were affected (Smith and Beresford, 2005). For 2005 conditions, according to the model simulations, $113,000\,\mathrm{km}^2$ and about eight million people would have been contaminated around Chernobyl[5]. In general, the highest risks are found in the vicinity of large agglomerations in North America, e.g., the Boston-to-Washington region and Japan around Tokyo and Osaka. The largest risk of radioactive contamination occurs in West Europe, especially around the borders of Germany, Belgium and France.

8.4.4 Sensitivity to annual and short-term emissions

The simulations have been performed with continuous, constant sources of radioactivity throughout the year 2005 from each reactor. This reduces the computational expense dramatically (by more than a factor of 50) compared to considering shorter duration emissions. From these annual, continuous release simulations, the fallout and consequently the risk of

---

[5] For the 1986 simulation, this number is an order of magnitude smaller. For the $\mathrm{NS}_{\mathrm{act}}$ tracer 25,300 km^2 and for the $\mathrm{NS}_{\mathrm{act}}$ tracer 10,500 km^2 are affected. The numbers are smaller due to the effects discussed in the text above.

contamination was calculated, thus accounting for the annual range of meteorological conditions. In the last section the contamination risk was additionally presented for a monthly release. However, employing a continuous long-term source might not be considered as a realistic scenario for major accidents, since the past showed that most radioactivity was released within the first days to weeks[6].

A real accident can unfold in many different ways, thus a general source term is not available. However, to test the sensitivity of the results to using a continuous, long-term source versus short-term emissions, additional model calculations have been performed. For two locations, Fukushima and Chernobyl, the same amount of ^{137}Cs was released during each week of the year 2005 as was emitted in the entire year in the standard, continuous emission simulations discussed above. For both emission locations, 52 independent deposition fields from the weekly release are obtained which are integrated between the beginning of 2005 and the end of March 2006 when only a negligible fraction ($< 0.01\,\%$) of tracer mass is still in the atmosphere even for tracers emitted in the last week of December. An averaged deposition field is assessed from the 52 deposition fields which is then compared to the deposition field from the continuous annual emissions.

Figure 8.9 shows the atmospheric burden of ^{137}Cs resulting from each of the weekly emission events. In most cases the radioactivity is removed from the atmosphere within a month. The lifetimes of the aerosols are largest during periods with low rain frequency, e.g., for Chernobyl in April and September. For Fukushima the variability is lower throughout the year. Most removal, i.e., the shortest lifetime, is simulated during summer (end of June-August) and the longest atmospheric residence times during April and the beginning of November. The

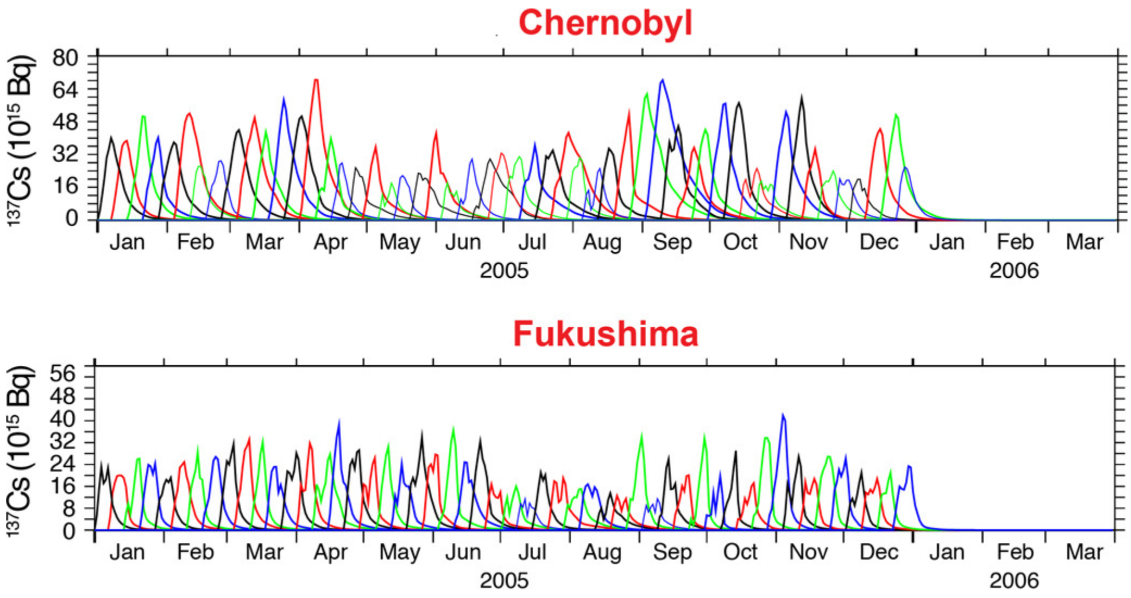

Figure 8.9: Atmospheric load of ^{137}Cs (in 10^{15} Bq) by applying the emissions of Chernobyl (85 PBq) each week. The simulations were performed for the locations of Chernobyl and Fukushima, applying the same source term. This figure has also been published in Lelieveld et al. (2012a).

---

[6] For more details it is referred to the interactive discussion in Atmospheric Chemistry and Physics Discussion, see: http://www.atmos-chem-phys-discuss.net/11/31207/2011/acpd-11-31207-2011-discussion.html

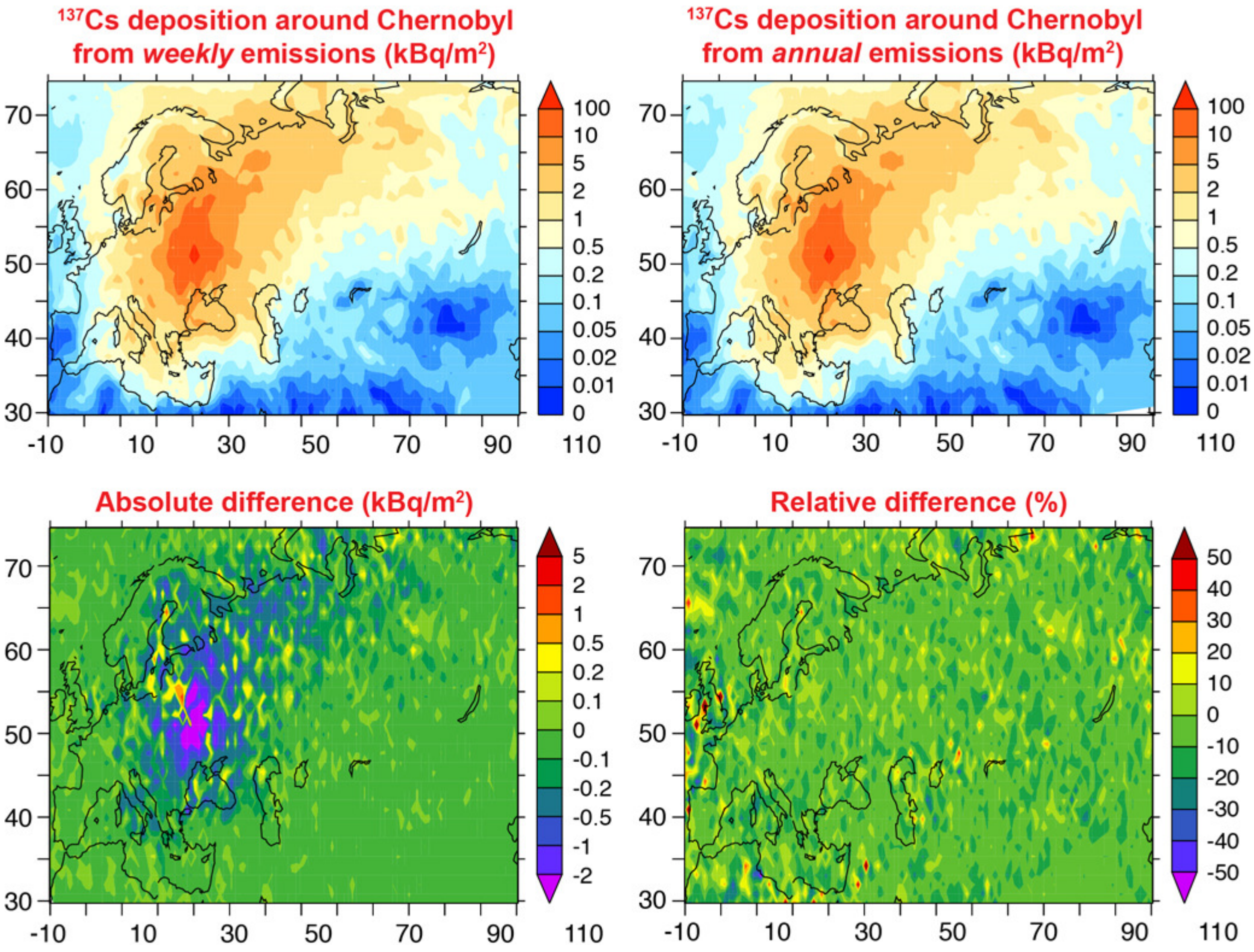

Figure 8.10: Yearly-integrated fallout of ^{137}Cs (year 2005), comparing annually continuous to weekly emissions $\left(\text{absolute}: \ \text{weekly} - \text{annual}, \ \text{and relative}: \ \frac{\text{weekly}-\text{annual}}{\text{weekly}}\right)$, both having the same total source strength of Chernobyl, released from the location of Chernobyl. This figure has also been published in Lelieveld et al. (2012a).

maximum atmospheric loads per week are larger for Chernobyl ($\sim 20 - 70\,\mathrm{PBq}\,^{137}$Cs) than from the same emission in Fukushima ($\sim 10 - 40\,\mathrm{PBq}\,^{137}$Cs). Thus, the removal of aerosol particles is more efficient for Fukushima, since the outflow from East Asia often occurs in frontal systems.

Figures 8.10 and 8.11 compare the cesium-137 fallout patterns of the mean of the weekly and the annual emission simulations. In the case of Chernobyl, the absolute difference (annual - weekly) is small, the relative difference shows only deviations between $\pm 10\,\%$. For Fukushima the differences are somewhat larger, probably a result of the generally higher dependence on the prevailing weather conditions. Nevertheless, the differences are generally small, mostly below $20\,\%$, thus corroborating the validity of the approach. For Fukushima, however, the approach could lead to a conservative estimate of the contamination impact after major accidents.

Different ways to calculate the area of contamination provide further evidence that the continuous release results in a rather conservative estimate of the risks. The area of contamination only differs slightly between the annual and the mean of the weekly deposition field: 184,000 km^2 (annual) to 172,000 km^2 (mean of weekly) for Fukushima and 113,000

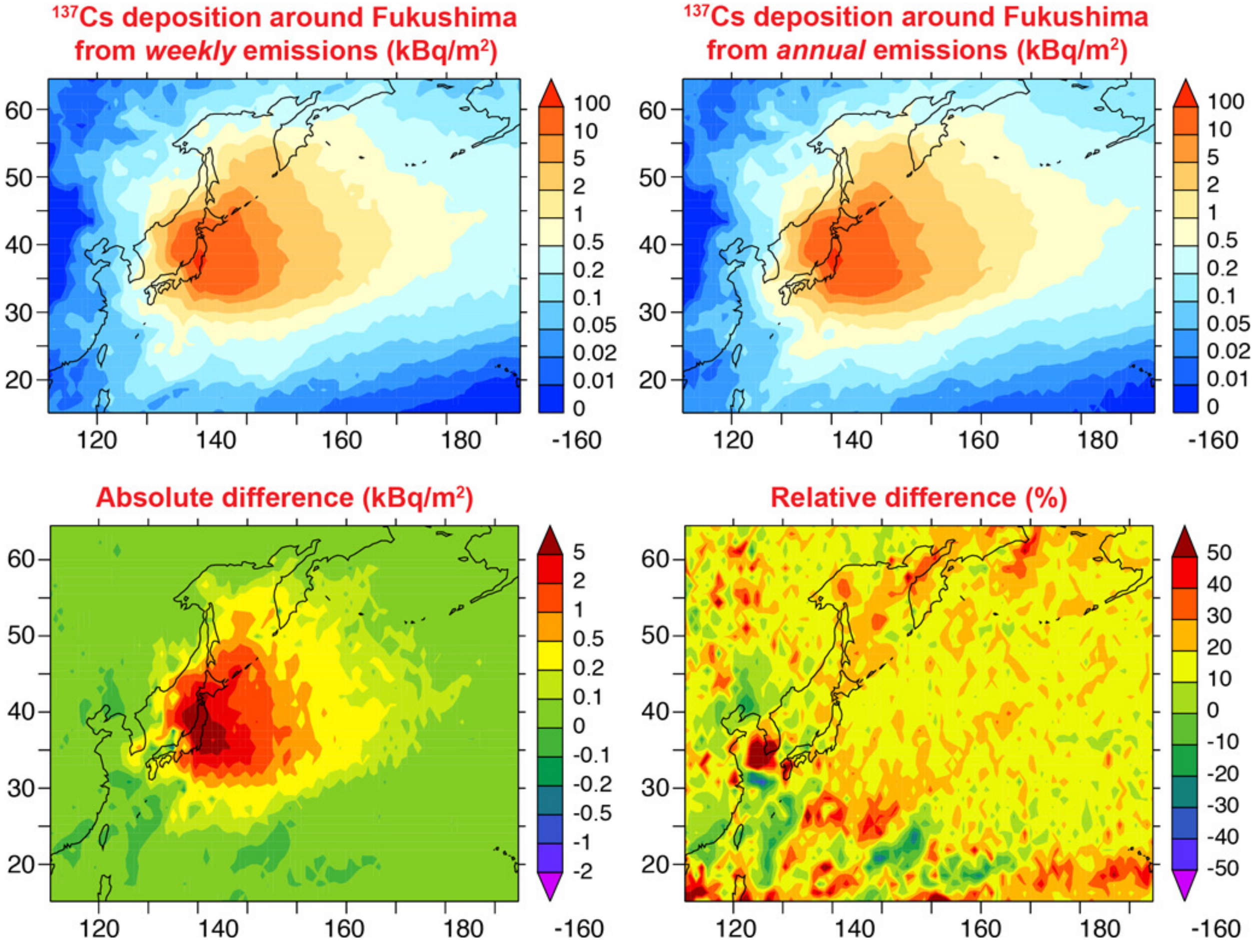

Figure 8.11: Yearly-integrated fallout of ^{137}Cs (year 2005), comparing annually continuous to weekly emissions $\left(\text{absolute: weekly} - \text{annual, and relative: } \frac{\text{weekly}-\text{annual}}{\text{weekly}}\right)$, both having the same total source strength of Chernobyl, released from the location of Fukushima. This figure has also been published in Lelieveld et al. (2012a).

km^2 (annual) to 107,000 km^2 (mean of weekly). In contrast, if the area of contamination is first calculated for each weekly release and then averaged, the area increases by about a factor of two in both cases. For the weekly emissions the outflow plume has a much higher concentration of radioactivity. Since most of the small aerosol tracers are scavenged in clouds and in precipitation, much of the radioactivity is simultaneously removed. Thus, an area might become contaminated by a single removal event, which would not necessarily be the case for the gradual release. Since the concentration of radioactivity is lower in this case, too little radioactivity might be deposited to immediately contaminate an area. Hence, for the continuous source more removal events are generally needed to obtain enough radioactive deposition to contaminate a particular area.

8.4.5 Phase-out of nuclear power plants

After the major accident in Fukushima several governments decided that they would either systematically phase out of nuclear energy production (e.g., Germany) or will not consider it in the future (e.g., Italy). This was decided on for many reasons but the question arises how the risk of contamination changes due to a country's phase-out. Figure 8.12a presents

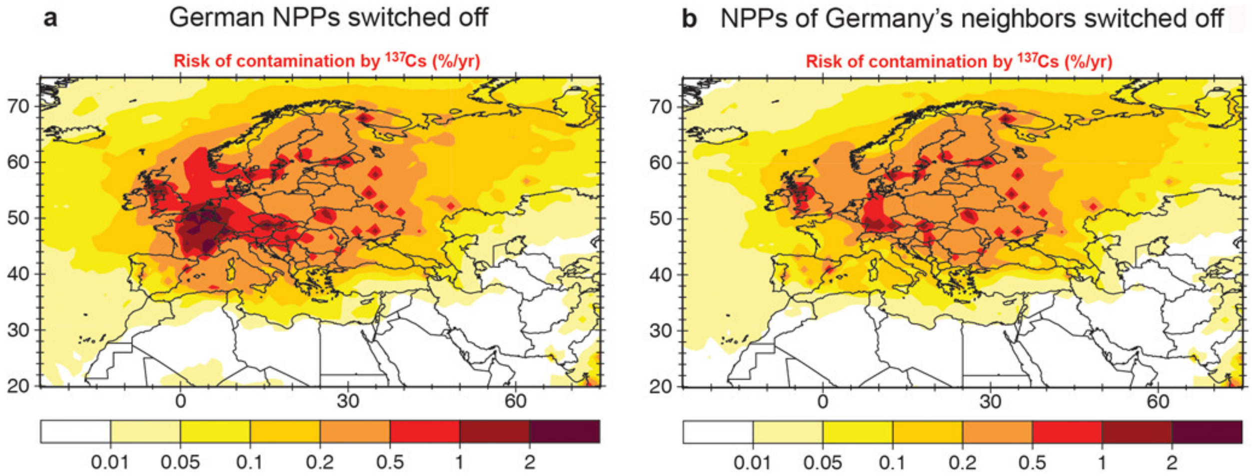

Figure 8.12: Phasing out nuclear power plants. a) Same as Figure 8.5b, indicating the regional risks of contamination by ^{137}Cs with German reactors switched off. b) Same as Figure 8.5b with reactors in the neighboring countries of Germany switched off, i.e., France, Belgium, the Netherlands, Switzerland, and the Czech Republic. This figure has also been published in Lelieveld et al. (2012a).

calculations in which all 17 German reactors have been switched off, which cuts the risk in half in Germany, though it still is one of the highest worldwide. Figure 8.12b shows the risk computed upon switching off the reactors in neighboring countries, i.e., France, Belgium, the Netherlands, Switzerland, and the Czech Republic, but leaving all 17 German reactors active. The risk in Germany is more efficiently reduced in this case than by the national efforts alone. This emphasizes that trans-boundary coordination is required if the goal is set to effectively reduce the risk of exposure to radioactivity, especially when NPPs are located in the vicinity of international borders.

8.5 Summary and discussion

In this chapter the locations of nuclear power plants were applied to study the transport and subsequent deposition of radionuclides released during major nuclear reactor accidents. The most prominent and well documented major accident occurred in Chernobyl in 1986. For ten days radionuclides such as cesium-137 and iodine-131, which have the potential for long-range transport, where released during initial explosions and a following fire. The radioactive fallout of cesium-137 was measured afterwards, which provides the opportunity of testing the transport and deposition patterns in the model. An emission source function was applied, which has been widely used in regional modeling studies. The resulting deposition field qualitatively matches the observations, though shows an underestimation of the peak values, because of the uncertainties in the emission source function and the still coarse model resolution.

Moreover, pollution potentials from nuclear power plants show different results than those from MPCs. Most of the nuclear power plants are located in the middle latitudes, whereas major population centers are more evenly distributed in tropical, sub-tropical, and extra-tropical regions. This results in relatively more low-level (25 % more than for MPCs), rather than vertical (33 % less than for MPCs) export from the nuclear power plants. Nevertheless, the long-range transport, measured as the remote deposition potential, is of almost equal magnitude for both source types.

Finally, generic aerosol and gas phase tracers have been applied to conduct a risk assessment study with the main objective to obtain a global map of the risk of contamination by major accidents. The risk of contamination depends on the probability of a major accident, the deposition field of the radionuclide, here cesium-137, and a deposition threshold, here $40\,\mathrm{kBq\,m^{-2}}$. This risk is highest in western Europe, the eastern US, and in Japan, where on average contamination by major accidents is expected about every 50 years, which is in accord with the frequency of the past events in Europe and Japan. However, there are many uncertainties in this calculation.

First of all, the empirically derived probability of a major accident is equally used for all types of nuclear reactors. The risk profiles need further scrutiny by accounting for several aspects such as: reactor type and capacity, reactor maintenance, safety culture, human factors, safety improvements with the progress of technology, degradation of the concrete reactor shell with age, likelihood of natural disasters (tsunamis, earthquakes), and the susceptibility of aircraft impacts, sabotage, and terrorist attacks. Additionally, the probability of major accidents may be derived from a combined empirical and statistical analysis of nuclear accidents. The empirical probability given here deviates by a factor of two from the probability of core melts given by NRC (1990). A re-assessment by using for example statistical extreme value distributions, for instance the Poisson distribution, may increase the confidence in these numbers. Furthermore, the emission scenario needs to be re-considered. For this assessment, the emission data for cesium-137 and iodine-131 from Chernobyl has been applied, since until today this data set has the lowest but still large uncertainties. In general, the information on such data is poor (see Table 8.2), although the amount of data becomes more comprehensive for Fukushima. Based on preliminary estimates of the radioactive emissions from Fukushima, the risk of contamination would decrease and the results presented here could be considered as a worst-case scenario. However, only cesium-137 and iodine-131 have been used in this study while other semi-volatile radioactive gases such as cesium-134 or strontium-90 can, at least on short time scales, increase the radioactive contamination of a region substantially. Moreover, fuel particles carrying isotopes such as plutonium have been released in particular in Chernobyl but also in Fukushima, which have much longer half-lifetimes than the semi-volatile isotopes. A last point which needs to be addressed is the level of dangerous contamination. Here, only a threshold value of 40 $\mathrm{kBq\,m^{-2}}$ was used, which was defined for beta- and gamma-emitters like cesium-137 after Chernobyl. However, this does not necessarily account for the dangers from the short-lived iodine-131 or extremely long-lived isotopes such as plutonium.

Taken together, the passive tracers are a useful tool for such a risk assessment study. Their application is justified as long as the largest uncertainties emanate from the emissions and the risk profiles of the different nuclear reactors. First these uncertainties need to be accounted for in a more comprehensive manners, before there will be the need to better represent the radionuclides in the model.

Part IV

Conclusions

9

Overall summary and future prospects

9.1 Summary

The work in this thesis contributes to our understanding of the dispersion and the atmospheric impact of emissions of man-made pollutants or contaminants from small scale sources, focusing on two different types of anthropogenic emission source points. A global three-dimensional atmospheric chemistry global circulation model (AC-GCM) was used to study anthropogenic aerosol particles and gas phase species, which were released from major population centers (MPCs, Chapters 4-7) and from nuclear power plants (NPPs, Chapter 8).

Large urban agglomerations are crucial to consider in future air quality and climate assessments, since they are strong localized sources of anthropogenic pollutants and regions of dense populations often surrounded by agricultural areas and forests, all of which can be adversely affected by the atmospheric pollution. To obtain a comprehensive picture on the impacts of pollutants from major population centers on the atmosphere, two different approaches were applied:

- quantifying the export pathways and the balance between pollution build-up and pollution export, and
- assessing the impact of MPC emissions on the atmospheric burden of the major anthropogenic aerosol types.

This extends significantly beyond the few previous studies of the global effects of megacities (Lawrence et al., 2007; Butler et al., 2008; Butler and Lawrence, 2009; Butler et al., 2012).

In the first approach, generic tracer experiments were conducted with various aerosols of different sizes and solubilities as well as with insoluble gas phase tracers, emitted from 46 MPCs distributed around the world. The simulation setup was designed such that the results depend only on the emission location and the tracer properties, since all tracers at each source point were continuously released with the same emission flux.

The low-level outflow for both aerosols and insoluble gases was determined to be similar to what was found by Lawrence et al. (2007), there only for insoluble gases, with the strongest outflow being simulated at middle and high latitudes. Furthermore, the results indicated that the location and thus the prevailing meteorology, in particular the atmospheric stability, are more important in determining the strength of the low-level outflow than the properties of the tracers. In contrast, the tracer properties, in particular the solubility, are crucial in determining the export of aerosols into the upper troposphere. The vertical export of insoluble gas phase tracers is greatest in regions with the strongest lifting potential, i.e., the tropics. Since lifting processes are in most cases moist, through clouds, the water vapor abundance can significantly limit the upward transport of soluble species. On average, about $3-4\,\%$ (small aerosol tracers) and about $2.5-3.5\,\%$ (large aerosol tracers) of the atmospheric mass is above 5 km, while about $16-20\,\%$ (small aerosol tracers) and $12-15\,\%$ (large aerosol tracers), or about five times more, of the atmospheric mass has undergone low-level long-range transport. Moreover, on average and for the same emission magnitude, one third of the atmospheric burden of the insoluble gas phase tracers (e-folding time of ten days) is above 5 km, which is about ten times more than for the aerosol tracers. The strongest upward transport of aerosols was found to occur in temperate dry winter regions, not in the tropics, due to the lower precipitation scavenging.

A fraction of the emitted mass is also retained around the source and causes a build-up of pollution. This mass fraction was found to be highest in regions where pollutants have short atmospheric residence times, due to fast removal, mainly by scavenging. Close to the source, where the outflow plume is almost undiluted, humans are affected most. However, the number of people who live in an area where a certain tracer density threshold is exceeded was determined to depend more strongly on the population density than on the geographical size of the polluted area. Thus, on a per unit mass of emission basis most, people are likely to be affected by high pollutant levels from megacities in South and East Asia.

A major result of this thesis was that small aerosol particles (diameter $\leq 2.5\,\mu\mathrm{m}$) can undergo substantial long-range transport: on average about half of their emitted mass is deposited beyond 1000 km away from the source location. Observations of extreme long-range transport of aerosols from small release points are typically associated with pyrogenic convection or volcanic eruptions with much higher effective emission height, as well as with desert dust plumes. Anthropogenic surface emissions are typically associated with more local effects, with a few exceptions, for instance the outflow to the Indian Ocean during the winter monsoon (Lawrence and Lelieveld, 2010). The results here clearly indicate that small scale anthropogenic surface emissions also contribute significantly to remote deposition around the world, though generally diluted compared to more local deposition.

In addition to the remote deposition of aerosol particles, the areas onto which a large fraction of the emitted aerosol mass is deposited were also studied in more detail. These areas are found to be larger for MPCs in regions which are frequently affected by heavy precipitation, e.g., around Lagos, as well as for MPCs in poorly ventilated geographical locations, e.g., around Bogotá. Although about half of the MPCs are directly situated along coastlines, most of the deposition was found to occur over land surfaces. The results further revealed that forests are more exposed to the MPC aerosol deposition than other land ecosystems such as cropland and pasture.

Several assumptions and uncertainties of the generic tracer experiments could influence the results presented in this thesis. Three of these were discussed in more detail. First, the emission of tracers at the surface rather than in higher model layers was found to lead to less remote deposition, i.e., less long-range transport, but has only little effect on the export into the upper troposphere or on the low-level long-range transport. Second, ambient aerosols were treated as generic tracers, which are of computational advantage but lack in their microphysical representativity. To address this issue, the generic tracers were compared to more complex aerosol tracers and the results of this comparison showed that the removal of aerosol particles by nucleation scavenging influences the outflow and deposition results at least as much as the additional treatment of several microphysical processes together. Thus, the results with the generic aerosol tracers can be considered a good approximation. Finally, the results of model simulations at different horizontal resolutions were compared. The distribution of aerosol mass in the atmosphere was found to depend on the resolution, especially the amount of aerosol mass in the upper troposphere: more soluble aerosol mass is lifted to higher altitudes when the horizontal model resolution is chosen to be lower. This results from less large-scale precipitation and consequently less scavenging in large-scale clouds, which tend to remove aerosol mass more efficiently than scavenging in convective clouds.

In reality, the emissions from these MPCs vary in time, differently for the various species, and the species interact with other constituents in the atmosphere after being emitted. To take all of this into account, the second approach noted above was employed: anthropogenic emissions of black carbon, particulate organic matter, sulfur dioxide, and nitrogen oxides were removed at the locations of the MPCs in the global emission inventory used in simulations with the AC-GCM EMAC. The simulations showed that the regional and global impacts of the MPC emissions are larger for the secondary aerosol species, sulfate and nitrate, than for the primary species, black carbon and particulate organic matter. Tropospheric sulfate concentrations were found to be reduced in large areas over the entire Northern Hemisphere, while nitrate and black carbon were mainly affected at the MPC locations and in downwind regions. Atmospheric particulate organic matter concentrations were found to experience the least change due to reduced MPC emissions. While the primary species were not found to have significant implications for other gaseous or particulate species, the reduction of sulfur dioxide emissions affects most species which are involved in the oxidation of sulfur dioxide to sulfuric acid and also several gas-aerosol equilibria, for instance between ammonia and ammonium as well as between nitric acid and aerosol nitrate. Nitrogen oxides are not only important in the formation of nitric acid and dinitrogen pentoxide but also in the production and destruction of ozone. In line with the results of Butler and Lawrence (2009) it was confirmed that MPC NO_x emissions generally contribute to reducing ozone in the extra-topics and to increasing ozone in the tropics. Generally, reduced MPC NO_x emissions lead to a global reduction in tropospheric ozone, as well as reduced concentrations of the hydroxyl radical, and thus decrease the oxidation capacity of the atmosphere, reflected for instance in an increase of the global burden of carbon monoxide.

By altering the emissions of all four species simultaneously, the results indicated that changes in MPC emissions of black carbon, particulate organic matter, and sulfur dioxide lead to nearly linear responses in the atmospheric burden of the corresponding species. However, this was not found to be the case for nitrogen oxides in boreal summer, since the ammonium nitrate dissociates into its gaseous components at high temperatures. Moreover, aerosol nitrate concentrations increased when the MPC sulfur dioxide emissions are reduced, even when the nitrogen oxides emissions were simultaneously reduced.

The generic tracer approach was further applied to assess the worldwide risk of contamination after nuclear reactor accidents, the first study of its kind for nuclear power plants. Passive aerosol and gas phase tracers representing the radionuclides cesium-137 and iodine-131, respectively, were released in the model from the nuclear power plant source locations. Many uncertainties needed to be accounted for in this assessment, especially regarding the emission and the risk profile of each reactor. The cumulative risk was assessed by multiplying an empirically derived probability of nuclear reactor core melts with the normalized modeled deposition. The risk was found to be highest in the eastern US, western Europe, and Japan. It was shown that contamination by major accidents is expected about every 50 years on average in these regions. Furthermore, it was found that the results are nearly insensitive to the emission duration and that, in general, continuously emitted passive tracers are a useful tool in such an assessment because they are accurate enough to represent radionuclides, especially in light of other uncertainties of such an assessment.

9.2 Future prospects

This section focuses on future work regarding pollution from major population centers, since most of the work in this thesis concentrates on major population centers, and since future work on the assessment of the risk of contamination after nuclear reactor accidents is extensively discussed in Section 8.5 and also in Lelieveld et al. (2012a).

Since the goal was to include as many major population centers as possible in one framework, this thesis used global modeling as the main tool. There are still many possible tasks left open. For instance the representation of megacities in global models can be improved. Butler et al. (2008) already showed that still much work is needed to represent megacities quantitatively well in global emission inventories. Furthermore, since global models cannot yet resolve megacities on the horizontal grid, the introduction of the emissions in the model still offers room for improvement. A step which would be feasible with the next generation of supercomputers is to apply a higher horizontal resolution to better resolve the area which represents a megacity. However, since it is also known that the tracer transport is affected by the horizontal resolution, this task would require careful testing and eventually modifying some of the basic model parameters and parameterizations. Moreover, effects from urban areas could be taken into account, such as the changes in the land surface and the urban heat island effect. These urbanization effects can potentially increase the effective emission altitude, as well as changing its diurnal cycle. A general improvement of sub-grid scale emissions can be obtained by using a Gaussian plume model, which, however, would increase the computational expense.

Future assessments of impacts of megacities on atmospheric composition have to take into account two aspects: 1) the contribution of individual species to the overall emissions from MPCs and 2) the location of the megacities, since it is expected that many cities or regions will grow to megacities in the near future. These regions need to be identified, since the impact of a set of source points changes depending on the locations.

Future work also needs to consider various pathways to confirm or contradict the findings in this thesis. One approach is to apply regional atmospheric chemistry models, such as WRF-Chem (Grell et al., 2005; Fast et al., 2006). For chosen emission points, the results from the global model study can be evaluated with the advantage of better resolving small scales. Since regional models can be run with horizontal resolutions of one to a few kilometers, they would also make it possible to obtain the pollution potentials of different source points within a megacity, or of different emission sectors.
Moreover, to overcome the limitation of pure modeling studies, comparable observations are clearly needed. Large field campaigns require substantial coordination and are expensive. Furthermore, they are generally only conducted for several weeks. They are clearly of tremendous value for individual cities to discover the different sources of air pollution. However, the results of such field campaigns are often difficult to compare between cities, since different instruments and sampling times and strategies are used. On the other hand, most cities employ an air pollution measurement network, which may be coordinated in terms of measurement instruments, location of measurement stations, and sampling methods, but, since this is already often a problem on national levels, it is very difficult to realize practically on an international level.

Taken together, further observations and model studies are both necessary to better assess the air pollution impacts of megacities on a regional and global basis. Projects like MILAGRO and MEGAPOLI combined both measurements and modeling, but have been limited to individual cities. In the MEGAPOLI project the impacts of all megacities on the global scale were addressed using numerical models for the first time in such an international project, to which the work in this thesis also contributed. The path of combining measurements and modeling would also need to be followed in future projects to develop a comprehensive understanding of how urban agglomerations will change the atmosphere in the future.

Part V

Appendix

A

Description of statistical methods

The statistical tools applied in this thesis are commonly considered as standard. For completeness a brief overview is given following Schönwiese (2000):

Arithmetic Mean The arithmetic mean $\bar{x}$ is the central tendency of a collection of numbers. If a sample space $\{x_1, ..., x_n\}$ is given, then $\bar{x}$ is assessed to:

$$\bar{x} \;=\; \frac{1}{n}\sum_{i=1}^{n} x_i \qquad . \tag{A.1}$$

Weighted mean - expected value In probability theory, the expected value (also expectation) E of a random variable X is the weighted mean (first moment) of all possible values x_i that X can take on. The weights correspond to probabilities p_i:

$$E\left[X\right] = \sum_{i=1}^{n} x_i p_i \qquad . \tag{A.2}$$

Mean absolute deviation The mean absolute deviation x_d of a data set $\{x_1, ..., x_n\}$ is the average of the absolute deviations, i.e., a measure of the average distance of the data set from its mean:

$$x_d = \frac{1}{n}\sum_{i=1}^{n} |x_i - \bar{x}| \qquad . \tag{A.3}$$

Standard deviation The standard deviation s is another measure of the variation of a data set $\{x_1, ..., x_n\}$ from its mean. It is the square root of the variance V and calculates to:

$$s = \sqrt{\frac{1}{n-1}\sum_{i=1}^{n}(x_i - \bar{x})^2} \qquad . \tag{A.4}$$

Linear regression In statistics, linear regression is used to model the relationship between a scalar dependent variable y and one or more explanatory variables x. If several prerequisites are fulfilled, i.e., samples large enough ($n \geq 30$), independence of data, data points are Gaussian distributed, a linear regression model of the form

$$\hat{y} = \; A \, + \, Bx \tag{A.5}$$

with intercept A and slope B, is considered the best fit $\hat{y}$ according to the method of least squares.

Correlation coefficient The correlation coefficient r is a measure of the linear dependence between two variables x and y. In this work different methods have been applied to calculate r:

- *Pearson* The Pearson product-moment correlation coefficient r gives a value between +1 and −1 inclusive. It is defined as the covariance of two variables divided by the product of their standard deviations. For variables $\{x_1, ..., y_n\}$ and $\{y_1, ..., y_n\}$ it is calculated to:
$$r = \frac{\sum_{i=1}^{n}(x_i - \bar{x})(y_i - \bar{y})}{\sqrt{\sum_{i=1}^{n}(x_i - \bar{x})^2}\sqrt{\sum_{i=1}^{n}(y_i - \bar{y})^2}} = \frac{\sum_{i=1}^{n} x_i y_i - n\bar{x}\bar{y}}{(n-1)s_x s_y} \tag{A.6}$$
with $\bar{x}$,$\bar{y}$ and s_x, s_y the means and standard deviations of the samples and n the size of the samples.
- *Spearman* An alternative approach to determine the correlation coefficient is to use Spearman's rank correlation coefficient. This approach is also suited when the data does not follow a Gaussian distribution and gives reliable results even for non-linear regressions. However, the data needs to be monotonic. For this the data is first ranked. Then the correlation coefficient r_r is determined to:
$$r_r = 1 - \frac{6\sum_{i=1}^{n} D_i^2}{n^3 - n} \tag{A.7}$$
where D_i are the rank differences. r_r varies also between +1 and −1.
- *Coefficient of determination* The coefficient of determination which is the square of the correlation coefficient, often denoted as R^2. It is often given in per cent and denotes the relative explained variance, i.e., the variance that is captured by the regression model relative to the total variance.

Student's t-test For assessing the statistical significance of the difference between two sample means, $\bar{x}$ and $\bar{y}$, the Student's t-test was applied which is based on the t-distribution. If both samples have the same dimension n, the test statistic is calculated to

$$\hat{t} = \frac{|\bar{x} - \bar{y}|\sqrt{n}}{\sqrt{s_x^2 + s_y^2}} \quad \text{with } \Phi = 2n - 2 \tag{A.8}$$

with Φ the degrees of freedom. The test statistic is compared to a value $t_{\Phi,\alpha}$ derived from the theoretical distribution (here t-distribution), which depends on the degrees of freedom and the significance level α. Commonly, α can take values of 0.1, 0.05 or 0.01 which corresponds to confidence levels of 90 % (significant), 95 % (very significant), and 99 % (highly significant), respectively. Based on which of the parameters $\hat{t}$ or $t_{\Phi,\alpha}$ is larger, the decision is made whether the two means are different on the chosen significance level or not.

B

Representativity of the year 2005

According to measurements provided by NOAA[1] 2005 was the hottest year in terms of global mean temperature since the beginning of weather monitoring. Although indices of large-scale circulation patterns like the North Atlantic Oscillation (NAO)[2] or El-Niño-Southern-Oscillation (ENSO)[3] show no extreme values, the question still remains whether the year 2005 is representative to conduct the tracer studies, especially when using observational data to nudge the meteorology.

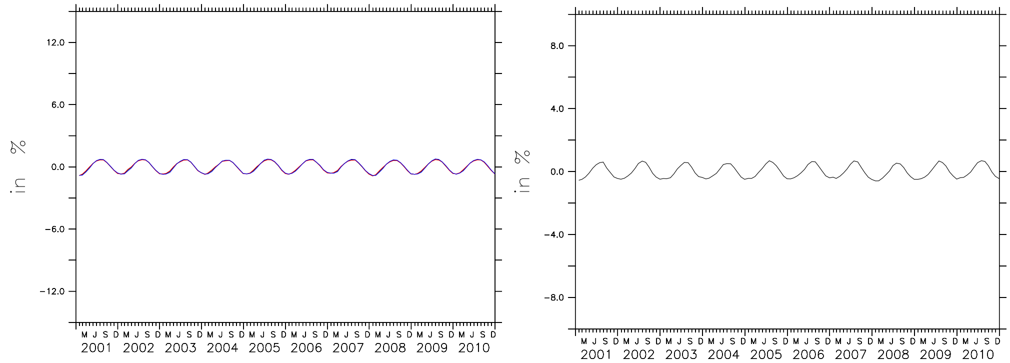

Globally averaged 2m temperature   Globally averaged geopotential height, 500 hPa

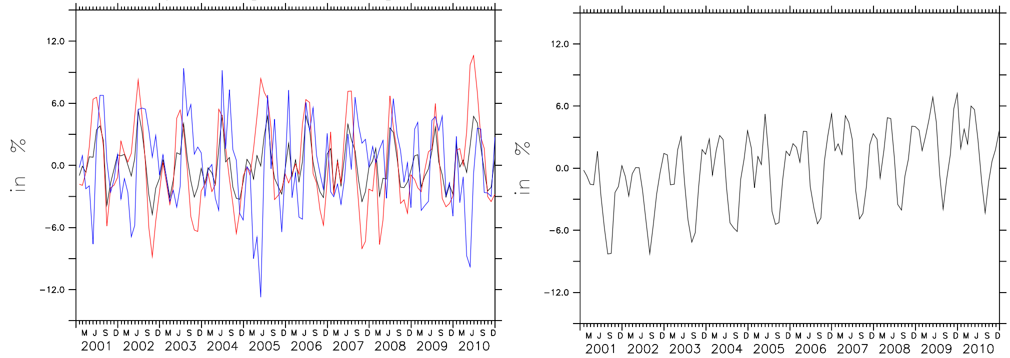

Globally averaged precipitation   Globally averaged total cloud cover

Figure B.1: Time series of the relative changes (in %) with respect to the ten year mean of modeled temperature (black line = mean 2m temperature, red line = maximum 2m temperature, blue line = minimum 2m temperature), precipitation (black line = total precipitation, red line = large-scale precipitation, blue line = convective precipitation), geopotential height, and cloud cover from 2001 to 2010.

---

[1] http://www.ncdc.noaa.gov/sotc/global/2011/13, as of 17.09.2012

[2] http://www.cpc.ncep.noaa.gov/products/precip/CWlink/pna/nao.shtml, as of 17.09.2012

[3] http://www.ncdc.noaa.gov/sotc/enso/2005/1, as of 17.09.2012

To study this, an eleven year simulation, starting in January 2000 and ending in January 2011, has been conducted. The meteorology has been nudged with ERA-INTERIM data and soluble, i.e., nucleation scavenging active (NS_{act}), generic aerosol tracers with a fixed diameter of 1.0 µm have been initialized at the megacity locations. The first twelve months are used for model spin-up, while the last ten year are used for comparison.

The inter-annual variability is small for global means of meteorological variables such as the 2m temperature, total precipitation, 500hPa geopotential height. Only for the cloud cover an increasing trend is simulated from 2001 to 2010 (Figure B.1). However, the global means can indicate similar values but the spatial variability can still be large. When comparing the annual means to the ten year mean several variables do not show larger variation than one per cent, e.g., geopotential height at 500 hPa, the 2m temperature or the surface pressure. In contrast, cloud cover, total precipitation, and net mass flux at 850 hPa show inter-annual variations up to 10 % (not shown).

The time evolution of the total global tracer mass of each megacity is shown for the years 2001 to 2010 in Figure B.2, with no strong excursions being simulated during this time. Most

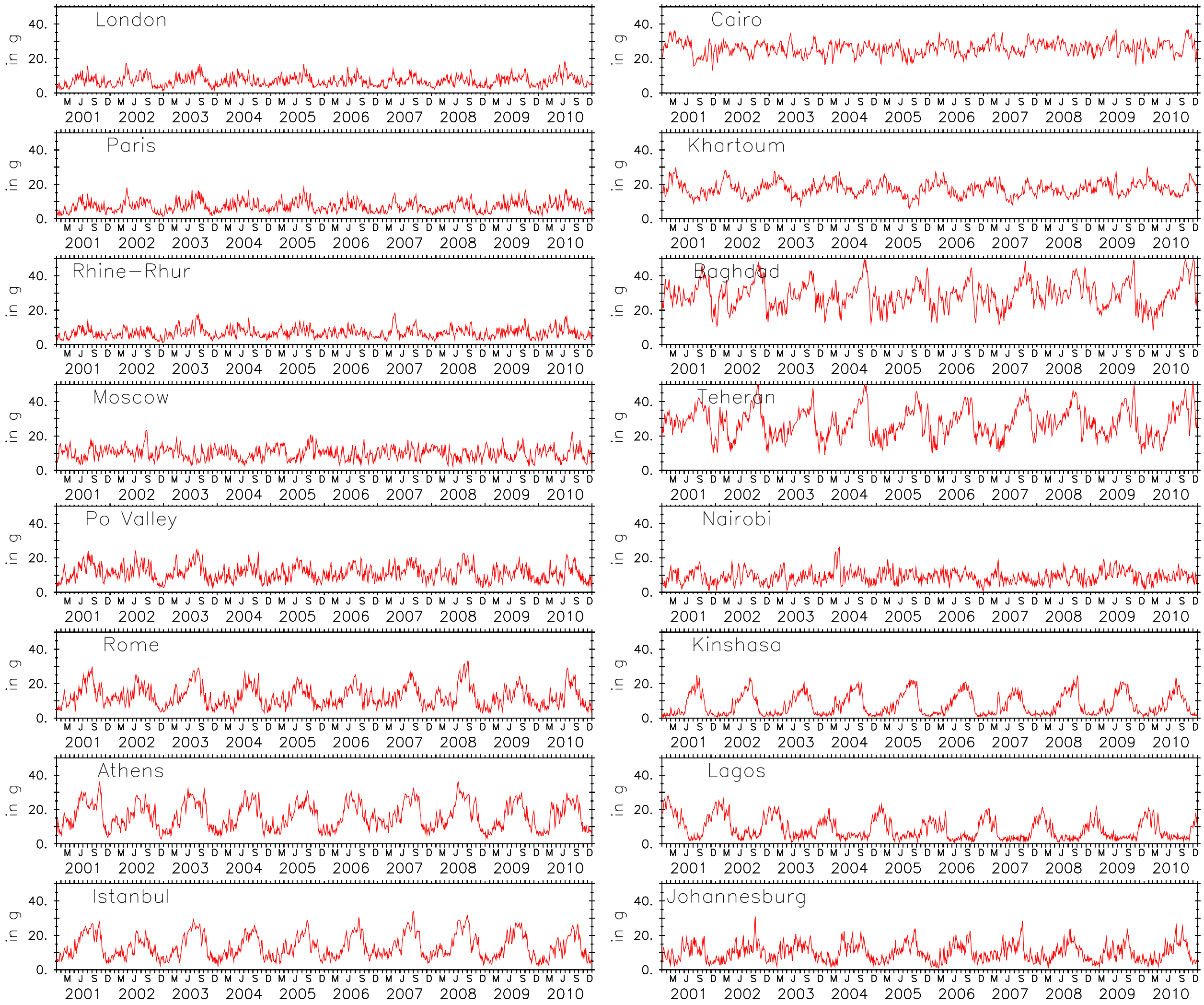

Figure B.2: Time series of total global burden (in g) of the tracers released at the 46 megacities from 2001 to 2010.

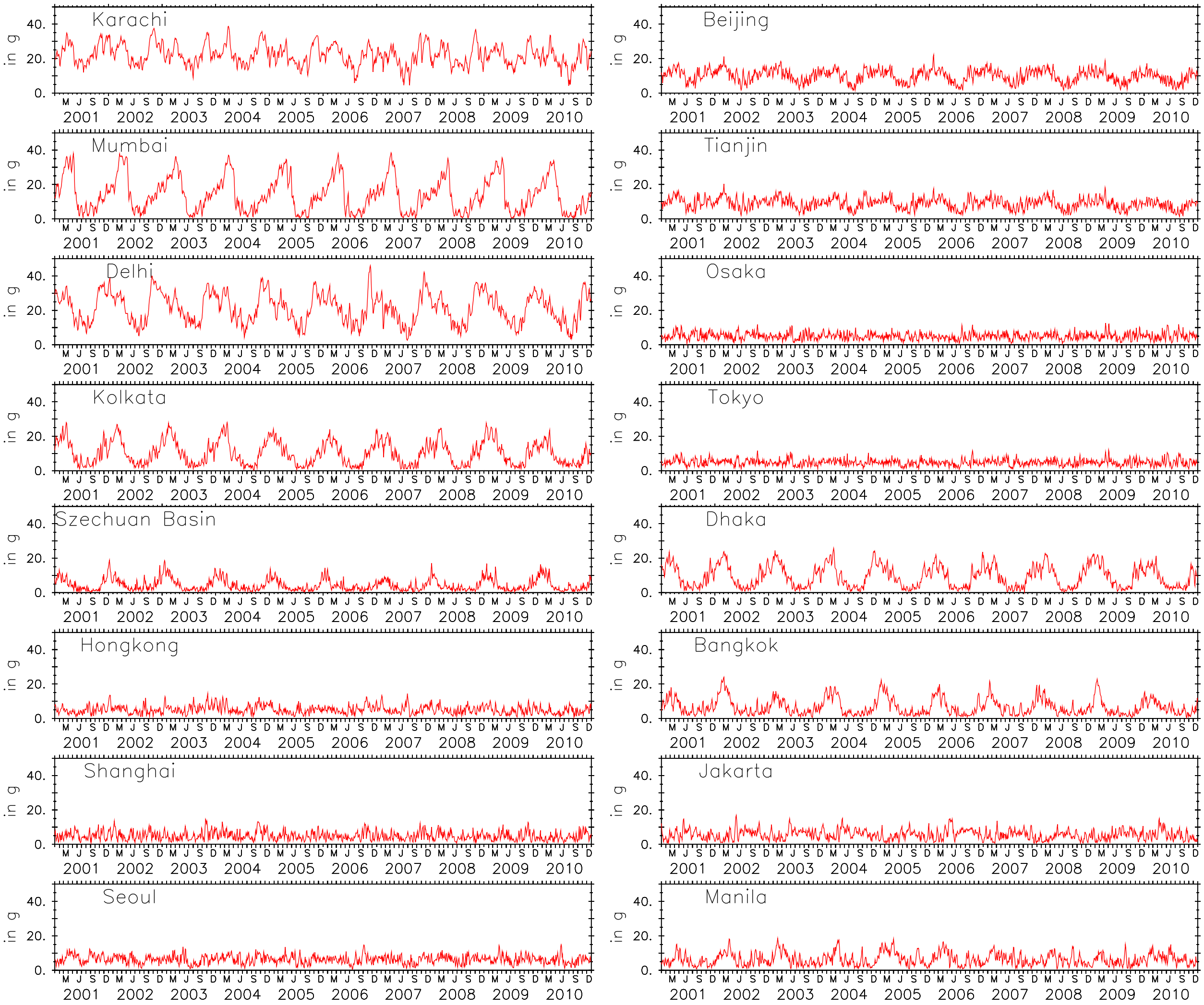

Figure B.2: continued

tracer masses follow the same annual cycle in all years, with only minor deviations due to the inter-annual variability of local weather conditions. As mentioned before, the atmospheric mass burden of small aerosol tracers is mainly governed by the occurrence of precipitation. Nevertheless, similar total global masses does not necessarily mean that the tracer masses are equally distributed over the globe in each year and that the outflow pathways and the pollution build-up around the source have to be the same each year. To check this, the annual mean metrics were calculated for each tracer in each year. In total high coefficients of determination (R^2) were assessed between the single years. All calculated R^2 (based on Pearson and Spearman correlation coefficients, see Tables B.1 and B.2) are at least larger than 0.8 and most of them are even larger than 0.9. From this it is followed that the inter-annual variation between the pollution potentials is small and also that the ranking of the MPCs is very similar from year to year.

From this it is followed that the year 2005 is representative for the first decade of this century.

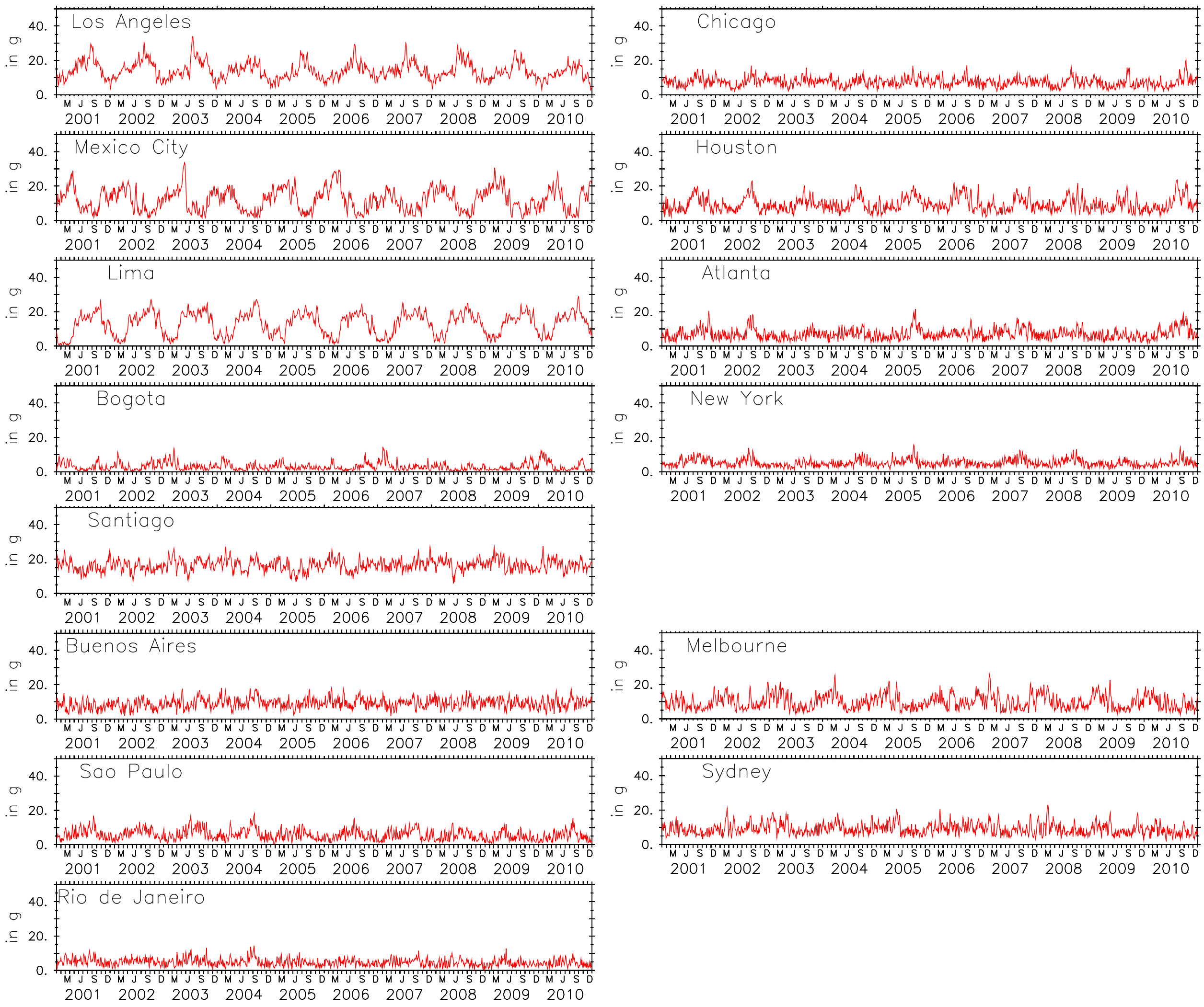

Figure B.2: continued

Table B.1: Coefficients of determination (R^2) of the annual means for the upper tropospheric mass fraction (E_{UT}), the low-level remote mass fraction ($ELR_{1\mathrm{km}}$), the mass fraction retained around the source ($RCL_{0.5\mathrm{km}}$), the area of tracer density threshold exceedance (A_{10}), and the remote deposition (DRT). The upper triangular matrices show the coefficients of determination based on the Pearson correlation coefficients, the lower triangular matrices show the coefficients of determination based on the Spearman correlation coefficients.

E_{UT}		2001	2002	2003	2004	2005	2006	2007	2008	2009	2010
	2001	1.00	0.98	0.97	0.95	0.95	0.95	0.96	0.94	0.97	0.95
	2002	0.94	1.00	0.97	0.96	0.96	0.95	0.97	0.94	0.96	0.94
	2003	0.93	0.95	1.00	0.95	0.95	0.96	0.97	0.94	0.98	0.96
	2004	0.91	0.96	0.96	1.00	0.98	0.95	0.93	0.96	0.95	0.91
R^2	2005	0.91	0.95	0.94	0.95	1.00	0.95	0.92	0.97	0.95	0.94
	2006	0.92	0.95	0.95	0.95	0.92	1.00	0.95	0.97	0.96	0.95
	2007	0.92	0.94	0.94	0.94	0.90	0.93	1.00	0.93	0.97	0.95
	2008	0.94	0.95	0.91	0.93	0.94	0.94	0.93	1.00	0.95	0.95
	2009	0.93	0.93	0.94	0.95	0.93	0.94	0.93	0.95	1.00	0.96
	2010	0.92	0.94	0.92	0.93	0.95	0.91	0.92	0.95	0.93	1.00
$ELR_{1\mathrm{km}}$		2001	2002	2003	2004	2005	2006	2007	2008	2009	2010
	2001	1.00	0.93	0.93	0.94	0.93	0.91	0.94	0.92	0.95	0.92
	2002	0.92	1.00	0.95	0.94	0.97	0.96	0.95	0.94	0.95	0.94
	2003	0.91	0.95	1.00	0.96	0.95	0.94	0.95	0.94	0.93	0.91
	2004	0.92	0.90	0.91	1.00	0.96	0.94	0.95	0.94	0.95	0.93
R^2	2005	0.92	0.97	0.94	0.94	1.00	0.95	0.96	0.96	0.95	0.93
	2006	0.91	0.97	0.94	0.90	0.95	1.00	0.96	0.94	0.95	0.92
	2007	0.94	0.95	0.96	0.92	0.94	0.95	1.00	0.96	0.96	0.94
	2008	0.92	0.92	0.91	0.93	0.93	0.93	0.94	1.00	0.95	0.96
	2009	0.93	0.92	0.92	0.95	0.94	0.93	0.94	0.95	1.00	0.96
	2010	0.91	0.91	0.90	0.92	0.91	0.92	0.92	0.96	0.95	1.00
$RCL_{0.5\mathrm{km}}$		2001	2002	2003	2004	2005	2006	2007	2008	2009	2010
	2001	1.00	0.94	0.91	0.90	0.94	0.90	0.90	0.92	0.92	0.93
	2002	0.93	1.00	0.94	0.93	0.97	0.94	0.92	0.94	0.95	0.94
	2003	0.91	0.93	1.00	0.93	0.93	0.95	0.92	0.92	0.95	0.92
	2004	0.90	0.94	0.92	1.00	0.95	0.96	0.96	0.96	0.96	0.94
R^2	2005	0.92	0.96	0.93	0.97	1.00	0.95	0.94	0.96	0.96	0.96
	2006	0.91	0.95	0.93	0.96	0.96	1.00	0.94	0.94	0.96	0.94
	2007	0.91	0.94	0.91	0.94	0.95	0.94	1.00	0.97	0.93	0.94
	2008	0.91	0.93	0.91	0.96	0.96	0.96	0.96	1.00	0.96	0.95
	2009	0.90	0.93	0.94	0.96	0.96	0.96	0.91	0.95	1.00	0.95
	2010	0.92	0.93	0.91	0.94	0.95	0.94	0.94	0.95	0.94	1.00
A_{10}		2001	2002	2003	2004	2005	2006	2007	2008	2009	2010
	2001	1.00	0.98	0.96	0.95	0.94	0.95	0.96	0.95	0.96	0.93
	2002	0.96	1.00	0.96	0.96	0.96	0.95	0.95	0.94	0.95	0.92
	2003	0.93	0.93	1.00	0.95	0.96	0.95	0.96	0.93	0.96	0.94
	2004	0.93	0.94	0.93	1.00	0.93	0.93	0.94	0.93	0.97	0.91
R^2	2005	0.93	0.95	0.96	0.92	1.00	0.93	0.96	0.91	0.93	0.94
	2006	0.93	0.94	0.96	0.93	0.95	1.00	0.97	0.97	0.95	0.95
	2007	0.96	0.96	0.96	0.95	0.96	0.97	1.00	0.96	0.96	0.95
	2008	0.95	0.96	0.94	0.95	0.94	0.95	0.98	1.00	0.96	0.95
	2009	0.93	0.91	0.93	0.95	0.93	0.93	0.95	0.96	1.00	0.94
	2010	0.89	0.87	0.92	0.90	0.94	0.92	0.92	0.90	0.91	1.00
DRT		2001	2002	2003	2004	2005	2006	2007	2008	2009	2010
	2001	1.00	0.95	0.91	0.92	0.90	0.87	0.92	0.93	0.89	0.90
	2002	0.90	1.00	0.95	0.95	0.95	0.92	0.94	0.93	0.93	0.92
	2003	0.83	0.91	1.00	0.96	0.94	0.96	0.95	0.95	0.96	0.94
	2004	0.88	0.92	0.92	1.00	0.94	0.96	0.95	0.95	0.97	0.94
R^2	2005	0.81	0.93	0.90	0.89	1.00	0.94	0.94	0.96	0.95	0.97
	2006	0.81	0.88	0.94	0.92	0.89	1.00	0.94	0.95	0.95	0.93
	2007	0.88	0.89	0.89	0.89	0.88	0.88	1.00	0.97	0.92	0.95
	2008	0.90	0.91	0.92	0.93	0.91	0.93	0.96	1.00	0.95	0.96
	2009	0.82	0.89	0.93	0.94	0.91	0.94	0.84	0.91	1.00	0.95
	2010	0.81	0.89	0.87	0.88	0.95	0.89	0.89	0.92	0.90	1.00

Table B.2: Coefficients of determination (R^2) of the annual means for the dry deposited mass fraction (DED), the mass fraction removed by gravitational settling (SED), the mass fraction scavenged in large-scale clouds (LSS), the mass fraction scavenged in convective clouds (CVS), and the fraction of mass, which is removed over continents (CON). The upper triangular matrices show the coefficients of determination based on the Pearson correlation coefficients, the lower triangular matrices show the coefficients of determination based on the Spearman correlation coefficients.

DED		2001	2002	2003	2004	2005	2006	2007	2008	2009	2010
	2001	1.00	0.98	0.97	0.96	0.97	0.95	0.96	0.97	0.96	0.96
	2002	0.98	1.00	0.97	0.98	0.98	0.97	0.97	0.97	0.98	0.97
	2003	0.97	0.98	1.00	0.98	0.97	0.97	0.98	0.97	0.98	0.98
	2004	0.97	0.98	0.99	1.00	0.98	0.97	0.97	0.98	0.98	0.97
R^2	2005	0.96	0.97	0.97	0.97	1.00	0.97	0.97	0.97	0.98	0.98
	2006	0.96	0.97	0.97	0.96	0.97	1.00	0.97	0.98	0.97	0.97
	2007	0.96	0.97	0.96	0.97	0.95	0.98	1.00	0.99	0.98	0.98
	2008	0.97	0.96	0.96	0.97	0.96	0.97	0.98	1.00	0.98	0.98
	2009	0.95	0.97	0.98	0.98	0.97	0.97	0.96	0.97	1.00	0.98
	2010	0.95	0.96	0.97	0.97	0.97	0.98	0.97	0.97	0.98	1.00
SED		2001	2002	2003	2004	2005	2006	2007	2008	2009	2010
	2001	1.00	0.98	0.96	0.97	0.96	0.95	0.97	0.97	0.95	0.96
	2002	0.97	1.00	0.97	0.97	0.95	0.96	0.97	0.97	0.97	0.95
	2003	0.91	0.94	1.00	0.97	0.96	0.97	0.98	0.96	0.98	0.96
	2004	0.93	0.96	0.96	1.00	0.94	0.96	0.97	0.96	0.97	0.95
R^2	2005	0.91	0.93	0.95	0.95	1.00	0.95	0.96	0.94	0.94	0.97
	2006	0.91	0.94	0.98	0.97	0.95	1.00	0.98	0.97	0.97	0.96
	2007	0.94	0.96	0.96	0.97	0.95	0.96	1.00	0.98	0.97	0.97
	2008	0.94	0.96	0.94	0.96	0.94	0.95	0.96	1.00	0.97	0.97
	2009	0.89	0.94	0.96	0.96	0.95	0.96	0.96	0.94	1.00	0.96
	2010	0.91	0.93	0.97	0.96	0.97	0.96	0.97	0.94	0.96	1.00
LSS		2001	2002	2003	2004	2005	2006	2007	2008	2009	2010
	2001	1.00	0.98	0.97	0.96	0.94	0.95	0.97	0.96	0.96	0.93
	2002	0.96	1.00	0.98	0.98	0.95	0.96	0.98	0.96	0.97	0.94
	2003	0.94	0.94	1.00	0.98	0.95	0.96	0.98	0.94	0.97	0.93
	2004	0.93	0.94	0.95	1.00	0.96	0.97	0.98	0.97	0.98	0.96
R^2	2005	0.92	0.92	0.94	0.95	1.00	0.97	0.97	0.95	0.97	0.95
	2006	0.93	0.94	0.94	0.95	0.94	1.00	0.98	0.97	0.97	0.96
	2007	0.95	0.95	0.97	0.96	0.95	0.96	1.00	0.97	0.98	0.95
	2008	0.96	0.95	0.92	0.95	0.92	0.94	0.96	1.00	0.97	0.95
	2009	0.94	0.94	0.96	0.96	0.95	0.95	0.98	0.96	1.00	0.97
	2010	0.93	0.93	0.93	0.94	0.93	0.96	0.96	0.94	0.95	1.00
CVS		2001	2002	2003	2004	2005	2006	2007	2008	2009	2010
	2001	1.00	0.98	0.97	0.96	0.94	0.95	0.98	0.96	0.96	0.94
	2002	0.97	1.00	0.98	0.98	0.96	0.97	0.98	0.97	0.97	0.95
	2003	0.94	0.96	1.00	0.98	0.96	0.96	0.98	0.95	0.98	0.94
	2004	0.93	0.95	0.96	1.00	0.97	0.97	0.98	0.97	0.98	0.96
R^2	2005	0.92	0.94	0.94	0.95	1.00	0.97	0.98	0.96	0.98	0.96
	2006	0.93	0.95	0.95	0.96	0.95	1.00	0.98	0.97	0.98	0.97
	2007	0.96	0.96	0.97	0.96	0.97	0.97	1.00	0.97	0.99	0.96
	2008	0.95	0.95	0.93	0.95	0.92	0.94	0.95	1.00	0.97	0.96
	2009	0.94	0.95	0.97	0.96	0.96	0.96	0.97	0.94	1.00	0.98
	2010	0.95	0.93	0.92	0.94	0.94	0.96	0.97	0.94	0.94	1.00
CON		2001	2002	2003	2004	2005	2006	2007	2008	2009	2010
	2001	1.00	0.98	0.95	0.96	0.96	0.95	0.97	0.97	0.96	0.95
	2002	0.98	1.00	0.97	0.98	0.98	0.97	0.99	0.97	0.97	0.96
	2003	0.93	0.95	1.00	0.98	0.97	0.98	0.97	0.97	0.98	0.96
	2004	0.95	0.98	0.95	1.00	0.97	0.98	0.98	0.98	0.98	0.96
R^2	2005	0.94	0.97	0.96	0.97	1.00	0.97	0.98	0.97	0.98	0.97
	2006	0.93	0.95	0.96	0.97	0.95	1.00	0.98	0.98	0.98	0.96
	2007	0.97	0.98	0.96	0.98	0.97	0.97	1.00	0.98	0.97	0.98
	2008	0.96	0.96	0.95	0.97	0.96	0.97	0.97	1.00	0.98	0.97
	2009	0.94	0.95	0.96	0.96	0.97	0.96	0.96	0.96	1.00	0.96
	2010	0.91	0.93	0.93	0.92	0.94	0.93	0.95	0.94	0.93	1.00

C

Comparison between EMAC and MATCH-MPIC

The same 36 major population centers as in Lawrence et al. (2007) are used to test the reproducibility of their results. For this EMAC was applied in a setup comparable to the setup of Lawrence et al. (2007) who used the semi-offline, three dimensional, chemical transport model MATCH-MPIC (e.g., Rasch et al., 1997; Lawrence et al., 1999; von Kuhlmann et al., 2003). EMAC calculates its own meteorology and is nudged towards meteorological fields from ECMWF whereas MATCH-MPIC relies on a limited set of meteorological input fields, i.e., surface pressure, geopotential, temperature, horizontal winds, surface latent and sensible heat fluxes as well as zonal and meridional wind stresses from NCEP/NCAR reanalysis data (Kalnay et al., 1996) for every six hours. These variables are interpolated in time to the model time step of 30 minutes, and are used to diagnose on-line the transport by advection, deep convection, vertical diffusion, and also the hydrological cycle, i.e., water vapor transport, cloud condensate formation, and precipitation. A horizontal resolution of 1.9 ° × 1.9 ° in latitude and longitude, corresponding to T63 with 28 vertical sigma levels was applied from the surface up to 2 hPa. To obtain higher accordance in the model setup, EMAC was run in T63 but with 31 hybrid sigma-pressure levels in the vertical from the surface up to 10 hPa with a model time step of 15 minutes. Both models rely on different physical parameterizations, e.g., for convection or advection tracer transport algorithms, but on the same convective tracer transport scheme (Lawrence and Rasch, 2005). The main differences between the two models are summarized in Table C.1. Furthermore, since 1995 was the year of analysis in Lawrence et al. (2007), I also use the year 1995 for analysis which is "neutral" with regards to ENSO. In both models a passive gas phase tracer was released

Table C.1: Differences in model setup between EMAC and MATCH-MPIC.

	EMAC	MATCH-MPIC
Vertical levels	31	28
Uppermost level ends at	10 hPa	2 hPa
Meteorological data	ECMWF	NCEP/NCAR reanalysis data
Coupling	on-line	semi-offline
Time step	15 min	30 min
Advection	Lin and Rood (1996)	Rasch and Lawrence (1998)
Convection	Tiedtke (1989) Nordeng (1994)	Zhang and McFarlane (1995) Hack (1994)

with a continuous and constant emission rate of 1.0 kg s^{-1} in each box hosting one of the 36 MPCs.

On the left side in Figure C.1 the same color-scale was applied to the EMAC data as in their Figure 1 of Lawrence et al. (2007) (right side of Figure C.1). The total column densities look similar in both simulations with only slight differences in the outflow from East Asia over the Pacific Ocean. A large part of the tracer mass in this outflow originates from the Indian subcontinent where convective mass fluxes at 850 hPa and 700 hPa are stronger in EMAC leading to a stronger upward transport of tracer mass. Contrary, the burden in the outflow region from eastern South America over the southern Atlantic Ocean is smaller in the EMAC simulation since convective mass fluxes are higher in the MATCH-MPIC simulation in this region. However, the lifting of tracer mass out of the lowest layers is generally stronger in EMAC and consequently the surface densities in MATCH-MPIC simulations are higher, although the surface layer is slightly deeper for MATCH-MPIC with about 80 m in contrast to about 60 m in case of EMAC.

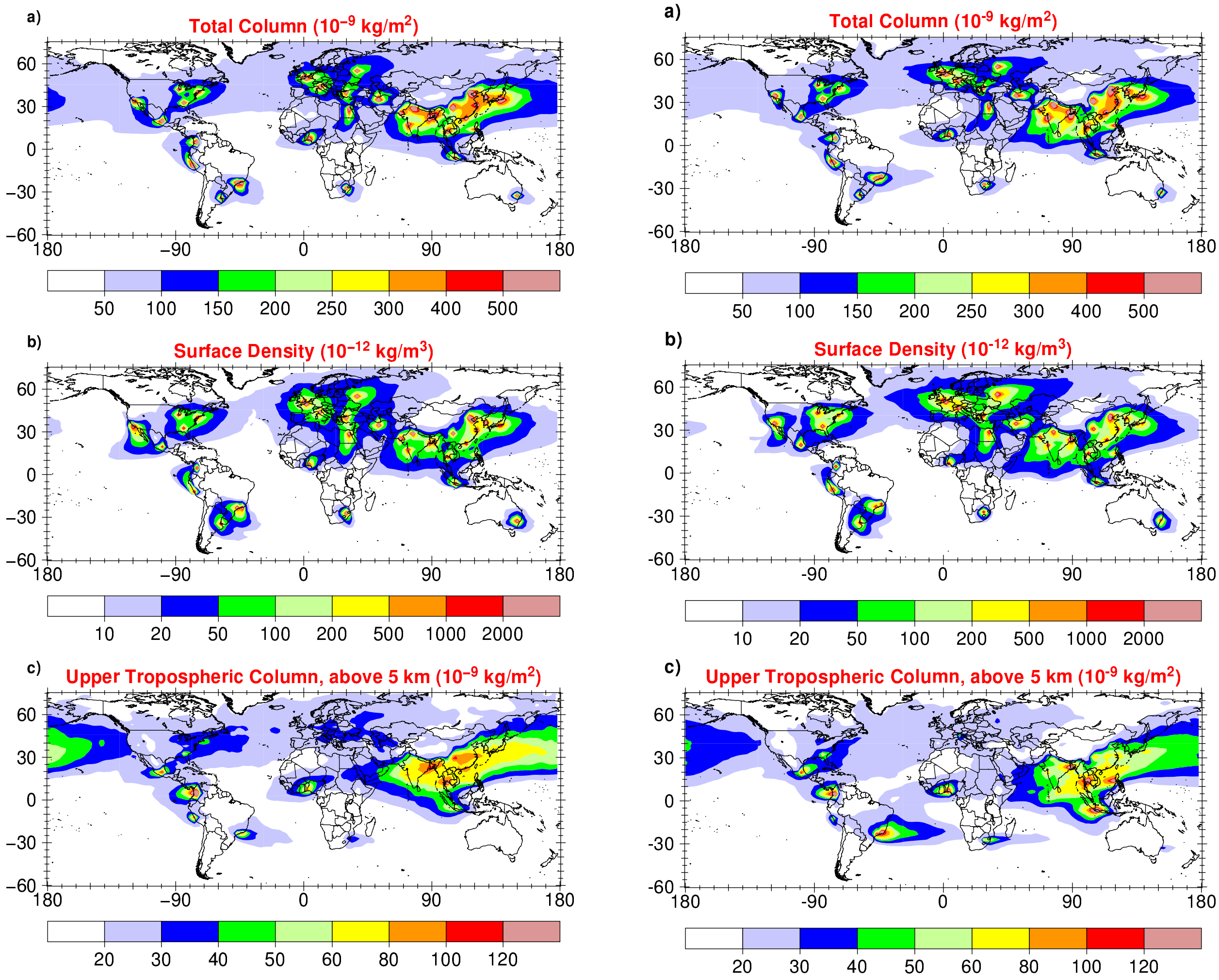

Figure C.1: Annual mean sum of 36 MPCs for a) the total column density (in 10^{-9} kg m^{-2}), b) the surface density (in 10^{-12} kg m^{-2}), and c) upper tropospheric column above 5 km (in 10^{-9} kg m^{-2}). On the left for EMAC simulations, on the right for MATCH-MPIC, adopted from Lawrence et al. (2007), copyright 2007 by the European Geophysical Union.

Furthermore, the metrics $ELR_{1\mathrm{km}}$, E_{UT} and A_{10} are applied to the model data and are compared to the results reported by Lawrence et al. (2007). Figure C.2 shows the corresponding scatter plot of the three metrics for each major population center. A fairly good agreement is achieved for all three metrics, which is supported by high coefficients of determination (R^2, based on the Pearson correlation coefficient) of 0.78 ($ELR_{1\mathrm{km}}$), 0.72 (E_{UT}) and 0.75 (A_{10}). The explanation of missing variance (about one quarter) is attributable to uncertainties in the underlying meteorological fields as well as model uncertainties, e.g., parameterizations for sub-grid scale processes or errors introduced by the numerical representation of physical equations.

Moreover, Table C.2 provides a city by city listing of differences in the annual mean of the metrics, $ELR_{1\mathrm{km}}$, E_{UT} and A_{10}, and in the calculated ranks of each MPC. On average metrics calculated from MATCH-MPIC simulations show larger low-level outflow (negative mean in $ELR_{1\mathrm{km}}$) and a larger area with a mass threshold exceedance of 10 ng m^{-3} (negative mean in A_{10}) while the upper tropospheric pollution E_{UT} is larger in EMAC. Often a change for an MPC in low-level pollution is accompanied by a change in upper level pollution of opposite sign. In addition, these results are consistent with findings in Figure C.1 that in the case for EMAC simulations the ventilation of the boundary layer is stronger than for MATCH-MPIC due to generally more vertical transport. Maximum changes for $ELR_{1\mathrm{km}}$ are found for Moscow with -11% and $+3.1\%$ for Rio de Janeiro while most MPCs range between -1.0 % and -6.0 %. Changes in E_{UT} cover a broad range with 16 % more mass above 5 km in MATCH-MPIC results for Rio de Janeiro while Mumbai has about 14 % more mass in the upper troposphere in the EMAC results. For A_{10} there is one outlier, Moscow, which shows a large difference of 5.9 $\times$ 10^6 km^2 while most other cities do not differ more than 2.7 $\times$ 10^6 km^2.

In general, the main results from Lawrence et al. (2007) are well reproduced when using

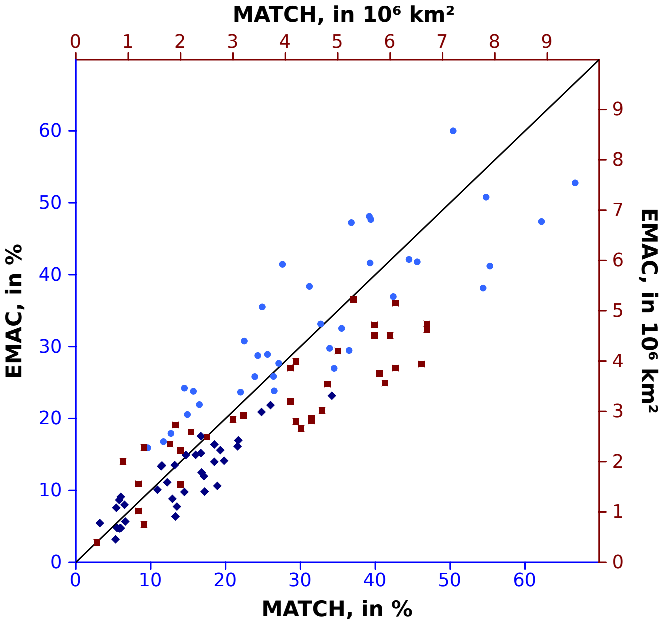

Figure C.2: Scatter plot of $ELR_{1\mathrm{km}}$ (dark blue diamonds), E_{UT} (light blue dots), and A_{10} (red squares) obtained from EMAC (ordinate) and MATCH-MPIC (abscissa) data.

EMAC which underlines the robustness of the results. The metrics mainly depend on the underlying meteorological fields and advective and convective transport schemes, which introduce the largest uncertainties in such calculations.

Table C.2: Differences between EMAC and MATCH-MPIC annual values and corresponding ranks for $ELR_{1\mathrm{km}}$, E_{UT}, and A_{10} for the 36 MPCs: $\bar{x}$, mean differences; x_d, corresponding mean absolute deviations, with $\bar{x} = \Sigma_{i=1}^{N} x_i/N$, $x_d = \Sigma_{i=1}^{N}|x_i'|/N$, $x_i' = x_i - \bar{x}$, x_i metric value of an MPC, and N total number of MPCs.

	$ELR_{1\mathrm{km}}$		E_{UT}		A_{10}	
	%	Rank	%	Rank	$\times\ 10^6\mathrm{km}^2$	Rank
Europe						
London	-4.14	0	5.08	0	-2.07	4
Paris	-3.9	0	5.22	0	-1.96	1
Moscow	-11.03	0	6.32	0	-5.92	1
Po Valley	-2.11	-4	5.43	2	-0.8	-4
Istanbul	-4.74	1	5.65	1	-0.98	-6
West Asia						
Teheran	-7.37	11	8.08	-1	-1.64	7
Africa						
Cairo	-5.47	2	9.72	-5	-0.95	-2
Lagos	-1.25	5	-2.38	0	1.1	-4
Johannesburg	1.49	-1	-5.45	6	0.36	-2
Southern Asia						
Karachi	-5.12	6	8.27	-9	-1.19	-3
Mumbai	-4.72	5	13.84	-9	-1.68	3
Delhi	-8.28	12	10.62	-9	-2.66	7
Kolkata	-5.75	9	10.44	-6	-1.26	2
Dhaka	-6.93	10	8.91	-8	-1.69	6
Eastern Asia						
Szechuan Basin	-1.09	4	8.28	-5	-0.55	4
Beijing	-5.67	6	4.45	-3	-2.34	7
Tianjin	-4.53	4	3.31	-2	-2.24	7
Shanghai	-4.31	4	0.45	-1	-1.49	1
Seoul	-1.52	-6	0.57	3	-0.21	-10
Tokyo	1.97	-9	-7.04	7	0.39	0
Osaka	0.32	-7	-4.14	3	-0.28	-4
Hong Kong/PRD	-4.08	3	2.33	-1	-1.64	3
Southeast Asia						
Manila	2.86	-6	-14.81	4	0.83	-5
Bangkok	-0.93	4	-4.02	-1	-0.45	5
Jakarta	2.25	-4	-13.93	1	0.98	-3
Australia						
Sydney	1.95	-9	-7.53	9	-0.01	2
North America						
Chicago	-3.7	1	1.92	0	-2.05	5
New York	-1.06	-6	-0.55	3	-0.9	-4
Los Angeles	0.84	-10	1.66	2	-0.08	-11
Atlanta	-1.08	-4	-2.97	3	-1.4	4
Mexico City	-0.72	0	-3.81	2	-0.18	1
South America						
Bogotá	-2.1	1	9.61	-5	-0.01	0
Lima	-0.82	-5	7.17	-6	-0.16	-3
Rio de Janeiro	3.1	-6	-16.26	9	0.55	-2
São Paulo	2.18	-5	-14.1	9	0.22	3
Buenos Aires	0.22	-6	-2.66	7	-0.24	-10
$\bar{x}$	-2.32	0	1.05	0	-0.91	0
x_d	2.88	4.89	6.41	3.94	0.99	4.06

D

Precipitation formation and tracer transport: dependence on horizontal model resolution

In Section 6.2 the difference of tracer results were discussed regarding the choice of different horizontal resolutions. This sensitivity is discussed in a bit more detail now. The passive tracer transport from urban emission hot spots was simulated in three different horizontal resolutions, T42, T63 and T106, with the same number of vertical levels (31). The left side of Figure D.1 shows the column densities above 5 km for the three different resolutions for gas phase tracers, with no significant differences between the different resolutions. Recall that the passive gas phase tracers are only removed from the atmosphere by an exponential

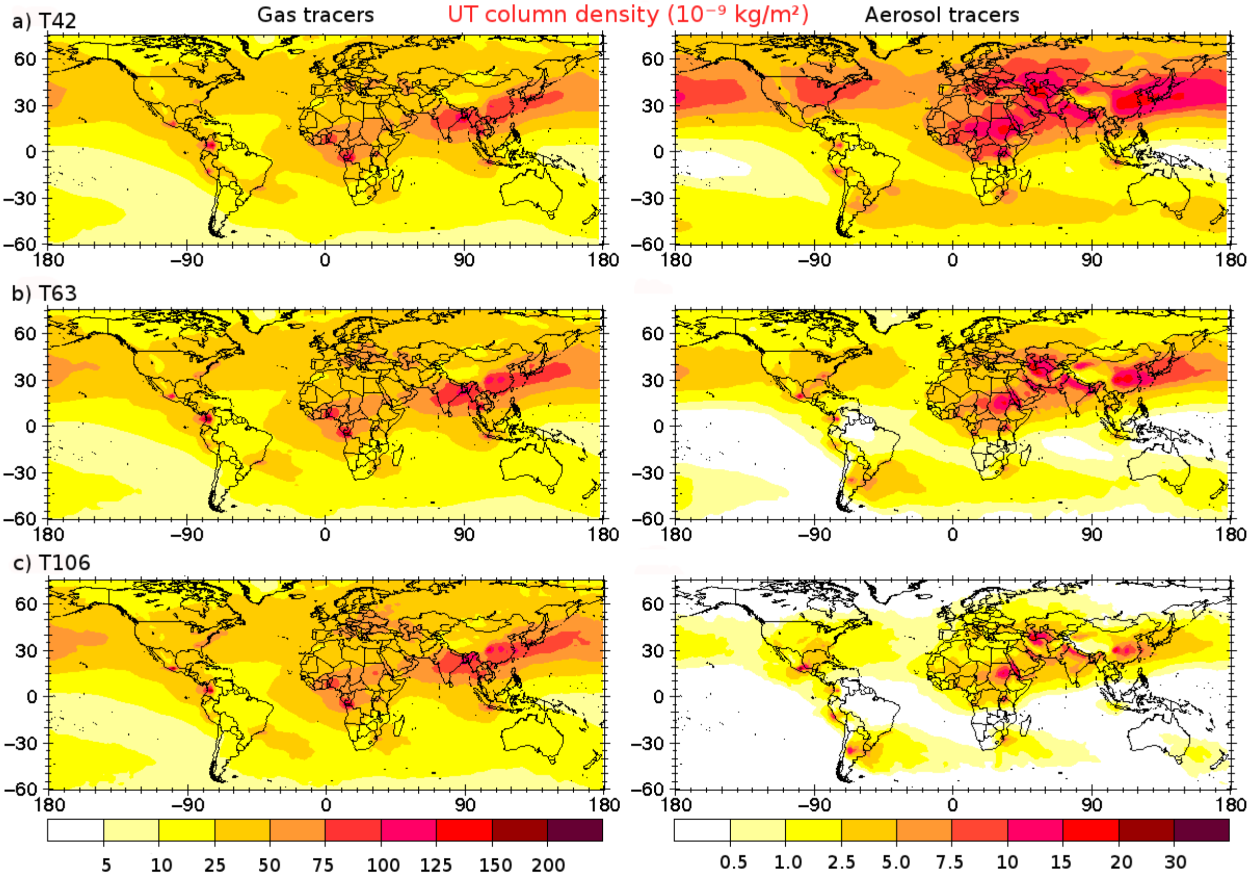

Figure D.1: UT column densities (in $10^{-9}\,\mathrm{kg\,m^{-2}}$) for generic gas phase and aerosol tracer simulations in different horizontal resolutions. On the left for gas phase tracers, on the right for aerosol tracers ($\mathrm{NS_{act}}$ 1.0 µm) for a) T42, b) T63, and c) T106.

decay with an e-folding time of 10 days.

In contrast, the upper tropospheric column densities on the right side of Figure D.1 clearly show a decrease with increasing horizontal resolution. The passive aerosol tracers undergo deposition processes via dry deposition, sedimentation, and large-scale and convective scavenging. The question arises why the aerosol burden above 5 km changes depending on the horizontal model resolution. In Figure D.2, the atmospheric mass fractions above 5 km are plotted for different sensitivity studies in two horizontal resolutions, T106 (ordinate) and T42 (abscissa). For gas phase tracers (dark blue diamonds) almost no difference is present. The same is evident for generic aerosol tracers when all scavenging processes are turned off (light blue diamonds). In contrast, when scavenging is turned on more mass is present above 5 km in the low resolution model (red diamonds). Switching off single parts of the scavenging process leads in some cases to a better agreement between the two resolutions but in no case it is fully satisfactory in terms of equal mass fractions above 5 km. Thus, scavenging of tracers leads to different burdens in the upper atmosphere which can not be neglected.

The scavenging process is a column process which is written to be independent from the horizontal model resolution. However, several variables are used in the process which are calculated in the cloud parameterizations, which depend on the resolution, e.g., the autoconversion rate which determines the transition from cloud droplets to precipitation droplets. From Hagemann et al. (2006) it is known that, although the total precipitation is almost constant for the different horizontal model resolutions which are applicable in ECHAM5, the contribution of convective and large-scale precipitation to total precipitation shift towards

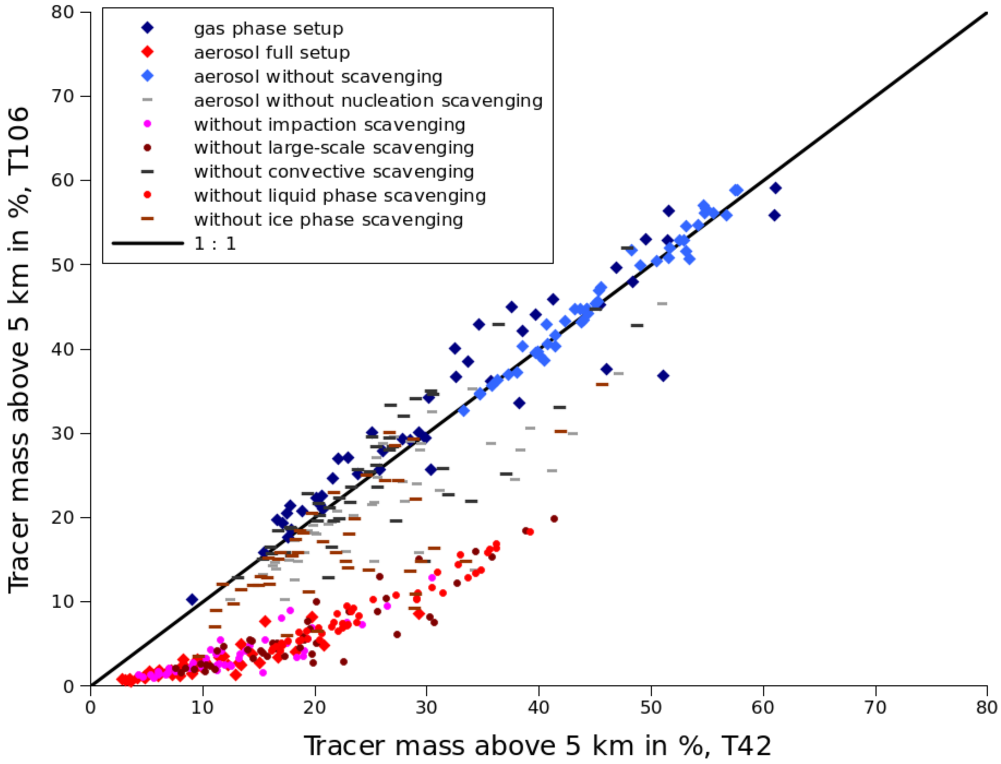

Figure D.2: UT mass fractions (in %) above 5 km for T106 and T42, shown for different test simulations.

more large-scale precipitation with higher horizontal model resolution. This subsequently affects the removal of tracer mass by scavenging. Convective precipitation commonly only affects a small fraction of a grid box/column. Consequently, only a small fraction of aerosol mass in this box/column is removed. In the case of large-scale precipitation, a larger fraction or the entire box/column is affected and hence also a larger fraction of the aerosol mass. The shift from convective precipitation to more large-scale precipitation consequently leads to a shift to larger LSS (T42-NS$_{\text{act}}$: 61.2 %, T42-NS$_{\text{inact}}$: 46.1 %, T106-NS$_{\text{act}}$: 67.9 %, T106-NS$_{\text{inact}}$: 57.7 %) and smaller CVS (T42-NS$_{\text{act}}$: 30.4 %, T42-NS$_{\text{inact}}$: 43.0 %, T106-NS$_{\text{act}}$: 25.2 %, T106-NS$_{\text{inact}}$: 33.7 %) values with increasing model resolution.

Possible solutions include a more sophisticated and also resolution independent representation of the cloud parameterizations as well as a combined treatment of convective tracer transport and scavenging which both are non-trivial tasks to fulfill.

E

Publication list

The following articles have been published during the time of my PhD. It is distinguished between publications related to the PhD and others.

Publications related to PhD work

Kunkel, D., Lawrence, M. G., Tost, H., Kerkweg, A., Jöckel, P., and Borrmann, S.: Urban emission hot spots as sources for remote aerosol deposition, Geophysical Research Letters, 39, 6 PP., doi: 10.1029/2011GL049634, 2012a

Lelieveld, J., Kunkel, D., and Lawrence, M. G.: Global risk of radioactive fallout after major nuclear reactor accidents, Atmospheric Chemistry and Physics, 12, 4245–4258, doi: 10.5194/acp-12-4245-2012, 2012a

Kunkel, D., Tost, H., and Lawrence, M. G.: Aerosol pollution potential from major population centers, Atmospheric Chemistry and Physics Discussions, 12, 25 389–25 440, doi: 10.5194/acpd-12-25389-2012, 2012b

Lelieveld, J., Lawrence, M. G., and Kunkel, D.: Comment on "Global risk of radioactive fallout after major nuclear reactor accidents" by J. Lelieveld et al. (2012), Atmospheric Chemistry and Physics Discussions, 12, 19 303–19 309, doi: 10.5194/acpd-12-19303-2012, 2012b

Other publications

de Reus, M., Borrmann, S., Bansemer, A., Heymsfield, A. J., Weigel, R., Schiller, C., Mitev, V., Frey, W., Kunkel, D., Kürten, A., Curtius, J., Sitnikov, N. M., Ulanovsky, A., and Ravegnani, F.: Evidence for ice particles in the tropical stratosphere from in-situ measurements, Atmospheric Chemistry and Physics, 9, D0001, doi: 10.5194/acp-9-6775-2009, 2009

Borrmann, S., Kunkel, D., Weigel, R., Minikin, A., Deshler, T., Wilson, J. C., Curtius, J., Volk, C. M., Homan, C. D., Ulanovsky, A., Ravegnani, F., Viciani, S., Shur, G. N., Belyaev, G. V., Law, K. S., and Cairo, F.: Aerosols in the tropical and subtropical UT/LS: in-situ measurements of submicron particle abundance and volatility, Atmospheric Chemistry and Physics, 10, 5573–5592, doi: 10.5194/acp-10-5573-2010, 2010

Real, E., Orlandi, E., Law, K. S., Fierli, F., Josset, D., Cairo, F., Schlager, H., Borrmann, S., Kunkel, D., Volk, C. M., McQuaid, J. B., Stewart, D. J., Lee, J., Lewis, A. C., Hopkins, J. R., Ravegnani, F., Ulanovski, A., and Liousse, C.: Cross-hemispheric transport of central African biomass burning pollutants: implications for downwind ozone production, Atmospheric Chemistry and Physics, 10, 3027–3046, doi: 10.5194/acp-10-3027-2010, 2010

Law, K. S., Fierli, F., Cairo, F., Schlager, H., Borrmann, S., Streibel, M., Real, E., Kunkel, D., Schiller, C., Ravegnani, F., Ulanovsky, A., D'Amato, F., Viciani, S., and Volk, C. M.: Air mass origins influencing TTL chemical composition over West Africa during 2006 summer monsoon, Atmospheric Chemistry and Physics, 10, 10 753–10 770, doi: 10.5194/acp-10-10753-2010, 2010

Frey, W., Borrmann, S., Kunkel, D., Weigel, R., de Reus, M., Schlager, H., Roiger, A., Voigt, C., Hoor, P., Curtius, J., Krämer, M., Schiller, C., Volk, C. M., Homan, C. D., Fierli, F., Di Donfrancesco, G., Ulanovsky, A., Ravegnani, F., Sitnikov, N. M., Viciani, S., D'Amato, F., Shur, G. N., Belyaev, G. V., Law, K. S., and Cairo, F.: In situ measurements of tropical cloud properties in the West African Monsoon: upper tropospheric ice clouds, Mesoscale Convective System outflow, and subvisual cirrus, Atmospheric Chemistry and Physics, 11, 5569–5590, doi: 10.5194/acp-11-5569-2011, 2011

Weigel, R., Borrmann, S., Kazil, J., Minikin, A., Stohl, A., Wilson, J. C., Reeves, J. M., Kunkel, D., de Reus, M., Frey, W., Lovejoy, E. R., Volk, C. M., Viciani, S., D'Amato, F., Schiller, C., Peter, T., Schlager, H., Cairo, F., Law, K. S., Shur, G. N., Belyaev, G. V., and Curtius, J.: In situ observations of new particle formation in the tropical upper troposphere: the role of clouds and the nucleation mechanism, Atmospheric Chemistry and Physics, 11, 9983–10 010, doi: 10.5194/acp-11-9983-2011, 2011

List of Figures

List of Tables

Nomenclature

List of Abbreviations

A-TRAIN	Afternoon Train, satellite constellation
ABC	Atmospheric Brown Cloud
ABWR	Advanced Boiling Water Reactor
AC-GCM	Atmospheric Chemistry General Circulation Model
AEROCOM	Aerosol Comparisons between Observations and Models
AEROPT	Aerosol optical depth calculation in EMAC
AGR	Advanced Gas Cooled Graphite Reactor
AI	Hydrophobic accumulation mode
AOD	Aerosol Optical Depth
AS	Hydrophilic accumulation mode
AVHRR	Advanced Very High Resolution Radiometer
BN	Russian Fast Neutron Reactor
BWR	Boiling Water Reactor
CANDU	Canada Deuterium Uranium Reactor
CAPE	Convective available potential energy
CAREBEIJING	Regional formation processes and controlling effects of air pollution before and during the Beijing Olympics
CFCs	Chloro-Fluoro-Carbons
CI	Hydrophobic coarse mode
CityZEN	megaCITY Zoom for the ENvironment
Climate class A	Tropical climate class
Climate class B	Arid climate class
Climate class C	Temperate climate class
Climate class Cf	Temperate no dry season climate class
Climate class Cs	Temperate summer dry climate class
Climate class Cw	Temperate winter dry climate class
Climate class D	Cold climate class
CLOUD	Large-scale condensation in EMAC
CONVECT	Convective cloud parameterization in EMAC

CPR	Chinese Pressurized Reactor
CPU	Computer Process Unit
CRU	Climate Research Unit
CS	Hydrophilic coarse mode
CVTRANS	Convective tracer transport in EMAC
DLR	Deutsches Zentrum für Luft- und Raumfahrt
DMF	Deposition mass flux
DRC	Democratic Republic of the Congo
DRYDEP	Dry deposition in EMAC
ECHAM5	5th generation European Centre Hamburg general circulation model
ECMWF	European Centre for Medium-Range Weather Forecasts
EDGAR3.2FT 2000	Emission Database for Global Research, version 3.2, fast track
EMAC	ECHAM5/MESSy Atmospheric Chemistry Model
ENSO	El-Niño-Southern Oscillation
EPR	European Pressurized Reactor
ERA-INTERIM	Reanalysis data from ECMWF
FBR	Fast Breeder Reactor
FRA 2000	US Geological Survey Global Forest Resource Assessment, 2000
GBWR	Russian Graphite Moderated Reactor
GCM	General Circulation Model
GMXe	Global Modal-aerosol eXtention, aerosol scheme in EMAC
GPCC	Global Precipitation Climatology Centre
GRS	Gesellschaft für Reaktorsicherheit
HETCHEM	Heterogeneous reactions in EMAC
IAEA	International Atomic Energy Agency
INES	International Nuclear Event Scale
IPCC-AR5	International Panel on Climate Change, fifth Assessment Report
ISORROPIA-II	Thermodynamic equilibrium model in `GMXe`/EMAC
ITCZ	InterTropical Convergence Zone
JVAL	Photolysis rate coefficients calculation in EMAC
KI	Hydrophobic Aitken mode
KPP	Kinetic PreProcessor
KS	Hydrophilic Aitken mode
LNOX	$\mathrm{NO_x}$ production from lightning in EMAC
M7	Modal-aerosol scheme of Vignati et al. (2004)
MAECHAM5	Middle atmosphere version of ECHAM5
Magnox	Gas Cooled Reactor
MATCH-MPIC	Model of ATmospheric CHemistry - Max Planck Institute for Chemistry version
MCMA-2003	Mexico City Metropolitan Area Field Campaign 2003

MECCA	Module Efficiently Calculating the Chemistry of the Atmosphere, chemistry module in EMAC
MEGAPOLI	Megacities: Emissions, urban, regional and Global Atmospheric POLlution and climate effects, and Integrated tools for assessment and mitigation
MESSy	Modular Earth Submodel System
MILAGRO	Megacity Initiative: Local And Global Research Observations
MODIS	Moderate-resolution imaging spectroradiometer
MPC	Major Population Center
NAO	North Atlantic Oscillation
NASA	National Space Agency
NCAR	National Center for Atmospheric Research
NCEP	National Centers for Environmental Protection
NMHCs	Non-Methane HydroCarbons
NOAA	National Oceanic and Atmospheric Administration
NPP	Nuclear Power Plant
NRC	US Nuclear Regulatory Commission
NS	Hydrophilic nucleation mode
NS_{act}	Nucleation scavenging active aerosols
NS_{inact}	Nucleation scavenging inactive aerosols
OFFLEM	Off-line emissions in EMAC
ONLEM	On-line emissions in EMAC
PAm	Passive aerosol tracers with microphysics
PAs	Generic aerosol tracers
PHWR	Pressurized High Water Reactor
$PM_{2.5}$	Aerosol mass of particles with an aerodynamic diameter smaller $2.5\,\mu m$
PRC	People's Republic of China
PRD	Pearl River Delta
PRIDE-PRD	Program of Regional Integrated Experiments on Air Quality over Pearl River Delta of China
PTRAC	Generic tracer initialization in EMAC
PWR	Pressurized Water Reactor
RAD4ALL	Radiation scheme of EMAC
RBMK	Russian Light Water Cooled Reactors
RC	Republic of the Congo
RCP	Representative Concentration Pathway
ROK	Republic of Korea
SCAV	Wet removal in EMAC
SEDI	Sedimentation in EMAC
T106	Truncation at wavenumber 106
T159	Truncation at wavenumber 159
T21	Truncation at wavenumber 21

T42	Truncation at wavenumber 42
T63	Truncation at wavenumber 63
T85	Truncation at wavenumber 85
TNUDGE	Tracer nudging in EMAC
TRACER	General tracer initialization in EMAC
TROPOP	Diagnostic determination of the tropopause and boundary layer height in EMAC
UHI	Urban Heat Island
UT	Upper troposphere, upper tropospheric
WASO	WAter SOluble compounds
WHO	World Health Organization
WMO	World Meteorological Organization
WWER	Water-Water Energetic Reactor

List of Constants

π	3.14159265

List of Species

^{103}Ru	Ruthenium-103
^{106}Ru	Ruthenium-106
^{131}I	Iodine-131
^{132}Te	Tellurium-132
^{133}I	Iodine-133
^{134}Cs	Cesium-134
^{137}Cs	Cesium-137
^{140}Ba	Barium-140
^{89}Sr	Strontium-89
^{90}Sr	Strontium-90
BC	Black carbon
C_2H_4	Ethene
C_2H_6	Ethane
C_3H_6	Propene
C_3H_8	Propane
C_4H_{10}	Butane
C_5H_8	Isoprene
Ca^{2+}	Calcium
CCl_4	Tetrachloromethane
CF_2Cl_2	Dichlorodifluoromethane, CFC-12

CF_2ClBr	Bromochlorodifluoromethane, Halon 1211
CF_3Br	Bromotrifluoromethane, Halon 1301
$CFCl_3$	Trichlorofluoromethane, CFC-11
CH_3Br	Bromomethane
CH_3CCl_3	1,1,1-trichloroethane, Methyl chloroform
CH_3CHO	Ethanal, Acetaldehyde
CH_3Cl	Chloromethane
CH_3COCH_3	2-Propanone, Acetone
CH_3COOH	Acetic acid
CH_3OH	Methanol
CH_4	Methane
Cl^-	Chloride
CO_2	Carbon dioxide
CO	Carbon monoxide
DMS	Dimethyl sulfide
DU	Dust
H_2O_2	Dihydrogen dioxide, hydrogen peroxide
H_2O	Water
H_2SO_4	Sulfuric acid
H_2	Hydrogen
HCHO	Methanal, Formaldehyde
HCOOH	Formic acid
HNO_3	Nitric acid
HO_2	Hydroperoxyl, peroxyl radical
HSO_4^-	Bisulfate
K^+	Potassium
MEK	Butan-2-one, Methyl ethyl ketone (CH3C(O)CH2CH3)
Mg^{2+}	Magnesium
N_2O_5	Dinitrogen pentoxide
N_2O	Nitrous oxide
Na^+	Sodium
NH_3	Ammonia
NH_4^+	Ammonium
NO_2	Nitrogen dioxide
NO_3^-	Nitrate
NO_x	Nitrogen oxides
NO	Nitrogen oxide
O_3	Ozone
OC	Organic carbon
OH	Hydroxyl radical

POM	Particulate organic matter
SF_6	Sulfur hexafluoride
SO_2	Sulfur dioxides
SO_4^{2-}	Sulfate
SS	Sea spray
VOCs	Volatile organic compounds

List of Symbols

Symbol	**Description**	**Unit**
Δt	Model time step	s
Λ	Impaction scavenging efficiency	s^{-1}
Λ_{B}	Scavenging coefficient for Brownian motion	s^{-1}
γ_{sw}	Shortwave asymmetry factor	–
ω_{sw}	Shortwave single scattering albedo	–
$\partial X_{\mathrm{mod}}/\partial t$	Non-physical relaxation term, ”nudging”	$[X]\,s^{-1}$
$\sigma(k)$	Standard deviation of lognormal mode k	–
σ_{lw}	Longwave extinction coefficient	–
σ_{sw}	Shortwave extinction coefficient	–
τ	Aerosol optical depth	–
D_{p}	Diffusivity of the particle	$m^2\,s^{-1}$
E	Collection efficiency	–
F_{D}	Dry deposition flux	$kg\,m^{-2}\,s^{-1}$
F_{rain}	Effective rain flux	$kg\,m^{-2}\,s^{-1}$
$G(X)$	Relaxation coefficient	s^{-1}
M_{i}	Total atmospheric burden in the insoluble mode	kg
M_{s}	Total atmospheric burden in the soluble mode	kg
M_{t}	Total atmospheric burden in all modes	kg
N_{k}	Aerosol number concentration of mode k	cm^{-3}
R_{a}	Aerodynamic resistance	$s\,m^{-1}$
R_{qbr}	Quasi-laminar boundary layer resistance	$s\,m^{-1}$
R_{s}	Surface resistance	$s\,m^{-1}$
RH	Relative humidity	%
T	Atmospheric temperature	K
V_{D}	Dry deposition velocity	$m\,s^{-1}$
$\bar{r_{\mathrm{k}}}$	Aerosol number mean radius	m
c	Concentration of a species	$kg\,m^{-3}$
d	Aerosol diameter	µm
d_{e}	Aerosol diameter at emission	nm

f_{Csf}	Cunningham-slip-flow correction	–
f_{Slinn}	Slinn factor	–
m_{i}	Mass of the insoluble mode fulfilling the criteria of the metric	kg
m_{s}	Mass of all soluble modes fulfilling the criteria of the metric	kg
m_{t}	Mass of all modes fulfilling the criteria of the metric	kg
r_{p}	Aerosol radius	m
r_{rain}	Cloud droplet radius	m
v_{St}	Stokes velocity	$\mathrm{m\,s^{-1}}$
v_{t}	Terminal fall speed	$\mathrm{m\,s^{-1}}$
X_{mod}	Modeled state of the atmosphere	[X]
X_{obs}	Observed state of the atmosphere	[X]
A_{Y}	Area of tracer density threshold exceedance	$10^6\,\mathrm{km^2}$
CON	Mass fraction removed over land surfaces	%
CVS	Mass fraction removed by scavenging in convective clouds	%
D_{X}	Area of deposition threshold exceedance	$10^3\,\mathrm{km^2}$
DED	Mass fraction removed by dry deposition	%
DEP_{accu}	Accumulated deposition mass flux	$\mathrm{kg\,m^{-2}\,s^{-1}}$
DRD	Dry fraction of remote deposition potential	%
DRT	Remote deposition potential	%
DRY	Mass fraction of dry deposited mass	%
E_{UT}	Upper tropospheric pollution potential	%
ELR_{Z}	Remote low-level pollution potential	%
EM_{total}	Mean global emission flux	$\mathrm{kg\,m^{-2}\,s^{-1}}$
LSS	Mass fraction removed by scavenging in large-scale clouds	%
LWC	Liquid water content	$\mathrm{g\,cm^{-3}}$
RCL_{X}	City retention pollution potential	%
SED	Mass fraction removed by sedimentation	%

References

Andreae, M. and Rosenfeld, D.: Aerosol-cloud-precipitation interactions. Part 1. The nature and sources of cloud-active aerosols, Earth-Science Reviews, 89, 13–41, doi: 10.1016/j.earscirev.2008.03.001, 2008.

Andreae, M., Artaxo, P., Fischer, H., Freitas, S., Gregoire, J., Hansel, A., Hoor, P., Kormann, R., Krejci, R., Lange, L., Lelieveld, J., Lindinger, W., Longo, K., Peters, W., de Reus, M., Scheeren, B., Dias, M., Strom, J., van Velthoven, P., and Williams, J.: Transport of biomass burning smoke to the upper troposphere by deep convection in the equatorial region, Geophysical Research Letters, 28, 951–954, 2001.

Anspaugh, L. R., Catlin, R. J., and Goldman, M.: The global impact of the Chernobyl reactor accident, Science, 242, 1513–1519, doi: 10.1126/science.3201240, 1988.

Arakawa, A. and Schubert, W. H.: Interaction of a Cumulus Cloud Ensemble with the Large-Scale Environment, Part I, Journal of the Atmospheric Sciences, 31, 674–701, doi: 10.1175/1520-0469(1974)031$<$0674$:$IOACCE$>$2.0.CO;2, 1974.

Arnfield, A. J.: Two decades of urban climate research: a review of turbulence, exchanges of energy and water, and the urban heat island, International Journal of Climatology, 23, 1–26, doi: 10.1002/joc.859, 2003.

Asselin, R.: Frequency Filter for Time Integrations, Monthly Weather Review, 100, 487–490, doi: 10.1175/1520-0493(1972)100<0487:FFFTI>2.3.CO;2, 1972.

Baklanov, A., Lawrence, M., Pandis, S., Mahura, A., Finardi, S., Moussiopoulos, N., Beekmann, M., Laj, P., Gomes, L., Jaffrezo, J., Borbon, A., Coll, I., Gros, V., Sciare, J., Kukkonen, J., Galmarini, S., Giorgi, F., Grimmond, S., Esau, I., Stohl, A., Denby, B., Wagner, T., Butler, T., Baltensperger, U., Builtjes, P., van den Hout, D., van der Gon, H. D., Collins, B., Schluenzen, H., Kulmala, M., Zilitinkevich, S., Sokhi, R., Friedrich, R., Theloke, J., Kummer, U., Jalkinen, L., Halenka, T., Wiedensholer, A., Pyle, J., and Rossow, W. B.: MEGAPOLI: concept of multi-scale modelling of megacity impact on air quality and climate, Advances in Science and Research, 4, 115–120, 2010.

Baklanov, A. A. and Mahura, A. G.: Assessment of possible airborne impact from risk sites: methodology for probabilistic atmospheric studies, Atmospheric Chemistry and Physics, 4, 485–495, doi: 10.5194/acp-4-485-2004, 2004.

Beirle, S., Boersma, K. F., Platt, U., Lawrence, M. G., and Wagner, T.: Megacity Emissions and Lifetimes of Nitrogen Oxides Probed from Space, Science, 333, 1737 –1739, doi: 10.1126/science.1207824, 2011.

Bergin, M. S., West, J. J., Keating, T. J., and Russell, A. G.: Regional Atmospheric Pollution and Transboundary Air Quality Management, Annual Review of Environment and Resources, 30, 1–37, doi: 10.1146/annurev.energy.30.050504.144138, 2005.

Berntsen, T. K., Karlsdóttir, S., and Jaffe, D. A.: Influence of Asian emissions on the composition of air reaching the north western United States, Geophysical Research Letters, 26, 2171–2174, doi: 10.1029/1999GL900477, 1999.

Betzer, P. R., Carder, K. L., Duce, R. A., Merrill, J. T., Tindale, N. W., Uematsu, M., Costello, D. K., Young, R. W., Feely, R. A., Breland, J. A., Bernstein, R. E., and Greco, A. M.: Long-range transport of giant mineral aerosol particles, Nature, 336, 568–571, doi: 10.1038/336568a0, 1988.

Borrmann, S., Kunkel, D., Weigel, R., Minikin, A., Deshler, T., Wilson, J. C., Curtius, J., Volk, C. M., Homan, C. D., Ulanovsky, A., Ravegnani, F., Viciani, S., Shur, G. N., Belyaev, G. V., Law, K. S., and Cairo, F.: Aerosols in the tropical and subtropical UT/LS: in-situ measurements of submicron particle abundance and volatility, Atmospheric Chemistry and Physics, 10, 5573–5592, doi: 10.5194/acp-10-5573-2010, 2010.

Brandt, J., Christensen, J. H., and Frohn, L. M.: Modelling transport and deposition of caesium and iodine from the Chernobyl accident using the DREAM model, Atmospheric Chemistry and Physics, 2, 397–417, URL http://www.atmos-chem-phys.net/2/397/2002/, 2002.

Bristow, C. S., Hudson-Edwards, K. A., and Chappell, A.: Fertilizing the Amazon and equatorial Atlantic with West African dust, Geophysical Research Letters, 37, L14 807, doi: 10.1029/2010GL043486, 2010.

Bromet, E. J., Havenaar, J. M., and Guey, L. T.: A 25 year retrospective review of the psychological consequences of the Chernobyl accident, Clinical oncology (Royal College of Radiologists (Great Britain)), 23, 297–305, doi: 10.1016/j.clon.2011.01.501, 2011.

Buesseler, K. O., Jayne, S. R., Fisher, N. S., Rypina, I. I., Baumann, H., Baumann, Z., Breier, C. F., Douglass, E. M., George, J., Macdonald, A. M., Miyamoto, H., Nishikawa, J., Pike, S. M., and Yoshida, S.: Fukushima-Derived Radionuclides in the Ocean and Biota Off Japan, Proceedings of the National Academy of Sciences, 109, 5984–5988, doi: 10.1073/pnas.1120794109, 2012.

Burkhardt, J.: Hygroscopic particles on leaves: nutrients or desiccants?, Ecological Monographs, 80, 369–399, doi: 10.1890/09-1988.1, WOS:000279801300002, 2010.

Burns, P. C., Ewing, R. C., and Navrotsky, A.: Nuclear Fuel in a Reactor Accident, Science, 335, 1184–1188, doi: 10.1126/science.1211285, 2012.

Burrows, S. M., Butler, T., Jöckel, P., Tost, H., Kerkweg, A., Pöschl, U., and Lawrence, M. G.: Bacteria in the global atmosphere – Part 2: Modeling of emissions and transport between different ecosystems, Atmospheric Chemistry and Physics, 9, 9281–9297, doi: 10.5194/acp-9-9281-2009, 2009.

Butler, T., Lawrence, M., Gurjar, B., van Aardenne, J., Schultz, M., and Lelieveld, J.: The representation of emissions from megacities in global emission inventories, Atmospheric Environment, 42, 703–719, doi: 10.1016/j.atmosenv.2007.09.060, 2008.

Butler, T. M. and Lawrence, M. G.: The influence of megacities on global atmospheric chemistry: a modelling study, Environmental Chemistry, 6, 219–225, doi: 10.1071/EN08110, 2009.

Butler, T. M., Stock, Z. S., Russo, M. R., Denier van der Gon, H. A. C., and Lawrence, M. G.: Megacity ozone air quality under four alternative future scenarios, Atmospheric Chemistry and Physics, 12, 4413–4428, doi: 10.5194/acp-12-4413-2012, 2012.

Cermak, J. and Knutti, R.: Beijing Olympics as an aerosol field experiment, Geophysical Research Letters, 36, L10 806, doi: 10.1029/2009GL038572, 2009.

Chan, C. K. and Yao, X.: Air pollution in mega cities in China, Atmospheric Environment, 42, 1 – 42, doi: 10.1016/j.atmosenv.2007.09.003, 2008.

Chin, M., Diehl, T., Ginoux, P., and Malm, W.: Intercontinental transport of pollution and dust aerosols: implications for regional air quality, Atmospheric Chemistry and Physics, 7, 5501–5517, doi: 10.5194/acp-7-5501-2007, 2007.

Chino, M., Nakayama, H., Nagai, H., Terada, H., Katata, G., and Yamazawa, H.: Preliminary Estimation of Release Amounts of 131I and 137Cs Accidentally Discharged from the Fukushima Daiichi Nuclear Power Plant into the Atmosphere, Journal of Nuclear Science and Technology, 48, 1129–1134, doi: 10.1080/18811248.2011.9711799, 2011.

Christodouleas, J. P., Forrest, R. D., Ainsley, C. G., Tochner, Z., Hahn, S. M., and Glatstein, E.: Short-Term and Long-Term Health Risks of Nuclear-Power-Plant Accidents, New England Journal of Medicine, 364, 2334–2341, doi: 10.1056/NEJMra1103676, 2011.

Christoudias, T., Pozzer, A., and Lelieveld, J.: Influence of the North Atlantic Oscillation on air pollution transport, Atmospheric Chemistry and Physics, 12, 869–877, doi: 10.5194/acp-12-869-2012, 2012.

Clarisse, L., Fromm, M., Ngadi, Y., Emmons, L., Clerbaux, C., Hurtmans, D., and Coheur, P.: Intercontinental transport of anthropogenic sulfur dioxide and other pollutants: An infrared remote sensing case study, Geophysical Research Letters, 38, 5 PP., doi: 10.1029/2011GL048976, 2011.

Cooper, O. R., Forster, C., Parrish, D., Trainer, M., Dunlea, E., Ryerson, T., Hübler, G., Fehsenfeld, F., Nicks, D., Holloway, J., de Gouw, J., Warneke, C., Roberts, J. M., Flocke, F., and Moody, J.: A case study of transpacific warm conveyor belt transport: Influence of merging airstreams on trace gas import to North America, Journal of Geophysical Research, 109, 17 PP, doi: 10.1029/2003JD003624, 2004.

Courant, R., Friedrichs, K., and H., L.: Über die partiellen Differenzialgleichungen der mathematischen Physik, Mathematische Annalen, 100, 32–74, 1928.

Crutzen, P. J. and Lawrence, M. G.: The Impact of Precipitation Scavenging on the Transport of Trace Gases: A 3-Dimensional Model Sensitivity Study, Journal of Atmospheric Chemistry, 37, 81–112–112, 2000.

Cuvelier, C., Thunis, P., Vautard, R., Amann, M., Bessagnet, B., Bedogni, M., Berkowicz, R., Brandt, J., Brocheton, F., Builtjes, P., Carnavale, C., Coppalle, A., Denby, B., Douros, J., Graf, A., Hellmuth, O., Hodzic, A., Honoré, C., Jonson, J., Kerschbaumer, A., de Leeuw, F., Minguzzi, E., Moussiopoulos, N., Pertot, C., Peuch, V., Pirovano, G., Rouil, L., Sauter, F., Schaap, M., Stern, R., Tarrason, L., Vignati, E., Volta, M., White, L., Wind, P., and Zuber, A.: CityDelta: A model intercomparison study to explore the impact of emission reductions in European cities in 2010, Atmospheric Environment, 41, 189 – 207, doi: 10.1016/j.atmosenv.2006.07.036, 2007.

Damian, V., Sandu, A., Damian, M., Potra, F., and Carmichael, G. R.: The kinetic preprocessor KPP-a software environment for solving chemical kinetics, Computers & Chemical Engineering, 26, 1567 – 1579, doi: 10.1016/S0098-1354(02)00128-X, 2002.

Davoine, X. and Bocquet, M.: Inverse modelling-based reconstruction of the Chernobyl source term available for long-range transport, Atmospheric Chemistry and Physics, 7, 1549–1564, doi:

10.5194/acp-7-1549-2007, 2007.

De Cort, M., Dubois, G., Fridman, S., Germenchuk, M., Izrael, Y. A., Janssens, A., Jones, A., Kelly, G., Kvasnikova, E., Matveenko, I., Nazarov, I., Pokumeiko, Y. M., Sitak, V., Stukin, E., Tabachny, L. Y., Tsaturov, Y. S., and Avdyushin, S.: Atlas of caesium deposition on Europe after the Chernobyl accident, Office for Official Publications of the European Communities, Luxembourg, iSBN 92-828-3140-X, 1998.

de Reus, M., Borrmann, S., Bansemer, A., Heymsfield, A. J., Weigel, R., Schiller, C., Mitev, V., Frey, W., Kunkel, D., Kürten, A., Curtius, J., Sitnikov, N. M., Ulanovsky, A., and Ravegnani, F.: Evidence for ice particles in the tropical stratosphere from in-situ measurements, Atmospheric Chemistry and Physics, 9, D0001, doi: 10.5194/acp-9-6775-2009, 2009.

Dee, D. P., Uppala, S. M., Simmons, A. J., Berrisford, P., Poli, P., Kobayashi, S., Andrae, U., Balmaseda, M. A., Balsamo, G., Bauer, P., Bechtold, P., Beljaars, A. C. M., van de Berg, L., Bidlot, J., Bormann, N., Delsol, C., Dragani, R., Fuentes, M., Geer, A. J., Haimberger, L., Healy, S. B., Hersbach, H., Hólm, E. V., Isaksen, L., Kållberg, P., Köhler, M., Matricardi, M., McNally, A. P., Monge-Sanz, B. M., Morcrette, J., Park, B., Peubey, C., de Rosnay, P., Tavolato, C., Thépaut, J., and Vitart, F.: The ERA-Interim reanalysis: configuration and performance of the data assimilation system, Quarterly Journal of the Royal Meteorological Society, 137, 553–597, doi: 10.1002/qj.828, 2011.

Dentener, F., Kinne, S., Bond, T., Boucher, O., Cofala, J., Generoso, S., Ginoux, P., Gong, S., Hoelzemann, J. J., Ito, A., Marelli, L., Penner, J. E., Putaud, J., Textor, C., Schulz, M., van der Werf, G. R., and Wilson, J.: Emissions of primary aerosol and precursor gases in the years 2000 and 1750 prescribed data-sets for AeroCom, Atmospheric Chemistry and Physics, 6, 4321–4344, doi: 10.5194/acp-6-4321-2006, 2006.

Di Pierro, M., Jaeglé, L., and Anderson, T. L.: Satellite observations of aerosol transport from East Asia to the Arctic: three case studies, Atmospheric Chemistry and Physics, 11, 2225–2243, doi: 10.5194/acp-11-2225-2011, 2011.

Dickerson, R. R., Huffman, G. J., Luke, W. T., Nunnermacker, L. J., Pickering, K. E., Leslie, A. C. D., Lindsey, C. G., Slinn, W. G. N., Kelly, T. J., Daum, P. H., Delany, A. C., Greenberg, J. P., Zimmerman, P. R., Boatman, J. F., Ray, J. D., and Stedman, D. H.: Thunderstorms: An Important Mechanism in the Transport of Air Pollutants, Science, 235, 460 –465, doi: 10.1126/science.235.4787.460, 1987.

Dickerson, R. R., Doddridge, B. G., Kelley, P., and Rhoads, K. P.: Large-scale pollution of the atmosphere over the remote Atlantic Ocean: Evidence from Bermuda, Journal of Geophysical Research, 100, PAGES 8945–8952, doi: 10.1029/95JD00073, 1995.

Dockery, D. W., Pope, C. A., Xu, X., Spengler, J. D., Ware, J. H., Fay, M. E., Ferris, B. G., and Speizer, F. E.: An Association between Air Pollution and Mortality in Six U.S. Cities, New England Journal of Medicine, 329, 1753–1759, doi: doi:10.1056/NEJM199312093292401, 1993.

Dorrian, M.: Particle Size Distributions of Radioactive Aerosols in the Environment, Radiation Protection Dosimetry, 69, 117 –132, URL http://rpd.oxfordjournals.org/content/69/2/117.abstract, 1997.

Emmons, L. K., Apel, E. C., Lamarque, J., Hess, P. G., Avery, M., Blake, D., Brune, W., Campos, T., Crawford, J., DeCarlo, P. F., Hall, S., Heikes, B., Holloway, J., Jimenez, J. L., Knapp, D. J., Kok, G., Mena-Carrasco, M., Olson, J., O'Sullivan, D., Sachse, G., Walega, J., Weibring, P., Weinheimer, A., and Wiedinmyer, C.: Impact of Mexico City emissions on regional air quality from MOZART-4 simulations, Atmos. Chem. Phys., 10, 6195–6212, doi: 10.5194/acp-10-6195-2010, 2010.

EU: Recent scientific findings and publications on the health effects of Chernobyl, Summary report Radiation Protection No. 170, Directorate-General for Energy Directorate D — Nuclear Energy Unit D.4, European Commission, Bruxelles, 2011.

Fang, Y., Fiore, A. M., Horowitz, L. W., Gnanadesikan, A., Ii, H. L., Hu, Y., and Russell, A. G.: Estimating the contribution of strong daily export events to total pollutant export from the United States in summer, Journal of Geophysical Research, 114, D23 302, doi: 10.1029/2008JD010946, 2009.

Fast, J. D., Jr., W. I. G., Easter, R. C., Zaveri, R. A., Barnard, J. C., Chapman, E. G., Grell, G. A., and Peckham, S. E.: Evolution of ozone, particulates, and aerosol direct radiative forcing in the vicinity of Houston using a fully coupled meteorology-chemistry-aerosol model, Journal of Geophysical Research, 111, D21 305, doi: 10.1029/2005JD006721, 2006.

Finlayson-Pitts, B. J. and Pitts, J. N.: Tropospheric Air Pollution: Ozone, Airborne Toxics, Polycyclic Aromatic Hydrocarbons, and Particles, Science, 276, 1045–1051, doi: 10.1126/science.276.5315.1045, 1997.

Fischer, H., de Reus, M., Traub, M., Williams, J., Lelieveld, J., de Gouw, J., Warneke, C., Schlager, H., Minikin, A., Scheele, R., and Siegmund, P.: Deep convective injection of boundary layer air into the lowermost stratosphere at midlatitudes, Atmospheric Chemistry and Physics, 3, 739–745, doi: 10.5194/acp-3-739-2003, 2003.

Fountoukis, C. and Nenes, A.: ISORROPIA II: a computationally efficient thermodynamic equilibrium model for K^+-Ca^{2+}-Mg^{2+}-NH_4^+-Na^+-SO_4^2-NO_3^--Cl^--H2O aerosols, Atmospheric Chemistry and Physics, 7, 4639–4659, doi: 10.5194/acp-7-4639-2007, 2007.

Frey, W., Borrmann, S., Kunkel, D., Weigel, R., de Reus, M., Schlager, H., Roiger, A., Voigt, C., Hoor, P., Curtius, J., Krämer, M., Schiller, C., Volk, C. M., Homan, C. D., Fierli, F., Di Donfrancesco, G., Ulanovsky, A., Ravegnani, F., Sitnikov, N. M., Viciani, S., D'Amato, F., Shur, G. N., Belyaev, G. V., Law, K. S., and Cairo, F.: In situ measurements of tropical cloud properties in the West African Monsoon: upper tropospheric ice clouds, Mesoscale Convective System outflow, and subvisual cirrus, Atmospheric Chemistry and Physics, 11, 5569–5590, doi: 10.5194/acp-11-5569-2011, 2011.

Fromm, M. D. and Servranckx, R.: Transport of forest fire smoke above the tropopause by supercell convection, Geophysical Research Letters, 30, 4 PP., doi: 10.1029/2002GL016820, 2003.

Fuchs, N.: The Mechanics of aerosols, Pergamon Press, 1964.

Galloway, J. N., Likens, G. E., Keene, W. C., and Miller, J. M.: The Composition of Precipitation in Remote Areas of the World, Journal of Geophysical Research, 87, 8771–8786, doi: 10.1029/JC087iC11p08771, 1982.

Ganzeveld, L. and Lelieveld, J.: Dry deposition parameterization in a chemistry general circulation model and its influence on the distribution of reactive trace gases, Journal of Geophysical Research, 100, 20 999–21,012, doi: 10.1029/95JD02266, 1995.

Ganzeveld, L., Lelieveld, J., and Roelofs, G.: A dry deposition parameterization for sulfur oxides in a chemistry and general circulation model, Journal of Geophysical Research, 103, 5679–5694, doi: 10.1029/97JD03077, 1998.

Gao, Y., Liu, X., Zhao, C., and Zhang, M.: Emission controls versus meteorological conditions in determining aerosol concentrations in Beijing during the 2008 Olympic Games, Atmospheric Chemistry and Physics, 11, 12 437–12 451, doi: 10.5194/acp-11-12437-2011, 2011.

Gauss, M.: CityZEN: Project Final Report, Tech. rep., Norwegian Meteorological Institute, 2011.

Geiger, R.: Landolt-Börnstein – Zahlenwerte und Funktionen aus Physik, Chemie, Astronomie, Geophysik und Technik, alte Serie Vol. 3, Ch. Klassifikation der Klimate nach W. Köppen, Springer, Berlin, 1954.

Geiger, R.: Überarbeitete Neuausgabe von Geiger, R.: Köppen-Geiger / Klima der Erde, Wandkarte 1:16 Mio, Klett-Perthes, Gotha, 1961.

Giorgetta, M. A., Manzini, E., Roeckner, E., Esch, M., and Bengtsson, L.: Climatology and Forcing of the Quasi-Biennial Oscillation in the MAECHAM5 Model, Journal of Climate, 19, 3882–3901, doi: 10.1175/JCLI3830.1, 2006.

Greenfield, S.: Rain Scavenging of radioactive particulate matter from the atmosphere, Journal of Meteorology, 14, 115–125, doi: 10.1175/1520-0469(1957)014<0115:RSORPM>2.0.CO;2, 1957.

Grell, G. A., Peckham, S. E., Schmitz, R., McKeen, S. A., Frost, G., Skamarock, W. C., and Eder, B.: Fully coupled "online" chemistry within the WRF model, Atmospheric Environment, 39, 6957 – 6975, doi: DOI:10.1016/j.atmosenv.2005.04.027, 2005.

Grewe, V., Brunner, D., Dameris, M., Grenfell, J., Hein, R., Shindell, D., and Staehelin, J.: Origin and variability of upper tropospheric nitrogen oxides and ozone at northern mid-latitudes, Atmospheric Environment, 35, 3421–3433, doi: 10.1016/S1352-2310(01)00134-0, URL http://pubs.giss.nasa.gov/abs/gr04000r.html, 2001.

Grimm, N. B., Faeth, S. H., Golubiewski, N. E., Redman, C. L., Wu, J., Bai, X., and Briggs, J. M.: Global Change and the Ecology of Cities, Science, 319, 756 –760, doi: 10.1126/science.1150195, 2008.

GRS: Deutsche Risikostudie Kernkraftwerke - Eine Untersuchung zu dem durch Störfälle in Kernkraftwerken verursachten Risiko, Tech. rep., Gesellschaft für Reaktorsicherheit, Köln: Verl. TÜV Rheinland, 1980.

GRS: Deutsche Risikostudie Kernkraftwerke Phase B, Tech. rep., Gesellschaft für Reaktorsicherheit, Köln: Verl. TÜV Rheinland, 1990.

Guenther, A., Hewitt, C. N., Erickson, D., Fall, R., Geron, C., Graedel, T., Harley, P., Klinger, L., Lerdau, M., Mckay, W. A., Pierce, T., Scholes, B., Steinbrecher, R., Tallamraju, R., Taylor, J., and Zimmerman, P.: A global model of natural volatile organic compound emissions, Journal of Geophysical Research, 100, 8873–8892, doi: 10.1029/94JD02950, 1995.

Gurjar, B. and Lelieveld, J.: New Directions: Megacities and global change, Atmospheric Environment, 39, 391 – 393, doi: 10.1016/j.atmosenv.2004.11.002, 2005.

Guttikunda, S. K., Carmichael, G. R., Calori, G., Eck, C., and Woo, J.: The contribution of megacities to regional sulfur pollution in Asia, Atmospheric Environment, 37, 11–22, doi: 10.1016/S1352-2310(02)00821-X, 2003.

Guttikunda, S. K., Tang, Y., Carmichael, G. R., Kurata, G., Pan, L., Streets, D. G., Woo, J., Thongboonchoo, N., and Fried, A.: Impacts of Asian megacity emissions on regional air quality during spring 2001, Journal of Geophysical Research, 110, 18 PP., doi: 200510.1029/2004JD004921, 2005.

Hack, J. J.: Parameterization of moist convection in the National Center for Atmospheric Research community climate model (CCM2), Journal of Geophysical Research, 99, PP. 5551–5568, doi: 199410.1029/93JD03478, 1994.

Hadley, O., Ramanathan, V., Carmichael, G. R., Tang, Y., , Corrigan, C., Roberts, G., and Mauger, G. S.: Trans-Pacific transport of black carbon and fine aerosols ($D < 2.5$umum) into North America, Journal of Geophysical Research, 112, D05 309, doi: 10.1029/2006JD007632, 2007.

Hagemann, S., Arpe, K., and Roeckner, E.: Evaluation of the Hydrological Cycle in the ECHAM5 Model, Journal of Climate, 19, 3810–3827, doi: 10.1175/JCLI3831.1, 2006.

Hall, N. M. and Peyrillé, P.: Dynamics of the West African monsoon, Journal de Physique IV (Proceedings), 139, 81–99, doi: 10.1051/jp4:2006139007, 2007.

Hass, H., Memmesheimer, M., Geiß, H., Jakobs, H., Laube, M., and Ebel, A.: Simulation of the chernobyl radioactive cloud over Europe using the eurad model, Atmospheric Environment. Part A. General Topics, 24, 673–692, doi: 16/0960-1686(90)90022-F, 1990.

Hastenrath, S.: Climate and Circulation in the Tropics, D. Reidel, 1985.

Heald, C. L., Jacob, D. J., Park, R. J., Alexander, B., Fairlie, T. D., Yantosca, R. M., and Chu, D. A.: Transpacific transport of Asian anthropogenic aerosols and its impact on surface air quality in the United States, Journal of Geophysical Research, 111, 13 PP., doi: 10.1029/2005JD006847, 2006.

Hicks, B. B., Baldocchi, D. D., Meyers, T. P., Hosker, R. P., and Matt, D. R.: A preliminary multiple resistance routine for deriving dry deposition velocities from measured quantities, Water, Air, & Soil Pollution, 36, 311–330, doi: 10.1007/BF00229675, 1987.

Holloway, T., Fiore, A., and Hastings, M. G.: Intercontinental Transport of Air Pollution: Will Emerging Science Lead to a New Hemispheric Treaty?, Environmental Science & Technology, 37, 4535–4542, doi: 10.1021/es034031g, 2003.

Houze, R. A.: Mesoscale convective systems, Reviews of Geophysics, 42, 43 PP., doi: 10.1029/2004RG000150, 2004.

Huntrieser, H., Heland, J., Schlager, H., Forster, C., Stohl, A., Aufmhoff, H., Arnold, F., Scheel, H. E., Campana, M., Gilge, S., Eixmann, R., and Cooper, O.: Intercontinental air pollution transport from North America to Europe: Experimental evidence from airborne measurements and surface observations, Journal of Geophysical Research, 110, 22 PP., doi: 10.1029/2004JD005045, 2005.

IAEA: Regulations for the Safe Transport of Radioactive Material, IAEA Safety Standards for protecting people and the environment Safety Requirements No. TS-R-1, International Atomic Energy Agency, Vienna, iSBN: 92–0–103005–3, 2005.

IAEA: Environmental consequences of the Chernobyl accident and their remediation: twenty years of experience - Report of the Chernobyl Forum Expert Group 'Environment', Radiological assessment reports series, International Atomic Energy Agency, Vienna, 2006.

Itahashi, S., Yumimoto, K., Uno, I., Eguchi, K., Takemura, T., Hara, Y., Shimizu, A., Sugimoto, N., and Liu, Z.: Structure of dust and air pollutant outflow over East Asia in the spring, Geophysical Research Letters, 37, 7 PP., doi: 201010.1029/2010GL044776, 2010.

Jacobson, M. Z.: Atmospheric Pollution: History, Science, and Regulation, Cambridge University Press, 2002.

Jaffe, D., Anderson, T., Covert, D., Kotchenruther, R., Trost, B., Danielson, J., Simpson, W., Berntsen, T., Karlsdottir, S., Blake, D., Harris, J., Carmichael, G., and Uno, I.: Transport of Asian air pollution to North America, Geophysical Research Letters, 26, 711–714, doi: 10.1029/1999GL900100, 1999.

Jeuken, A. B. M., Siegmund, P. C., Heijboer, L. C., Feichter, J., and Bengtsson, L.: On the potential of assimilating meteorological analyses in a global climate model for the purpose of model validation, Journal of Geophysical Research, 101, PP. 16,939–16,950, doi: 10.1029/96JD01218, 1996.

Jöckel, P., von Kuhlmann, R., Lawrence, M. G., Steil, B., Brenninkmeijer, C. a. M., Crutzen, P. J., Rasch, P. J., and Eaton, B.: On a fundamental problem in implementing flux-form advection schemes for tracer transport in 3-dimensional general circulation and chemistry transport models, Quarterly Journal of the Royal Meteorological Society, 127, 1035–1052, doi: 10.1002/qj.49712757318, 2001.

Jöckel, P., Sander, R., Kerkweg, A., Tost, H., and Lelieveld, J.: Technical Note: The Modular Earth Submodel System (MESSy) - a new approach towards Earth System Modeling, Atmospheric Chemistry and Physics, 5, 433–444, doi: 10.5194/acp-5-433-2005, 2005.

Jöckel, P., Tost, H., Pozzer, A., Brühl, C., Buchholz, J., Ganzeveld, L., Hoor, P., Kerkweg, A., Lawrence, M. G., Sander, R., Steil, B., Stiller, G., Tanarhte, M., Taraborrelli, D., van Aardenne, J., and Lelieveld, J.: The atmospheric chemistry general circulation model ECHAM5/MESSy1: consistent simulation of ozone from the surface to the mesosphere, Atmospheric Chemistry and Physics, 6, 5067–5104, doi: 10.5194/acp-6-5067-2006, 2006.

Jöckel, P., Kerkweg, A., Buchholz-Dietsch, J., Tost, H., Sander, R., and Pozzer, A.: Technical Note: Coupling of chemical processes with the Modular Earth Submodel System (MESSy) submodel TRACER, Atmospheric Chemistry and Physics, 8, 1677–1687, doi: 10.5194/acp-8-1677-2008, 2008.

Jöckel, P., Kerkweg, A., Pozzer, A., Sander, R., Tost, H., Riede, H., Baumgaertner, A., Gromov, S., and Kern, B.: Development cycle 2 of the Modular Earth Submodel System (MESSy2), Geoscientific Model Development, 3, 717–752, doi: 10.5194/gmd-3-717-2010, 2010.

Kalnay, E. and Cai, M.: Impact of urbanization and land-use change on climate, Nature, 423, 528–531, doi: 10.1038/nature01675, 2003.

Kalnay, E., Kanamitsu, M., Kistler, R., Collins, W., Deaven, D., Gandin, L., Iredell, M., Saha, S., White, G., Woollen, J., Zhu, Y., Leetmaa, A., Reynolds, R., Chelliah, M., Ebisuzaki, W., Higgins, W., Janowiak, J., Mo, K. C., Ropelewski, C., Wang, J., Jenne, R., and Joseph, D.: The NCEP/NCAR 40-Year Reanalysis Project, Bulletin of the American Meteorological Society, 77, 437–471, doi: 10.1175/1520-0477(1996)077<0437:TNYRP>2.0.CO;2, 1996.

Kanakidou, M., Mihalopoulos, N., Kindap, T., Im, U., Vrekoussis, M., Gerasopoulos, E., Dermitzaki, E., Unal, A., KoÃ§ak, M., Markakis, K., Melas, D., Kouvarakis, G., Youssef, A. F., Richter, A., Hatzianastassiou, N., Hilboll, A., Ebojie, F., Wittrock, F., von Savigny, C., Burrows, J. P., Ladstaetter-Weissenmayer, A., and Moubasher, H.: Megacities as hot spots of air pollution in the East Mediterranean, Atmospheric Environment, 45, 1223 – 1235, doi: 10.1016/j.atmosenv.2010.11.048, 2011.

Karydis, V. A., Tsimpidi, A. P., Fountoukis, C., Nenes, A., Zavala, M., Lei, W., Molina, L. T., and Pandis, S. N.: Simulating the fine and coarse inorganic particulate matter concentrations in a polluted megacity, Atmospheric Environment, 44, 608 – 620, doi: 10.1016/j.atmosenv.2009.11.

023, 2010.

Kerkweg, A., Buchholz, J., Ganzeveld, L., Pozzer, A., Tost, H., and Jöckel, P.: Technical Note: An implementation of the dry removal processes DRY DEPosition and SEDImentation in the Modular Earth Submodel System (MESSy), Atmospheric Chemistry and Physics, 6, 4617–4632, doi: 10.5194/acp-6-4617-2006, 2006a.

Kerkweg, A., Sander, R., Tost, H., and Jöckel, P.: Technical note: Implementation of prescribed (OFFLEM), calculated (ONLEM), and pseudo-emissions (TNUDGE) of chemical species in the Modular Earth Submodel System (MESSy), Atmospheric Chemistry and Physics, 6, 3603–3609, doi: 10.5194/acp-6-3603-2006, 2006b.

Kinoshita, N., Sueki, K., Sasa, K., Kitagawa, J.-i., Ikarashi, S., Nishimura, T., Wong, Y., Satou, Y., Handa, K., Takahashi, T., Sato, M., and Yamagata, T.: Assessment of individual radionuclide distributions from the Fukushima nuclear accident covering central-east Japan, Proceedings of the National Academy of Sciences, 108, 19 526 –19 529, doi: 10.1073/pnas.1111724108, 2011.

Kottek, M., Grieser, J., Beck, C., Rudolf, B., and Rubel, F.: World Map of the Köppen-Geiger climate classification updated, Meteorologische Zeitschrift, 15, 259–263, doi: 10.1127/0941-2948/2006/0130, 2006.

Kraas, F.: Megacities and global change: key priorities, The Geographical Journal, 173, 79–82, doi: 10.1111/j.1475-4959.2007.232_2.x, 2007.

Kunkel, D., Lawrence, M. G., Tost, H., Kerkweg, A., Jöckel, P., and Borrmann, S.: Urban emission hot spots as sources for remote aerosol deposition, Geophysical Research Letters, 39, 6 PP., doi: 10.1029/2011GL049634, 2012a.

Kunkel, D., Tost, H., and Lawrence, M. G.: Aerosol pollution potential from major population centers, Atmospheric Chemistry and Physics Discussions, 12, 25 389–25 440, doi: 10.5194/acpd-12-25389-2012, 2012b.

Lamarque, J., Bond, T. C., Eyring, V., Granier, C., Heil, A., Klimont, Z., Lee, D., Liousse, C., Mieville, A., Owen, B., Schultz, M. G., Shindell, D., Smith, S. J., Stehfest, E., Van Aardenne, J., Cooper, O. R., Kainuma, M., Mahowald, N., McConnell, J. R., Naik, V., Riahi, K., and van Vuuren, D. P.: Historical (1850-2000) gridded anthropogenic and biomass burning emissions of reactive gases and aerosols: methodology and application, Atmospheric Chemistry and Physics, 10, 7017–7039, doi: 10.5194/acp-10-7017-2010, 2010.

Landgraf, J. and Crutzen, P. J.: An Efficient Method for Online Calculations of Photolysis and Heating Rates, Journal of the Atmospheric Sciences, 55, 863–878, doi: 10.1175/1520-0469(1998)055<0863:AEMFOC>2.0.CO;2, 1998.

Lauer, A., Eyring, V., Hendricks, J., Jöckel, P., and Lohmann, U.: Global model simulations of the impact of ocean-going ships on aerosols, clouds, and the radiation budget, Atmospheric Chemistry and Physics, 7, 5061–5079, doi: 10.5194/acp-7-5061-2007, 2007.

Law, K. S., Fierli, F., Cairo, F., Schlager, H., Borrmann, S., Streibel, M., Real, E., Kunkel, D., Schiller, C., Ravegnani, F., Ulanovsky, A., D'Amato, F., Viciani, S., and Volk, C. M.: Air mass origins influencing TTL chemical composition over West Africa during 2006 summer monsoon, Atmospheric Chemistry and Physics, 10, 10 753–10 770, doi: 10.5194/acp-10-10753-2010, 2010.

Lawrence, M. G. and Lelieveld, J.: Atmospheric pollutant outflow from southern Asia: a review, Atmospheric Chemistry and Physics, 10, 11 017–11 096, doi: 10.5194/acp-10-11017-2010, 2010.

Lawrence, M. G. and Rasch, P. J.: Tracer Transport in Deep Convective Updrafts: Plume Ensemble versus Bulk Formulations, Journal of the Atmospheric Sciences, 62, 2880–2894, doi: 10.1175/JAS3505.1, URL .1, 2005.

Lawrence, M. G. and Salzmann, M.: On interpreting studies of tracer transport by deep cumulus convection and its effects on atmospheric chemistry, Atmospheric Chemistry and Physics, 8, 6037–6050, doi: 10.5194/acp-8-6037-2008, 2008.

Lawrence, M. G., Crutzen, P. J., Rasch, P. J., Eaton, B. E., and Mahowald, N. M.: A model for studies of tropospheric photochemistry: Description, global distributions, and evaluation, Journal of Geophysical Research, 104, 26,245–26,277, doi: 10.1029/1999JD900425, 1999.

Lawrence, M. G., Butler, T. M., Steinkamp, J., Gurjar, B. R., and Lelieveld, J.: Regional pollution potentials of megacities and other major population centers, Atmospheric Chemistry and Physics, 7, 3969–3987, doi: 10.5194/acp-7-3969-2007, 2007.

Lelieveld, J., Berresheim, H., Borrmann, S., Crutzen, P. J., Dentener, F. J., Fischer, H., Feichter, J., Flatau, P. J., Heland, J., Holzinger, R., Korrmann, R., Lawrence, M. G., Levin, Z., Markowicz, K. M., Mihalopoulos, N., Minikin, A., Ramanathan, V., de Reus, M., Roelofs, G. J., Scheeren, H. A., Sciare, J., Schlager, H., Schultz, M., Siegmund, P., Steil, B., Stephanou, E. G., Stier, P., Traub, M., Warneke, C., Williams, J., and Ziereis, H.: Global Air Pollution Crossroads over the Mediterranean, Science, 298, 794 –799, doi: 10.1126/science.1075457, 2002.

Lelieveld, J., Brühl, C., Jöckel, P., Steil, B., Crutzen, P. J., Fischer, H., Giorgetta, M. A., Hoor, P., Lawrence, M. G., Sausen, R., and Tost, H.: Stratospheric dryness: model simulations and satellite observations, Atmospheric Chemistry and Physics, 7, 1313–1332, doi: 10.5194/acp-7-1313-2007, 2007.

Lelieveld, J., Kunkel, D., and Lawrence, M. G.: Global risk of radioactive fallout after major nuclear reactor accidents, Atmospheric Chemistry and Physics, 12, 4245–4258, doi: 10.5194/acp-12-4245-2012, 2012a.

Lelieveld, J., Lawrence, M. G., and Kunkel, D.: Comment on "Global risk of radioactive fallout after major nuclear reactor accidents" by J. Lelieveld et al. (2012), Atmospheric Chemistry and Physics Discussions, 12, 19 303–19 309, doi: 10.5194/acpd-12-19303-2012, 2012b.

Leon, J. D., Jaffe, D., Kaspar, J., Knecht, A., Miller, M., Robertson, R., and Schubert, A.: Arrival time and magnitude of airborne fission products from the Fukushima, Japan, reactor incident as measured in Seattle, WA, USA, Journal of Environmental Radioactivity, 102, 1032–1038, doi: 10.1016/j.jenvrad.2011.06.005, 2011.

Li, Q., Jiang, J. H., Wu, D. L., Read, W. G., Livesey, N. J., Waters, J. W., Zhang, Y., Wang, B., Filipiak, M. J., Davis, C. P., Turquety, S., Wu, S., Park, R. J., Yantosca, R. M., and Jacob, D. J.: Convective outflow of South Asian pollution: A global CTM simulation compared with EOS MLS observations, Geophysical Research Letters, 32, 4 PP, doi: 10.1029/2005GL022762, 2005.

Lin, J., Wuebbles, D. J., and Liang, X.: Effects of intercontinental transport on surface ozone over the United States: Present and future assessment with a global model, Geophysical Research Letters, 35, 6 PP., doi: 10.1029/2007GL031415, 2008.

Lin, S. and Rood, R. B.: Multidimensional Flux-Form Semi-Lagrangian Transport Schemes, Monthly Weather Review, 124, 2046–2070, doi: 10.1175/1520-0493(1996)124<2046:MFFSLT>2.0.CO;2, 1996.

Liu, H., Jacob, D. J., Bey, I., Yantosca, R. M., Duncan, B. N., and Sachse, G. W.: Transport pathways for Asian pollution outflow over the Pacific: Interannual and seasonal variations, Journal of Geophysical Research, 108, 26 PP, doi: 10.1029/2002JD003102, 2003.

Liu, J., Mauzerall, D. L., and Horowitz, L. W.: Analysis of seasonal and interannual variability in transpacific transport, Journal of Geophysical Research, 110, 17 PP, doi: 10.1029/2004JD005207, 2005.

Liu, J., Mauzerall, D. L., Horowitz, L. W., Ginoux, P., and Fiore, A. M.: Evaluating intercontinental transport of fine aerosols: (1) Methodology, global aerosol distribution and optical depth, Atmospheric Environment, 43, 4327–4338, doi: 10.1016/j.atmosenv.2009.03.054, 2009.

Lohmann, U. and Roeckner, E.: Design and performance of a new cloud microphysics scheme developed for the ECHAM general circulation model, Climate dynamics, 12, 557–572, doi: 10.1007/BF00207939, 1996.

Lohmann, U., Sausen, R., Bengtsson, L., Perlwitz, J., and Roeckner, E.: The Köppen climate classification as a diagnostic tool for general circulation models, Climate Research, 3, 177–193, 1993.

Mahowald, N. M., Baker, A. R., Bergametti, G., Brooks, N., Duce, R. A., Jickells, T. D., Kubilay, N., Prospero, J. M., and Tegen, I.: Atmospheric global dust cycle and iron inputs to the ocean, Global Biogeochemical Cycles, 19, GB4025, doi: 10.1029/2004GB002402, 2005.

Mari, C., Evans, M. J., Palmer, P. I., Jacob, D. J., and Sachse, G. W.: Export of Asian pollution during two cold front episodes of the TRACE-P experiment, Journal of Geophysical Research, 109, D15S17, doi: 10.1029/2003JD004307, 2004.

Mayer, B. and Kylling, A.: Technical note: The libRadtran software package for radiative transfer calculations - description and examples of use, Atmospheric Chemistry and Physics, 5, 1855–1877, doi: 10.5194/acp-5-1855-2005, 2005.

Meilinger, S. K.: Heterogeneous chemistry in the tropopause region: Impact of aircraft emissions, Phd thesis, ETH Zürich, doi: 10.3929/ethz-a-004071378, nr.13819, 2000.

Molina, L. T., Kolb, C. E., de Foy, B., Lamb, B. K., Brune, W. H., Jimenez, J. L., Ramos-Villegas, R., Sarmiento, J., Paramo-Figueroa, V. H., Cardenas, B., Gutierrez-Avedoy, V., and Molina, M. J.: Air quality in North America's most populous city – overview of the MCMA-2003 campaign, Atmospheric Chemistry and Physics, 7, 2447–2473, doi: 10.5194/acp-7-2447-2007, 2007.

Molina, L. T., Madronich, S., Gaffney, J. S., Apel, E., de Foy, B., Fast, J., Ferrare, R., Herndon, S., Jimenez, J. L., Lamb, B., Osornio-Vargas, A. R., Russell, P., Schauer, J. J., Stevens, P. S., Volkamer, R., and Zavala, M.: An overview of the MILAGRO 2006 Campaign: Mexico City emissions and their transport and transformation, Atmospheric Chemistry and Physics, 10, 8697–8760, doi: 10.5194/acp-10-8697-2010, 2010.

Molina, M. J. and Molina, L. T.: Megacities and Atmospheric Pollution, Journal of Air and Waste Management Association, 54, 644–680, 2004.

Monks, P., Granier, C., Fuzzi, S., Stohl, A., Williams, M., Akimoto, H., Amann, M., Baklanov, A., Baltensperger, U., Bey, I., Blake, N., Blake, R., Carslaw, K., Cooper, O., Dentener, F., Fowler, D., Fragkou, E., Frost, G., Generoso, S., Ginoux, P., Grewe, V., Guenther, A., Hansson, H., Henne, S., Hjorth, J., Hofzumahaus, A., Huntrieser, H., Isaksen, I., Jenkin, M., Kaiser, J., Kanakidou, M., Klimont, Z., Kulmala, M., Laj, P., Lawrence, M., Lee, J., Liousse, C., Maione, M., McFiggans, G., Metzger, A., Mieville, A., Moussiopoulos, N., Orlando, J., O'Dowd, C., Palmer, P., Parrish, D., Petzold, A., Platt, U., Pöschl, U., Prévôt, A., Reeves, C., Reimann, S., Rudich, Y., Sellegri, K., Steinbrecher, R., Simpson, D., ten Brink, H., Theloke, J., van der Werf, G., Vautard, R., Vestreng, V., Vlachokostas, C., and von Glasow, R.: Atmospheric composition change - global and regional air quality, Atmospheric Environment, 43, 5268–5350, doi: 10.1016/j.atmosenv.2009.08.021, 2009.

Moteki, N., Kondo, Y., Oshima, N., Takegawa, N., Koike, M., Kita, K., Matsui, H., and Kajino, M.: Size dependence of wet removal of black carbon aerosols during transport from the boundary layer to the free troposphere, Geophysical Research Letters, 39, L13 802, doi: 10.1029/2012GL052034, 2012.

Nenes, A., Pandis, S. N., and Pilinis, C.: ISORROPIA: A new thermodynamic equilibrium model for multiphase multicomponent inorganic aerosols, Aquatic Geochemistry, 4, 123–152, doi: 10.1023/A:1009604003981, 1998.

Newell, R. E. and Evans, M. J.: Seasonal changes in pollutant transport to the North Pacific: The relative importance of Asian and European sources, Geophysical Research Letters, 27, 2509–2512, URL http://www.agu.org/journals/gl/v027/i016/2000GL011501/, 2000.

Nordeng, T.: Extended versions of the convective parametrization scheme at ECMWF and their impact on the mean and transient activity of the model in the tropics, Tech. Rep. 206, European Centre for Medium-Range Weather Forecasts, 1994.

NRC: Reactor Safety Study – An Assessment of Accident Risk in U.S. Commercial Nuclear Power Plants, WASH-1400, Tech. Rep. NUREG 75/014, Nuclear Regulatory Commission, 1975.

NRC: Severe Accident Risks – An Assessment for Five U.S. Nuclear Power Plants, Tech. Rep. NUREG 1150, Nuclear Regulatory Commission, 1990.

Okin, G. S., Mahowald, N., Chadwick, O. A., and Artaxo, P.: Impact of desert dust on the biogeochemistry of phosphorus in terrestrial ecosystems, Global Biogeochemical Cycles, 18, GB2005, doi: 10.1029/2003GB002145, 2004.

Owen, R. C., Cooper, O. R., Stohl, A., and Honrath, R. E.: An analysis of the mechanisms of North American pollutant transport to the central North Atlantic lower free troposphere, Journal of Geophysical Research, 111, 14 PP, doi: 10.1029/2006JD007062, 2006.

Park, R. J., Jacob, D. J., Chin, M., and Martin, R. V.: Sources of carbonaceous aerosols over the United States and implications for natural visibility, Journal of Geophysical Research, 108, 19 PP, doi: 10.1029/2002JD003190, 2003.

Parker, D. E.: Urban heat island effects on estimates of observed climate change, Wiley Interdisciplinary Reviews: Climate Change, 1, 123–133, doi: 10.1002/wcc.21, 2010.

Parrish, D. D. and Zhu, T.: Clean Air for Megacities, Science, 326, 674–675, doi: 10.1126/science.1176064, 2009.

Parrish, D. D., Kuster, W. C., Shao, M., Yokouchi, Y., Kondo, Y., Goldan, P. D., de Gouw, J. A., Koike, M., and Shirai, T.: Comparison of air pollutant emissions among mega-cities, Atmospheric Environment, 43, 6435–6441, doi: 10.1016/j.atmosenv.2009.06.024, 2009.

Parrish, D. D., Singh, H. B., Molina, L., and Madronich, S.: Air quality progress in North American megacities: A review, Atmospheric Environment, 45, 7015–7025, doi: 10.1016/j.atmosenv.2011.09.039, 2011.

Peel, M. C., Finlayson, B. L., and McMahon, T. A.: Updated world map of the Köppen-Geiger climate classification, Hydrology and Earth System Sciences, 11, 1633–1644, doi: 10.5194/

hess-11-1633-2007, 2007.

Peplow, M.: Special Report: Counting the dead, Nature, 440, 982–983, doi: 10.1038/440982a, 2006.

Persson, C., Rodhe, H., and De Geer, L.: The Chernobyl accident - A meteorological analysis of how radionucleides reached Sweden, Tech. Rep. RMK No. 55, Swedish Meteorological and Hydrological Institute, Nörköping, 49 pp., 1986.

Pope, C. A., Ezzati, M., and Dockery, D. W.: Fine-Particulate Air Pollution and Life Expectancy in the United States, New England Journal of Medicine, 360, 376–386, doi: doi: 10.1056/NEJMsa0805646, 2009.

Pozzer, A., Jöckel, P., Tost, H., Sander, R., Ganzeveld, L., Kerkweg, A., and Lelieveld, J.: Simulating organic species with the global atmospheric chemistry general circulation model ECHAM5/MESSy1: a comparison of model results with observations, Atmospheric Chemistry and Physics, 7, 2527–2550, doi: 10.5194/acp-7-2527-2007, 2007.

Pozzer, A., Jöckel, P., and Van Aardenne, J.: The influence of the vertical distribution of emissions on tropospheric chemistry, Atmospheric Chemistry and Physics, 9, 9417–9432, doi: 10.5194/acp-9-9417-2009, 2009.

Pozzer, A., de Meij, A., Pringle, K. J., Tost, H., Doering, U. M., van Aardenne, J., and Lelieveld, J.: Distributions and regional budgets of aerosols and their precursors simulated with the EMAC chemistry-climate model, Atmospheric Chemistry and Physics, 12, 961–987, doi: 10.5194/acp-12-961-2012, 2012a.

Pozzer, A., Zimmermann, P., Doering, U., van Aardenne, J., Tost, H., Dentener, F., Janssens-Maenhout, G., and Lelieveld, J.: Effects of business-as-usual anthropogenic emissions on air quality, Atmospheric Chemistry and Physics, 12, 6915–6937, doi: 10.5194/acp-12-6915-2012, 2012b.

Pregger, T. and Friedrich, R.: Effective pollutant emission heights for atmospheric transport modelling based on real-world information, Environmental Pollution, 157, 552–560, doi: 16/j.envpol.2008.09.027, 2009.

Price, C. and Rind, D.: Modeling Global Lightning Distributions in a General Circulation Model, Monthly Weather Review, 122, 1930–1939, doi: 10.1175/1520-0493(1994)122<1930:MGLDIA>2.0.CO;2, 1994.

Price, H. U., Jaffe, D. A., Cooper, O. R., and Doskey, P. V.: Photochemistry, ozone production, and dilution during long-range transport episodes from Eurasia to the northwest United States, Journal of Geophysical Research, 109, 10 PP., doi: 200410.1029/2003JD004400, 2004.

Pringle, K. J., Tost, H., Message, S., Steil, B., Giannadaki, D., Nenes, A., Fountoukis, C., Stier, P., Vignati, E., and Lelieveld, J.: Description and evaluation of GMXe: a new aerosol submodel for global simulations (v1), Geoscientific Model Development, 3, 391–412, doi: 10.5194/gmd-3-391-2010, 2010a.

Pringle, K. J., Tost, H., Pozzer, A., Pöschl, U., and Lelieveld, J.: Global distribution of the effective aerosol hygroscopicity parameter for CCN activation, Atmospheric Chemistry and Physics, 10, 5241–5255, doi: 10.5194/acp-10-5241-2010, 2010b.

Prinn, R. G., Weiss, R. F., Fraser, P. J., Simmonds, P. G., Cunnold, D. M., Alyea, F. N., O'Doherty, S., Salameh, P., Miller, B. R., Huang, J., Wang, R. H. J., Hartley, D. E., Harth, C., Steele, L. P., Sturrock, G., Midgley, P. M., and McCulloch, A.: A history of chemically and radiatively important gases in air deduced from ALE/GAGE/AGAGE, Journal of Geophysical Research, 105, 17 751–17,792, doi: 10.1029/2000JD900141, 2000.

Prospero, J. M., Bonatti, E., Schubert, C., and Carlson, T. N.: Dust in the Caribbean atmosphere traced to an African dust storm, Earth and Planetary Science Letters, 9, 287–293, doi: 16/0012-821X(70)90039-7, 1970.

Pruppacher, H. R. and Klett, J.: Microphysics of Clouds and Precipitation, Kluwer Acad. Publ., 2000.

Pöschl, U.: Atmospheric Aerosols: Composition, Transformation, Climate and Health Effects, Angewandte Chemie International Edition, 44, 7520–7540, doi: 10.1002/anie.200501122, 2005.

Ramanathan, V., Li, F., Ramana, M. V., Praveen, P. S., Kim, D., Corrigan, C. E., Nguyen, H., Stone, E. A., Schauer, J. J., Carmichael, G. R., Adhikary, B., and Yoon, S. C.: Atmospheric brown clouds: Hemispherical and regional variations in long-range transport, absorption, and radiative forcing, Journal of Geophysical Research, 112, 26 PP., doi: 200710.1029/2006JD008124, 2007.

Ramankutty, N., Evan, A. T., Monfreda, C., and Foley, J. A.: Farming the planet: 1. Geographic distribution of global agricultural lands in the year 2000, Global Biogeochemical Cycles, 22, 19 PP, doi: 10.1029/2007GB002952, 2008.

Rasch, P. J. and Lawrence, M.: Recent developments in transport methods at NCAR, Tech. Rep. 265, Max-Planck-Institute for Meteorology, Hamburg, Germany, edited by B. Machenhauer, 1998.

Rasch, P. J., Mahowald, N. M., and Eaton, B. E.: Representations of transport, convection, and the hydrologic cycle in chemical transport models: Implications for the modeling of short-lived and soluble species, Journal of Geophysical Research, 102, PP. 28,127–28,138, doi: 10.1029/97JD02087, 1997.

Real, E., Orlandi, E., Law, K. S., Fierli, F., Josset, D., Cairo, F., Schlager, H., Borrmann, S., Kunkel, D., Volk, C. M., McQuaid, J. B., Stewart, D. J., Lee, J., Lewis, A. C., Hopkins, J. R., Ravegnani, F., Ulanovski, A., and Liousse, C.: Cross-hemispheric transport of central African biomass burning pollutants: implications for downwind ozone production, Atmospheric Chemistry and Physics, 10, 3027–3046, doi: 10.5194/acp-10-3027-2010, 2010.

Roeckner, E., Bäuml, G., Bonaventura, L., Brokopf, R., Esch, M., Giorgetta, M., Hagemann, S., Kirchner, I., Kornblueh, L., Manzini, E., Rhodin, A., Schlese, U., Schulzweida, U., and Tompkins, A.: The atmospheric general circulation model ECHAM 5. PART I: Model description, Tech. Rep. 349, Max-Planck-Institute for Meteorology, 2003.

Roeckner, E., Brokopf, R., Esch, M., Giorgetta, M., Hagemann, S., Kornblueh, L., Manzini, E., Schlese, U., and Schulzweida, U.: Sensitivity of Simulated Climate to Horizontal and Vertical Resolution in the ECHAM5 Atmosphere Model, Journal of Climate, 19, 3771–3791, doi: 10.1175/JCLI3824.1, 2006.

Sander, R., Kerkweg, A., Jöckel, P., and Lelieveld, J.: Technical note: The new comprehensive atmospheric chemistry module MECCA, Atmospheric Chemistry and Physics, 5, 445–450, doi: 10.5194/acp-5-445-2005, 2005.

Sandu, A. and Sander, R.: Technical note: Simulating chemical systems in Fortran90 and Matlab with the Kinetic PreProcessor KPP-2.1, Atmospheric Chemistry and Physics, 6, 187–195, doi: 10.5194/acp-6-187-2006, 2006.

Schmale, J., Schneider, J., Jurkat, T., Voigt, C., Kalesse, H., Rautenhaus, M., Lichtenstern, M., Schlager, H., Ancellet, G., Arnold, F., Gerding, M., Mattis, I., Wendisch, M., and Borrmann, S.: Aerosol layers from the 2008 eruptions of Mount Okmok and Mount Kasatochi: In situ upper troposphere and lower stratosphere measurements of sulfate and organics over Europe, Journal of Geophysical Research, 115, D00L07, doi: 10.1029/2009JD013628, 2010.

Schmitt, A. and Brunner, B.: Emissions from aviation adn their development over time, in: Pollutants from air traffic – results of atmospheric research 1992-1997. Final report on the BMBF Verbundprogramm "Schadstoffe in der Luftfahrt", Tech. rep., DLR-Mitteilung 97-04, 1997.

Schönwiese, C.-D.: Praktische Statistik für Meteorologen und Geowissenschaftler, Gebr. Borntraeger, Berlin, 2000.

Schroeder, W. H. and Munthe, J.: Atmospheric mercury: An overview, Atmospheric Environment, 32, 809–822, doi: 10.1016/S1352-2310(97)00293-8, 1998.

Seinfeld, J. H. and Pandis, S. N.: Atmospheric Chemistry and Physics - From Air Pollution to Climate Change, John Wiley & Sons, 1998.

Seto, K. C., Güneralp, B., and Hutyra, L. R.: Global forecasts of urban expansion to 2030 and direct impacts on biodiversity and carbon pools, Proceedings of the National Academy of Sciences, 109, 16 083–16 088, doi: 10.1073/pnas.1211658109, 2012.

Sillman, S. and He, D.: Some theoretical results concerning O3-NOx-VOC chemistry and NOx-VOC indicators, Journal of Geophysical Research, 107, 4659, doi: 10.1029/2001JD001123, 2002.

Slinn, W. G. N.: Atmospheric Science and Power Production - 1979, chap. 11 - Precipitation scavenging, Technical Information Center, Office of Scientific and Technical Information, U.S. Department of Energy, Washington, D. C., 1984.

Smith, J. T. and Beresford, N. A.: Chernobyl: catastrophe and consequences, Springer, 2005.

Socioeconomic Data and Applications Center (SEDAC): Gridded Population of the World Version 3 (GPWv3), http://sedac.ciesin.columbia.edu/gpw, [Online, accessed: 04-April-2011], 2005.

Solomon, S., Qin, D., Manning, M., Alley, R., Berntsen, T., Bindoff, N., Chen, Z., Chidthaisong, A., Gregory, J., Hegerl, G., Heimann, M., Hewitson, B., Hoskins, B., Joos, F., Jouzel, J., Kattsov, V., Lohmann, U., Matsuno, T., Molina, M., Nicholls, N., Overpeck, J., Raga, G., Ramaswamy, V., Ren, J., Rusticucci, M., Somerville, R., Stocker, T., Whetton, P., Wood, R., and Wratt, D.: Technical Summary. In: Climate Change 2007: The Physical Science Basis. Contribution of Working Group I to the Fourth Assessment Report of the Intergovernmental Panel on Climate Change, Cambridge University Press, Cambridge, United Kingdom and New York, NY, USA, 2007.

Stanek, L. W., Sacks, J. D., Dutton, S. J., and Dubois, J. B.: Attributing health effects to apportioned components and sources of particulate matter: An evaluation of collective results, Atmospheric Environment, 45, 5655–5663, doi: 10.1016/j.atmosenv.2011.07.023, 2011.

Staudt, A. C., Jacob, D. J., Logan, J. A., Bachiochi, D., Krishnamurti, T. N., and Sachse, G. W.: Continental sources, transoceanic transport, and interhemispheric exchange of carbon monoxide over the Pacific, Journal of Geophysical Research, 106, PP. 32,571–32,589, doi: 200110.1029/2001JD900078, 2001.

Steil, B., Dameris, M., Brühl, C., Crutzen, P. J., Grewe, V., Ponater, M., and Sausen, R.: Development of a chemistry module for GCMs: first results of a multiannual integration, Annales Geophysicae, 16, 205–228, doi: 10.1007/s00585-998-0205-8, 1998.

Stier, P., Feichter, J., Kinne, S., Kloster, S., Vignati, E., Wilson, J., Ganzeveld, L., Tegen, I., Werner, M., Balkanski, Y., Schulz, M., Boucher, O., Minikin, A., and Petzold, A.: The aerosol-climate model ECHAM5-HAM, Atmospheric Chemistry and Physics, 5, 1125–1156, doi: 10.5194/

acp-5-1125-2005, 2005.

Stohl, A., Eckhardt, S., Forster, C., James, P., and Spichtinger, N.: On the pathways and timescales of intercontinental air pollution transport, Journal of Geophysical Research, 107, 4684, doi: 10.1029/2001JD001396, 2002.

Stohl, A., Forster, C., Eckhardt, S., Spichtinger, N., Huntrieser, H., Heland, J., Schlager, H., Wilhelm, S., Arnold, F., and Cooper, O.: A backward modeling study of intercontinental pollution transport using aircraft measurements, Journal of Geophysical Research, 108, 18 PP, doi: 10.1029/2002JD002862, 2003a.

Stohl, A., Huntrieser, H., Richter, A., Beirle, S., Cooper, O. R., Eckhardt, S., Forster, C., James, P., Spichtinger, N., Wenig, M., Wagner, T., Burrows, J. P., and Platt, U.: Rapid intercontinental air pollution transport associated with a meteorological bomb, Atmospheric Chemistry and Physics, 3, 969–985, doi: 10.5194/acp-3-969-2003, 2003b.

Stohl, A., Seibert, P., Wotawa, G., Arnold, D., Burkhart, J. F., Eckhardt, S., Tapia, C., Vargas, A., and Yasunari, T. J.: Xenon-133 and caesium-137 releases into the atmosphere from the Fukushima Dai-ichi nuclear power plant: determination of the source term, atmospheric dispersion, and deposition, Atmospheric Chemistry and Physics, 12, 2313–2343, doi: 10.5194/acp-12-2313-2012, 2012.

Stull, R.: An Introduction to Boundary Layer Meteorology, Kluwer Acad. Publ., 1988.

Takemura, T., Uno, I., Nakajima, T., Higurashi, A., and Sano, I.: Modeling study of long-range transport of Asian dust and anthropogenic aerosols from East Asia, Geophysical Research Letters, 29, 4 PP., doi: 200210.1029/2002GL016251, 2002.

Textor, C., Schulz, M., Guibert, S., Kinne, S., Balkanski, Y., Bauer, S., Berntsen, T., Berglen, T., Boucher, O., Chin, M., Dentener, F., Diehl, T., Easter, R., Feichter, H., Fillmore, D., Ghan, S., Ginoux, P., Gong, S., Grini, A., Hendricks, J., Horowitz, L., Huang, P., Isaksen, I., Iversen, I., Kloster, S., Koch, D., Kirkevåg, A., Kristjansson, J. E., Krol, M., Lauer, A., Lamarque, J. F., Liu, X., Montanaro, V., Myhre, G., Penner, J., Pitari, G., Reddy, S., Seland, Ø., Stier, P., Takemura, T., and Tie, X.: Analysis and quantification of the diversities of aerosol life cycles within AeroCom, Atmospheric Chemistry and Physics, 6, 1777–1813, doi: 10.5194/acp-6-1777-2006, 2006.

Tiedtke, M.: A Comprehensive Mass Flux Scheme for Cumulus Parameterization in Large-Scale Models, Monthly Weather Review, 117, 1779–1800, doi: 10.1175/1520-0493(1989)117<1779:ACMFSF>2.0.CO;2, 1989.

Tompkins, A. M.: A prognostic parameterization for the subgrid-scale variability of water vapor and clouds in large-scale models and its use to diagnose cloud cover, Journal of the Atmospheric Sciences, 59, 1917–1942, doi: 10.1175/1520-0469(2002)059<1917:APPFTS>2.0.CO;2, 2002.

Tost, H.: Global Modelling of Cloud, Convection and Precipitation Influences on Trace Gases and Aerosols, Ph.D. thesis, Rheinische-Friedrich-Wilhems-Universität Bonn, URL http://hss.ulb.uni-bonn.de/2006/0731/0731.htm, urn:nbn:de:hbz:5N-07314, 2006.

Tost, H. and Pringle, K. J.: Improvements of organic aerosol representations and their effects in large-scale atmospheric models, Atmospheric Chemistry and Physics, 12, 8687–8709, doi: 10.5194/acp-12-8687-2012, 2012.

Tost, H., Jöckel, P., Kerkweg, A., Sander, R., and Lelieveld, J.: Technical note: A new comprehensive SCAVenging submodel for global atmospheric chemistry modelling, Atmospheric Chemistry and Physics, 6, 565–574, doi: 10.5194/acp-6-565-2006, 2006a.

Tost, H., Jöckel, P., and Lelieveld, J.: Influence of different convection parameterisations in a GCM, Atmospheric Chemistry and Physics, 6, 5475–5493, doi: 10.5194/acp-6-5475-2006, 2006b.

Tost, H., Jöckel, P., Kerkweg, A., Pozzer, A., Sander, R., and Lelieveld, J.: Global cloud and precipitation chemistry and wet deposition: tropospheric model simulations with ECHAM5/MESSy1, Atmospheric Chemistry and Physics, 7, 2733–2757, doi: 10.5194/acp-7-2733-2007, 2007a.

Tost, H., Jöckel, P., and Lelieveld, J.: Lightning and convection parameterisations – uncertainties in global modelling, Atmospheric Chemistry and Physics, 7, 4553–4568, doi: 10.5194/acp-7-4553-2007, 2007b.

Tost, H., Lawrence, M. G., Brühl, C., Jöckel, P., The GABRIEL Team, and The SCOUT-O3-DARWIN/ACTIVE Team: Uncertainties in atmospheric chemistry modelling due to convection parameterisations and subsequent scavenging, Atmospheric Chemistry and Physics, 10, 1931–1951, doi: 10.5194/acp-10-1931-2010, 2010.

UNECE: The 1979 Geneva Convention on Long-range Transboundary Air Pollution, URL http://www.unece.org/env/lrtap/lrtap_h1.html, 1979.

UNFPA: State of World Population 2007: Unleashing the Potential of Urban Growth, 2007.

van Aardenne, J., Dentener, F., Olivier, J., Peters, J., and Ganzeveld, L.: The EDGAR 3.2 Fast Track 2000 dataset (32FT2000), Tech. rep., PBL Netherlands Environmental Assessment Agency, URL http://themasites.pbl.nl/tridion/en/themasites/edgar/emission_data/edgar_32ft2000/index-2.html, 2005.

Vehkamaki, H., Kulmala, M., Napari, I., Lehtinen, K., and Timmreck, C.: An improved parameterization for sulfuric acid-water nucleation rates for tropospheric and stratospheric conditions, Journal of Geophysical Research, 107, 10 PP, doi: 10.1029/2002JD002184, 2002.

Verma, R. L., Kondo, Y., Oshima, N., Matsui, H., Kita, K., Sahu, L. K., Kato, S., Kajii, Y., Takami, A., and Miyakawa, T.: Seasonal variations of the transport of black carbon and carbon monoxide from the Asian continent to the western Pacific in the boundary layer, Journal of Geophysical Research, 116, 22 PP., doi: 201110.1029/2011JD015830, 2011.

Vignati, E., J., W., and P., S.: M7: An efficient size-resolved aerosol microphysics module for large-scale aerosol transport models, Journal of Geophysical Research, 109, 17 PP., doi: 10.1029/2003JD004485, 2004.

von Kuhlmann, R., Lawrence, M. G., Crutzen, P. J., and Rasch, P. J.: A model for studies of tropospheric ozone and nonmethane hydrocarbons: Model description and ozone results, Journal of Geophysical Research, 108, 22 PP, doi: 10.1029/2002JD002893, 2003.

Wagstrom, K. and Pandis, S.: Contribution of long range transport to local fine particulate matter concerns, Atmospheric Environment, 45, 2730–2735, doi: 10.1016/j.atmosenv.2011.02.040, 2011.

Wagstrom, K. M. and Pandis, S. N.: Source-receptor relationships for fine particulate matter concentrations in the Eastern United States, Atmospheric Environment, 45, 347–356, doi: 10.1016/j.atmosenv.2010.10.019, 2010.

Wang, T., Nie, W., Gao, J., Xue, L. K., Gao, X. M., Wang, X. F., Qiu, J., Poon, C. N., Meinardi, S., Blake, D., Wang, S. L., Ding, A. J., Chai, F. H., Zhang, Q. Z., and Wang, W. X.: Air quality during the 2008 Beijing Olympics: secondary pollutants and regional impact, Atmospheric Chemistry and Physics, 10, 7603–7615, doi: 10.5194/acp-10-7603-2010, 2010.

Watson, J. G.: Visibility: science and regulation, Journal of the Air & Waste Management Association (1995), 52, 628–713, URL http://www.ncbi.nlm.nih.gov/pubmed/12074426, PMID: 12074426, 2002.

Weigel, R., Borrmann, S., Kazil, J., Minikin, A., Stohl, A., Wilson, J. C., Reeves, J. M., Kunkel, D., de Reus, M., Frey, W., Lovejoy, E. R., Volk, C. M., Viciani, S., D'Amato, F., Schiller, C., Peter, T., Schlager, H., Cairo, F., Law, K. S., Shur, G. N., Belyaev, G. V., and Curtius, J.: In situ observations of new particle formation in the tropical upper troposphere: the role of clouds and the nucleation mechanism, Atmospheric Chemistry and Physics, 11, 9983–10 010, doi: 10.5194/acp-11-9983-2011, 2011.

Wesely, M.: Parameterization of surface resistances to gaseous dry deposition in regional-scale numerical models, Atmospheric Environment (1967), 23, 1293 – 1304, doi: DOI:10.1016/0004-6981(89)90153-4, 1989.

WHO: Health Effects of the Chernobyl Accident and Special Health Care Programmes - Report of the UN Chernobyl Forum Expert Group "Health", World Health Organization, Geneva, 2006.

Wilkening, K. E., Barrie, L. A., and Engle, M.: Trans-Pacific Air Pollution, Science, 290, 65 –67, doi: 10.1126/science.290.5489.65, 2000.

Wiman, B. L., Unsworth, M. H., Lindberg, S. E., Bergkvist, B., Jaenicke, R., and Hansson, H.-C.: Perspectives on aerosol deposition to natural surfaces: interactions between aerosol residence times, removal processes, the biosphere and global environmental change, Journal of Aerosol Science, 21, 313 – 338, doi: DOI:10.1016/0021-8502(90)90051-X, 1990.

Winiarek, V., Bocquet, M., Saunier, O., and Mathieu, A.: Estimation of errors in the inverse modeling of accidental release of atmospheric pollutant: Application to the reconstruction of the cesium-137 and iodine-131 source terms from the Fukushima Daiichi power plant, Journal of Geophysical Research, 117, 16 PP., doi: 201210.1029/2011JD016932, 2012.

WMO: International Meteorological Vocabulary, Secretariat to World Meteorological Organization, iSBN: 92-63-02182-1, 1992.

Yanai, M., Esbensen, S., and Chu, J.-H.: Determination of Bulk Properties of Tropical Cloud Clusters from Large-Scale Heat and Moisture Budgets, Journal of the Atmospheric Sciences, 30, 611–627, doi: 10.1175/1520-0469(1973)030<0611:DOBPOT>2.0.CO;2, 1973.

Yasunari, T. J., Stohl, A., Hayano, R. S., Burkhart, J. F., Eckhardt, S., and Yasunari, T.: Cesium-137 deposition and contamination of Japanese soils due to the Fukushima nuclear accident, Proceedings of the National Academy of Sciences, 108, 19 530 –19 534, doi: 10.1073/pnas.1112058108, 2011.

Zhang, D.-L., Shou, Y.-X., and Dickerson, R. R.: Upstream urbanization exacerbates urban heat island effects, Geophysical Research Letters, 36, L24 401, doi: 10.1029/2009GL041082, 2009.

Zhang, G. and McFarlane, N. A.: Sensitivity of climate simulations to the parameterization of cumulus convection in the Canadian climate centre general circulation model, Atmosphere-Ocean, 33, 407–446, doi: 10.1080/07055900.1995.9649539, 1995.

Zhang, Y., Hu, M., Zhong, L., Wiedensohler, A., Liu, S., Andreae, M., Wang, W., and Fan, S.: Regional Integrated Experiments on Air Quality over Pearl River Delta 2004 (PRIDE-PRD2004): Overview, Atmospheric Environment, 42, 6157–6173, doi: 10.1016/j.atmosenv.2008.03.025, 2008.